ISSN 2074-272X

науково-практичний журнал

2024/3

Електротехніка і Електромеханіка

Electrical Engineering & Electromechanics

Електричні машини та апарати
Електротехнічні комплекси та системи
Промислова електроніка
Теоретична електротехніка
Інженерна електрофізика.
Техніка сильних електричних та магнітних полів
Електроізоляційна та кабельна техніка
Електричні станції, мережі і системи

Журнал включено до найвищої категорії «А»
Переліку фахових видань України

З 2019 р. журнал індексується у Scopus

З 2015 р. журнал індексується
у Web of Science Core Collection:
Emerging Sources Citation Index

Electrical Engineering & Electromechanics

Scientific Journal was founded in 2002
Founder – National Technical University «Kharkiv Polytechnic Institute» (Kharkiv, Ukraine)

From no. 1 2019 Journal «Electrical Engineering & Electromechanics» is indexing in **Scopus** and from no. 1 2015 Journal is indexing in **Web of Science Core Collection: Emerging Sources Citation Index (ESCI)**.

Also included in DOAJ (Directory of Open Access Journals), in EBSCO's database, in ProQuest's databases – Advanced Technologies & Aerospace Database and Materials Science & Engineering Database, in Gale/Cengage Learning databases.

Editorial office address:
National Technical University «Kharkiv Polytechnic Institute», Kyrpychova Str., 2, Kharkiv, 61002, Ukraine
phones: +380 57 7076281, +380 67 3594696, **e-mail:** a.m.grechko@gmail.com (**Grechko O.M.)**

ISSN (print) 2074-272X
ISSN (online) 2309-3404

Printed 01 May 2024. Format 60 × 90 ⅛. Paper – offset. Laser printing. Edition 50 copies.
Printed by Printing house «Madrid Ltd» (18, Gudanova Str., Kharkiv, 61024, Ukraine)

Electrical Engineering & Electromechanics
Scientific Journal

no. 3, 2024

Table of Contents

UDC 621.313:536.2.24:539.2 https://doi.org/10.20998/2074-272X.2024.3.01

V.F. Bolyukh, O.I. Kocherga

Efficiency of multi-armature linear pulse electromechanical power and speed converters

Introduction. *High-speed linear pulse electromechanical converters (LPEC) provide acceleration of the executive element in a short active section to high speed with significant displacement, while power-purpose LPECs create powerful power impulses of the executive element on the object of influence with minor movements. One of the areas of improvement of LPEC is the creation of multi-armature structures.* ***Methodology.*** *To analyze the electromechanical characteristics and indicators of LPEC, a mathematical model was used, which takes into account the interconnected electrical, magnetic, mechanical and thermal processes that occur when connected to a pulse energy source with a capacitive energy storage. The main results of the calculations were performed in the COMSOL Multiphysics software environment and confirmed by experimental studies in laboratory conditions.* ***Results.*** *The features of the electromechanical processes of multi-armature LPECs are established and their indicators are determined. With the help of efficiency criteria, which take into account electrical, power, speed and magnetic indicators in a relative form with different options for their evaluation strategy, it was established that multi-armature LPECs for power purposes have increased efficiency, and for high-speed LPECs the use of multi-armature configurations is impractical. The conducted experimental studies confirm the reliability of the calculated results.* ***Originality.*** *It has been established that almost all multi-armature LPECs for power purposes have higher efficiency compared to a converter with one armature, and for high-speed LPECs it is advisable to use traditional LPECs with one armature.* ***Practical value.*** *On the basis of multi-armature LPECs, models of an electromagnetic UAV catapult, a magnetic pulse press for ceramic powder materials, an electromechanical device for dumping ice and snow deposits from a power line wire, a device for destroying information on a solid-state digital SSD drive have been developed and tested.* References 20, tables 4, figures 8.

Key words: **linear pulsed electromechanical converter, multi-armature configuration, continuous electrically conductive armature, coil armature, ferromagnetic armature, efficiency criterion, experimental studies.**

Вступ. *Лінійні імпульсні електромеханічні перетворювачі (ЛІЕП) швидкісного призначення забезпечують розгін виконавчого елемента на короткій активній ділянці до високої швидкості зі значним його переміщенням, а ЛІЕП силового призначення створюють потужні силові імпульси виконавчим елементом на об'єкт впливу при незначних його переміщеннях. Одним із напрямків удосконалення ЛІЕП є створення багатоякірних конструкцій.* ***Методика.*** *Для аналізу електромеханічних характеристик та показників ЛІЕП використана математична модель, в якій враховані взаємопов'язані електричні, магнітні, механічні та теплові процеси, які виникають при підключенні до імпульсного джерела енергії з ємнісним накопичувачем енергії. Основні результати розрахунків виконані в програмному середовищі COMSOL Multiphysics і підтверджені експериментальними дослідженнями в лабораторних умовах.* ***Результати.*** *Встановлені особливості електромеханічних процесів багатоякірних ЛІЕП та визначено їх показники. За допомогою критеріїв ефективності, які у відносному вигляді враховують електричні, силові, швидкісні та магнітні показники при різних варіантах стратегії їх оцінки, встановлено, що багатоякірні ЛІЕП силового призначення мають підвищену ефективність, а для ЛІЕП швидкісного призначення використання багатоякірних конфігурацій недоцільно. Проведені експериментальні дослідження підтверджують достовірність розрахункових результатів.* ***Наукова новизна.*** *Встановлено, що практично всі багатоякірні ЛІЕП силового призначення мають більш високу ефективність в порівнянні з перетворювачем з одним якорем, а для ЛІЕП швидкісного призначення доцільно застосовувати традиційні ЛІЕП з одним якорем.* ***Практична цінність.*** *На базі багатоякірних ЛІЕП розроблено та випробувано моделі електромагнітної катапульти БПЛА, магнітно-імпульсного пресу для керамічних порошкових матеріалів, електромеханічного пристрою для скидання ожеледних і снігових відкладень з проводу лінії електропередачі, пристрою для знищення інформації на твердотільному цифровому SSD накопичувачі.* Бібл. 20, табл. 4, рис. 8.

Ключові слова: **лінійний імпульсний електромеханічний перетворювач, багатоякірна конфігурація, суцільний електропровідний якір, котушковий якір, феромагнітний якір, критерій ефективності, експериментальні дослідження.**

Introduction. One of the promising devices of modern electromechanics are linear pulse electromechanical converters (LPEC) for speed and power purposes. High-speed LPECs provide acceleration of the executive element in a short active section to high speed with significant movement of it, and power LPECs create powerful power impulses of the executive element on the object of influence with minor movements [1-4].

LPECs are characterized by significant electromagnetic and mechanical loads, which significantly exceed similar indicators of traditional linear electric motors with long-term operation. They are used in many areas of science, technology and security. Among the technological applications, it is possible to mention shock-condenser welding, metal processing, stamping, riveting, assembly and forming operations, etc. These converters are used for testing systems for shock loads, high-speed electrical devices, destruction of information in case of unauthorized access, valve and switching equipment, seismic sources, cleaning of bunkers from remaining materials and power lines from icing, launchers, etc. [5-10].

In the coaxial LPEC, opposite the disk inductor winding (IW), which is excited by current from a pulsed electric source with a capacitive energy storage (CES), a disk armature is located, which moves in the axial direction. The most widespread are induction, electromagnetic and electrodynamics types of LPEC.

In the induction-type LPEC, the armature is made solid in the form of a thin conductive disk. In the LPEC of the electrodynamics type, the armature is made in the form of a multi-turn coil, which is connected in series or in parallel with the IW. In the LPEC of the electromagnetic type, the armature is made in the form of a relatively thick ferromagnetic disk.

In the LPEC of the electromagnetic type, electromagnetic forces (EMF) of attraction act on the ferromagnetic armature (FA) from the side IW. In the LPEC of the electrodynamics type, electrodynamic forces (EDF) of repulsion arise between the coil armature (CA) and the stationary IW. In the induction-type LPEC, when the magnetic field IW interacts with the induced current

in the solid electrically conductive armature (EA), a repulsive EDF occurs.

The specified LPECs are characterized by different speeds of electromagnetic processes, different directions of action of electrodynamic and electromagnetic forces relative to IW, etc. In order to strengthen the power effect and increase the speed indicators, ferromagnetic cores and shields, additional secondary windings, mechanical power elements, cryogenic cooling, etc. are used in LPEC [11-13]. But the analysis of the specified types of LPEC with a traditional configuration with one armature showed that their efficiency remains at a rather low level and their efficiency when working as an accelerator does not exceed 10-15 % [14].

One of the areas of improvement of LPEC is the creation of multi-armature structures [15, 16]. In [17], a LPEC with two EA, which form an increased pulse of mechanical force on two opposite sides, is described. The work [18] presents the design scheme of LPEC, which consists of two stationary IW and movable EA and FA. The armatures are interconnected through a system of rods, which in turn are connected to the executive element. But the lack of a comprehensive study of the electromechanical characteristics and main indicators of multi-armature LPECs makes it impossible to determine effective configurations for various purposes.

The **purpose** of the work is to determine configurations of LPEC that provide increased efficiency due to the use of several armatures interacting with an inductor that is excited by a pulsed source of energy from CES.

Multi-armature LPECs must provide a unidirectional force on the executive element at high-speed assignment or the summation of all forces at the power assignment of the converter.

Mathematical model of LPEC. Interrelated electromagnetic, thermal and mechanical processes occur in LPEC, which occur when connected to a pulse energy source from CES.

We consider that the coaxial LPEC has a disk IW and the movement of the disk armatures is carried out along the z axis. Consider the LPEC, which includes stationary IW and FA, moving CA and EA. For the instantaneous values of the tangential component of the vector magnetic potential $\boldsymbol{A}_\varphi$ in the cylindrical coordinate system, we write down the system of differential equations:

$$\gamma_1\frac{\partial A_{1\varphi}}{\partial t}+\frac{\partial}{\partial z}\left(\frac{1}{\mu_0}\frac{\partial A_{1\varphi}}{\partial z}\right)+\frac{\partial}{\partial r}\left(\frac{1}{\mu_0 r}\frac{\partial(rA_{1\varphi})}{\partial r}\right)=-j_1(t)\,; \quad (1)$$

$$\gamma_2\frac{\partial A_{2\varphi}}{\partial t}+\frac{\partial}{\partial z}\left(\frac{1}{\mu_0}\frac{\partial A_{2\varphi}}{\partial z}\right)+\frac{\partial}{\partial r}\left(\frac{1}{\mu_0 r}\frac{\partial(rA_{2\varphi})}{\partial r}\right)-$$
$$-v_2(t)\frac{\gamma_2}{\mu_0}\frac{\partial A_{2\varphi}}{\partial z}=-j_2(t); \quad (2)$$

$$\gamma_3\frac{\partial A_{3\varphi}}{\partial t}+\frac{\partial}{\partial z}\left(\frac{1}{\mu_0}\frac{\partial A_{3\varphi}}{\partial z}\right)+\frac{\partial}{\partial r}\left(\frac{1}{\mu_0 r}\frac{\partial(rA_{3\varphi})}{\partial r}\right)-$$
$$-v_3(t)\frac{\gamma_3}{\mu_0}\frac{\partial A_{3\varphi}}{\partial z}=0; \quad (3)$$

$$\gamma_4\frac{\partial A_{4\varphi}}{\partial t}+\frac{\partial}{\partial z}\left(\frac{1}{\mu_4}\frac{\partial A_{4\varphi}}{\partial z}\right)+\frac{\partial}{\partial r}\left(\frac{1}{\mu_4 r}\frac{\partial(rA_{4\varphi})}{\partial r}\right)=0\,, \quad (4)$$

$$\frac{\partial}{\partial z}\left(\frac{1}{\mu_0}\frac{\partial A_{5\varphi}}{\partial z}\right)+\frac{\partial}{\partial r}\left(\frac{1}{\mu_0 r}\frac{\partial(rA_{5\varphi})}{\partial r}\right)=0\,, \quad (5)$$

where the index of the element (space) n = 1 – IW, 2 – CA, 3 – EA, 4 – FA, 5 – airspace; $i_1(t)$, $i_2(t)$ – currents IW and CA, respectively; $j_1(t) = i_1(t)N_1S_1^{-1}k_1$, $j_2(t) = i_2(t)N_2S_2^{-1}k_2$ – current density IW and CA, respectively; γ_n – specific conductivity of the material of the n^{th} element; μ_0 – magnetic constant; μ_4 – magnetic permeability FA; $v_2(t)$, $v_3(t)$ – speed CA and EA, respectively; N_1, N_2 – the number of turns IW and CA, respectively; S_1, S_2 – cross-sectional area IW and CA, respectively; k_1, k_2 – filling factor IW and CA, respectively.

Differential equations (1) – (5) are supplemented with boundary and initial conditions.

To calculate the axial component of the force acting on the corresponding LPEC armature, we use Maxwell's tension tensor:

$$f_z=\oint_S 2\pi r T_z\,\mathrm{d}s=\frac{1}{\mu_0}\oint_S 2\pi r(B_r\cdot B_z)\,\mathrm{d}s\,, \quad (6)$$

where $B_r=-\dfrac{\partial A_\varphi}{\partial z}$, $B_z=\dfrac{1}{r}\dfrac{\partial(rA_\varphi)}{\partial r}$ are components of the magnetic field induction vector $\boldsymbol{B}$.

The electrical circuit of the LPEC with the serial connection of the stationary IW with the movable CA, which interacts with the movable EA, can be represented by the substitution diagram (Fig. 1) and described by the system of equations:

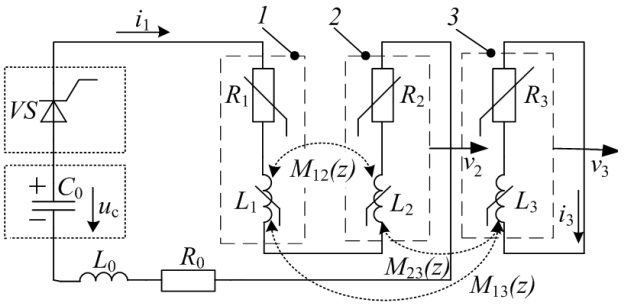

Fig. 1. Electrical diagram of LPEC with a series connection of IW (1) with CA (2), which interacts with EA (3)

$$2\pi\frac{N_1}{S_1}\cdot\int_{S_1}\frac{\mathrm{d}rA_{1\varphi}}{\mathrm{d}t}\mathrm{d}r\mathrm{d}z+2\pi\frac{N_2}{S_2}\cdot\int_{S_2}\frac{\mathrm{d}rA_{2\varphi}}{\mathrm{d}t}\mathrm{d}r\mathrm{d}z+L_0\frac{\mathrm{d}i_1}{\mathrm{d}t}+$$
$$+i_1\left[R_0+R_1(T_1)+R_2(T_2)\right]+u_c=0; \quad (7)$$

$$2\pi\frac{N_3}{S_3}\cdot\int_{S_3}\frac{\mathrm{d}rA_{3\varphi}}{\mathrm{d}t}\mathrm{d}r\mathrm{d}z+i_3R_3(T_3)=0\,; \quad (8)$$

$$\frac{\mathrm{d}u_c}{\mathrm{d}t}=\frac{i_1}{C_0}\,, \quad (9)$$

where R_0, L_0 – resistance and inductance of power cables, respectively; $R_1(T_1)$, $R_2(T_2)$, $R_3(T_3)$ – resistance IW, CA and EA, respectively; T_1, T_2, T_3 – temperature IW, CA and EA, respectively; i_3 – current EA; u_c – voltage of CES; C_0 – CES capacity; S_3 – cross-sectional area EA.

The system of equations describing the electrical and magnetic connections between the active elements of the LPEC in parallel connection of IW with movable CA, which interacts with movable EA, takes the following form:

$$2\pi\frac{N_1}{S_1}\cdot\int_{S_1}\frac{\mathrm{d}rA_{1\varphi}}{\mathrm{d}t}\mathrm{d}r\mathrm{d}z+L_0\frac{\mathrm{d}i}{\mathrm{d}t}+R_0i+i_1R_1(T_1)+u_C=0\,; \quad (10)$$

$$2\pi\frac{N_2}{S_2}\cdot\int_{S_2}\frac{\mathrm{d}rA_{2\varphi}}{\mathrm{d}t}\mathrm{d}r\mathrm{d}z+L_0\frac{\mathrm{d}i}{\mathrm{d}t}+R_0i+i_2R_2(T_2)+u_C=0\,; \quad (11)$$

$$2\pi\frac{N_3}{S_3}\cdot\int_{S_3}\frac{\mathrm{d}rA_{3\varphi}}{\mathrm{d}t}\mathrm{d}r\mathrm{d}z+i_3R_3(T_3)=0\,; \quad (12)$$

$$\frac{\mathrm{d}u_c}{\mathrm{d}t}=\frac{i}{C_0}, \quad (13)$$

where $i(t) = i_1(t) + i_2(t)$ – current of CES.

The mechanical processes of LPEC are described by a system of equations:

$$(m_3+m_e)\frac{\mathrm{d}v_3}{\mathrm{d}t}=f_3(t)-K_{mp}v_3(t)\,; \quad (14)$$

$$(m_3+m_2+m_e)\frac{\mathrm{d}v_2}{\mathrm{d}t}=f_2(t)-K_{mp}[v_3(t)+v_2(t)]-$$
$$-K_B[v_3(t)+v_2(t)]^2-K_P[z_3(t)+z_2(t)], \quad (15)$$

where m_2, m_3, m_e – the mass of CA, EA and the executive element, respectively; $z_2(t)$, $z_3(t)$ – moving CA and EA, respectively; $f_2(t)$, f_3it) – EDF on CA and EA, respectively; K_{mp} – coefficient of dynamic friction; K_B – drag coefficient; K_P – coefficient of elasticity of the return element (spring).

The system of equations (14), (15) is supplemented by the corresponding initial conditions.

The temperature T_n in the n^{th} active current-conducting element of the LPEC is described as:

$$c_n(T)\gamma_n\frac{\partial T_n}{\partial t}=\lambda_n(T)\left(\frac{\partial^2T_n}{\partial r^2}+\frac{1}{r}\frac{\partial T_n}{\partial r}+\frac{\partial^2T_n}{\partial z^2}\right)+$$
$$+j_n^2(t)k_n\rho_n(T), \quad (16)$$

where $c_n(T)$, γ_n, $\lambda_n(T)$, $\rho_n(T)$ – specific heat capacity, material density, thermal conductivity coefficient, specific resistance of the n^{th} active element.

On the cooled surfaces of the active elements, the system of equations (16) is supplemented by boundary conditions of the third kind, and on the axis of symmetry of the LPEC by boundary conditions of the second kind. To implement the mathematical model, a system of partial differential equations with respect to spatial and temporal variables is used using the software package Comsol Multiphysics 5.3.

Analysis of indicators of multi-armature LPEC. For the analysis of LPEC, we introduce the following notations. In the presence of a continuous conductive armature, «E» is added, in the presence of a coil armature, «C», and in the presence of a ferromagnetic armature, «F». We will analyze multi-armature converters with two armatures (LPEC-E2, LPEC-C-E, LPEC-E-F, LPEC-C-F) and three armatures (LPEC-C-E2, LPEC-C-E-F). With a parallel connection, CA with IW – C_p, with a serial connection – C_s. CA and IW are wound in opposite directions so that repulsion forces act between them.

Let's consider the electromechanical characteristics of LPEC with the following parameters. IW (CA): outer diameter D_{ex1}=100 mm, inner diameter D_{in1}=10 mm, height H_1=10 mm, number of turns N_1=46, cross section of copper bus $S_1=a_1\cdot b_1$=1.8·4.8=8.64 mm^2. EA: material – copper M2, outer diameter D_{ex3}=100 mm, inner diameter D_{in3}=10 mm, height H_3=3 mm. FA: material – Steel 3, outer diameter D_{ex4}=100 mm, inner diameter D_{in4}=10 mm, height H_4=12 mm. The distance between IW and CA h_{12}=2 mm, between CA and EA h_{23}=2 mm. The power source includes a CES with parameters C_0=2500 μF, U_0=450 V and a reverse diode that provides a polar aperiodic pulse of the excitation current [19].

We will use the following designations of elements. Active elements: 1 – IW, 2 – front EA, 3 – rear EA, 4 – CA, 5 – FA. Passive elements: 6 – executive element, 7 – movable or immovable fixators, 8 – object of influence, 9 – internal power ferromagnetic device (Fig. 2).

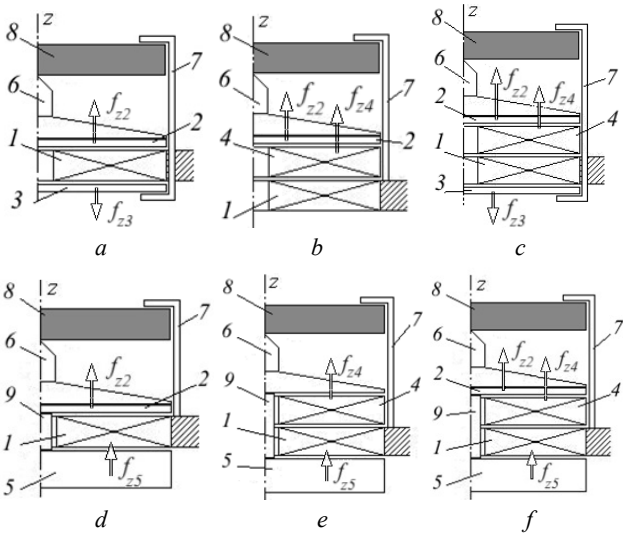

Fig. 2. Design schemes of multi-armature LPEC for power purposes: LPEC-E2 (*a*), LPEC-C-E (*b*), LPEC-C-E2 (*c*), LPEC-E-F (*d*), LPEC-C-F (*e*), LPEC-C-E-F (*f*)

In multi-armature LPECs of power purpose, slow-moving armatures transmit axially directed force to the object of influence through an executive element in the form of a striker, external fasteners and internal power devices.

For the LPEC of power purpose, we will conduct an analysis of the amplitude f_{zm} and the magnitude of the impulse $F_z=\int f_z(z,t)\mathrm{d}t$ of axial electrodynamic and electromagnetic forces that are transmitted to the object of influence.

In LPEC-E2, two EA cover IW from opposite sides and act on the movable latch, forming oppositely directed EDF repulsions of the front 2 f_{z2} and rear 3 f_{z3} EA (Fig. 2,*a*). In this LPEC, the current density in IW j_1 has the form of a polar aperiodic pulse, while the current density in the front j_2 and in the back j_3 EA for 1.3 ms have the opposite polarity. The amplitude of the current density in IW j_{1m}=266.7 A/mm^2, and in the armatures – $j_{2,3m}$=390.2 A/mm^2. The EDF pulses acting on the front F_{z2} and rear F_{z3} EA have the opposite polarity. The EDF amplitudes acting between the two EA are $f_{z2,3m}$=8.55 kN, and the magnitude of the EDF pulse is $F_{z2,3}$=3.3 N·s. The total force is transmitted from armatures 2 and 3 to the impact object 8 with the help of movable retainers 7.

In the LPEC-C_p-E with the front EA and CA, which is connected in parallel with IW, the force is transmitted to the fixed retainer (Fig. 2,*b*). With such a connection, the magnitudes of the currents in IW and CA differ due to induction interaction with EA. EDF acting on EA f_{z2} and CA f_{z4} form corresponding EDF pulses F_{z2} and F_{z4}. Amplitudes of EDF acting on EA f_{z2m}=7.28 kN, and on CA f_{z4m}=5.72 kN. The corresponding EDF pulse values are F_{z2}=2.35 N·s and F_{z4}=6.04 N·s.

In LPEC-C_p-E2, CA is connected in parallel with IW, and the front 2 and rear 3 EA act on the movable latch 7 (Fig. 2,*c*). Oppositely directed EDF act on each EA, the amplitudes of which are $f_{z2,3m}$=6.42 kN. EDF act on CA, the amplitude of which is f_{z4m}=4.09 kN. The corresponding values of EDF pulses acting on EA and CA are $F_{z2,3}$=1.98 N·s and F_{z4}=4.07 N·s.

In the LPEC-E-F with a fixed latch 7 and an internal power device 9, unidirectional action of all forces on the object of influence 8 is ensured. Amplitudes of the current density in IW j_{1m}=156 A/mm^2, in EA j_{2m}=385 A/mm^2 (Fig. 2,*d*) However, the current in EA changes polarity to the opposite after 2 ms. The magnitude of the EDF pulse is F_{z2}=5.42 N·s, and the EMF pulse is F_{z5}=3.49 N·s.

In LPEC-C_p-F, forces are transmitted to the object of influence 8 (Fig. 2,*e*) through the internal device 9 and the fixed retainer 7. The currents of density j_1 in IW and j_4 in CA have the form of a polar pulse with a short front and a long back front. Amplitudes of current densities IW j_{1m}=177.7 A/mm^2, CA j_{4m}=204.7 A/mm^2. The smaller value of the current amplitude in IW can be explained by the influence of the magnetic field on it from the side of the adjacent FA 5. CA is acted upon by repulsive EDF f_{z4}, the amplitude of which is f_{z4m}=13.03 kN. The electromagnetic attraction f_{z5} acting on FA is much smaller and their amplitude is only f_{z5m}=1.19 kN. The value of the EDF pulse is F_{z4}=12.25 N·s, and the value of the EMF pulse is F_{z5}=1.2 N·s. In this converter, the value of F_z is 1.21 times greater than in a LPEC with one CA and almost 2 times more than in a LPEC with one FA.

In LIEP-C_p-E-F IW 1 interacts with FA 5 and with CA 4, which, in turn, interacts with EA 2 (Fig. 2,*f*). The currents in IW and CA have the form of an aperiodic polar pulse with a short leading edge and a long trailing edge. At the same time, the amplitudes of the current densities in IW and CA are different: j_{1m}=168.8 A/mm^2, j_{4m}=279.8 A/mm^2. The current amplitude in EA is j_{2m}=368.7 A/mm^2. The current in EA after reaching the maximum value decreases and changes polarity after 1 ms. Electromagnetic f_{z5} and electrodynamic f_{z4} forces during the entire work process maintain their polarities, and EDF f_{z2} acting on EA practically disappear after 1 ms. Repulsive EDF with amplitude f_{z4m}=5.58 kN act on CA from side IW. FA is acted upon by EMF attraction f_{z5}, with amplitude f_{z5m}=0.92 kN. The amplitude of the EDF acting on EA is f_{z2m} =7.48 kN. The magnitude of the EDF impulse acting on CA is F_{z4}=6.59 N·s, the magnitude of the EMF impulse acting on FA is F_{z5}=0.89 N·s, the magnitude of the EDF impulse acting on EA is F_{z2}=2,45 N·s.

Figure 3 presents the distributions of current densities j and magnetic field induction B in active elements at the moment of the maximum value of the current in IW for multi-armature LPEC of power purpose.

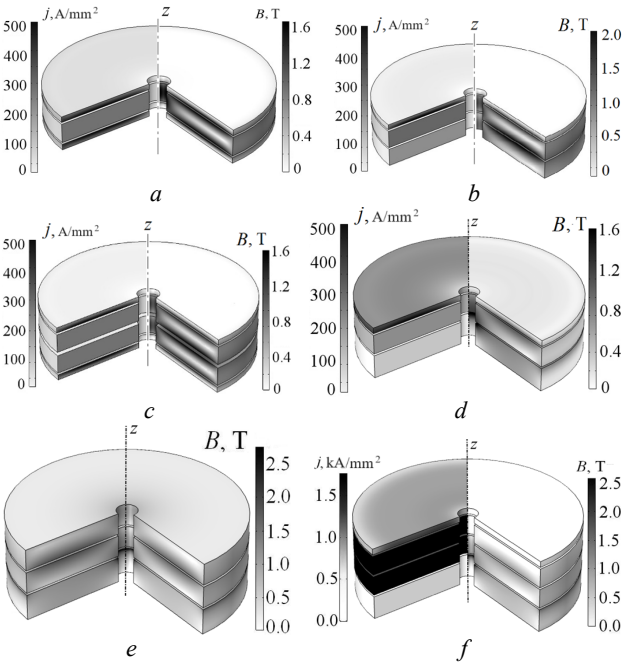

Fig. 3. Distributions of current densities j and magnetic field induction B in active elements at the moment of the maximum value of the current in IW for multi-armature LPEC of power purpose: LPEC-E2 (a), LPEC-C-E (b), LPEC-C-E2 (c), LPEC-E-F (d), LPEC-C-F (e), LPEC-C-E-F (f)

Figure 4 presents the electromechanical characteristics of LPEC-C_p-E2 and LPEC-C_p-F, which show that in the presence of FA, the amplitudes of the currents in IW decrease, which leads to a decrease in the EDF amplitude. But due to the slower attenuation of the currents, the magnitude of the force impulse not only does not decrease, but even increases.

In order to evaluate the most effective LPEC of the considered configurations, we will conduct a comparative analysis of them. As a basic option, we use the LPEC-E converter. At the same time, the amplitude of the excitation current density j_{1m} should be minimal, which is important for a pulse source, the amplitude f_{zm} and the magnitude of the force pulse F_z should be maximal, which is important for LPEC of power purpose, and the maximum induction of the scattering magnetic field on the defined circuit $B_{ex\,m}$ should be minimal, which is important for service personnel on nearby electronic equipment.

Let's introduce the efficiency criterion K*, which takes into account the specified electrical, power, and magnetic indicators in a relative form [20]:

$$K^* = \beta\left(\frac{\alpha_1}{j_{1m}^*} + \alpha_2 f_{zm}^* + \alpha_3 F_z^* + \frac{\alpha_4}{B_{ex\,m}^*}\right);\quad \sum_{n=1}^{4}\alpha_n = 1, \quad (17)$$

where β – LPEC reliability coefficient; α_n – n^{th} weighting factor of the corresponding LPEC indicator.

We believe that the reliability coefficient for LPEC without CA is β=1, and in the presence of CA it decreases to β=0.9 due to the presence of a moving contact between IW and CA and its implementation in the form of a multi-turn coil.

We will apply five variants of the LPEC efficiency assessment strategy: I ($\alpha_{1\text{-}4}$=0.25), II (α_1=0.4, $\alpha_{2,3,4}$=0.2), III (α_2=0.4, $\alpha_{1,3,4}$=0.2), IV (α_3=0.4, $\alpha_{1,2,4}$=0.2), V (α_4=0.4, $\alpha_{1,2,3}$=0.2). In the first option, all indicators are evaluated

equally, and in other options, priority is given to one of the indicators, which is evaluated twice as high as the others. Table 1 presents the relative values of K^* performance criteria of multi-armature LPEC for power purposes with different variants of their evaluation strategy.

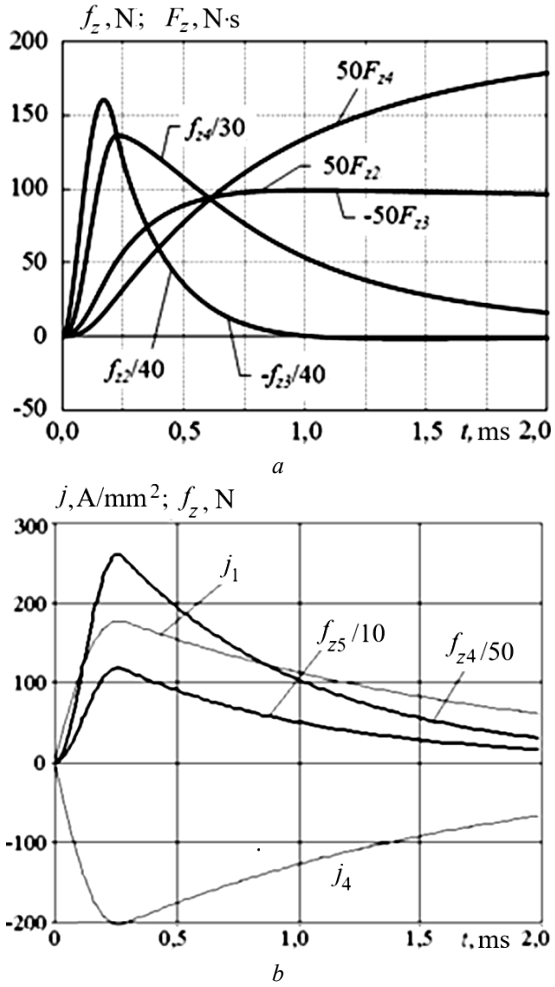

Fig. 4. Electromechanical characteristics LPEC-C_p-E2 (*a*), LPEC-C_p-F (*b*)

Table 1

Relative values of K^* performance criteria of multi-armature LPEC for power purposes

LPEC	Option strategy				
	I	II	III	IV	V
LPEC-E2	1,569	1,393	1,659	1,544	1,679
LPEC-E-F	1,410	1,364	1,371	1,492	1,414
LPEC-C_s-E	0,962	0,939	0,892	0,969	1,048
LPEC-C_p-E	1,011	0,907	1,039	1,084	1,012
LPEC-C_s-E2	4,028	3,348	3,442	3,438	5,883
LPEC-C_p-E2	2,155	1,832	2,024	1,988	2,778
LPEC-C_s-F	1,544	1,398	1,468	1,558	1,751
LPEC-C_p-F	1,192	1,147	1,098	1,228	1,293
LPEC-C_s-E-F	1,340	1,227	1,324	1,513	1,296
LPEC-C_p-E-F	1,237	1,192	1,131	1,274	1,352

As can be seen from the Table 1, almost all multi-armature LPEC have higher efficiency compared to the basic single-armature converter. LPEC-C-E2 with two EA and CA is the most effective, and the converter in which CA and IW are connected in series shows higher performance compared to the converter in which CA and IW are connected in parallel. This high efficiency is largely due to the reduced level of the scattering magnetic field $B_{ex\,m}$ and the reduced amplitude of the excitation current density j_{1m}. LPEC with CA and EA provides a 1.46-fold increase in the EDF amplitude and a 2.09-fold increase in the EDF pulse, which is important for power purposes.

Consider the LPEC of high-speed purpose, for which the amplitude of the speed V_{zm} should be maximal. For this converter, we introduce the efficiency criterion K^*:

$$K^* = \beta\left(\frac{\alpha_1}{j_{1m}^*} + \alpha_2 V_{zm}^* + \frac{\alpha_3}{B_{ex\,m}^*}\right); \quad \sum_{n=1}^{3}\alpha_n = 1. \quad (18)$$

We will apply four variants of the LPEC efficiency evaluation strategy: I ($\alpha_{1\text{-}3}$=0,(3)), II (α_1=0.5, $\alpha_{2,3}$=0.25), III (α_2=0.5, $\alpha_{1,3}$=0.25), IV (α_3=0.5, $\alpha_{1,2}$=0.25). In the first option, all indicators are evaluated equally, and in other options, priority is given to one of the indicators, which is evaluated twice as high as the others. Since IW is stationary, we will consider only those LPEC variants of high-speed assignment that ensure the unidirectionality of all forces on the anchor at a stationary FA.

Table 2 presents the values of K^* efficiency criteria of high-speed multi-armature LPEC with different variants of their evaluation strategy in a relative form.

Table 2

Relative values of K^* performance criteria of multi-armature LPEC for high-speed purposes

LPEC	Option strategy			
	I	II	III	IV
LPEC-E-F	0,972	0,996	0,846	1,082
LPEC-C_p-F	1,096	1,020	1,074	1,198
LPEC-C_s-F	1,311	1,294	1,144	1,494
LPEC-C_p-E	0,855	0,781	0,899	0,886
LPEC-C_s-E	0,912	0,941	0,845	0,952
LPEC-C_p-E-F	0,763	0,776	0,837	0,680
LPEC-C_s-E-F	1,075	1,419	0,999	1,119

The efficiency of multi-armature LPEC for high-speed performance in comparison with the basic version is significantly lower than for multi-armature LPEC for power purposes. This is primarily due to the fact that the speed of the moving combined armature does not increase significantly, and in some variants the LPEC even decreases due to the increased weight of such an armature.

Thus, it can be concluded that only for power LPEC, it is advisable to use multi-armature structures, and for high-speed LPEC, it is advisable to use traditional single-armature LPEC, which have a simpler design.

Experimental studies of LPEC. LPEC studies were conducted in laboratory conditions to verify the main theoretical propositions and calculation results. Experimental studies were performed for LPEC with parameters of active elements similar to the calculated ones. The experimental results were obtained with an aperiodic excitation pulse IW from CES with parameters U_0 =250 V, C_0=2500 μF.

The peculiarity of this technique was the simultaneous measurement of all indicators with the subsequent display of data on the screen of a digital oscilloscope and subsequent transfer of information to a personal computer for processing.

The CES voltage $u_c(t)$ was measured using a PVP2150 digital meter, and the current $i_1(t)$ in IW was measured using a 75ShSM shunt (Fig. 5).

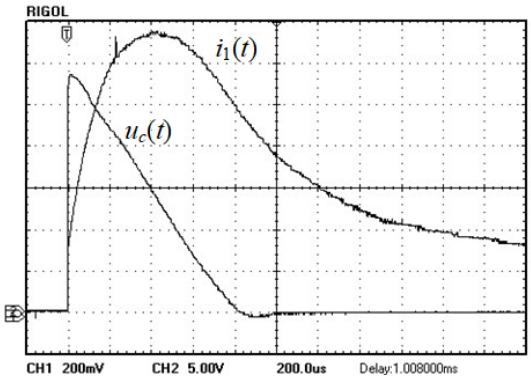

Fig. 5. Oscillogram of voltage $u_c(t)$ and current $i_1(t)$ LPEC-C_s-E

When studying the LPEC power purpose, the striker acts as an executive element, which carries out force impulses on the shock plate (Fig. 6,*a*,*b*). The T6000 piezo sensor was used to record the indicated pulses. The oscillogram of the force of the executive element $f_z(t)$ on the shock plate and the current in IW $i_1(t)$ is shown in Fig. 6,*c*.

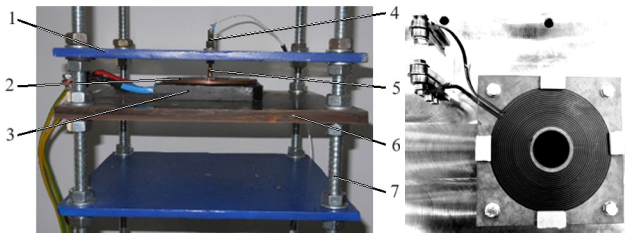

a *b*

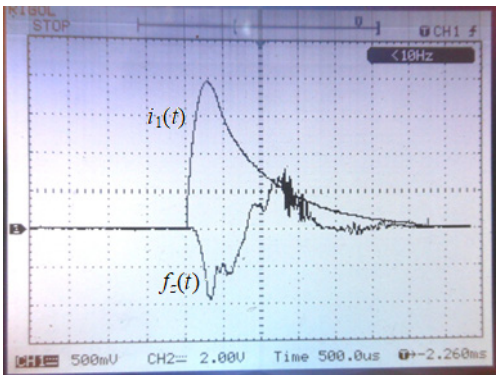

c

Fig. 6. Photo of the experimental setup (*a*), top view (*b*), oscillogram (*c*) of force $f_z(t)$ and current $i_1(t)$ LPEC-C_p-E: 1 – impact plate; 2 – EA; 3 – IW; 4 – piezo sensor; 5 – fight; 6 – support plate; 7 – adjusting supports

When studying the LPEC for high-speed purposes, the executive element (a guide rod with a disk) makes a vertical movement (Fig. 7,*a*). Registration of the movement process is carried out using a variable resistor SP3-23, which is powered by a direct current source. The oscillogram of the movement of the executive element Δz and the current in IW $i_1$is presented in Fig. 7,*b*.

Measurement of the axial induction component of the LPEC B_z scattering magnetic field was performed using an induction sensor.

Tables 3, 4 present the experimental and calculated parameters of the LPEC for power and speed purpose: the amplitude of the current IW I_{1m}, the maximum axial component of the induction of the magnetic scattering field B_{zm}, the force f_{zm}, the speed v_{zm}.

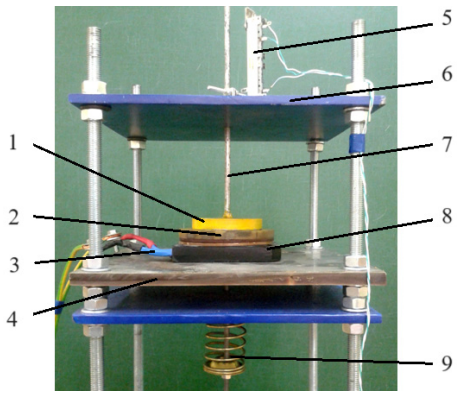

a

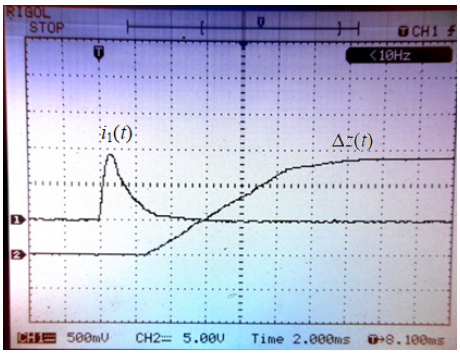

b

Fig. 7. Photo of the experimental setup (*a*), oscillogram (*b*) of displacement $\Delta z(t)$ and current $i_1(t)$ LPEC-C_p-F: 1 – executive element; 2 – CA; 3 – current outlets IW; 4 – support plate; 5 – movement sensor; 6 – guide plate; 7 – guide pin of the executive element; 8 – IW; 9 – loading spring

Table 3
Experimental (Exp.) and calculated (Calc.) parameters of LPEC for power purpose

LPEC	I_{1m}, kA		f_{zm}, kN		$B_{z\,m}$, mT	
	Exp.	Calc.	Exp.	Calc.	Exp.	Calc.
LPEC-E	1.12	1.178	2.20	2.360	20	24
LPEC-F	0.57	0.610	0.38	0.408	17	20
LPEC-C_p	1.37	1.430	3.55	3.815	28	32
LPEC-C_s	0.96	1.001	1.74	1.830	30	34
LPEC-E-F	1.01	1.035	2.60	2.780	14	16
LPEC-C_p-F	1.42	1.485	3.86	4.140	21	25
LPEC-C_s-F	1.11	1.157	1.93	2.065	18	22
LPEC-C_p-F	2.00	2.085	8.50	9.125	19	21
LPEC-C_s-E	1.10	1.160	4.20	4.510	16	18
LPEC-C_p-E-F	1.38	1.453	5.28	5.660	22	24
LPEC-C_s-E-F	0.96	0.997	3.18	3454	13	15

Table 4
Experimental (Exp.) and calculated (Calc.) parameters of LPEC for high-speed purpose

LPEC	I_{1m}, kA		v_{zm}, m/s		$B_{z\,m}$, mT	
	Exp.	Calc.	Exp.	Calc.	Exp.	Calc.
LPEC-E	1.01	1.050	3.0	3.5	22	25
LPEC-F	0.42	0.439	1.5	1.9	17	20
LPEC-C_p	1.16	1.210	3.1	3.5	30	35
LPEC-C_s	0.80	0.835	1.5	1.9	32	39
LPEC-E-F	0.86	0.899	1.6	1.8	14	16
LPEC-C_p-F	1.15	1.200	3.5	3.9	13	15
LPEC-C_s-F	0.73	0.760	2.1	2.5	9	11
LPEC-C_p-E	1.62	1.695	3.7	4.0	20	23
LPEC-C_s-E	0.89	0.925	2.0	2.5	19	21
LPEC-C_p-E-F	1.12	1.165	3.5	4.1	48	53
LPEC-C_s-E-F	0.76	0.785	2,5	3,0	15	18

Figure 8 presents the calculated and experimental currents i_1 in IW LPEC-C_p-E for power and speed purposes, which show that at the leading edge of the pulses, there is an almost complete coincidence of the calculated and experimental values, and at the trailing edge the difference between them increases.

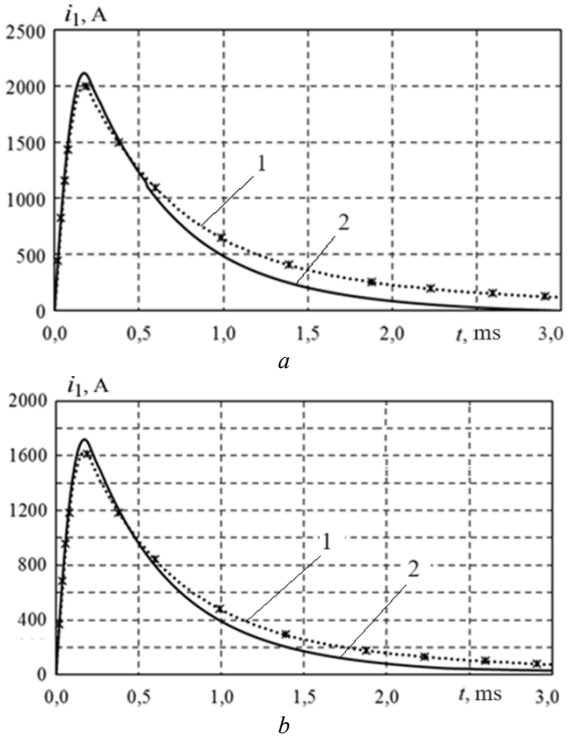

Fig. 8. Calculated (1) and experimental (2) currents i_1 LPEC-C_p-E power (*a*) and speed (*b*) purpose

In LPEC for power purposes, the relative errors between the calculated and experimental amplitudes of the current IW I_{1m} are 2.7-7 %, between the amplitudes of the force f_{zm} – 6.9-8.6 %, between the amplitudes of the axial component of the scattering magnetic field B_{zm} – 9.1-22.1 %.

In the high-speed LPEC, the relative errors between the calculated and experimental amplitudes of the current IW I_{1m} are 3.2-4.4 %, between the maximum speeds of the executive element v_{zm} – 6.7-19.5 %, between the amplitudes of the axial component of the scattering magnetic field B_{zm} – 10.4-22.2 %.

The obtained errors are acceptable for engineering studies in laboratory conditions and generally show the validity of the calculated results.

Based on the research conducted, a number of experimental models of electromechanical devices were developed and tested in laboratory conditions.

On the basis of LPEC-C-E2, a model of an electromagnetic UAV catapult was developed, which is characterized by reduced weight and size parameters and provides an increased departure speed. On the experimental model, it was established that when IW and CA are connected in parallel, the amplitudes of the excitation currents I_{1m} are 43 % higher, and the maximum speed is 60 % higher than when they are connected in series.

On the basis of LPEC-E-F, a model of a magnetic pulse press for ceramic powder materials was developed. The experimental model of the press provided a force pulse on the ceramic powder with amplitude of 85 MPa at each work cycle. It was determined that impulse pressing of ceramic powders allows obtaining compacts, the density of which is 12 % higher than the density of samples obtained by static pressing.

On the basis of LPEC-E-F, a model of an electromechanical device for removing ice and snow deposits from a power line wire has been developed. The device generates horizontally directed forces of variable sign, which contributes to the effective removal of ice and snow deposits from the wire.

On the basis of LPEC-E2, a model of the device was developed for the destruction of information on a solid-state digital SSD drive in case of unauthorized access or on demand.

Conclusions.

1. On the basis of a mathematical model implemented in the COMSOL Multiphysics software environment and taking into account interconnected electromagnetic, mechanical, and thermal processes, the features of electromechanical processes in multi-armature LPEC were established and their indicators were determined.

2. Practically all multi-armature LPEC for power purposes have higher efficiency compared to a single-armature converter. Thus, compared to LPEC with one electroconductive armature, LPEC with coiled and solid electroconductive armatures provides an increase in the amplitude of electrodynamic forces by 1.46 times and the magnitude of the impulse of electrodynamic forces by 2.09 times.

3. For high-speed LPEC, it is advisable to use traditional LPEC with one armature.

4. Experimental studies of LPEC with simultaneous measurement of electrical, mechanical and magnetic parameters were carried out. It was established that in laboratory LPEC for power and speed purposes, the calculated and experimental indicators of the current amplitudes of the inductor winding coincide with an accuracy of up to 7 %, for the amplitude of the force – up to 9 %, for the maximum speed of the executive element – up to 20 %, for the maximum value of the axial component of the magnetic field dispersion up to 22 %.

5. On the basis of multi-armature LPEC, models of an electromagnetic UAV catapult, a magnetic pulse press for ceramic powder materials, an electromechanical device for dumping ice and snow deposits from a power line wire, a device for destroying information on a solid-state digital SSD drive have been developed and tested.

Conflict of interest. The authors declare no conflict of interest.

REFERENCES

1. Chemeris V.T. Impulse electromechanical converters of translational and rotational motion. *Energetics and energy saving*, 2012, no. 5(1), pp. 9-10. (Ukr).

2. Bissal A. *On the design of ultra-fast electro-mechanical actuators. Licentiate Thesis*. Stockholm, Sweden, 2013. 76 p. Available at: https://www.diva-portal.org/smash/get/diva2:617236/FULLTEXT01.pdf (accessed 15 May 2021).

3. Kondratiuk M., Ambroziak L. Concept of the magnetic launcher for medium class unmanned aerial vehicles designed on the basis of numerical calculations, *Journal of Theoretical and Applied Mechanics*, 2016, vol. 54, no. 1, pp. 163-177. doi: https://doi.org/10.15632/jtam-pl.54.1.163.

4. Go B., Le D., Song M., Park M., Yu I. Design and Electromagnetic Analysis of an Induction-Type Coilgun System With a Pulse Power Module. *IEEE Transactions on Plasma Science*, 2019, vol. 47, no. 1, pp. 971-976. doi: https://doi.org/10.1109/TPS.2018.2874955.
5. Reck B. First design study of an electrical catapult for unmanned air vehicles in the several hundred kilogram range. *IEEE Transactions on Magnetics*, 2003, vol. 39, no. 1, pp. 310-313. doi: https://doi.org/10.1109/tmag.2002.805921.
6. Torlin V.N. Vetrogon A.A., Ogryzkov S.V. Behavior of electronic units and devices under the influence of shock loads in an accident, *Automobile transport*, 2009, vol. 25, pp. 178-180. (Rus). Available at: https://dspace.khadi.kharkov.ua/dspace/bitstream/123456789/807/1/39.pdf (accessed 15 May 2021).
7. Jeong Y., Lee H., Kim Y., Lee S. High-speed AC circuit breaker and high-speed OCR. *22nd International Conference and Exhibition on Electricity Distribution (CIRED 2013)*, Stockholm, 2013, pp. 1-4. doi: https://doi.org/10.1049/cp.2013.0834.
8. Kondratenko I.P., Zhyltsov A.V., Pashchyn N.A., Vasyuk V.V. Selecting induction type electromechanical converter for electrodynamic processing of welds. *Tekhnichna Elektrodynamika*, 2017, no. 5, pp. 83-88. (Ukr). doi: https://doi.org/10.15407/techned2017.05.083.
9. Soda R., Tanaka K., Takagi K., Ozaki K. Simulation-aided development of magnetic-aligned compaction process with pulsed magnetic field. *Powder Technology*, 2018, vol. 329, pp. 364-370. doi: https://doi.org/10.1016/j.powtec.2018.01.035.
10. Gorodzha K.A., Podoltsev A.D., Troshchynckyi B.O. Electromagnetic processes in pulsed electrodynamic emitter to excite elastic vibrations in concrete structures. *Technical Electrodynamics*, 2019, no. 3, pp. 23-28. (Ukr). doi: https://doi.org/10.15407/techned2019.03.023.
11. Angquist L., Baudoin A., Norrga S., Nee S., Modeer T. Low-cost ultra-fast DC circuit-breaker: Power electronics integrated with mechanical switchgear. *2018 IEEE International Conference on Industrial Technology (ICIT)*, 2018, pp. 1708-1713. doi: https://doi.org/10.1109/icit.2018.8352439.
12. Puumala V., Kettunen L. Electromagnetic design of ultrafast electromechanical switches. *IEEE Transactions on Power Delivery*, 2015, vol. 30, no. 3, pp. 1104-1109. doi: https://doi.org/10.1109/tpwrd.2014.2362996.
13. Zhou Y., Huang Y., Wen W., Lu J., Cheng T., Gao S. Research on a novel drive unit of fast mechanical switch with modular double capacitors. *The Journal of Engineering*, 2019, vol. 2019, no. 17, pp. 4345-4348. doi: https://doi.org/10.1049/joe.2018.8148.
14. Bolyukh V.F., Shchukin I.S. Influence of limiting the duration of the armature winding current on the operating indicators of a linear pulse electromechanical induction type converter. *Electrical Engineering & Electromechanics*, 2021, no. 6, pp. 3-10. doi: https://doi.org/10.20998/2074-272X.2021.6.01.
15. Zhang M., Wang Y., Li P., Wen H. Comparative studies on two electromagnetic repulsion mechanisms for high-speed vacuum switch. *IET Electric Power Applications*, 2018, vol. 12, no. 2, pp. 247-253. doi: https://doi.org/10.1049/iet-epa.2017.0396.
16. Bolyukh V.F., Kocherga A.I. Multi-armature Electromechanical Converters of Impact-Force Action. *2021 IEEE International Conference on Modern Electrical and Energy Systems (MEES)*, 2021, pp. 1-6. doi: https://doi.org/10.1109/MEES52427.2021.9598788.
17. Vilchis-Rodriguez D.S., Shuttleworth R., Barnes M. Double-sided Thomson coil based actuator: Finite element design and performance analysis. *8th IET International Conference on Power Electronics, Machines and Drives (PEMD 2016)*, Glasgow, UK, 2016, pp. 1-6. doi: https://doi.org/10.1049/cp.2016.0201.
18. Bach J., Bricquet C. *Electric switching device with ultra-fast actuating mechanism and hybrid switch comprising one such device*. Schneider Electric Industries SAS. Patent US no. 8686814, 2014.
19. Bolyukh V.F., Katkov I.I. Influence of the Form of Pulse of Excitation on the Speed and Power Parameters of the Linear Pulse Electromechanical Converter of the Induction Type. *Volume 2B: Advanced Manufacturing*, Nov. 2019, 8 p. doi: https://doi.org/10.1115/imece2019-10388.
20. Bolyukh V.F., Kocherga A.A., Shchukin I.S. Comparative analysis of constructive types of combined linear pulse electromechanical converters. *Tekhnichna Elektrodynamika*, 2018, no. 4, pp. 84-88. (Ukr). doi: https://doi.org/10.15407/techned2018.04.084.

Received 24.11.2023
Accepted 30.12.2023
Published 01.05.2024

V.F. Bolyukh[1], *Doctor of Technical Science*, *Professor*,
O.I. Kocherga[1], *PhD*, *Assistant Professor*,
[1] National Technical University «Kharkiv Polytechnic Institute», 2, Kyrpychova Str., Kharkiv, 61002, Ukraine,
e-mail: vfbolyukh@gmail.com (Corresponding Author);
kocherga.oleksandr07@gmail.com

How to cite this article:
Bolyukh V.F., Kocherga O.I. Efficiency of multi-armature linear pulse electromechanical power and speed converters. *Electrical Engineering & Electromechanics*, 2024, no. 3, pp. 3-10. doi: https://doi.org/10.20998/2074-272X.2024.3.01

UDC 621.313 https://doi.org/10.20998/2074-272X.2024.3.02

M.M. Zablodskiy, R.M. Chuenko, S.I. Kovalchuk, H.V. Kruhliak, O.I. Kovalchuk

Internal capacitive compensation of the reactive power of the screw electromechanical converter

Introduction. *A special category among induction machines with a massive rotor is occupied by the class of multifunctional electromechanical energy converters, which are integrated with the links of technological processes* ***Problem.*** *The exchange of reactive energy between the source and the electromechanical converter during periods of operation with a low load leads to a significant decrease in its efficiency and power factor. With the use of non-linear loads and taking into account possible resonance, it has become more difficult to improve the power factor by installing capacitor banks.* ***Goal.*** *Increasing the energy indicators of the electromechanical converter by spatial displacement of the main and additional stator windings and internal capacitive compensation.* ***Methodology.*** *Comparative analysis of connection schemes and spatial arrangement of stator windings when using internal capacitive compensation. Modeling and experimental studies of electromagnetic and electromechanical characteristics of a screw electromechanical converter.* ***Results****. The distribution of electromagnetic quantities was established and the choice of the angle of spatial displacement of the main and additional windings of the stator phases of the modified converter, which ensure an increase in the value of the electromagnetic torque and power factor, was justified. The results of experimental studies of the screw electromechanical converter are presented.* ***Originality.*** *For the first time, a method of internal capacitive compensation of reactive power is proposed for multifunctional electromechanical converters of technological purpose.* ***Practical value.*** *The use of the proposed method of spatial displacement of the main and additional stator windings and internal capacitive compensation will ensure an increase in the energy performance of the screw electromechanical converter.* References 23, tables 3, figures 15.
Key words: **Maxwell's equation, multifunctional electromechanical converter, stator winding, finite element method, capacitor capacity.**

Вступ*. Особливу категорію серед асинхронних машин з масивним ротором займає клас поліфункціональних електромеханічних перетворювачів енергії, які інтегровані з ланками технологічних процесів.* ***Проблема****. Обмін реактивною енергією між джерелом і електромеханічним перетворювачем в періоди роботи з низьким навантаженням приводить до суттєвого зниження його ефективності і коефіцієнта потужності. З використанням нелінійних навантажень і урахуванням можливого резонансу покращити коефіцієнт потужності встановленням батарей конденсаторів стало складніше.* ***Мета****. Підвищення енергетичних показників шнекового електромеханічного перетворювача шляхом внутрішньої ємнісної компенсації реактивної потужності.* ***Методологія****. Порівняльний аналіз схем з'єднання і просторового розташування обмоток статора при застосуванні внутрішньої ємнісної компенсації. Моделювання та експериментальні дослідження електромагнітних і електромеханічних характеристик шнекового електромеханічного перетворювача.* ***Результати****. Встановлено розподіл електромагнітних величин і обґрунтовано вибір кута просторового зміщення основної і додаткової обмоток фаз статора модифікованого перетворювача, які забезпечують збільшення електромагнітного моменту та коефіцієнта потужності. Наведено результати експериментальних досліджень шнекового електромеханічного перетворювача.* ***Оригінальність****. Вперше для поліфункціональних електромеханічних перетворювачів технологічного призначення запропоновано метод внутрішньої ємнісної компенсації реактивної потужності.* ***Практичне значення****. Використання запропонованого методу просторового зміщення основної і додаткової обмоток статора та внутрішньої ємнісної компенсації забезпечить підвищення енергетичних показників шнекового електромеханічного перетворювача.* Бібл. 23, табл. 3, рис. 15.
Ключові слова: **рівняння Максвелла, поліфункціональний електромеханічний перетворювач, обмотка статора, метод скінченних елементів, ємність конденсатора.**

Introduction. The dominant part of electric motors used in industry are three-phase induction motors (IMs) with a short-circuited rotor. However, in the most widely used IMs with power of up to 11 kW, the efficiency and the power factor cosφ are very low and amount to 0,7-0,9. The exchange of reactive energy between the source and the consumer leads to the appearance in the system of an additional, unproductive reactive current in addition to the active current, overloading of all elements of the electrical system, including the source, the consumer and the power transmission line. In addition, in periods of operation with a low load, it is necessary to take into account the factor of a significant decrease in the efficiency and power factor of the motors. Thus, variable frequency drives for IMs require mechanisms for at least internal buffering of energy for reactive power at the network frequency to correct the power factor and organize effective control [1, 2]. The traditional approach to power factor correction in industrial applications involves installing capacitor banks with microcontrollers for switching synchronous capacitors [3]. The use of parallel capacitor compensation during switching on and start-up is effective in reducing the transient current in large induction motors [4]. But with the widespread use of non-linear loads such as variable speed drives, improving power factor has become more difficult. The resonance problem arises from power system inductance and compensation capacitors, which increases harmonic distortion. A new method of damping harmonic resonances in the power supply system is proposed in [5]. The main feature of this technique is that the active static compensation circuit can simultaneously work as a harmonics injector, a power factor corrector, and a resonance eliminator. But the proposed model is developed only for a single-phase system and should be extended for a three-phase system with different linear and non-linear loads.

The use of automatic switching of the connection of the stator winding in motors with a variable load is common. In [6], the concept of a multi-flow motor with various possible connections of the windings, which allow adjusting the magnetizing flux at six different levels, is proposed. At the same time, the efficiency and power factor of motors can be significantly improved at low load. Compared to the savings potential for the corresponding loads, the additional cost of such a motor is not high, but the cost of automatic switching equipment (control device and contactors) can be significant.

In [7], multi-cascaded induction motors, which are mechanically connected in the form of a cascade with the same power, are considered. In addition, to compare the results, a single induction motor (SIM) is considered, the power of which is the sum of the powers of all multi-cascade induction motors (MCIM). The effect of balance voltage and unbalanced frequency on the highest and stable torque, power factor, active and reactive input power, and losses was studied. The results show the highest torque of MCIM compared to SIM. Also, copper losses are reduced when MCIM is used instead of SIM. As a result, the energy conversion procedure is significantly improved.

Problem definition. A special category of induction machines consists of electric motors with a massive (solid) rotor made of ferromagnetic steel, which, thanks to their rigid construction and integrity, can operate at the highest required rotation speeds. Another useful feature of these machines is their ability to operate in aggressive environments and environments with high humidity. The disadvantage of this design is a relatively low power factor compared to machines with a short-circuited cage or permanent magnets [8]. At the same time, today a promising class of multifunctional electromechanical energy converters is being formed, in which constructive and functional integration with links of technological processes is provided. At the same time, all types of dissipative energy component of electromechanical converters are used in the technological process, in particular, for the processing of raw materials. The external massive rotor, for example, of the screw electromechanical converter (SEMC), combined with the executive body – the screw, is in direct contact with the loading and cooling medium and is able to form multiphysics processes of processing raw materials [9]. To increase the power factor of the SEMC, a means of reactive power compensation is required. This article proposes a method that overcomes most of the drawbacks noted above.

The goal of the work is to increase the energy performance of the screw electromechanical converter by means of internal capacitive compensation of reactive power.

Analysis of recent research and publications. In the practice of researching the parameters and characteristics of electromechanical converters, the methods of numerical field calculations, substitution circuits, are widely used, which significantly increases the accuracy of the results of the analysis of the reconfiguration of windings and magnetic systems.

In [10], a method for calculating active and reactive parameters of windings, mechanical characteristics of an induction motor with a short-circuited rotor based on a numerical field approach is proposed, which does not require conditional correction coefficients and reference graphic functions. An increase in magnetic conductivities was revealed due to a more natural structure of the lines of force of the magnetic field in the upper parts of the slots, while the classical technique is a priori based on an overly simplified structure of the lines of force.

The work [11] is aimed at reviewing and analyzing various methods that are used to determine the parameters of the substitution circuit and transient characteristics of a three-phase induction motor under different conditions. In [12], an accurate procedure for calculating the losses in the iron core is proposed, which is used in the model of the substitution circuit of an induction machine to improve the calculations of the machine's performance. An important factor in the calculation procedure is taking into account the surface effect and magnetic saturation, as well as the effect of the change in the temperature of the iron core on the losses in it.

The authors of the work [13] investigated the influence of the angular shift in the arrangement of windings for a double three-phase stator winding of an induction motor with a short-circuited rotor with an emphasis on the relationships of phase flow, speed characteristics and torque characteristics.

In recent years, a large amount of research has focused on methods of increasing the energy efficiency of external rotor induction motors with a split phase winding operating with high slip. In [14], an analytical model based on a magnetic equivalent circuit is proposed to evaluate the performance of induction motors with a short-circuited external rotor, which are widely used in ceiling fans, pumps, and wheel drives. In addition, copper losses in the windings and iron losses in the core are calculated using the proposed model. The results of the presented model are compared with the results of transient finite element analysis, and the experimental measurements closely match the results confirming the success of the proposed model in terms of accuracy. Issues of inaccuracy in the equivalent circuit method for applications in low power motors for external rotor geometry are discussed in [15] with experimental verification using different equivalent circuit approaches.

The work [16] presents a new six-phase induction motor with an external rotor, equipped with pseudo-concentrated windings. Several aspects of the proposed motor design, such as the design algorithm and analytical modeling based on the modified winding function considering the skew effect, are investigated. An appropriate optimization task is also defined for maximizing the power factor and efficiency and minimizing output torque ripples.

Three-phase induction motors of small and medium power are most dominant in the industrial sector, providing a wide range of constant and variable speeds and loads where dynamic response requirements are not critical, such as pumps, fans and compressors. However, they are still burdened by low power factor at partial loads, which can only be mitigated by adding power factor correction capacitors. In [17], in contrast to variable-speed drives, which have torque or speed control and use pulse-width modulation strategies [5-7], it is proposed to overcome the typical disadvantages of conventional induction motors, mainly low efficiency and power factor, by using less expensive partial power converter. According to the approach [17], a special induction machine is used, which includes a main winding connected to the network and an auxiliary three-phase winding with a smaller number of turns, located in the same slots of the stator as the main one. The auxiliary winding is powered by a voltage inverter with a floating DC bus capacitor. A strategy is implemented to effectively control the power factor, mitigate the harmful effects associated with distorted mains voltage and mechanical torque vibrations, and reduce the large inrush current caused by the induction motor during the starting period. First, the proposed technique is presented theoretically then the feasibility assessment is performed by modeling.

For high-speed induction machines with a solid rotor, which have high eddy current losses, the use of a two-layer asymmetric winding with a short step and collecting coils is known. However, the asymmetrical winding also introduces some current imbalance due to the three-phase asymmetrical stator inductance. Current imbalance can have harmful effects on both the machine and the power supply, such as torque ripple, unbalanced magnetic attraction, and thermal load on the power supply network and power electronics. To mitigate the current imbalance, the work [18] proposes an improvement of the method, which consists in slightly increasing the height of the stator slot and placing the sides of the coil above or below within the slot height for different phases. Based on the 2D finite element method, the stator slot height is optimized in terms of current unbalance mitigation. Using the result of the optimization, they proceed to additional adjustment of the position of the coil for a specific phase. Unlike conventional power electronics current imbalance mitigation methods, the proposed method suppresses current imbalance solely by adjusting the machine design, which avoids additional investment for power electronics devices.

Therefore, the methods of reducing eddy current losses for machines with a solid rotor considered above are associated with the occurrence of current imbalance and additional complications of power electronics devices. But for SEMCs, taking into account the scope of their functional tasks [9, 19], the problem of reducing eddy current losses in the rotor is not critical, with the exception of effective control of the power factor.

Comparative analysis of the connection schemes and spatial arrangement of the stator windings of the basic and modified versions of SEMC. The SEMC is presented in Fig. 1, which shows its electromagnetic system and calculation scheme for modeling.

As stators of the basic version, the moving part of the MTF-011-6 crane motor with nominal power P_n = 1,4 kW, phase connection scheme – star, number of poles $2p$ = 6, winding type – single-layer concentric was used.

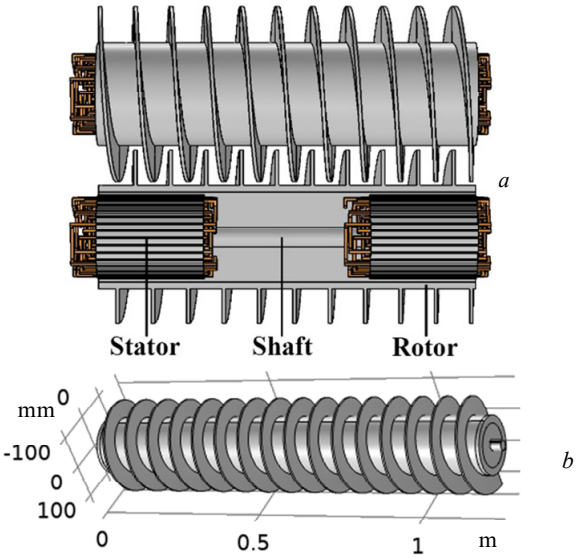

Fig. 1. SEMC: electromagnetic system (*a*); calculation scheme (*b*)

To increase the rotational electromagnetic torque of the modified device, it is proposed to use internal capacitive compensation of reactive power [20]. In the stator of the basic SEMC, a single-layer concentric winding with a full step (Fig. 2,*a*) is used, which has one parallel branch (a = 1). Here, the number of coils in the coil group is 2. In the modified SEMC, a winding with two parallel turns a = 2 is used, in this case, the number of coils in the coil group is reduced to one, and the number of coil groups is doubled (Fig. 2,*b*).

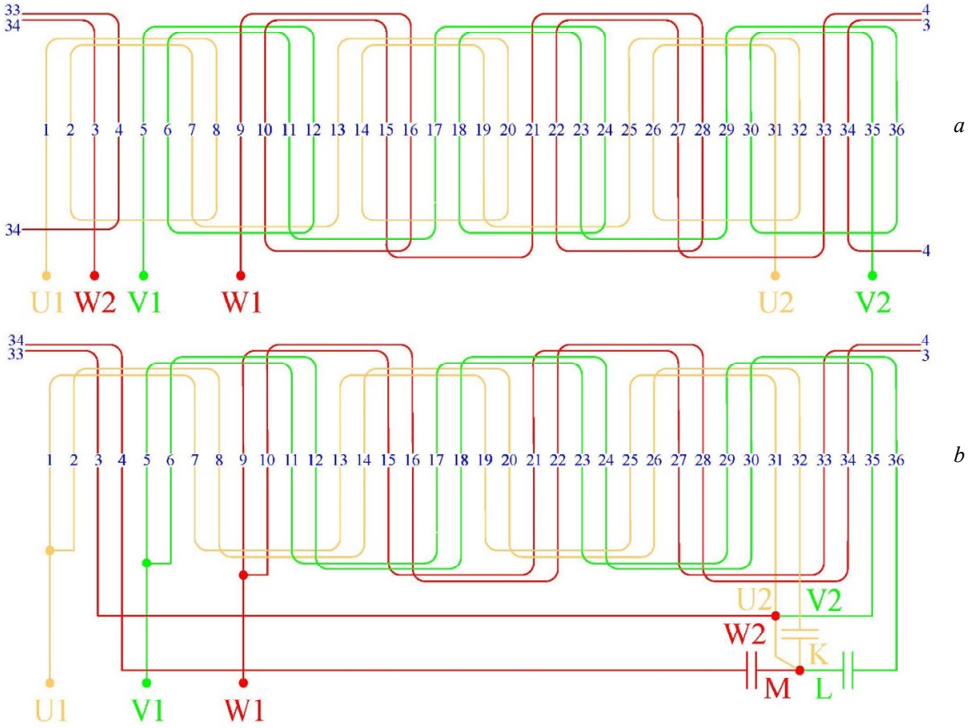

Fig. 2. Expanded electrical diagrams of the stator windings of the basic (*a*) and modified (*b*) SEMC

One of the parallel branches forms the so-called main or working winding, which is connected to the power supply network. Another parallel branch, displaced in the slots of the core by 30° relative to the main

winding, forms an additional winding, which is switched on according to the circuit of a rotary autotransformer on electrical capacity (Fig. 3,*a*).

The use of internal capacitive compensation of the modified SEMC for a wide range of changes in the angle of spatial displacement of the main and additional windings and compensating capacitors allows changing the value and phase of currents, magnetomotive forces and other electrical quantities. As a result, there is an opportunity to increase the energy efficiency and torque of the modified SEMC. Unlike the basic SEMC, where the current of the single stator winding has an active-inductive character both in the starting and operating modes of operation, the stator winding of the modified SEMC has two working turns. The current of the main winding I_1 retains an active-inductive character, and the current of the additional winding I_Δ with a capacitor connected in series acquires a capacitive-active character (Fig. 3,*b*).

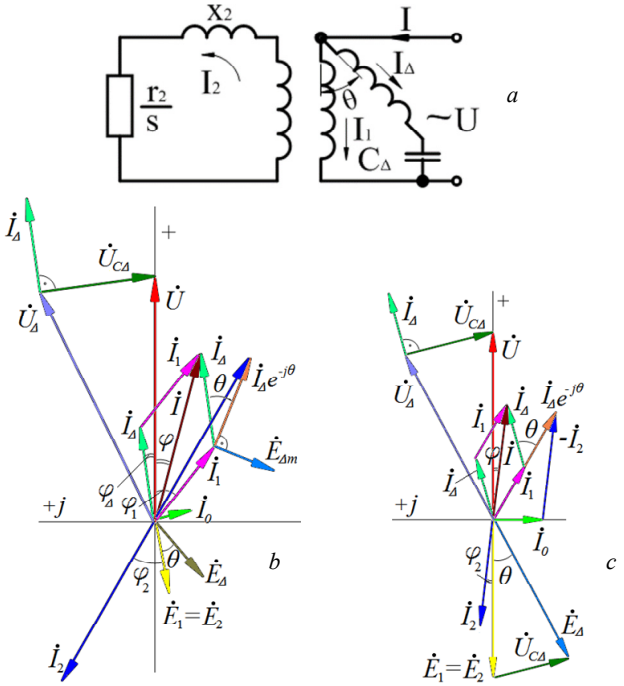

Fig. 3. Schematic electrical diagram of the phase (*a*) and vector diagram during start-up (*b*) and at nominal load (*c*) of the modified SEMC

The current I_Δ depends not only on the supply voltage and machine parameters, but also on the capacity of the capacitor C_Δ. The current $\dot{I}_\Delta e^{-j\theta}$, as reduced to the axis of the main phase winding of the stator, participates in the creation of the magnetizing current of the device $\dot{I}_0 = \dot{I}_1 + \dot{I}_\Delta e^{-j\theta} + \dot{I}_2$ and creates an additional EMF $\dot{E}_{\Delta m} = -jx_m \dot{I}_\Delta e^{-j\theta}$. The EMF $\dot{E}_{\Delta m}$ induced by the spatially shifted current $\dot{I}_\Delta$ of the additional winding increases the main EMF of the stator and rotor. An increase in the EMF of the rotor with its constant active and inductive resistances leads to an increase in the starting current of the rotor, and, therefore, the starting torque of the modified SEMC. Under the influence of the increased starting torque, the acceleration process of the device is accelerated and it reaches a tougher mechanical characteristic in the operating mode compared to the basic SEMC. The vector diagram of the modified SEMC under the nominal load is shown in Fig. 3,*c*.

The angle of spatial displacement of the main and additional windings of the stator phases of the modified SEMC of 30° was chosen in view of the fact that precisely at this angle, an increase of 20-30 % of the starting torque is provided at a constant starting current compared to the basic device. The technological simplicity of performing the stator windings of the modified SEMC by dividing the 60° phase zone of the basic device winding into two equal parts is also taken into account [20].

Initial conditions for modeling electromagnetic and electromechanical characteristics of SEMC. Modeling was carried out for SEMC with the following parameters: stator core length L_s = 90 mm; the length of the corresponding section of the common external rotor L_r = 300 mm; current frequency f_0 = 50 Hz; angular speed $\omega_0 = 2\pi f_0$, rad/s; volume density of rotor steel ρ_{st} = 7850 kg/m^3; amplitude value of the current $I_0 = 13\sqrt{2}$ A; t is the time parameter.

Basic device variables: phase U current $I_U = I_0 \cdot \sin(\omega_0 \cdot t)$ A; phase W current $I_W = I_0 \cdot \sin(\omega_0 \cdot t + 120°)$ A; phase V current $I_V = I_0 \cdot \sin(\omega_0 \cdot t - 120°)$ A.

Variables of the modified device: phase U current $I_U = I_0 \cdot \sin(\omega_0 \cdot t)$ A; phase W current $I_W = I_0 \cdot \sin(\omega_0 \cdot t + 120°)$ A; phase V current $I_V = I_0 \cdot \sin(\omega_0 \cdot t - 120°)$ A; phase K current $I_K = I_0 \cdot \sin(\omega_0 \cdot t + 30°)$ A; phase M current $I_M = I_0 \cdot \sin(\omega_0 \cdot t + 150°)$ A; phase L current $I_L = I_0 \cdot \sin(\omega_0 \cdot t - 90°)$ A.

The topology of the stator windings of the basic and modified versions of SEMC is shown in Fig. 4.

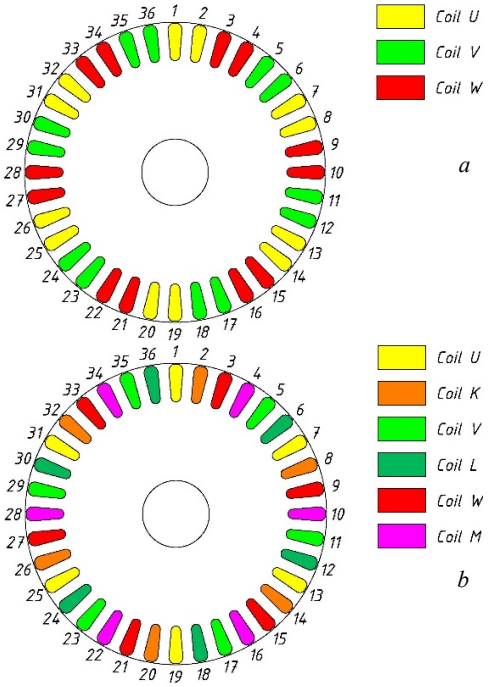

Fig. 4. Topology of SEMC stator windings: basic version (*a*); modified version (*b*)

The characteristics of the modified device both in the starting and operating modes depend on the capacity of the capacitor connected in series with the additional winding. Since the currents of the main and additional windings, the phase of the current of the additional winding, as well as the losses in the motor change in this

case, it is advisable to choose the capacity of the capacitor in the circuit of the additional winding, which provides the same currents in the main and additional windings of the stator phases of the device. To ensure this mode of operation of the modified device, the capacity of the capacitor is 25 μF per 1 kW of rated power.

The simulation was performed in the Comsol Multiphysics software environment [21] according to the calculation scheme (Fig. 1,*b*). Considering the identity of the electromagnetic, electromechanical, thermal and vibrational processes that occur on the «stator-corresponding section of the common rotor» modules of the SEMC electromagnetic system, the simulation was carried out for one of them. If there are differences in parameters or geometric dimensions, the simulation is carried out separately for each stator. The numerical analysis of the electromagnetic field is carried out using a mathematical model of a twin-screw electromechanical hydrolyzer [22]:

$$\nabla\times\boldsymbol{H}=\boldsymbol{J}, \tag{1}$$

where $\boldsymbol{H}$ is the magnetic field strength vector, A/m; $\boldsymbol{J}$ is the current density vector, A/m^2;

$$\boldsymbol{B}=\nabla\times\boldsymbol{A}, \tag{2}$$

where $\boldsymbol{B}$ is the magnetic flux density vector, T; $\boldsymbol{A}$ is the magnetic vector potential, Wb/m;

$$\boldsymbol{E}=-\partial A/\partial t, \tag{3}$$

where $\boldsymbol{E}$ is the electric field strength vector, V/m;

$$\boldsymbol{J}=\sigma\boldsymbol{E}, \tag{4}$$

where σ is the specific electrical conductance, S/m.

The formulation of the scalar potential is performed according to the equation:

$$\nabla\cdot\boldsymbol{B}=0. \tag{5}$$

At the external boundary with a magnetic scalar potential, the normal component of the magnetic flux density equals zero:

$$n\cdot\boldsymbol{B}=0. \tag{6}$$

The magnetization of the ferromagnetic rotor is given as a *B-H* curve and is determined from the equation:

$$B=f\left(\left|H\right|\right)\frac{H}{\left|H\right|}. \tag{7}$$

Multi-turn stator windings are used as a current source in the model (Fig. 2, 3). The windings provide the current density in the direction of the conductors J_e according to the equation:

$$J_e=\frac{N\cdot I_{coil}}{A}\cdot e_{coil}, \tag{8}$$

where N is the number of turns in the winding; A is the general section, area of the winding domain, m^2; I_{coil} is the current, A; e_{coil} is the vector variable for visualizing the direction of turns in the winding.

Modeling of thermal parameters was performed by combining the physics of magnetic fields, heat transfer in solids, and electromagnetic heating in the frequency-transition domain of research. The mathematical model of heat transfer is given in the most general form, the initial temperature is 293 K. Heat exchange according to Fourier law in a differential form containing a heat source is described by the following equation [23]:

$$d_z\rho C_p\frac{\partial T}{\partial t}+d_z\rho C_p\boldsymbol{u}\cdot\nabla T+\nabla\cdot q=d_zQ+q_0+d_zQ_{ted}, \tag{9}$$

where d_z is the thickness of the domain in the non-planar direction, m; ρ is the density, kg/m^3; C_p is the specific heat capacity at constant pressure, J/(kg·K); T is the temperature, K; t is the time, s; $\boldsymbol{u}$ is the velocity vector, m/s; q is the heat flow, W/m^2; Q is the heat source, W/m^3; q_0 is the external heat flow, W/m^2; Q_{ted} is the thermoelastic damping, W/m^3;

$$q=-d_zk\nabla T, \tag{10}$$

where k is the thermal conductivity, W/(m·K).

Thermal insulation is applied to the external boundaries of the model [23]:

$$-n\cdot q=0, \tag{11}$$

where n is the refractive index.

The heat flow from the surfaces is defined as [23]:

$$-n\cdot q=d_zq_0, \tag{12}$$

$$q_0=h\cdot(T_{ext}-T) \tag{13}$$

where h is the heat transfer coefficient, W/(m^2·K); T_{ext} is the ambient temperature, K.

Radiation from the surface of the model to the environment is determined from the equation [23]:

$$-n\cdot q=d_z\varepsilon\sigma(T^4_{amb}-T^4), \tag{14}$$

where ε is the emissivity of the surface; σ is the Stefan-Boltzmann constant, W/(m^2·K^4); T_{amb} is the temperature of the environment, K.

Electromagnetic heating is determined from equations [23]:

$$\rho C_p\frac{\partial T}{\partial t}+\rho C_p\boldsymbol{u}\cdot\nabla T=\nabla\cdot\left(k\nabla T\right)+Q_e, \tag{15}$$

where Q_e is the electromagnetic heat source, W/m^3:

$$Q_e=Q_{rh}+Q_{mi}, \tag{16}$$

where Q_{rh} are the resistive losses, W/m^3; Q_{mi} are the magnetic losses, W/m^3:

$$Q_{rh}=0{,}5\cdot\mathrm{Re}(\boldsymbol{J}\cdot\boldsymbol{E}^*); \tag{17}$$

$$Q_{mi}=0{,}5\cdot\mathrm{Re}(j\omega\boldsymbol{B}\cdot\boldsymbol{H}^*); \tag{18}$$

where $\boldsymbol{E}^*$ is the electric field strength vector at a given frequency at a certain moment in time, V/m; $\boldsymbol{H}^*$ is the magnetic field strength vector at a given frequency at a certain moment in time, A/m.

Simulation results and discussion. The main part of the characteristics based on the results of the simulation of the basic and modified SEMC is presented in the plane of its cross section. Figure 5 shows the distribution of the *z*-component of the current density. A significant difference in the current density distributions is noted for the slot zones of the stator. For the modified version of SEMC, the number of slots with near-zero current density is half as much as compared to the basic version. In the rotor of the modified version of the SEMC, at the depth of penetration of the electromagnetic wave, 6 sections (by the number of poles) are observed with current density values that are 15 % higher than the current density in the corresponding sections of the basic version of the SEMC.

Figure 6 shows the distribution of the volume density of electrical energy. A comparison of the images indicates that the volumetric electrical energy density of the stator of the modified SEMC is on average 19 % higher than the electrical energy density of the stator of the basic SEMC. Since the concept of «energy» according to physical principles is equivalent to the concept of «work», we are talking about the concentration and potential of active energy in the stator.

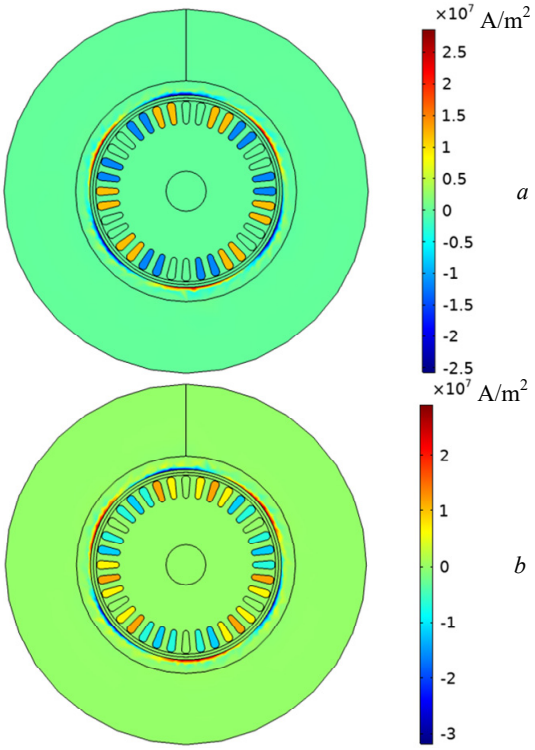

Fig. 5. Current density (*z*-component) of the basic (*a*) and modified (*b*) SEMC

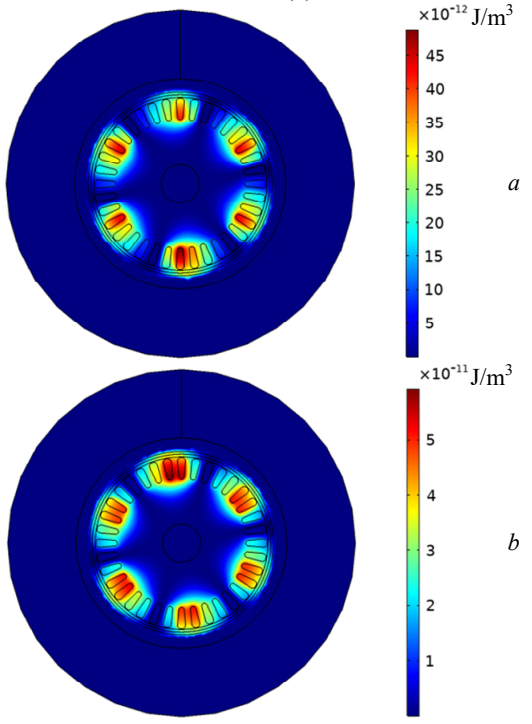

Fig. 6. Volume electrical energy density of the basic (*a*) and modified (*b*) SEMC

Figure 7 shows the time dependence of the electromagnetic torque of the two studied options. For the modified SEMC (Fig. 7,*b*), a significant (1,5 times) increase in value and a decrease in extreme pulsations of the electromagnetic torque were obtained.

Figures 8, 9 present the time dependence and phase angle of the currents of one SEMC module. In the modified SEMC, thanks to the use of internal capacitive compensation, it is possible to change the value and phase of the current of the additional stator winding.

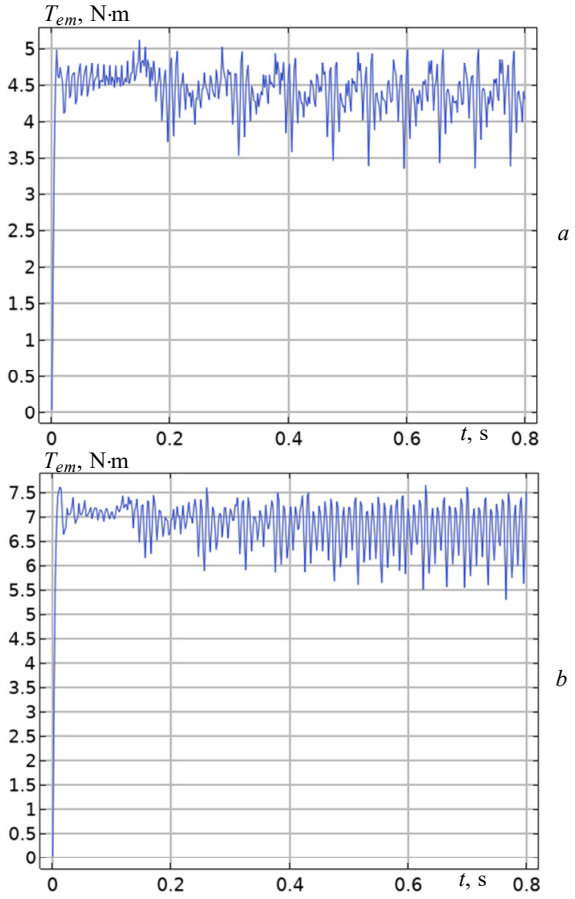

Fig. 7. Electromagnetic torque of the basic (*a*) and modified (*b*) SEMC

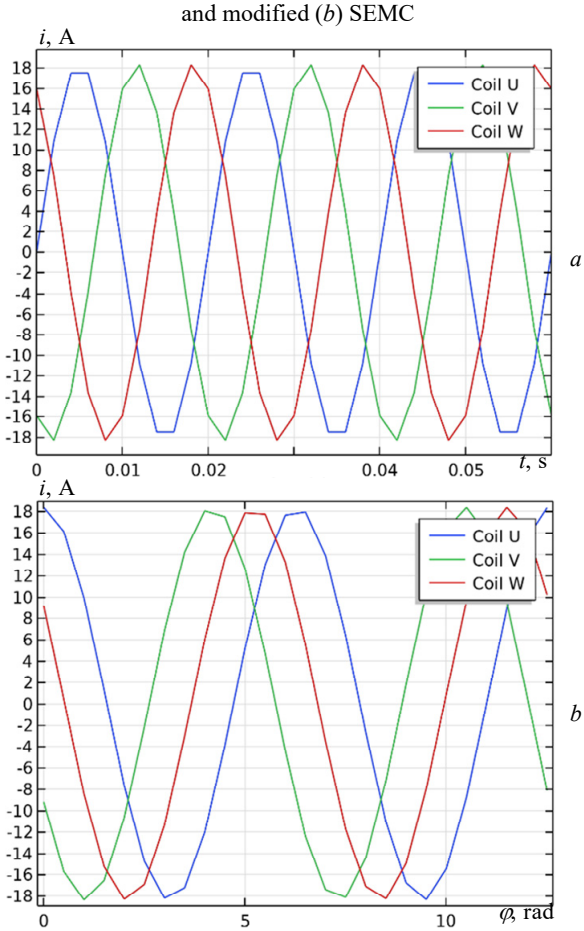

Fig. 8. Time dependence (*a*) and phase angle (*b*) of the currents of one module of the basic SEMC

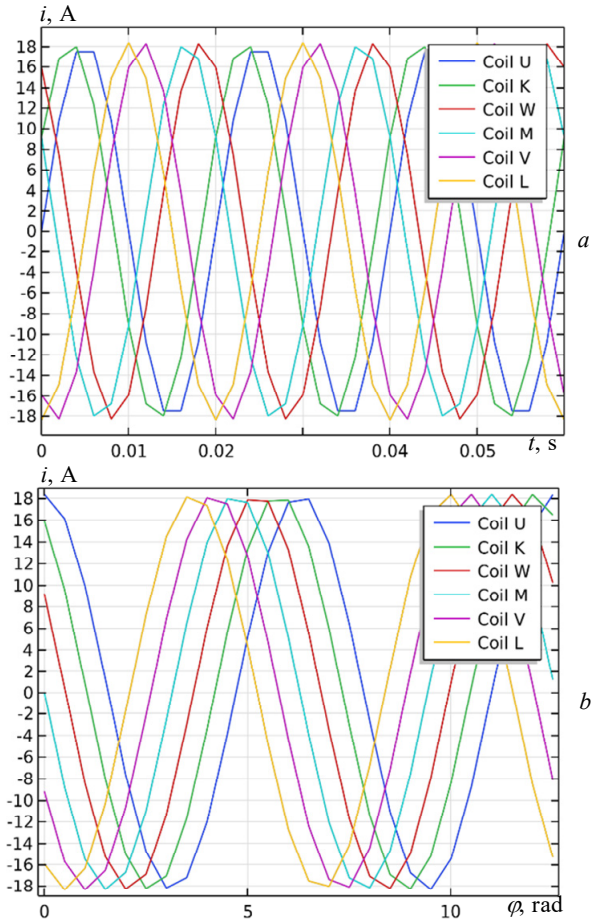

Fig. 9. Time dependence (*a*) and phase angle (*b*) of the currents of one module of the modified SEMC

To increase the torque of the modified SEMC, it is necessary to shift the phase of the current of the additional winding relative to the current of the main winding by 30°. Since in the modified SEMC the main and additional windings are shifted one relative another in space, this leads to an increase in the area of action of the eddy currents created in the rotor. In particular, the angle of the sector occupied by the maximum currents is 2,3 rad for the basic and 2,8 rad for the modified SEMC, respectively. Currents (Fig. 8,*b*) form the resultant magnetomotive force around the circumference of the air gap, the result of which is the creation of eddy currents in the rotor massive. The corresponding zone of action of the generated eddy currents in the rotor massive (Fig. 5) occupies the area opposite 5,5 tooth divisions of the stator for the basic and 6 tooth divisions for the modified SEMC. Therefore, the modified SEMC exceeds the basic SEMC version in terms of current density values and the width of their action zone. As a result of the influence of the phase shift, the SEMC demonstrates the best performance, the best time to establish speed and torque at start-up and load (Fig. 7), which is also observed in induction machines when considering the configuration of a double 3-phase winding [13, 22].

Figure 10 shows the distribution of the magnetic flux density, *X*-*Y* components of the basic and modified SEMC. A significant difference in the distribution of the magnetic flux density for the *X*-*Y* components for the basic and modified SEMC is noted. If for the basic variant, practically the same values of the magnetic flux density for the *X*-*Y* components are observed, for example, opposite the middle of the poles within their instantaneous location, then for the variant of the modified SEMC, the difference in the values of the magnetic flux density along the *X*-*Y* components is quite significant. In addition, a greater degree of branching of the magnetic flux in the stator yoke to the side of the hollow shaft is noted for the version of the modified SEMC.

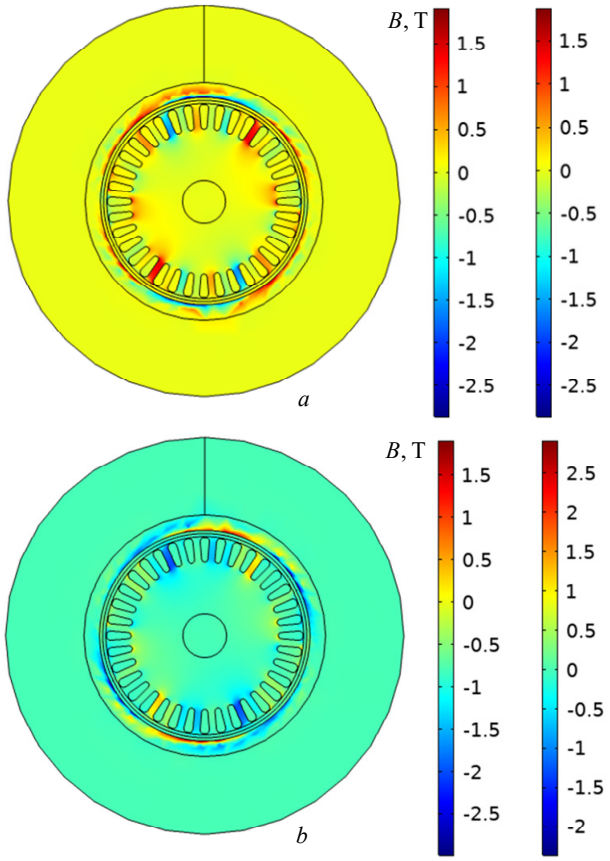

Fig. 10. Magnetic flux density (left legend – *X*-component, right legend – *Y*-component) of the basic (*a*) and modified (*b*) SEMC

This means the presence of a smaller magnetic resistance in the path of the magnetic flux for the variant of the modified SEMC and, accordingly, a smaller reactive power. At the same time, reactive power characterizes the conditions of transmission of active power at each moment of time, and based on Fig. 6, the volume density of the active energy of the stator of the modified SEMC exceeds the density of the active energy of the stator of the basic SEMC, which indirectly indicates a higher value of the power factor of the modified SEMC. This provision is also confirmed by a comparison of the magnetization distribution of the basic and modified SEMCs (Fig. 11).

With the same magnetization in the rotor massive ($2{,}5 \cdot 10^6$ A/m), there is an excess of 23 % of the magnetization of the stator magnetic core in the middle of the poles within the limits of their instantaneous location for the basic ($1{,}5 \cdot 10^6$ A/m) in comparison with the modified SEMC ($1{,}0 \cdot 10^6$ A/m).

Table 1 presents the results of modeling the energy characteristics of the basic and modified SEMCs.

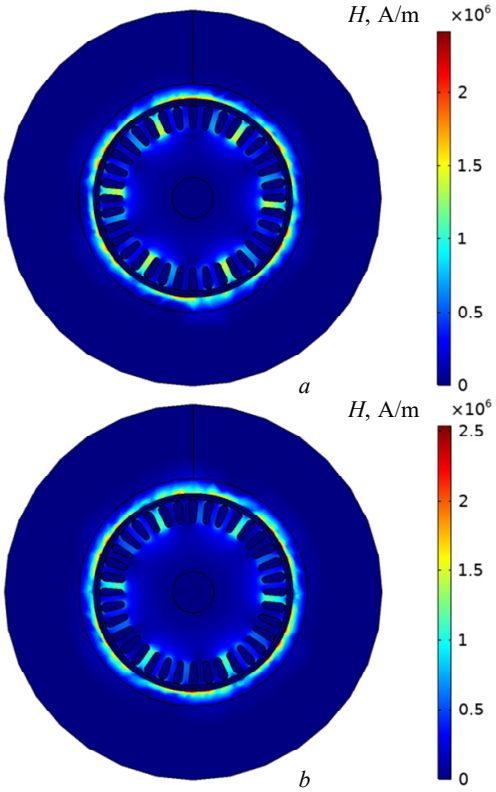

Fig. 11. Magnetization of the basic (*a*) and modified (*b*) SEMC

Table 1

The results of the calculation of the characteristics of the basic and modified SEMC

Indicator	Basic SEMC	Modified SEMC	Difference
Power consumption, W	1080,70	1293,56	212,86
Useful mechanical power, W	103,62	148,60	44,98
Losses in steel, W	484,28	652,13	167,85
Losses in copper, W	492,80	492,80	0
Rotation speed, rpm	180	200	20
Electromagnetic torque, N·m	5,5	7,1	1,6
Efficiency in terms of mechanical power, %	9,58	11,44	1,86
Power factor	0,59	0,71	0,12

The modified SEMC consumes 212,86 W (19,7 %) more active power from the power supply network compared to the basic SEMC. At the same time, the useful active mechanical power increases by 44,98 W (43,4 %) and losses in the steel of the modified SEMC increase by 167,85 W (34,7 %). The copper losses of the modified SEMC do not change compared to the basic device. The modified SEMC creates a 1,6 N·m (29 %) greater electromagnetic torque, as a result of which its rotation frequency increases by 20 rpm (11,1 %). Due to the use of internal capacitive compensation, the power factor of the modified SEMC increases to 0,71 (by 20,3 %), and the electrical efficiency, which takes into account only the mechanical useful power for transporting the raw material, increases from 9,58 to 11,4 %. It should be noted that due to the increase in losses in the steel of the modified SEMC, the amount of heat that will be directed to the processed material will increase, therefore the thermal efficiency of the modified SEMC will also increase.

Experimental studies of the mock-up sample of SEMC. To verify the simulation results, a mock-up sample of the basic (without internal capacitive compensation) variant of the two-stator SEMC was tested. Nominal data of SEMC: power consumption P = 2078 W; supply voltage U = 80 V; current consumption I = 30 A; power factor cosφ = 0,5; the number of poles is 6; rotation frequency with coordinated rotation of the magnetic fields of individual modules n = 450 rpm. Figure 12 shows the nodes of the SEMC mock-up sample with the determination of the measurement zones of electromagnetic and temperature parameters.

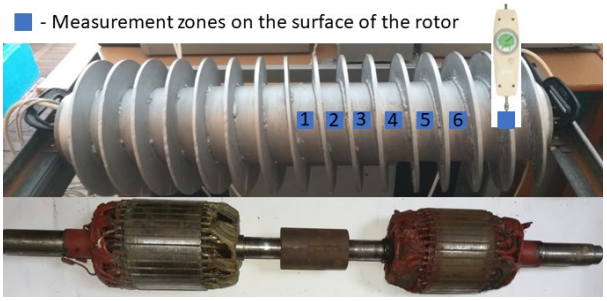

Fig. 12. Distribution of electromagnetic, temperature and mechanical parameters measurement zones on the surface outer rotor of the SEMC mock-up sample

Figure 12 shows the corresponding location of the system of adjacent stators, which are placed in the cavity of the external rotor, as well as the location of the dynamometer for measuring the starting torque.

Electromagnetic and temperature parameters were measured on mock-up samples in the short-circuit mode (braked rotor) when the supply voltage was reduced to the level at which the rated current was reached.

The following measuring devices were used during the research: Tenmars TM-191 Magnetic Field Meter, designed for measuring ultra-low frequency electromagnetic fields from 30 Hz to 300 Hz; Tenmars TM-190 Multi Field EMF Meter – a device for measuring high-frequency electromagnetic fields in the frequency range from 50 MHz to 3,5 GHz and low-frequency electric and magnetic fields in the frequency range of 50-60 Hz; infrared, optical pyrometer Benetech GM533A, measuring range –50 ... +530 °C, imaging index 12:1, coefficient of thermal radiation 0,1–1, spectrum 5–14 μm; thermal imager Xintest HTI HT-18, thermal sensitivity 0,07 °C, temperature range: –20...+300 °C, image capture frequency 8 Hz, wavelength range 8-14 μm; analog spring universal dynamometer NK-300, used to measure the starting torque, accuracy class 0,5 %; K540-3 transformer parameters meter was used to measure the electrical parameters of the SEMC. Table 2 presents the experimental data of electrical and energy parameters of the mock-up sample of the basic (without internal capacitive compensation) version of the two-stator SEMC.

The SEMC load was carried out by the frictional effect of the mechanical brake on the end part of the rotor-screw. The load torque is 7,4 N·m. Power, current and voltage were measured by K540-3 transformer parameters meter.

Table 3 presents the experimental data of the surface electromagnetic parameters of the mock-up sample of the basic (without internal capacitive compensation) version of the two-stator SEMC. Magnetic flux density, electric field strength, electromagnetic radiation flux density were measured in the short-circuit mode at the minimum possible distance of 1 mm from the surface of the SEMC rotor.

Table 2

Experimental data of electrical and energy parameters of the mock-up sample of SEMC

Voltage, V	Power, W		Current in the short-circuit mode, A		Current at load, A		Starting torque of the module, N·m	Power factor		Slip
	load mode	short-circuit mode	total	of the module	total	of the module		load mode	short-circuit mode	
60,5	1120	1320	23,17	11,6	23	11,5	4	0,508	0,546	0,84
70	1594	1876	27,5	13,75	26,2	13,1	5,6	0,5	0,556	0,73
77	1878	2266	30,12	15,7	28,5	14,3	12,3	0,492	0,562	0,63
81	2040	2384	33,7	22,5	29,8	14,9	13,7	0,486	0,57	0,55

Table 3

Experimental data of surface electromagnetic parameters of the SEMC mock-up sample

Measurement zones	Parameters at supply voltage $U = 81$ V				
	Magnetic flux density, mT	Electric field strength, V/m	Electromagnetic radiation flux density, mW/m²	Temperature, °C	
				Fig. 16,*a*	Fig. 16,*b*
1	60	0,03	0,7	28,5	48
2	100	0,03	0,9	30,5	51
3	170	0,03	1,8	41,2	62
4	400	0,2	523	61	74
5	380	0,15	520	63,3	76,2
6	410	0,15	525	63,1	76,3

Figure 13 shows a diagram of a measuring bench for recording current oscillograms using ACS758 current sensors on the Hall effect with a sensitivity of 40 mV/A.

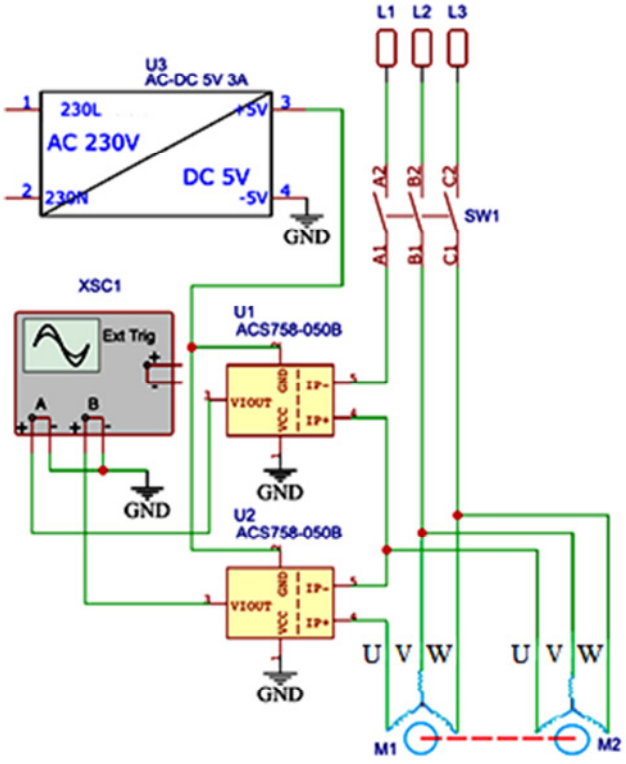

Fig. 13. Diagram of the measuring bench

Figure 14 shows the oscillograms of the total current of the SEMC and the current of a separate module at a supply voltage of $U = 81$ V.

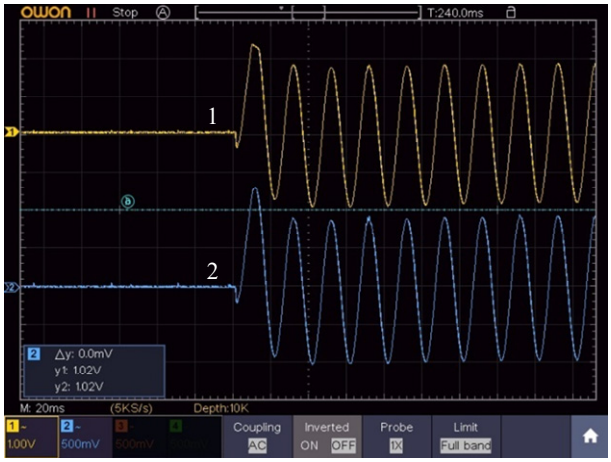

a

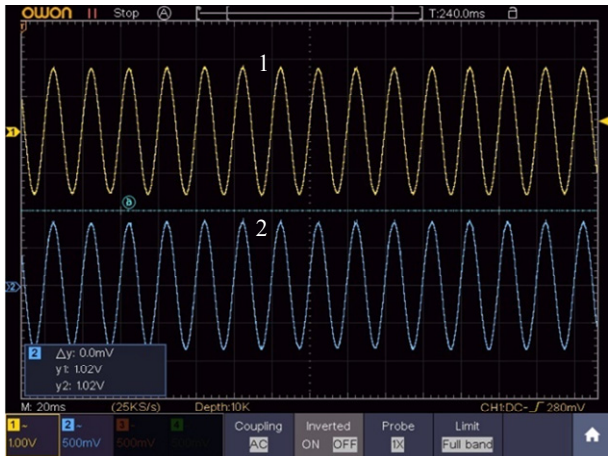

b

Fig. 14. Oscillograms of total current 1 and the current of a separate module 2 of SEMC: start-up period (*a*), after 7 minutes of SEMC operation (*b*)

Due to the change in the parameters of the stators and the rotor, there is a decrease in the amplitudes and effective

values of the currents by up to 5 % during 7 minutes of operation of the SEMC. A comparison of the distribution of the temperature field on the surface of the rotor of the SEMC mock-up sample with the simulation results was made. Thermograms were recorded after 7 minutes of operation in the short-circuit mode at a voltage $U = 73$ V. In Fig. 15,*a* the mock-up sample with an arbitrary azimuthal location of the frontal parts of adjacent stators is shown.

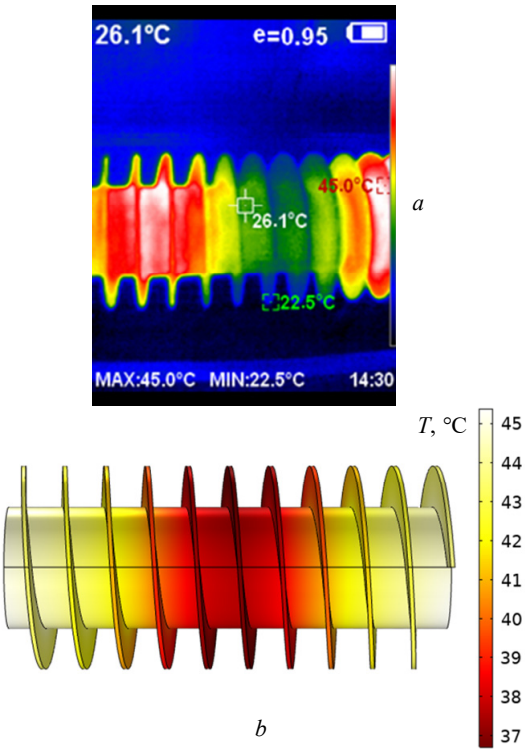

Fig. 15. Temperature distribution on the surface of the SEMC rotor: experimental thermogram of the mock-up sample after 7 minutes of rotation at idle speed at a voltage of 81 V, rotation frequency 450 rpm (*a*), simulation result (*b*)

The results of experimental studies (Tables 2, 3, Fig. 14, 15), namely of parameters and characteristics of the SEMC module: starting torque and current; torque and current under load, magnetic flux density, rotor surface temperature with an accuracy of 11 % coincide with the calculated ones, which indicates the reliability of the SEMC mathematical model.

Conclusions.

1. A method of spatial shift of the main and additional stator windings and internal capacitive compensation is proposed and a comparative analysis of the connection schemes and spatial arrangement of the stator windings of the basic and modified versions of the screw electromechanical converter (SEMC) is performed.

2. It has been proven that the application of internal capacitive compensation over a wide range of changes in the angle of spatial shift of the main and additional windings and compensating capacitors allows changing the value and phase of currents, magnetomotive forces and other electrical quantities. A significant (by 29 %) increase in the electromagnetic torque and a decrease in its extreme pulsations have been achieved for the modified SEMC.

3. Due to the use of internal capacitive compensation, an increase in energy performance is achieved: the power factor of the modified SEMC increases by 20,3 %, and the electrical efficiency, which takes into account only the mechanical useful power for transporting raw material, increases by 1,86 %.

4. The use of the proposed method of spatial shift of the main and additional stator windings and internal capacitive compensation is promising for increasing the energy performance of SEMC.

Acknowledgment. The work was carried out with the support of the Ministry of Education and Science of Ukraine (projects DB No. 0120U102105 and No. 0121U113746).

Conflict of interest. The authors declare no conflict of interest.

REFERENCES

1. Zhitao Han, Li Ding, Gang Wang. Experimental Investigation of Induction Motor Power Factor and Efficiency Impacted by Pulse Width Modulation Power and Voltage Controls of Variable-Frequency Drives. *ASHRAE Transactions*, 2021, vol. 127, pp. 817-828.

2. Bortoni E.C., Bernardes J.V., da Silva P.V.V., Faria V.A.D., Vieira P.A.V. Evaluation of manufacturers strategies to obtain high-efficient induction motors. *Sustainable Energy Technologies and Assessments*, 2019, vol. 31, pp. 221-227. doi: https://doi.org/10.1016/j.seta.2018.12.022.

3. Mbinkar E.N., Asoh D.A., Kujabi S. Microcontroller Control of Reactive Power Compensation for Growing Industrial Loads. *Energy and Power Engineering*, 2022, vol. 14, no. 9, pp. 460-476. doi: https://doi.org/10.4236/epe.2022.149024.

4. Habyarimana M., Dorrell D.G., Musumpuka R. Reduction of Starting Current in Large Induction Motors. *Energies*, 2022, vol. 15, no. 10, art. no. 3848. doi: https://doi.org/10.3390/en15103848.

5. Antar R.K., Suliman M.Y., Saleh A.A. Harmonics resonance elimination technique using active static compensation circuit. *Bulletin of Electrical Engineering and Informatics*, 2021, vol. 10, no. 5, pp. 2405-2413. doi: https://doi.org/10.11591/eei.v10i5.3148.

6. Ferreira F.J.T.E., de Almeida A.T. Novel Multiflux Level, Three-Phase, Squirrel-Cage Induction Motor for Efficiency and Power Factor Maximization. *IEEE Transactions on Energy Conversion*, 2008, vol. 23, no. 1, pp. 101-109. doi: https://doi.org/10.1109/TEC.2007.914355.

7. Guo J., Ma X., Ahmadpour A. Electrical–mechanical evaluation of the multi–cascaded induction motors under different conditions. *Energy*, 2021, vol. 229, art. no. 120664. doi: https://doi.org/10.1016/j.energy.2021.120664.

8. Jagiela M., Garbiec T. Determination of best rotor length in solid-rotor induction motor with axial slitting. *Archives of Electrical Engineering*, 2012, vol. 61, no. 2, pp. 267-276. doi: https://doi.org/10.2478/v10171-012-0022-2.

9. Zablodskiy M., Gritsyuk V., Rudnev Y., Brozhko R. Three-dimensional electromagnetic field model of an auger electromechanical converter with an external solid rotor. *Mining of Mineral Deposits*, 2019, vol. 13, no. 4, pp. 99-106. doi: https://doi.org/10.33271/mining13.04.099.

10. Milykh V.I. Numerical-field analysis of active and reactive winding parameters and mechanical characteristics of a squirrel-cage induction motor. *Electrical Engineering & Electromechanics*, 2023, no. 4, pp. 3-13. doi: https://doi.org/10.20998/2074-272X.2023.4.01.

11. Trisha, Gupta G.S., Shiva Kumar S. Review of the Parameter Estimation and Transient Analysis of Three-Phase Induction Motor. *Lecture Notes in Electrical Engineering*, 2021, vol. 693, pp. 223-232. doi: https://doi.org/10.1007/978-981-15-7675-1_21.

12. Nasir B.A. An Accurate Iron Core Loss Model in Equivalent Circuit of Induction Machines. *Journal of Energy*, 2020, vol. 2020, pp. 1-10. doi: https://doi.org/10.1155/2020/7613737.

13. Ekpo E.G., Umoh G.D., Udokah Y.O.N. Effect of Phase-Shift in Six-Phase Induction Machine. *Journal of Emerging Trends in Engineering and Applied Sciences*, 2022, vol. 13, no. 6, pp. 215-226.
14. Saneie H., Nasiri-Gheidari Z. Performance Analysis of Outer-Rotor Single-Phase Induction Motor Based on Magnetic Equivalent Circuit. *IEEE Transactions on Industrial Electronics*, 2021, vol. 68, no. 2, pp. 1046-1054. doi: https://doi.org/10.1109/TIE.2020.2969125.
15. Sharma U., Singh B. Robust design methodology for single phase induction motor ceiling fan. *IET Electric Power Applications*, 2020, vol. 14, no. 10, pp. 1846-1855. doi: https://doi.org/10.1049/iet-epa.2020.0017.
16. Rezazadeh G., Tahami F., Capolino G.-A., Nasiri-Gheidari Z., Henao H., Sahebazamani M. Improved Design of an Outer Rotor Six-Phase Induction Motor With Variable Turn Pseudo-Concentrated Windings. *IEEE Transactions on Energy Conversion*, 2022, vol. 37, no. 2, pp. 1020-1029. doi: https://doi.org/10.1109/TEC.2021.3126538.
17. Tornello L.D., Foti S., Cacciato M., Testa A., Scelba G., De Caro S., Scarcella G., Rizzo S.A. Performance Improvement of Grid-Connected Induction Motors through an Auxiliary Winding Set. *Energies*, 2021, vol. 14, no. 8, art. no. 2178. doi: https://doi.org/10.3390/en14082178.
18. Di C., Petrov I., Pyrhonen J.J. Design of a High-Speed Solid-Rotor Induction Machine With an Asymmetric Winding and Suppression of the Current Unbalance by Special Coil Arrangements. *IEEE Access*, 2019, vol. 7, pp. 83175-83186. doi: https://doi.org/10.1109/ACCESS.2019.2925131.
19. Zablodsky N., Chuenko R., Gritsyuk V., Kovalchuk S., Romanenko O. The Numerical Analysis of Electromechanical Characteristics of Twin-Screw Electromechanical Hydrolyzer. *2021 11th International Conference on Advanced Computer Information Technologies (ACIT)*, 2021, pp. 130-135. doi: https://doi.org/10.1109/ACIT52158.2021.9548392.
20. Kaplun V., Makarevych S., Chuenko R. Modelling of Asynchronous Motor with Split Stator Windings on the Principle of a Rotary Autotransformer. *Przeglad Elektrotechniczny*, 2022, vol. 98, no. 3, pp. 39-43. doi: https://doi.org/10.15199/48.2022.03.10.
21. *AC/DC Module User's Guide*. COMSOL Inc., Burlington, MA, USA, 2018.
22. Rezazadeh G., Tahami F., Capolino G.-A., Vaschetto S., Nasiri-Gheidari Z., Henao H. Improvement of Concentrated Winding Layouts for Six-Phase Squirrel Cage Induction Motors. *IEEE Transactions on Energy Conversion*, 2020, vol. 35, no. 4, pp. 1727-1735. doi: https://doi.org/10.1109/TEC.2020.2995433.
23. *Heat Transfer Module User's Guide*. COMSOL Inc., Burlington, MA, USA, 2018.

Received 16.10.2023
Accepted 12.01.2024
Published 01.05.2024

M.M. Zablodskiy[1]*, Doctor of Technical Science*, *Professor*,
R.M. Chuenko[1]*, PhD*, *Assistant Professor*,
S.I. Kovalchuk[1]*, PhD, Junior Research Scientist,*
H.V. Kruhliak[1]*, Assistant,*
O.I. Kovalchuk[1]*, Postgraduate Student,*
[1] National University of Life and Environmental Sciences of Ukraine,
12, Heroyiv Oborony Str., Kyiv, 03041, Ukraine,
e-mail: stas_kovalchuk@outlook.com (Corresponding Author)

How to cite this article:
Zablodskiy M.M., Chuenko R.M., Kovalchuk S.I., Kruhliak H.V., Kovalchuk O.I. Internal capacitive compensation of the reactive power of the screw electromechanical converter. *Electrical Engineering & Electromechanics*, 2024, no. 3, pp. 11-21. doi: https://doi.org/10.20998/2074-272X.2024.3.02

UDC 621.3.013 https://doi.org/10.20998/2074-272X.2024.3.03

B.I. Kuznetsov, T.B. Nikitina, I.V. Bovdui, K.V. Chunikhin, V.V. Kolomiets, B.B. Kobylianskyi

The method for design of combined electromagnetic shield for overhead power lines magnetic field

Aim. *Development of the method of designing a combined electromagnetic shield, consisting of active and passive parts, to improve the effectiveness of reduction of industrial frequency magnetic field created by two-circuit overhead power lines in residential buildings.* ***Methodology****. The problem of design of combined electromagnetic shield including robust system of active shielding and electromagnetic passive shield of initial magnetic field solved based on of the multi-criteria two-player antagonistic game. The game payoff vector calculated based on the finite element calculations system COMSOL Muliphysics. The game solution calculated based on the particles multiswarm optimization algorithms. During the design of combined electromagnetic shields spatial location coordinates of shielding winding, the currents and phases in the shielding winding of active shielding, geometric dimensions and thickness of the electromagnetic passive shield are calculated.* ***Results.*** *The results of theoretical and experimental studies of combined electromagnetic passive and active shielding of magnetic field in residential building from power transmission line with a «Barrel» type arrangement of wires presented.* ***Originality****. For the first time the method of designing a combined electromagnetic shield, consisting of active and passive parts, for more effective reduction of the magnetic field of industrial frequency created by two-circuit overhead power lines in residential buildings is developed.* ***Practical value****. Based on results of calculated and experimental study the shielding efficiency of the initial magnetic field determined that shielding factors whith only electromagnetic passive shield is more 2 units, whith only active shield is more 4 units and with combined electromagnetic passive and active shield is more 10 units. It is shown the possibility to reduce the level of magnetic field induction in residential building from power transmission line with a «Barrel» type arrangement of wires by means of a combined electromagnetic passive and active shielding with single compensating winding to 0.5 μT level safe for the population.* References 53, figures 15.

Key words: **overhead power line, magnetic field, combined electromagnetic passive and active shielding, computer simulation, experimental research.**

Мета*. Розробка методу проектування комбінованого електромагнітного екрану, що складається з активної та пасивної частин, для підвищення ефективності зниження магнітного поля промислової частоти, створюваного дволанцюговими повітряними лініями електропередачі в житлових будинках.* ***Методологія.*** *Задача проектування комбінованого електромагнітного екрану, що включає робастну систему активного екранування та електромагнітний пасивний екран вихідного магнітного поля, вирішується на основі багатокритеріальної антагоністичної гри двох гравців. Вектор виграшів гри розраховується на основі кінцево-елементної системи обчислень COMSOL Muliphysics. Рішення гри розраховується на основі алгоритмів оптимізації мультироїв частинок. При проектуванні комбінованих електромагнітних екранів розраховуються координати розташування екрануючої обмотки в просторі, струм і фаза в екрануючій обмотці робастної системи активного екранування, та геометричні розміри і товщина електромагнітного пасивного екрану.* ***Результати****. Наведено результати теоретичних та експериментальних досліджень комбінованого електромагнітного пасивного та активного екранування магнітного поля в житловому будинку від дволанцюгової лінії електропередач із розташуванням проводів типу «бочка».* ***Оригінальність****. Вперше розроблено метод проектування комбінованого електромагнітного екрану, що складається з активної та пасивної частин, для підвищення ефективності зниження магнітного поля промислової частоти, створюваного дволанцюговими повітряними лініями електропередачі в житлових будинках.* ***Практична цінність****. За результатами розрахункових та експериментальних досліджень ефективність екранування початкового магнітного поля визначено, що коефіцієнти екранування системи тільки з електромагнітним пасивним екраном дорівнює більше 2 одиниць, тільки з активним екраном дорівнює більше 4 одиниць, а з комбінованим електромагнітним пасивним і активним екраном дорівнює більше 10 одиниць. Показано можливість зниження рівня індукції магнітного поля в житловому будинку від дволанцюгової лінії електропередач із розташуванням проводів типу «бочка» за допомогою комбінованого електромагнітного пасивного та активного екранування з однією компенсуючою обмоткою до безпечного для населення рівня в 0,5 мкТл.* Бібл. 53, рис. 15.

Ключові слова: **повітряна лінія електропередачі, магнітне поле, комбіноване електромагнітне пасивне та активне екранування, комп'ютерне моделювання, експериментальні дослідження.**

Introduction. Prolonged exposure of the population to even weak levels of the industrial frequency magnetic field leads to an increased level of cancer in the population living in residential buildings near power lines [1-3]. The creation of methods and means of normalizing the level of the electromagnetic field in existing residential areas near power lines without evicting the population or decommissioning existing electrical networks determines the economic significance of such studies. Therefore, methods are being intensively developed all over the world to reduce the level of the magnetic field (MF) in existing residential buildings located near power lines to a safe level for the population to live in it [4-7].

To reduce the magnetic field inside residential premises, it is technically easiest to use passive shielding. The principle of operation of the electromagnetic shield can be described as follows [8-15]: under the action of the primary MF, conduction currents are induced in the shield; these currents create a secondary field; from the addition of the primary field with the secondary, the resulting field is formed, which is weaker than the primary in the protected area. Therefore, for the manufacture of electromagnetic shields, materials with a high electrical conductivity value should be used. The most widely used electromagnetic screens are made of aluminum, the cost of which is relatively low. However, the cost of such passive screens, especially when screening large volumes of residential premises, is the main limitation of the use of such screens, especially when using mu-metal passive screens. To increase the shielding efficiency, multilayer passive shields are widely used, consisting of several layers of conductive and ferromagnetic shields. Such screens are widely used for shielding the magnetic field in magnetically clean rooms together with active screens.

For shielding large volumes, it is economically most expedient to use active shields [16-23]. A feature of the use of active screens is the need to provide an active screening system and constant power consumption during the operation of the system. To save energy consumption, the active shielding system can only be switched on when there are people in the living space. Therefore, when designing shielding systems for residential premises, it can often be the most effective option to use combined shielding of the initial magnetic field, including an active shielding system and passive shielding.

Such combined screens are widely used in world practice [16]. On Fig. 1 show a room located near power lines. The main shielding effect is provided by an active shielding system with one compensation winding laid along the building. Additional screening is provided by passive screen sheets laid on the floor.

Fig. 1. The room located near power lines

The aim of the work is development of method of designing a combined electromagnetic shield, consisting of active and passive parts, to improve the effectiveness of reduction of industrial frequency magnetic field created by two-circuit overhead power lines in residential buildings.

Problem statement. We set the currents amplitude A_i and phases φ_i of power frequency ω wires currents in power lines. Then we set the wires currents in power lines in a complex form

$$I_i(t) = A_i \exp j(\omega t + \varphi_i). \quad (1)$$

Then the vector $\boldsymbol{B_p}(Q_i,t)$ of the magnetic field generated by all power lines wires in point Q_i of the shielding space can calculated based Biot-Savart law [6].

We set the vector $\boldsymbol{X_a}$ of initial geometric values of the dimensions of the compensating windings, as well as the currents amplitude A_{wi} and phases φ_{wi} in the compensating windings. We set the currents in the compensating windings wires in a complex form

$$I_{wi}(t) = A_{wi} \exp j(\omega t + \varphi_{wi}). \quad (2)$$

Then the vector $\boldsymbol{B_W}(Q_i,\ t)$ of the magnetic field generated by all compensating windings wires in point Q_i of the shielding space can also calculated based Biot-Savart law.

Let us set the vector $\boldsymbol{X_p}$ of initial values of the geometric dimensions, thickness and material of the passive shield. Then for the given geometric dimensions of the power lines wire and the initial values of the geometric dimensions of the compensation winding wires, as well as for the given values of currents and phases in the power lines wires and the initial values of currents and phases in the wires in the compensation windings, as well as for the initial values of the geometric dimensions, thickness and material of the passive screens, the vector $\boldsymbol{B_R}(Q_i,\ t)$ of the rezalting magnetic field induction in the Q_i point of the shielding space can be calculated.

We introduce the vector $\boldsymbol{X}$ of the desired parameters of the problem of designing a combined shield, the components of which are the vector $\boldsymbol{X_a}$ values of the geometric dimensions of the compensation windings, as well as the currents A_{wi} and phases φ_{wi} in the compensation windings, as well as the vector $\boldsymbol{X_p}$ of geometric dimensions, thickness and material of the passive shield.

Let us introduce the vector $\boldsymbol{\delta}$ of the uncertainty parameters of the problem of designing a combined shield, the components of which are inaccurate knowledge of the currents and phases in the wires of the power transmission line, as well as other parameters of the combined shielding system, which, firstly, are initially known inaccurately and, secondly, may change during the operation of the system [24-28].

Then for the given initial values of the $\boldsymbol{X}$ vector of the desired parameters and the vector $\boldsymbol{\delta}$ of the uncertainty parameters of the combined screen design problem, the value $\boldsymbol{B_R}(\boldsymbol{X},\ \boldsymbol{\delta},\ P_i)$ of the magnetic induction at the point P_i of the shielding space calculated based on the finite element calculations system COMSOL Muliphysics. Then the problem of designing a passive screen is reduced to computing the solution of the vector game

$$\boldsymbol{B_R}(\boldsymbol{X},\boldsymbol{\delta}) = \langle B_R(X,\delta,P_i)\rangle. \quad (3)$$

The components of the game payoff vector $\boldsymbol{B_R}(\boldsymbol{X},\ \boldsymbol{\delta})$ are the effective values of the induction of the resulting magnetic field $\boldsymbol{B_R}(\boldsymbol{X},\ \boldsymbol{\delta},\ P_i)$ at all considered points Q_i in the shielding space.

In this vector game it is necessary to find the minimum of the game payoff vector (11) by the vector $\boldsymbol{X}$, but the maximum of the same vector objective function by the vector $\boldsymbol{\delta}$.

At the same time, naturally, it is necessary to take into account constraints on the vector $\boldsymbol{X}$ desired parameters of a combined shield in the form of vector inequality and, possibly, vector equality [29-33]

$$\boldsymbol{G}(\boldsymbol{X}) \le \boldsymbol{G_{max}},\quad \boldsymbol{H}(\boldsymbol{X}) = 0. \quad (4)$$

Note that the components of the vector game (3) and vector constraints (4) are the nonlinear functions of the vector of the required parameters [5, 6].

The solutions of the vector game (3) subject to constraints (4) are calculated from the Pareto set of optimal solutions based on algorithms particles multiswarm optimization.

Solving problem agorithm. A feature of the problem under consideration is the presence of several conflicting goals. Minimization of the magnetic field at one point leads to an increase in the magnetic field at other points due to undercompensation or overcompensation of the initial magnetic field. Minimax problems are widely used in robust control. If it is necessary to find the minimum in one variable and the maximum in other variables of the same objective function, then the necessary condition for the optimal minimax problem is that the gradient of the objective function in all variables is equal to zero, regardless of whether the target function is minimized or maximized function [34-37].

When solving this minimax problem numerically, in order to find the direction of movement, it is necessary to use the components of the gradient of the objective function for those variables over which the maximization is performed, and it is necessary to use the components of the antigradient (i.e., the gradient taken with the opposite

sign) for those variables over which the minimization is performed [38-43].

Recently, in the synthesis of control systems, a game approach has become widespread, which makes it possible to formulate the problem of synthesizing a system for a game. In this case, the area of parameter variations is divided into two sets of friendly $\boldsymbol{X}$ and enemy $\boldsymbol{\delta}$. The goal of the players is to choose such values X at which the value of the optimized quality criterion (3) is minimized, and the task of the opponent is to choose such values of the parameters $\boldsymbol{\delta}$ at which the value of the quality criterion is maximized.

To solve this minimax problem of multi-criteria optimization (3), we use the simplest linear trade-off scheme, in which the original multi-criteria problem was reduced to a single-criteria

$$\boldsymbol{f(X,\delta)} = \sum_{i=1}^{J} \alpha_i \boldsymbol{B_R(X,\delta,}P_I) \tag{5}$$

where α_i are weight coefficients that characterize the importance of particular criteria and determine the preference for individual criteria by the decision maker.

A necessary condition for optimality

$$\boldsymbol{X}^* = \arg\min_{X} \sum_{i=1}^{J} \alpha_i \boldsymbol{B_R(X,\delta,}P_I); \tag{6}$$

$$\boldsymbol{\delta}^* = \arg\max_{\delta} \sum_{i=1}^{J} \alpha_i \boldsymbol{B_R(X,\delta,}P_I) \tag{7}$$

is the existence of a saddle point. In which the equality to zero of the gradients of the objective function

$$\nabla_{\boldsymbol{X}} \boldsymbol{f}/_{\boldsymbol{X}=\boldsymbol{X}^*} = 0, \quad \nabla_{\boldsymbol{\delta}} \boldsymbol{f}/_{\boldsymbol{\delta}=\boldsymbol{\delta}^*} = 0. \tag{8}$$

A sufficient condition for the existence of a saddle point is a change in the sign of the gradient $\nabla_{\boldsymbol{X}} \boldsymbol{f}$ when passing the minimum point from minus to plus, and a change in the signs of the gradient $\nabla_{\boldsymbol{\delta}} \boldsymbol{f}$ when passing the maximum point from plus to minus [44-47]. These conditions can be formulated as the positive definiteness $\boldsymbol{H_X}>0$ of the matrix of second derivatives – the Hessian matrix with respect to the choice of parameters X, and the negative definiteness $\boldsymbol{H_\delta}\leq 0$ of the Hessian matrix with respect to the parameters $\boldsymbol{\delta}$, i.e. the task becomes much more complicated if the quality criterion is vector $\boldsymbol{B_R(X,\delta)}$.

Note that the quality criterion $\boldsymbol{B_R(X,\delta)}$ usually includes both system state variables or their combination, characterizing the accuracy of the system, and state variables that need to be limited and the control vector is necessarily included. Otherwise, the original problem becomes degenerate and leads to infinite controls. Moreover, the choice of weight matrix functions in the quality criterion when solving specific problems is carried out iteratively by repeatedly solving the original optimization problem for different values of the weight functions until acceptable results are obtained.

In fact, the semantic statement of the problem is reduced to the synthesis of such a system, which provides the minimum value of the error characterizing the accuracy of the system when constraints (4) on the state vector component are met and when constraints on the control vector are met.

Consider the use of penalty (barrier functions) for solving a mathematical programming problem in the presence of restrictions. Let us first consider the application of the interior point method to solve a mathematical programming problem that does not contain restrictions in the form of equalities. Let us assume that near the optimal point, the local optimum conditions are satisfied in the following form

$$\begin{cases} g_i(x) \geq 0, i = \overline{1,m}, \\ u_i g_i(x) = r > 0, i = \overline{1,m}, \\ u_i \geq 0, i = \overline{1,m}, \\ \nabla f(x) - \sum_{i=1}^{m} u_i \nabla g_i(x) = 0. \end{cases} \tag{9}$$

Whence the following equality can be obtained

$$\nabla f(x(r)) - \sum_{i=1}^{m} \frac{r}{g_i(x(r))} \nabla g_i(x(r)) = 0. \tag{10}$$

This equality can be interpreted as a necessary condition for a local optimum in the form of zero gradient, under which the original objective function of the nonlinear programming problem takes the following form

$$L(x,r) = f(x) - r\sum_{i=1}^{m} \ln g_i(x). \tag{11}$$

Similarly, another objective function can be obtained, provided that from the expression

$$\lambda_i g_i(x) = r > 0, i = \overline{1,m} \tag{12}$$

for the gradient

$$\nabla f[x(r)] - \sum_{i=1}^{m} \frac{r^2}{g_i^2[x(r)]} \nabla g_i[x(r)] = 0. \tag{13}$$

The objective function $L_1(x, r)$ will take the following form

$$L_1(x,r) = f(x) + r^2 \sum_{i=1}^{m} \frac{1}{g_i(x)}. \tag{14}$$

These objective functions allow us to reduce the initial problem of nonlinear programming in the presence of restrictions to the solution of the problem of unconditional optimization in such a way that when approaching the boundary of the restrictions from the inside, the penalty for violation of the restrictions tends to infinity, which corresponds to the interior point method in the penalty functions algorithm.

Thus the problem of multicriteria synthesis (3) of nonlinear robust control using a linear compromise scheme (5) is reduced to a single-criteria problem of mathematical programming (12). Consider the application of the sequential quadratic programming method to solve this problem. This method and its software implementation were proposed by Schittkowski at the beginning for solving the least squares minimization problem. This method is a combination of the Gauss-Newton method with determining the direction of movement using a quasi-Newtonian algorithm.

Consider first the minimization of the quadratic norm L_2, usually called the unconstrained least squares problem

$$f(x) = \frac{1}{2} \sum_{i=1}^{l} f_i(x)^2. \tag{15}$$

The gradient of this objective function can be represented as follows

$$\nabla f(x) = \nabla F(x) F(x), \quad (16)$$

where the Jacobian $\nabla F(x) = (\nabla f_1(x),..., \nabla f_l(x))$ of this function is denoted and it is assumed that the components of the objective function can be doubly differentiated. Then the matrix of second derivatives of the objective function – the Hesse matrix can be written in the following form

$$\nabla^2 f(x) = \nabla F(x) \nabla F(x)^T + B(x), \quad (17)$$

where

$$B(x) = \sum_{i=1}^{l} f_i(x) \nabla^2 f_i(x) \nabla^2 f_i(x).$$

Then the iterative procedure for choosing the direction $d_k \in R^n$ of motion using the Newton method can be reduced to solving a linear system

$$\nabla^2 f(x_k) d + \nabla f(x_k) = 0, \quad (18)$$

or to the solution of an equivalent system in the following form

$$\nabla F(x_k) \nabla F(x_k)^T d + B(x_k) d + \ldots + \nabla F(x_k) F(x_k) = 0. \quad (19)$$

At the optimal solution point x^*, the following condition is satisfied

$$F(x^*) = \left(f_1(x^*),..., f_l(x^*)\right)^T = 0, \quad (20)$$

therefore, finding the motion step d can be reduced to solving the normal equation of the least squares problem

$$\min_{d \in R^n} \left\| \nabla F(x_k)^T d + F(x_k) \right\|, \quad (21)$$

from which a recurrent equation $x_{k+1} = x_k + \alpha_k d_k$ can be obtained for iteratively finding the vector of desired parameters, in which is the solution d_k to the optimization problem, and α_k is an experimentally determined parameter.

This algorithm uses the Gauss–Newton method, which is a traditional algorithm for solving the non-linear least squares problem, to calculate the direction of motion. In the general case, the Gauss-Newton method makes it possible to obtain a solution to the problem of sequential quadratic programming using only first-order derivatives, but in real situations it often fails to obtain a solution.

Therefore, to improve convergence, second-order methods are used, in which the matrix of second derivatives of the objective function is used - the Jacobian matrix when solving optimization problems without restrictions. Second-order algorithms, compared to first-order methods, allow one to efficiently obtain a solution in a region close to the optimal point, when the components of the gradient vector have sufficiently small values.

Recently, methods using Levenberg-Marquardt algorithms have become widespread in quasi-Newtonian methods. The idea of these methods is to replace the Hesse matrix with some matrix $\lambda_k I$ with a positive coefficient λ_k. Then we obtain the following system of linear equations

$$\nabla F(x_k) \nabla F(x_k)^T d + \lambda_k d + \nabla F(x_k) F(x_k) = 0. \quad (22)$$

There are many different methods for solving the non-linear least squares problem without restrictions. On the other hand, there is a simple approach for combining the properties of the Gauss-Newton method with the method of sequential quadratic programming. The main problem of applying the method of sequential quadratic programming is the need to use special methods to ensure negative eigenvalues when approximating the Hess matrix in the case of alternative approaches.

Deterministic optimization methods such as linear programming and non-linear programming are widely used to solve multiobjective optimization problems.

However, these methods use a one-point approach and the result of these classical optimization methods is a single optimal solution. For example, the method of the weighted sum of local criteria transforms the multicriteria optimization problem into a single-criteria optimization problem, which makes it possible to obtain one point on the front of Pareto-optimal solutions.

To find the global optimum from Pareto optimal solutions, it is necessary to consider all possible Pareto fronts. In this case, it is necessary that the algorithms for finding the global optimum point are performed iteratively, so as to ensure that each combination of weights has been used.

To exhaust all combinations of weight, it is necessary to repeat the algorithms of such a local search many times. Therefore, algorithms must be able to «learn» from the solutions obtained in order to guide the correct choice of weight in further evolutions. When using classical methods for finding a global optimal solution, problems arise if the optimal solution is located in non-convex or disconnected regions of the functional space.

Recently, metaheuristic methods such as evolutionary algorithms and group intelligence technologies have become increasingly popular for solving the optimization problem [48-50]. Evolutionary methods, due to their efficiency and simplicity, have been successfully used to solve optimization problems with one objective function. These methods have some advantages over classical optimization methods, since they allow calculating optimal solutions for non-linear and non-convex functions [51-53].

They use the set of solutions in each iteration and stochastic search, and therefore they can find a search anywhere in the entire search space and are able to overcome the problems of local optima. Stochastic search methods are also more suitable for solving problems of multiobjective optimization.

Among the metaheuristic techniques, until recently, particle swarm optimization was applied only to single-objective optimization problems. The high convergence rate of particle swarm optimization algorithms for developing a multi-objective optimization algorithm has some advantages in terms of better exploration and exploitation provided by the algorithm's global search capability.

In the standard particle swarm optimization algorithm, particle velocities change according to linear laws, in which the movement of particle i swarm j is described by the following expressions [49]

$$v_{ij}(t+1) = c_{1j} r_{1j}(t) \times \ldots \\ \ldots \times \left[y_{ij}(t) - x_{ij}(t) \right] + c_{2j} r_{2j}(t) \times \ldots \\ \ldots \times \left[y_j^*(t) - x_{ij}(t) \right], \quad (23)$$

$$x_{ij}(t+1) = x_{ij}(t) + v_{ij}(t+1), \quad (24)$$

where, are the position $x_{ij}(t)$ and speed $v_{ij}(t)$ of the particle i of the swarm j; c_1, c_2 – positive constants that determine the weights of the cognitive and social components of the speed of particle movement; $r_{1j}(t)$, $r_{2j}(t)$ are random

numbers from the range [0, 1], which determine the stochastic component of the particle velocity component. Here, $y_{ij}(t)$ and y_j^* – the best local-lbest and global-gbest positions of that particle i are found, respectively, only by one particle i and by all particles i of that swarm j. The use of the inertia coefficient w_j allows improving the quality of the optimization process.

In order to increase the speed of finding a global solution, special nonlinear algorithms of stochastic multi-agent optimization have recently become widespread [51-53].

Naturally, the formalization of the solution of the multiobjective optimization problem by reducing it to a single-objective problem makes it possible to reasonably choose one single point from the area of compromises – the Pareto area [48]. However, this «single» point can be further tested in order to further improve the trade-off scheme from the point of view of the decision maker [52, 53].

Simulation results. Let us consider the results of the design of combined electromagnetic passive and active shielding of overhead power lines magnetic field generated by a double-circuit power line in a residential building, as shown in Fig. 2.

Fig. 2. Residential building cloused to double-circuit power line

Figure 3 shows the scheme of the shielding system design.

Figure 4 shows the distribution of the calculated initial magnetic field induction.

Figure 5 shows the distribution of the calculated resulting magnetic field induction whith only electromagnetic passive shield. The calculated shielding factor maximum value of resulting magnetic field whith only electromagnetic passive shield is more 4 units.

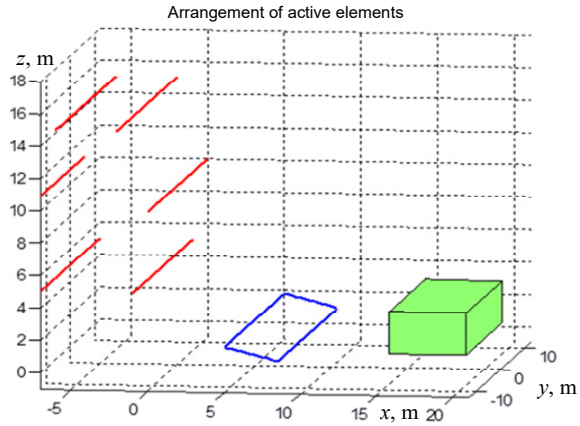

Fig. 3. Scheme of the shielding system design

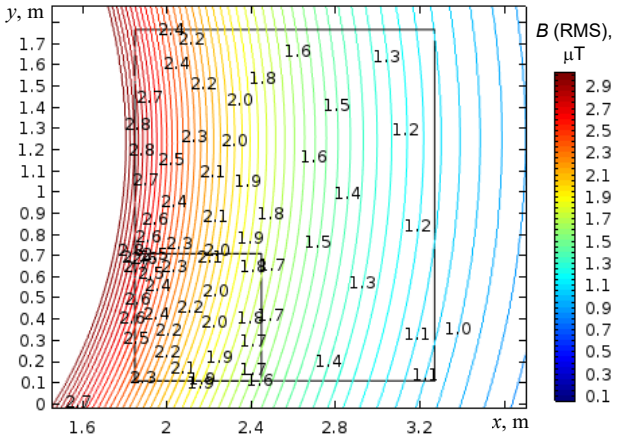

Fig. 4. Distribution of the calculated initial magnetic field induction

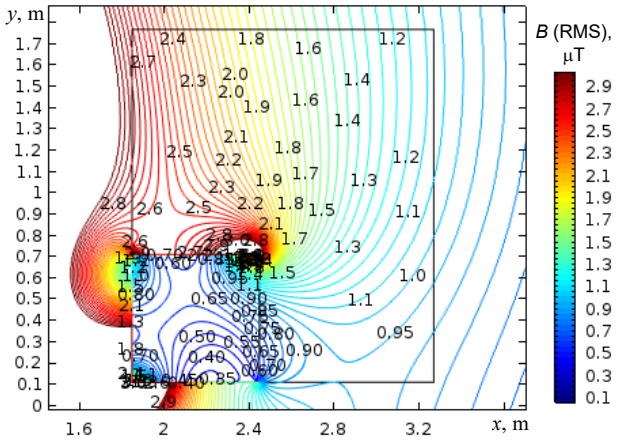

Fig. 5. Distribution of the calculated resulting magnetic field induction with only electromagnetic passive shield

Figure 6 shows the distribution of the calculated resulting magnetic field induction with only active shield. The calculated shielding factor maximum value of resulting magnetic field whith only active shield is more 4 units.

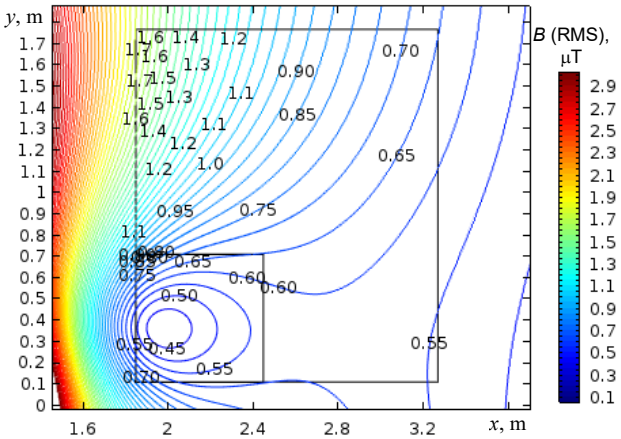

Fig. 6. Distribution of the calculated resulting magnetic field induction with only active shield

Figure 7 shows the distribution of the calculated resulting magnetic field induction with electromagnetic passive and active shield. The calculated shielding factor maximum value of resulting magnetic field whith electromagnetic passive and active shield is more 13 units.

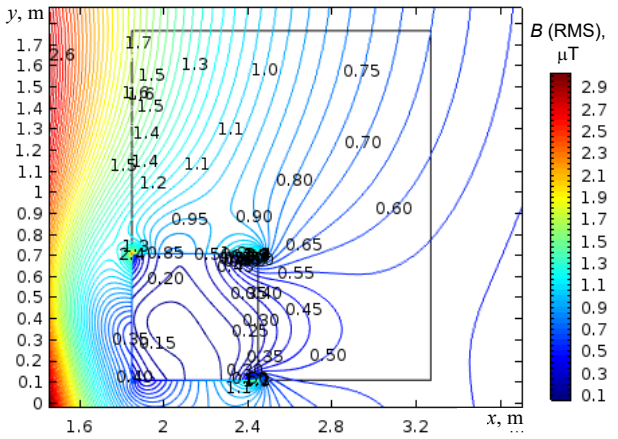

Fig. 7. Distribution of the calculated resulting magnetic field induction with combined electromagnetic passive and active shield

Results of experimental studies. Let us now consider the results of experimental studies of the electromagnetic passive and active shielding.

Figure 8 shows the compensation winding and electromagnetic passive shield of the experimental setup.

Figure 9 shows the control system of the experimental setup of electromagnetic passive and active shielding.

Fig. 8. Compensation winding and electromagnetic passive shield of the experimental setup of electromagnetic passive and active shielding

Fig. 9. Control system of the experimental setup

Figure 10 shows the experimental spatio-temporal characteristic of the initial magnetic field.

Figure 11 shows the experimental shielding factor of resulting magnetic field whith only electromagnetic passive shield. The experimental shielding factor maximum value of resulting magnetic field whith only electromagnetic passive shield is more 2 units.

Figure 12 shows the experimental spatio-temporal characteristic of the resulting magnetic field with only electromagnetic passive shield.

The experimental spatio-temporal characteristic of the resulting magnetic field with only electromagnetic passive shield is about 2 times less than the original characteristic, which is shown in Fig. 10 and rotated counterclockwise about 20 degrees clockwise.

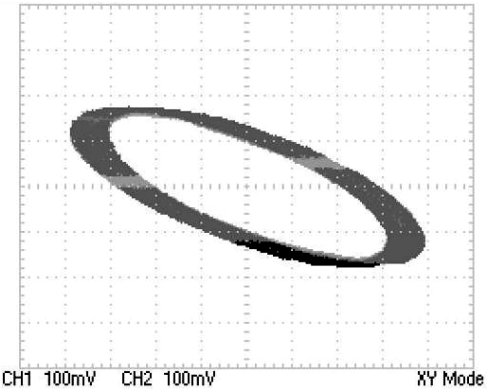

Fig. 10. Experimental spatio-temporal characteristic of the initial magnetic field

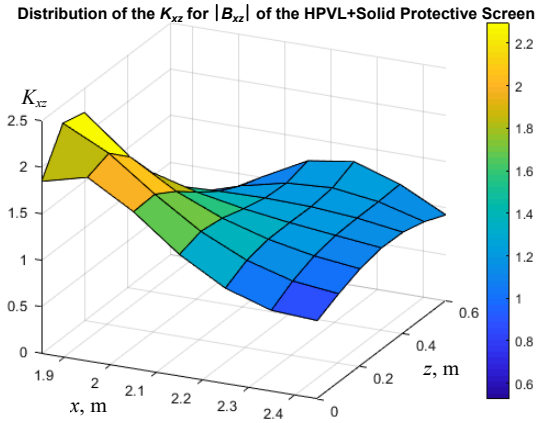

Fig. 11. Experimental shielding factor of resulting magnetic field with only electromagnetic passive shield

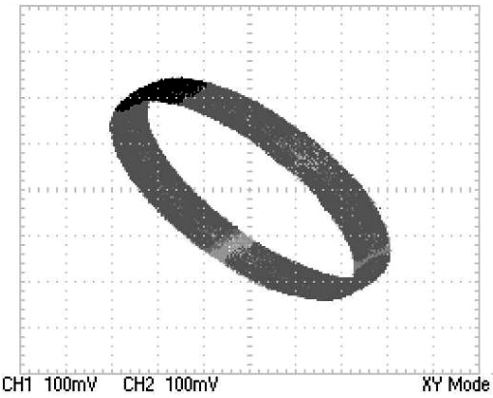

Fig 12. Experimental spatio-temporal characteristic of the resulting magnetic field with only electromagnetic passive shield

Figure 13 shows the experimental shielding factor of resulting magnetic field whith only active shield. The experimental shielding factor maximum value of resulting magnetic field whith only active shield is more 5 units.

Figure 14 shows the experimental spatio-temporal characteristic of the resulting magnetic field with only active shield. The experimental spatio-temporal characteristic of the resulting magnetic field with only active shield actually represents a point which is blurred by the noise of the magnetic sensors of the spatio-temporal characteristic measurement system.

Figure 15 shows the experimental shielding factor of resulting magnetic field with electromagnetic passive and

active shield. The experimental shielding factor maximum value of resulting magnetic field with electromagnetic passive and active shield is more 10 units.

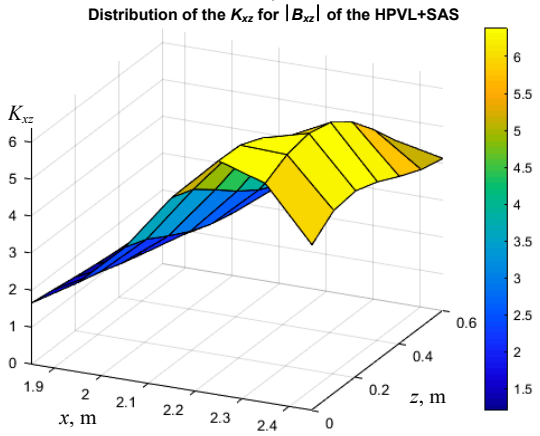

Fig. 13. Experimental shielding factor of resulting magnetic field whith only active shield

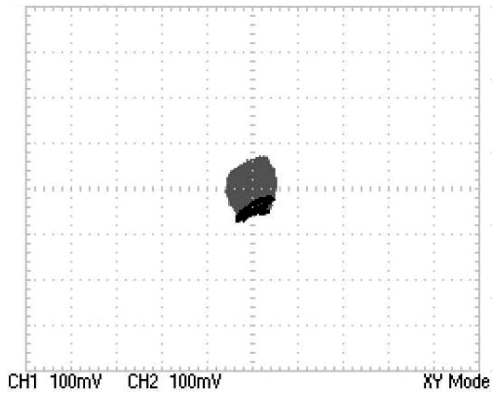

Fig. 14. Experimental spatio-temporal characteristic of the resulting magnetic field with only active shield

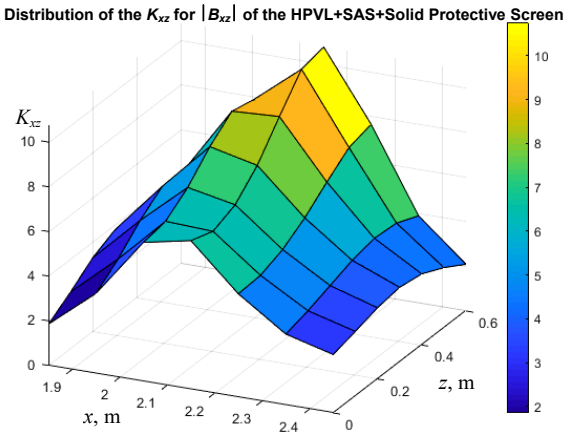

Fig. 15. Experimental shielding factor of resulting magnetic field with combined electromagnetic passive and active shield

Conclusions.

1. For the first time the method of designing a combined electromagnetic shield, consisting of active and passive parts, to improve the effectiveness of reduction of industrial frequency magnetic field created by two-circuit overhead power lines in residential buildings.

2. The problem of design of combined electromagnetic passive and active shielding solved based on the multi-criteria two-player antagonistic game. The game payoff vector calculated based on the finite element calculations system COMSOL Muliphysics. The solution of this game calculated based on algorithms of multi-swarm multi-agent optimization from sat of Pareto-optimal solutions based on binary preferences.

3. During the design of combined electromagnetic passive and active shields spatial location coordinates of shielding winding, the currents and phases in the shielding winding of active shielding, geometric dimensions and thickness of the electromagnetic passive shield are calculated.

4. Based on the developed method the combined electromagnetic passive and active shields for magnetic field generated by double-circuit overhead power lines in residential building were design. The results of calculating and experimental studi the shielding efficiency of the initial magnetic field using designed combined active and electromagnetic passive shielding are given.

5. The results of the performed theoretical and experimental studies have shown that the shielding factor is only passive electromagnetic screen made of a solid aluminum plate with a thickness of 1.5 mm is about 2 units, only active screen made in the form of a winding consisting of 20 turns is about 4 units. When using a combined electromagnetic passive and active screen, the shielding factor was more 10 units, which confirms its high efficiency, exceeding the product shielding factors of passive and active shields.

6. The practical use of the developed combined electromagnetic screen will allow reducing the level of the magnetic field in a residential building from a double-circuit power transmission line with a «barrel» type arrangement of wires to a safe level for the population of 0.5 μT.

Acknowledgments. The authors express their gratitude to PhD, Research Scientist O.O. Tkachenko of the Department of Magnetism of Technical Objects of Anatolii Pidhornyi Institute of Mechanical Engineering Problems of the National Academy of Sciences of Ukraine for your help in carrying out calculations for designing combined electromagnetic shield.

The authors also express their gratitude to the engineers Sokol A.V. and Shevchenko A.P. for the creative approach and courage shown during the creation under fire, under martial law, of an experimental installation and successful testing of a laboratory model of the system of active silencing.

Conflict of interest. The authors declare that they have no conflicts of interest.

REFERENCES

1. Sung H., Ferlay J., Siegel R.L., Laversanne M., Soerjomataram I., Jemal A., Bray, F. Global Cancer Statistics 2020: GLOBOCAN Estimates of Incidence and Mortality Worldwide for 36 Cancers in 185 Countries. *CA: A Cancer Journal for Clinicians*, 2021, vol. 71, no. 3, pp. 209-249. doi: https://doi.org/10.3322/caac.21660.

2. *Directive 2013/35/EU of the European Parliament and of the Council of 26 June 2013 on the minimum health and safety requirements regarding the exposure of workers to the risks arising from physical agents (electromagnetic fields)*. Available at: http://data.europa.eu/eli/dir/2013/35/oj (Accessed 25.07.2022).

3. *The International EMF Project. Radiation & Environmental Health Protection of the Human Environment World Health Organization*. Geneva, Switzerland, 1996. 2 p. Available at: https://www.who.int/initiatives/the-international-emf-project (Accessed 25.07.2022).

4. Rozov V., Grinchenko V., Tkachenko O., Yerisov A. Analytical Calculation of Magnetic Field Shielding Factor for Cable Line with Two-Point Bonded Shields. *2018 IEEE 17th International Conference*

on Mathematical Methods in Electromagnetic Theory (MMET), 2018, pp. 358-361. doi: https://doi.org/10.1109/MMET.2018.8460425.
5. Rozov V.Y., Pelevin D.Y., Levina S.V. Experimental research into indoor static geomagnetic field weakening phenomenon. *Electrical Engineering & Electromechanics*, 2013, no. 6, pp. 72-76. (Rus). doi: https://doi.org/10.20998/2074-272X.2013.6.13.
6. Rozov V.Y., Kvytsynskyi A.A., Dobrodeyev P.N., Grinchenko V.S., Erisov A.V., Tkachenko A.O. Study of the magnetic field of three phase lines of single core power cables with two-end bonding of their shields. *Electrical Engineering & Electromechanics*, 2015, no. 4, pp. 56-61. (Rus). doi: https://doi.org/10.20998/2074-272X.2015.4.11.
7. Rozov V.Yu., Reutskyi S.Yu., Pelevin D.Ye., Kundius K.D. Approximate method for calculating the magnetic field of 330-750 kV high-voltage power line in maintenance area under voltage. *Electrical Engineering & Electromechanics*, 2022, no. 5, pp. 71-77. doi: https://doi.org/10.20998/2074-272X.2022.5.12.
8. Salceanu A., Paulet M., Alistar B.D., Asiminicesei O. Upon the contribution of image currents on the magnetic fields generated by overhead power lines. *2019 International Conference on Electromechanical and Energy Systems (SIELMEN).* 2019. doi: https://doi.org/10.1109/sielmen.2019.8905880.
9. Del Pino Lopez J.C., Romero P.C. Influence of different types of magnetic shields on the thermal behavior and ampacity of underground power cables. *IEEE Transactions on Power Delivery*, Oct. 2011, vol. 26, no. 4, pp. 2659-2667. doi: https://doi.org/10.1109/tpwrd.2011.2158593.
10. Hasan G.T., Mutlaq A.H., Ali K.J. The Influence of the Mixed Electric Line Poles on the Distribution of Magnetic Field. *Indonesian Journal of Electrical Engineering and Informatics (IJEEI)*, 2022, vol. 10, no. 2, pp. 292-301. doi: https://doi.org/10.52549/ijeei.v10i2.3572.
11. Victoria Mary S., Pugazhendhi Sugumaran C. Investigation on magneto-thermal-structural coupled field effect of nano coated 230 kV busbar. *Physica Scripta*, 2020, vol. 95, no. 4, art. no. 045703. doi: https://doi.org/10.1088/1402-4896/ab6524.
12. Ippolito L., Siano P. Using multi-objective optimal power flow for reducing magnetic fields from power lines. *Electric Power Systems Research*, 2004, vol. 68, no. 2, pp. 93-101. doi: https://doi.org/10.1016/S0378-7796(03)00151-2.
13. Barsali S., Giglioli R., Poli D. Active shielding of overhead line magnetic field: Design and applications. *Electric Power Systems Research*, May 2014, vol. 110, pp. 55-63. doi: https://doi.org/10.1016/j.epsr.2014.01.005.
14. Bavastro D., Canova A., Freschi F., Giaccone L., Manca M. Magnetic field mitigation at power frequency: design principles and case studies. *IEEE Transactions on Industry Applications*, May 2015, vol. 51, no. 3, pp. 2009-2016. doi: https://doi.org/10.1109/tia.2014.2369813.
15. Beltran H., Fuster V., García M. Magnetic field reduction screening system for a magnetic field source used in industrial applications. *9 Congreso Hispano Luso de Ingeniería Eléctrica (9 CHLIE)*, Marbella (Málaga, Spain), 2005, pp. 84-99.
16. Bravo-Rodríguez J., Del-Pino-López J., Cruz-Romero P. A Survey on Optimization Techniques Applied to Magnetic Field Mitigation in Power Systems. *Energies*, 2019, vol. 12, no. 7, p. 1332. doi: https://doi.org/10.3390/en12071332.
17. Canova A., del-Pino-López J.C., Giaccone L., Manca M. Active Shielding System for ELF Magnetic Fields. *IEEE Transactions on Magnetics*, March 2015, vol. 51, no. 3, pp. 1-4. doi: https://doi.org/10.1109/tmag.2014.2354515.
18. Canova A., Giaccone L. Real-time optimization of active loops for the magnetic field minimization. *International Journal of Applied Electromagnetics and Mechanics*, Feb. 2018, vol. 56, pp. 97-106. doi: https://doi.org/10.3233/jae-172286.
19. Canova A., Giaccone L., Cirimele V. Active and passive shield for aerial power lines. *Proc. of the 25th International Conference on Electricity Distribution (CIRED 2019)*, 3-6 June 2019, Madrid, Spain. Paper no. 1096.
20. Canova A., Giaccone L. High-performance magnetic shielding solution for extremely low frequency (ELF) sources. *CIRED - Open Access Proceedings Journal*, Oct. 2017, vol. 2017, no. 1, pp. 686-690. doi: https://doi.org/10.1049/oap-cired.2017.1029.
21. Celozzi S. Active compensation and partial shields for the power-frequency magnetic field reduction. *2002 IEEE International Symposium on Electromagnetic Compatibility*, Minneapolis, MN, USA, 2002, vol. 1, pp. 222-226. doi: https://doi.org/10.1109/isemc.2002.1032478.
22. Celozzi S., Garzia F. Active shielding for power-frequency magnetic field reduction using genetic algorithms optimization. *IEE Proceedings - Science, Measurement and Technology*, 2004, vol. 151, no. 1, pp. 2-7. doi: https://doi.org/10.1049/ip-smt:20040002.
23. Celozzi S., Garzia F. Magnetic field reduction by means of active shielding techniques. *WIT Transactions on Biomedicine and Health*, 2003, vol. 7, pp. 79-89. doi: https://doi.org/10.2495/ehr030091.
24. Martynenko G. Analytical Method of the Analysis of Electromagnetic Circuits of Active Magnetic Bearings for Searching Energy and Forces Taking into Account Control Law. *2020 IEEE KhPI Week on Advanced Technology (KhPIWeek)*, 2020, pp. 86-91. doi: https://doi.org/10.1109/KhPIWeek51551.2020.9250138.
25. Popov A., Tserne E., Volosyuk V., Zhyla S., Pavlikov V., Ruzhentsev N., Dergachov K., Havrylenko O., Shmatko O., Averyanova Y., Ostroumov I., Kuzmenko N., Sushchenko O., Zaliskyi M., Solomentsev O., Kuznetsov B., Nikitina T. Invariant Polarization Signatures for Recognition of Hydrometeors by Airborne Weather Radars. *Computational Science and Its Applications – ICCSA 2023. Lecture Notes in Computer Science*, 2023, vol. 13956, pp. 201-217. doi: https://doi.org/10.1007/978-3-031-36805-9_14.
26. Sushchenko O., Averyanova Y., Ostroumov I., Kuzmenko N., Zaliskyi M., Solomentsev O., Kuznetsov B., Nikitina T., Havrylenko O., Popov A., Volosyuk V., Shmatko O., Ruzhentsev N., Zhyla S., Pavlikov V., Dergachov K., Tserne E. Algorithms for Design of Robust Stabilization Systems. *Computational Science and Its Applications – ICCSA 2022. ICCSA 2022. Lecture Notes in Computer Science*, 2022, vol. 13375, pp. 198-213. doi: https://doi.org/10.1007/978-3-031-10522-7_15.
27. Ostroverkhov M., Chumack V., Monakhov E., Ponomarev A. Hybrid Excited Synchronous Generator for Microhydropower Unit. *2019 IEEE 6th International Conference on Energy Smart Systems (ESS)*, Kyiv, Ukraine, 2019, pp. 219-222. doi: https://doi.org/10.1109/ess.2019.8764202.
28. Ostroverkhov M., Chumack V., Monakhov E. Ouput Voltage Stabilization Process Simulation in Generator with Hybrid Excitation at Variable Drive Speed. *2019 IEEE 2nd Ukraine Conference on Electrical and Computer Engineering (UKRCON)*, Lviv, Ukraine, 2019, pp. 310-313. doi: https://doi.org/10.1109/ukrcon.2019.8879781.
29. Tytiuk V., Chornyi O., Baranovskaya M., Serhiienko S., Zachepa I., Tsvirkun L., Kuznetsov V., Tryputen N. Synthesis of a fractional-order $PI^{\lambda}D^{\mu}$-controller for a closed system of switched reluctance motor control. *Eastern-European Journal of Enterprise Technologies*, 2019, no. 2 (98), pp. 35-42. doi: https://doi.org/10.15587/1729-4061.2019.160946.
30. Zagirnyak M., Chornyi O., Zachepa I. The autonomous sources of energy supply for the liquidation of technogenic accidents. *Przeglad Elektrotechniczny*, 2019, no. 5, pp. 47-50. doi: https://doi.org/10.15199/48.2019.05.12.
31. Chornyi O., Serhiienko S. A virtual complex with the parametric adjustment to electromechanical system parameters. *Technical Electrodynamics*, 2019, pp. 38-41. doi: https://doi.org/10.15407/techned2019.01.038.
32. Shchur I., Kasha L., Bukavyn M. Efficiency Evaluation of Single and Modular Cascade Machines Operation in Electric Vehicle. *2020 IEEE 15th International Conference on Advanced Trends in Radioelectronics, Telecommunications and Computer Engineering (TCSET)*, Lviv-Slavske, Ukraine, 2020, pp. 156-161. doi: https://doi.org/10.1109/tcset49122.2020.235413.
33. Shchur I., Turkovskyi V. Comparative Study of Brushless DC Motor Drives with Different Configurations of Modular Multilevel Cascaded Converters. *2020 IEEE 15th International Conference on Advanced Trends in Radioelectronics, Telecommunications and Computer Engineering (TCSET)*, Lviv-Slavske, Ukraine, 2020, pp. 447-451. doi: https://doi.org/10.1109/tcset49122.2020.235473.
34. Zhyla S., Volosyuk V., Pavlikov V., Ruzhentsev N., Tserne E., Popov A., Shmatko O., Havrylenko O., Kuzmenko N., Dergachov K., Averyanova Y., Sushchenko O., Zaliskyi M., Solomentsev O., Ostroumov I., Kuznetsov B., Nikitina T. Practical imaging algorithms in ultra-wideband radar systems using active aperture

synthesis and stochastic probing signals. *Radioelectronic and Computer Systems*, 2023, no. 1, pp. 55-76. doi: https://doi.org/10.32620/reks.2023.1.05.
35. Havrylenko O., Dergachov K., Pavlikov V., Zhyla S., Shmatko O., Ruzhentsev N., Popov A., Volosyuk V., Tserne E., Zaliskyi M., Solomentsev O., Ostroumov I., Sushchenko O., Averyanova Y., Kuzmenko N., Nikitina T., Kuznetsov B. Decision Support System Based on the ELECTRE Method. *Data Science and Security. Lecture Notes in Networks and Systems*, 2022, vol. 462, pp. 295-304. doi: https://doi.org/10.1007/978-981-19-2211-4_26.
36. Solomentsev O., Zaliskyi M., Averyanova Y., Ostroumov I., Kuzmenko N., Sushchenko O., Kuznetsov B., Nikitina T., Tserne E., Pavlikov V., Zhyla S., Dergachov K., Havrylenko O., Popov A., Volosyuk V., Ruzhentsev N., Shmatko O. Method of Optimal Threshold Calculation in Case of Radio Equipment Maintenance. *Data Science and Security. Lecture Notes in Networks and Systems*, 2022, vol. 462, pp. 69-79. doi: https://doi.org/10.1007/978-981-19-2211-4_6.
37. Shmatko O., Volosyuk V., Zhyla S., Pavlikov V., Ruzhentsev N., Tserne E., Popov A., Ostroumov I., Kuzmenko N., Dergachov K., Sushchenko O., Averyanova Y., Zaliskyi M., Solomentsev O., Havrylenko O., Kuznetsov B., Nikitina T. Synthesis of the optimal algorithm and structure of contactless optical device for estimating the parameters of statistically uneven surfaces. *Radioelectronic and Computer Systems*, 2021, no. 4, pp. 199-213. doi: https://doi.org/10.32620/reks.2021.4.16.
38. Volosyuk V., Zhyla S., Pavlikov V., Ruzhentsev N., Tserne E., Popov A., Shmatko O., Dergachov K., Havrylenko O., Ostroumov I., Kuzmenko N., Sushchenko O., Averyanova Yu., Zaliskyi M., Solomentsev O., Kuznetsov B., Nikitina T. Optimal Method for Polarization Selection of Stationary Objects Against the Background of the Earth's Surface. *International Journal of Electronics and Telecommunications*, 2022, vol. 68, no. 1, pp. 83-89. doi: https://doi.org/10.24425/ijet.2022.139852.
39. Halchenko V., Trembovetska R., Bazilo C., Tychkova N. Computer Simulation of the Process of Profiles Measuring of Objects Electrophysical Parameters by Surface Eddy Current Probes. *Lecture Notes on Data Engineering and Communications Technologies*, 2023, vol. 178, pp. 411-424. doi: https://doi.org/10.1007/978-3-031-35467-0_25.
40. Halchenko V., Bacherikov D., Filimonov S., Filimonova N. Improvement of a Linear Screw Piezo Motor Design for Use in Accurate Liquid Dosing Assembly. *Smart Technologies in Urban Engineering. STUE 2022. Lecture Notes in Networks and Systems*, 2023, vol. 536, pp. 237-247. doi: https://doi.org/10.1007/978-3-031-20141-7_22.
41. Ruzhentsev N., Zhyla S., Pavlikov V., Volosyuk V., Tserne E., Popov A., Shmatko O., Ostroumov I., Kuzmenko N., Dergachov K., Sushchenko O., Averyanova Y., Zaliskyi M., Solomentsev O., Havrylenko O., Kuznetsov B., Nikitina T. Radio-Heat Contrasts of UAVs and Their Weather Variability at 12 GHz, 20 GHz, 34 GHz, and 94 GHz Frequencies. *ECTI Transactions on Electrical Engineering, Electronics, and Communications*, 2022, vol. 20, no. 2, pp. 163-173. doi: https://doi.org/10.37936/ecti-eec.2022202.246878.
42. Chystiakov P., Chornyi O., Zhautikov B. Remote control of electromechanical systems based on computer simulators. *Proceedings of the International Conference on Modern Electrical and Energy Systems, MEES 2017* (2017), 2018. – January, pp. 364–367. doi: https://doi.org/10.1109/MEES.2017.8248934.
43. Zagirnyak M., Bisikalo O., Chorna O., Chornyi O. A Model of the Assessment of an Induction Motor Condition and Operation Life, Based on the Measurement of the External Magnetic Field. *2018 IEEE 3rd International Conference on Intelligent Energy and Power Systems (IEPS)*, Kharkiv, 2018, pp. 316-321. doi: https://doi.org/10.1109/ieps.2018.8559564.
44. Maksymenko-Sheiko K.V., Sheiko T.I., Lisin D.O., Petrenko N.D. Mathematical and Computer Modeling of the Forms of Multi-Zone Fuel Elements with Plates. *Journal of Mechanical Engineering*, 2022, vol. 25, no. 4, pp. 32-38. doi: https://doi.org/10.15407/pmach2022.04.032.
45. Hontarovskyi P.P., Smetankina N.V., Ugrimov S.V., Garmash N.H., Melezhyk I.I. Computational Studies of the Thermal Stress State of Multilayer Glazing with Electric Heating. *Journal of Mechanical Engineering*, 2022, vol. 25, no. 1, pp. 14-21. doi: https://doi.org/10.15407/pmach2022.02.014.
46. Kostikov A.O., Zevin L.I., Krol H.H., Vorontsova A.L. The Optimal Correcting the Power Value of a Nuclear Power Plant Power Unit Reactor in the Event of Equipment Failures. *Journal of Mechanical Engineering*, 2022, vol. 25, no. 3, pp. 40-45. doi: https://doi.org/10.15407/pmach2022.03.040.
47. Rusanov A.V., Subotin V.H., Khoryev O.M., Bykov Y.A., Korotaiev P.O., Ahibalov Y.S. Effect of 3D Shape of Pump-Turbine Runner Blade on Flow Characteristics in Turbine Mode. *Journal of Mechanical Engineering*, 2022, vol. 25, no. 4, pp. 6-14. doi: https://doi.org/10.15407/pmach2022.04.006.
48. Ummels M. *Stochastic Multiplayer Games Theory and Algorithms*. Amsterdam University Press, 2010. 174 p.
49. Ray T., Liew K.M. A Swarm Metaphor for Multiobjective Design Optimization. *Engineering Optimization*, 2002, vol. 34, no. 2, pp. 141-153. doi: https://doi.org/10.1080/03052150210915.
50. Xiaohui Hu, Eberhart R.C., Yuhui Shi. Particle swarm with extended memory for multiobjective optimization. *Proceedings of the 2003 IEEE Swarm Intelligence Symposium*. SIS'03 (Cat. No.03EX706), Indianapolis, IN, USA, 2003, pp. 193-197. doi: https://doi.org/10.1109/sis.2003.1202267.
51. Dergachov K., Havrylenko O., Pavlikov V., Zhyla S., Tserne E., Volosyuk V., Ruzhentsev N., Ostroumov I., Averyanova Y., Sushchenko O., Popov A., Shmatko O., Solomentsev O., Zaliskyi M., Kuzmenko N., Kuznetsov B., Nikitina T. GPS Usage Analysis for Angular Orientation Practical Tasks Solving. *2022 IEEE 9th International Conference on Problems of Infocommunications, Science and Technology (PIC S&T)*, 2022, pp. 187-192. doi: https://doi.org/10.1109/PICST57299.2022.10238629.
52. Zhyla S., Volosyuk V., Pavlikov V., Ruzhentsev N., Tserne E., Popov A., Shmatko O., Havrylenko O., Kuzmenko N., Dergachov K., Averyanova Y., Sushchenko O., Zaliskyi M., Solomentsev O., Ostroumov I., Kuznetsov B., Nikitina T. Statistical synthesis of aerospace radars structure with optimal spatio-temporal signal processing, extended observation area and high spatial resolution. *Radioelectronic and Computer Systems*, 2022, no. 1, pp. 178-194. doi: https://doi.org/10.32620/reks.2022.1.14.
53. Hashim F.A., Hussain K., Houssein E.H., Mabrouk M.S., Al-Atabany W. Archimedes optimization algorithm: a new metaheuristic algorithm for solving optimization problems. *Applied Intelligence*, 2021, vol. 51, no. 3, pp. 1531-1551. doi: https://doi.org/10.1007/s10489-020-01893-z.

Received 16.09.2023
Accepted 12.12.2023
Published 01.05.2024

B.I. Kuznetsov[1], *Doctor of Technical Science, Professor,*
T.B. Nikitina[2], *Doctor of Technical Science, Professor,*
I.V. Bovdui[1], *PhD, Senior Research Scientist,*
K.V. Chunikhin[1], *PhD, Research Scientist,*
V.V. Kolomiets[2], *PhD, Assistant Professor,*
B.B. Kobylianskyi[2], *PhD, Assistant Professor,*
[1] Anatolii Pidhornyi Institute of Mechanical Engineering Problems of the National Academy of Sciences of Ukraine,
2/10, Pozharskogo Str., Kharkiv, 61046, Ukraine,
e-mail: kuznetsov.boris.i@gmail.com (Corresponding Author)
[2] Educational Scientific Professional Pedagogical Institute V.N. Karazin Kharkiv National Univesity,
9a, Nosakov Str., Bakhmut, Donetsk Region, 84511, Ukraine,
e-mail: nnppiuipa@ukr.net

How to cite this article:
Kuznetsov B.I., Nikitina T.B., Bovdui I.V., Chunikhin K.V., Kolomiets V.V., Kobylianskyi B.B. The method for design of combined electromagnetic shield for overhead power lines magnetic field. *Electrical Engineering & Electromechanics*, 2024, no. 3, pp. 22-30. doi: https://doi.org/10.20998/2074-272X.2024.3.03

UDC 621.3 https://doi.org/10.20998/2074-272X.2024.3.04

R. Rouaibia, Y. Djeghader, L. Moussaoui

Artificial neural network and discrete wavelet transform for inter-turn short circuit and broken rotor bars faults diagnosis under various operating conditions

Introduction. *This work presents a methodology for detecting inter-turn short circuit (ITSC) and broken rotor bars (BRB) fault in variable speed induction machine controlled by field oriented control. If any of these faults are not detected at an early stage, it may cause an unexpected shutdown of the industrial processes and significant financial losses.* ***Purpose.*** *For these reasons, it is important to develop a new diagnostic system to detect in a precautionary way the ITSC and BRB at various load condition. We propose the application of discrete wavelet transform to overcome the limitation of traditional technique for no-stationary signals.* ***The novelty*** *of the work consists in developing a diagnosis system that combines the advantages of both the discrete wavelet transform (DWT) and artificial neural network (ANN) to identify and diagnose defects, related to both ITSC and BRB faults.* ***Methods.*** *The suggested method involves analyzing the electromagnetic torque signal using DWT to calculate the stored energy at each level of decomposition. Then, this energy is applied to train neural network classifier. The accuracy of ANN based on DWT, was improved by testing different orthogonal wavelet functions on simulated signal. The selection process identified 5 pertinent wavelet energies, concluding that, Daubechies44 (db44) is the best suitable mother wavelet function for effectively detecting and classifying failures in machines.* ***Results.*** *We applied numerical simulations by MATLAB/Simulink software to demonstrate the validity of the suggested techniques in a closed loop induction motor drive. The obtained results prove that this method can identify and classify these types of faults under various loads of the machine.* References 31, table 1, figures 9.

Key words: **diagnosis, short circuit, broken bars, induction motor, discrete wavelet transform, artificial neural network, indirect field oriented control.**

Вступ. *У цій роботі представлена методологія виявлення міжвиткового короткого замикання (ITSC) та несправності стрижнів ротора (BRB) в асинхронних машинах з регульованою швидкістю, керованих полеорієнтованим керуванням. Якщо будь-яка з цих несправностей не буде виявлена на ранній стадії, це може призвести до несподіваної зупинки виробничих процесів та значних фінансових втрат.* ***Мета.*** *З цих причин важливо розробити нову діагностичну систему для профілактичного виявлення ITSC та BRB за різних умов навантаження. Ми пропонуємо застосувати дискретне вейвлет перетворення, щоб подолати обмеження традиційної техніки для нестаціонарних сигналів.* ***Новизна*** *роботи полягає в розробці системи діагностики, що поєднує в собі як переваги дискретного вейвлет перетворення (DWT), так і штучної нейронної мережі (ANN) для виявлення та діагностики дефектів, пов'язаних як з несправностями ITSC, так і з BRB.* ***Методи.*** *Пропонований метод включає аналіз сигналу електромагнітного моменту, що крутить, з використанням DWT для розрахунку запасеної енергії на кожному рівні розкладання. Потім ця енергія застосовується на навчання класифікатора нейронної мережі. Точність ANN, заснованої на DWT, була підвищена за рахунок тестування різних ортогональних вейвлет функцій на сигналі, що моделюється. У процесі відбору було визначено п'ять відповідних енергій вейвлета, і було зроблено висновок, що Daubechies44 (db44) є найбільш підходящою материнською вейвлет функцією ефективного виявлення і класифікації відмов у машинах.* ***Результати.*** *Ми застосували чисельне моделювання за допомогою програмного забезпечення MATLAB/Simulink, щоб продемонструвати ефективність запропонованих методів приводу асинхронного двигуна із замкнутим контуром. Отримані результати доводять, що цей метод дозволяє виявити та класифікувати дані види несправностей при різних навантаженнях машини.* Бібл. 31, табл. 1, рис. 9.

Ключові слова: **діагностика, коротке замикання, обрив стрижнів, асинхронний двигун, дискретне вейвлет перетворення, штучна нейронна мережа, непряме полеорієнтоване керування.**

Introduction. The squirrel cage induction motor (IM) by its robustness, simplicity and relatively low cost, plays a most significant role in applications requiring high power in industrial applications, particularly for constant or variable speed applications. Despite these great benefits, various stresses may occur, during operating conditions. For these reasons, early recognition of abnormalities is important to identify any faults at an incipient stage can help to avoid catastrophic failure and global damage. Literature has reports that electrical faults are principal causes [1-3], inter-turn short circuit (ITSC) have a significant share with approximately 30 % to 40 % and broken rotor bars (BRB) which represent 5-10 % of all the IM faults. These faults are caused by several forms of stress such as thermal, electrical, mechanical and environmental.

Several publications have focused on stator winding defects. In [2] a mathematical model of an IM based on coupled magnetic circuit theory is presented. This model allows detection of short circuit (SC) faults in stator winding and predicts it before it grows and damages the machine completely. In [3], a thermal model analysis of IM relies on finite elements method used to identify how ITSC faults of different severity affect the temperature of the IM. However, this method needs times after starting the motor to estimate the failure severity. Another useful technique was proposed in [4], combines the genetic algorithm and simulated annealing method to identify ITSC in IM during load current variations. In [5] Least Squares Support Vector Machine technique is proposed for fault detection and classification of the short circuit in the stator phases of an IM using information provided by the stator current. Moreover In [6], the estimations of rotor and stator resistances parameters based on Model Reference Adaptive System technique. Work [7] proposes axial stray flux based on analysis of flux signals collected by sensor. The pattern obtained from two-phase quantities is observed to be circular in nature for healthy case and elliptical nature for stator malfunctions. However, it is costly and challenging to install a sensor on the inside of the machine. Also in [8], an off line signal processing techniques called the Fortescue transform is applied to obtain the zero sequence of the current and the Fast Fourier Transform (FFT) is applied to detect the occurrence of the ITSC from the current and voltage signals of synchronous reluctance motor. Other work [9] use the three-phase stator voltages of IM as inputs, and by using the short-time least square Prony's method, to extract phases and magnitudes of the fundamental harmonics to calculate indicator called zero voltage factor

that allows a rapid ITSC fault detection. However, this method is susceptible to load variation and the presence of unbalanced supply voltage. In [10], the residuals current between the estimated currents provided by the Extended Kalman Filter and the actual ones using FFT and Short-Time Fourier transform approaches are used for ITSC fault diagnosis and identification. The Artificial Neural Network (ANN) and Discrete Wavelet Transform (DWT) are proposed in [11], for ITSC fault diagnosis of IM. Three parameters (energy, Kurtosis and singular values) of DWT technique are computed under load variation and used as the input for the ANN classifier, using a single wavelet function db40. In [12], continuous and discrete wavelet methods are applied to study the stator current, at the start-up to identify BRB fault. But the limitation is that it is not always feasible to frequently restart the motor to capture starting current. The detection of BRB faults are detected by DWT based on harmonics characteristic, using vibration signal decomposition and ANN is presented in [13].The detection and classification of BRB fault in the IM, based a combination of the DWT, the slip and the ANN algorithm to solve the problem of low load has been discussed in [14]. Similarly, in [15, 16] the multiple signal processing tools using Hilbert Transform and ANN, are proposed for BRB fault diagnosis. In [17] suggests a hybrid combining a new electrical-time synchronous-averaging, DWT and fuzzy logic techniques was employed for dealing with the early identification of an incipient defect occurring at the rotor bar and classification of the severity of this defect.

Problem definition. Generally, diagnostic methods used for open-loop machine operation are not efficient when the control structure becomes more complex, particularly, in closed-loop drives. It's necessary to employ different analysis to interpret the acquired signals for the detection process. The FFT approach is widely applied and proven to be effective for stationary signals. However, this approach is not efficient and has limitations for non-stationary signals. In this context, to ameliorate the diagnosis procedure taking into account different faults of IM, a combination of DWT and ANN technique becomes our main focus to resolve these drawbacks for processing non-stationary, low load and over load. However, different types of the wavelet function can be used for early fault detection based electromechanical signal decomposition in closed loop operation. The comparison between the proposed methodology and the previously used methods is made based on the faults severity, operating mode, different load torques, and fault diagnosis methods. The work [18] focuses on the analysis of BRB faults in open-loop asynchronous machines powered by electrical network. The study utilized a single db40 wavelet function, and the acquisition of three current sensors for phases (I_a, I_b, I_c), the calculated energy of three-phase (E_{7a}, E_{7b}, E_{7c}), are employed as input of ANN to determine the faulty phases (a_s, b_s, c_s). However this work deals with the diagnosis of both short circuit faults and BRB at speeds, with a reference speed set to 100 rad/s controlled by Indirect Field Oriented Control (IFOC) technique. Various wavelet functions are used to compare the best suitable function such as BiorSplines, ReverseBior, Symlet, Coiflet, and Daubechies are used for diagnosis. Only one acquisition signal is used, which is the torque signal to differentiate between stator and rotor faults. The energy calculation of the electromagnetic torque signal involves selecting the pertinent energy, resulting 5 energies (E_1, E_2, E_6, E_7, E_8), after that these energies are used as input of ANN. The wavelet function db44 was found to be the best function to identify these faults. The application of this work is used in the first step to determine which fault occurs ITSC or BRB after that we use the method from [18], to locate the faulty phases. This study presents an effectiveness percentage of 98 %, taking into account both different severity levels of short circuited turns, 1, 2 and 3 BRB with different mechanical load levels (ranging from 1 to 7 N·m), in contrast to other works reviewed in [19-21], which analyze levels of fault and different operating conditions or different levels of fault and a constant load operating condition in open loop machine. Whereas, works [22-24] introduced a signal transformation and several nonlinear indices is required, along with an expert to interpret the obtained results. Other works [25-27] have good accuracy in diagnosing the highly incipient faults based fuzzy logic method but using number of fuzzy rules causes significant computation time, which is always longer

The goal of the paper is to identify ITSC and BRB fault when the IM operates in a closed-loop drive to preserve high performance. The used method for the fault detection combines DWT and ANN method to provide intelligent methodology for the diagnosis system.

Subject of investigations. This approach used DWT of electromechanical torque signal at steady state to compute the stored energy at each level of decomposition. Then, this energy is applied as input for the Neural Network (NN) classifier. Many test of orthogonal wavelet function are evaluated with ANN to find the best classification and lowest Root Mean Square Error (RMSE), and justified that db44 is the best suited mother wavelet function to detect and identify different severity for both the ITSC and BRB faults under various loads operation of IM.

IM mathematical model. An accurate model including a fault is needed to test fault diagnosis strategies in IM. The equivalent circuit diagram of the IM, in the reference frame (*d-q*) is considered, taking into account ITSC and BRB fault. Additionally, the following non-linear system equations are developed to validate IM performance [18]:

$$\begin{cases} \dot{X}(t) = A(\omega)X(t) + Bu(t); \\ Y(t) = CX(t) + Du(t), \end{cases} \quad (1)$$

where

$$X = \left[i_{ds}\ i_{qs}\ \phi_{dr}\ \phi_{qr}\right]^T, u = \begin{bmatrix} U_{ds} \\ U_{qs} \end{bmatrix}^T, Y = \begin{bmatrix} i_{ds} \\ i_{qs} \end{bmatrix}.$$

The expression of equivalent rotor resistance is:

$$R_{eq} = R_r \cdot I + \frac{\alpha}{1+\alpha} K(\theta_0) R_r; \quad \alpha = \frac{2}{3}\eta; \quad \eta = \frac{3N_{bc}}{N_b}; \quad (2)$$

$$K(\theta_0) = \begin{bmatrix} \cos(\theta_0)^2 & \cos(\theta_0)\sin(\theta_0) \\ \cos(\theta_0)\sin(\theta_0) & \sin(\theta_0)^2 \end{bmatrix}, \quad (3)$$

where N_b, N_{bc}, R_r, R_{eq} are the total number of bars in the rotor, the number of BRB, the rotor resistance and the equivalent resistance of rotor, respectively; θ_0 is the initial phase of the rotor.

By adding the mechanical equation to the system equation, we obtain the complete model of the machine taking account the ITSC and BRB in the Park coordinate system. The mechanical speed ω is the solution of the equation:

$$J\frac{\mathrm{d}\omega_r}{\mathrm{d}t} = T_e - T_l - f_v\omega\,, \tag{4}$$

and the electromagnetic torque in the Park coordinate system is given by the expression:

$$T_e = p(i_{qs}\phi_{dr} - i_{ds}\phi_{qr})\,, \tag{5}$$

where T_e is the electromagnetic torque; T_l is the load torque; J is inertia moment; f_v is friction coefficient.

Indirect field oriented control. The most significant aspect of field oriented control of the IM is transformation that converts a three-phase system into 2 components, which used to generate both the magnetizing flux and the electromagnetic torque [16, 24]. This transformation simplifies the structure of IM similar that of a DC machine as shown in Fig. 1. It implies that the 2 stator current components would be aligned as input references: the flux component (aligned with the d coordinate) and the torque component (aligned with the q coordinate).

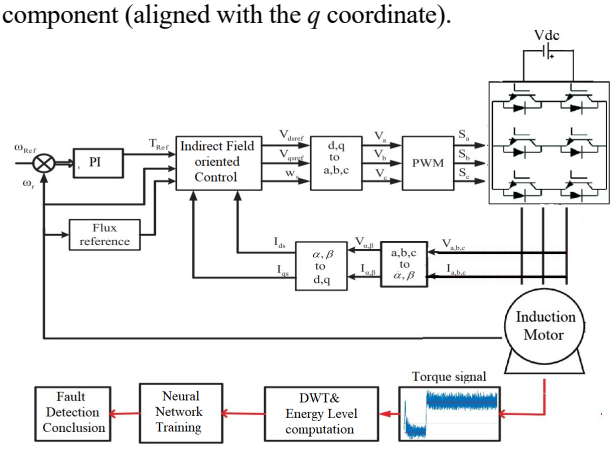

Fig. 1. Block diagram of the diagnosis system

The IFOC technique is known for its simplicity of implementation and high effectiveness what makes it widely used in industry applications. The flux component is aligned in the direction of rotor flux ϕ_r to achieve field orientation along the rotor flux direction:

$$\phi_{dr} = \phi_r\,, \quad \phi_{qr} = 0, \quad V_{dr} = 0, \quad V_{qr} = 0\,. \tag{6}$$

The advantage of using a reference linked to the rotating field frame is to have constant magnitudes. The control is then made easier by relying on the variables of direct axis current i_{ds} and the quadrature axis current i_{qs}. The magnitudes of flux ϕ_r and torque T_e are independent controlled is assumed as [16, 24]. The calculated rotor flux, given by:

$$\phi_r = \frac{L_{sm}\cdot i_{ds}}{1 + s\dfrac{L_r}{R_r}}\,, \tag{7}$$

where L_r, L_{sm} are the rotor and mutual inductance; s is the Laplace transform. The slip frequency is expressed by:

$$\omega_{sl} = \frac{L_{sm} i_{qs}}{T_r \phi_r}\,, \tag{8}$$

where $T_r = L_r / R_r$ is the rotor time constant.

The equation of the electromagnetic torque can be given by:

$$T_e = \frac{pL_{sm} i_{qs}\phi_r}{L_r} = K' i_{qs}\,, \tag{9}$$

where p is the number poles pairs; ϕ_r is the rotor flux. Therefore, the relation with DC motor is clearly demonstrated by holding the flux constant.

The two components magnetizing flux ϕ_r and electromagnetic torque T_e can independently controlled by acting on each variable separately, establishing the high performance of a DC machine. The simulation results of IFOC control IM drive in cases of healthy and faulty motors demonstrated through simulation in MATLAB/Simulink.

Figures 2-4 show the dynamic performance of speed, stator current and electromagnetic torque in healthy and when a fault appears in stator or rotor bars fault with reference speed set to 100 rad/s. After reaching the set value of motor speed, the step change of load torque (from 1 to 7 N·m) at the moment t = 0.6 s. It is evident that, the actual speed accurately follows the reference speed in healthy and faulty state, which be explain by the fact that the PI speed controller minimize the effects of ITSC and BRB faults on the speed (Fig. 2).

Figure 3 depicts the stator currents that are sinusoidal and have the same amplitude. But in the occurrence of the fault, there will be an imbalance at the level of the stator currents which increase in term of amplitude.

Similarly, we observe the influence of ITSC and BRB in the electromagnetic torque. During a fault condition, motor suffers from oscillations. The amplitude of these oscillations increases when the severity of fault increases (Fig. 4).

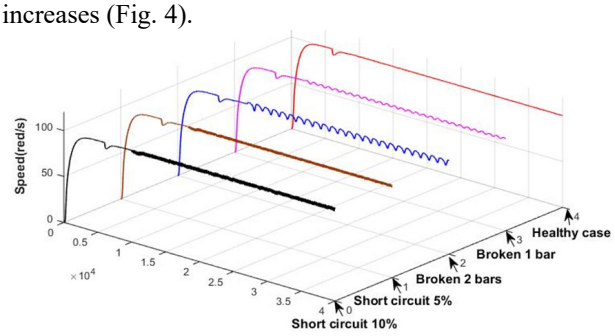

Fig. 2. Actual speed at full load

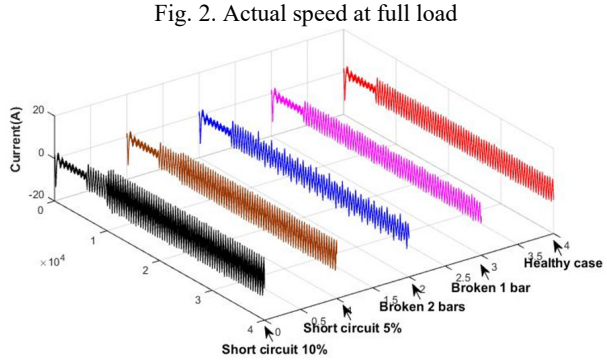

Fig. 3. Evolution of stator currents under full load

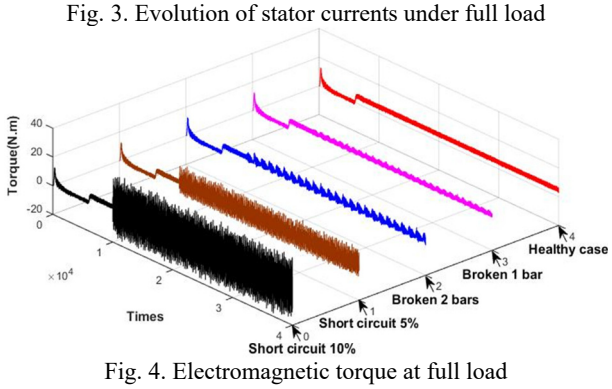

Fig. 4. Electromagnetic torque at full load

Discrete Wavelet Transform (DWT). The wavelet transform is an effective method for acquiring time-frequency information in both stationary and non-stationary signal processing, with the intention to solve the limitations of Fourier transform. This signal processing tool, characterized by robust time and frequency localization, is divided into Continuous Wavelet Transforms (CWT) and DWT. Adopting a mother wavelet $\Psi(t)$, the CWT of a function $x(t)$ can be expressed as:

$$CWT(a,\tau)=\frac{1}{\sqrt{|a|}}\int_{-\infty}^{+\infty}x(t)\psi^{*}\left(\frac{t-\tau}{a}\right)\mathrm{d}t\,, \tag{10}$$

where $\psi(t)^{*}$ is the complex conjugates form; τ is the time parameter; a is the scale factor; $\sqrt{|a|}$ is the energy normalization.

The translation and the expansion transform the signal into another timescale. The high-frequency components correspond to the smallest scales [28, 29].

A more computationally efficient form of the CWT which gives optimal accuracy at low frequency and non-stationary state is the DWT given by [20, 22]:

$$DWT(J,k)=\frac{1}{\sqrt{2^{J}}}\int_{-\infty}^{+\infty}x(t)\psi^{*}\left(\frac{t-k\cdot 2^{J}}{2^{J}}\right)\mathrm{d}t=2^{\frac{-J}{2}}\psi(2^{-J}\cdot t-k)\,. \tag{11}$$

The DWT decompose a given signal into its constituent level (scales), each one representing that part of the original signal occurring at particular time and frequency band. DWT is performed by a sequential operation using a high-pass filters H (details) and through a series of low-pass filters L (approximations).

The original signals $x(t)$ is divided into 2 parts high frequency part, and low frequency part used to decompose and reconstruct a signal (Fig. 5) [18-20].

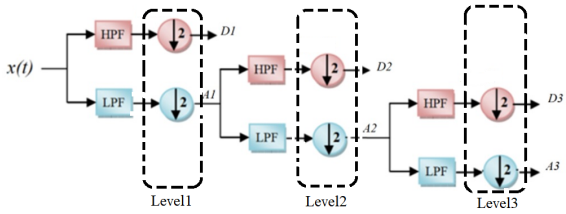

Fig. 5. DWT decomposition process of the signal at level 3

The low frequency part called approximations (A_j) contains the low-frequency information of the original signal belong to [0, $f_s\cdot 2^{-(j+1)}$]. The high-frequency part called detail (D_j) contain high frequency information included in the interval [$f_s\cdot 2^{-(j+1)}$, $f_s\cdot 2^{-j}$]. Practically, the DWT decomposition at level N of signal $x(t)$, giving rise to one approximation coefficient vector A_N and N detail coefficient vectors D_j are expressed by [29, 30]:

$$x(t)=A_N(t)+\sum_{j=1}^{N}D_j(t)\,. \tag{12}$$

It can be shown that the approximation and detail coefficients can be recursively calculated by:

$$\begin{aligned}A_{j,k}&=\sqrt{2}\sum_{-\infty}^{+\infty}L[n]A_{j-1,\,2k+n};\\ D_{j,k}&=\sqrt{2}\sum_{-\infty}^{+\infty}H[n]A_{j-1,\,2k+n}.\end{aligned} \tag{13}$$

The effectiveness of DWT relies on the careful choice of the wavelet function. Different types of mother wavelets exist, such as: Meyer, Coiflets, Symlets and Daubechies.

Preliminary step before selecting the wavelet function involves judiciously choosing the number of levels in order to cover the whole range of frequencies approximation and detail, given by the relationship:

$$\frac{f_s}{2^{N+1}}\le f_e\,, \tag{14}$$

where f_e is the fundamental frequency of the signal, f_e = 22 Hz; f_s is the sampling frequency, f_s = 10 kHz; N is the number of decomposition levels.

Wavelet energy. The consumed energy at each level of decomposition is calculated, to identify and validate the frequency bands containing the defect frequency for both faulty and healthy cases under different load conditions. For this purpose, the energy linked to each D_j detail signal of the torque signal is expressed as follow:

$$E_j=\sum_{k=1}^{n}D^2{}_{j,k}(n)\,, \tag{15}$$

where j is the decomposition level ($j\in[1, N]$); E_j is the detail energy; $D_{j,k}$ is the magnitude of the coefficient in corresponding level j; n is the DWT decomposition time.

The energy extracted from the torque signal through wavelet transformation, using db44 under different load and faults severity. The number of decomposition levels N depends on the sampling frequency f_s of the signal were performed up to the 10th level of the decomposition. By computing associated coefficient at each decomposition levels of the torque signal. The results of detail energy D_j for various instances of shorted turns and broken 1 bar and 2 bars under different loads are depicted in Fig. 6.

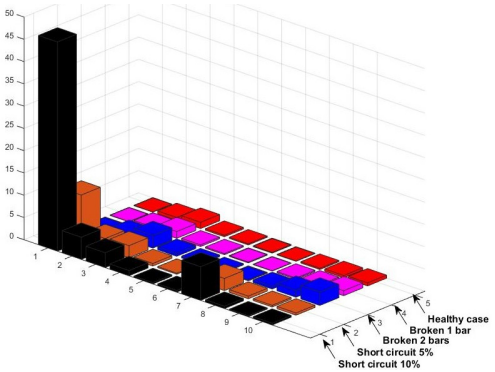

Fig. 6. The comparison of total energy

Artificial Neural Networks are complex intelligent structures inspired by biological neurons, have demonstrated remarkable performances to solve analytically challenging problems and the automation of the monitoring process. The most frequently used NN for classification purposes is feed forward multilayer perceptron NN, known for its simple structure making it easily implementable. Hence, it was chosen for the developing of the monitoring process. The training function used was Levenberg–Marquardt trained by back propagation algorithm and training results are used to attain the minimum Mean Square Errors (MSE) [28, 29]. Typically, an ANN consists of an input layer, hidden layers and an output layer, where each layer connected to other layer, with weights assigned to the connections. The

activation function used for the hidden layer is tangent sigmoid «tansig», while the activation function for the output layer is Logsigmoid «logsig» [30, 31].

The inputs are the pertinent wavelet energy value and outputs are the fault class of IM, respectively.

The training performance and parameters related to the training algorithm are illustrated in Fig. 7. After 85 epochs, a low training MSE of $2.3561 \cdot 10^{-11}$ is achieved, indicating suitability for accurately classifying the test set.

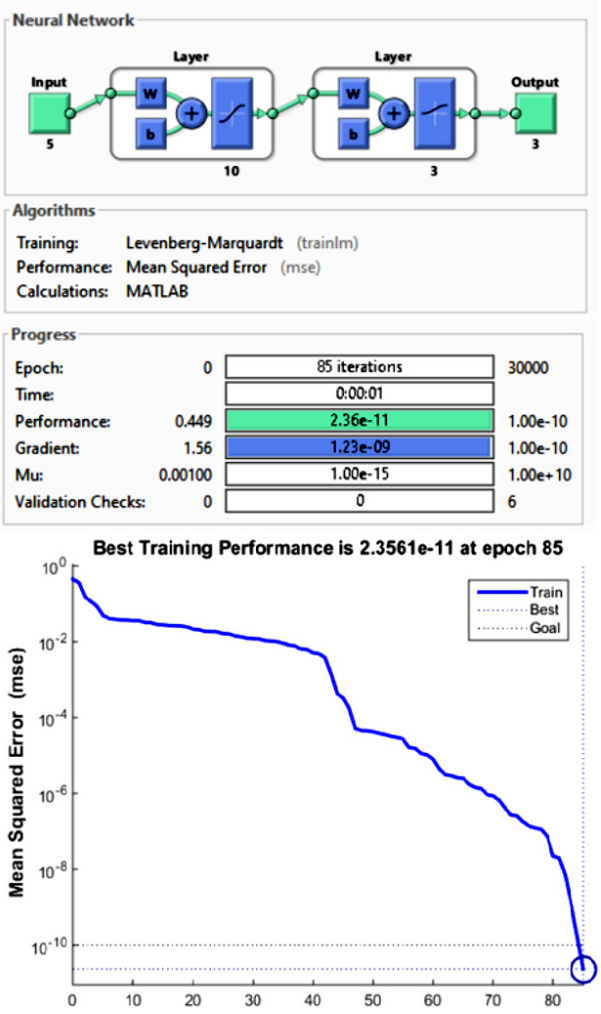

Fig. 7. Neural network performance

Preparation of training data. The NN is trained using a dataset comprising input and output sets. The number of input units in the ANN corresponds to the fault indicators, while the output units are determined by the number of faulty states. The inputs represent the pertinent stored energy calculated from the torque signal, which found the best value are 5 energies (E_1, E_2, E_6, E_7, E_8) and the outputs signify the fault classes: healthy case, short circuit and BRB fault. For an optimal compromise between complexity and accuracy, one hidden layer with 10 neurons is chosen. Input data are gathered through simulations under various loading conditions and fault severities, ranging from no load to full load. The NN is exposed to examples under 7 load torques (1–7 N·m), representing different operating conditions, including healthy states (7 samples), faults with an even number of shorted turns (2, 4, 6, 8, 10), and faults with single and 2 BRB. This results in a total of 56 cases ((7 healthy) + (7×5 shorted turns with different loads and severities) + (7×2 BRB with different loads)), as shown in Fig. 8. Consequently, the dimension of the training vector inputs for the NN is 5×56.

The target data required for supervised learning in the NN are defined accordingly:

T1 = [1; 0; 0] – healthy case;

T2 = [0; 1; 0] – short circuit fault;

T3 = [0; 0; 1] – BRB.

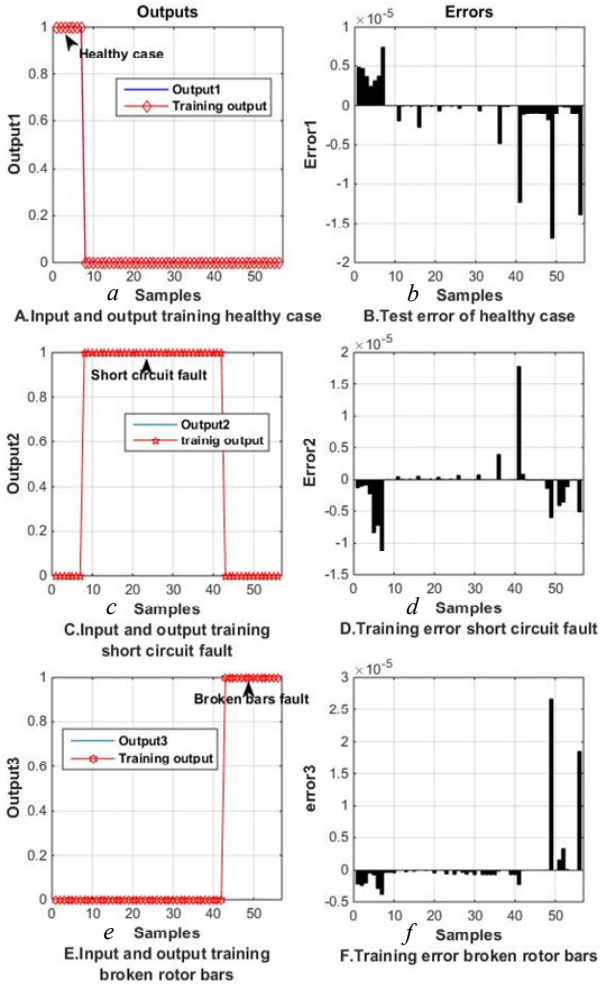

Fig. 8. Training and classification errors of the NN

Simulation results. The NN ability to generalize is assessed through its performance on the testing dataset. To evaluate classification effectiveness, 2 distinct datasets are compiled, representing both healthy and faulty cases. Various tests are conducted to determine the optimal structure and outcomes. The results indicate that the selected ANN model has achieved significant success in detecting and classifying these faults.

The dataset is divided into 2 parts, with 1 set applied for training while another for testing. An effective NN is expected to perform well on both training and testing data, showcasing its generalization capacity. The testing process involves a dataset separate from the one used for training, providing an assessment of the network's ability to generalize to new, unseen data.

Figure 9 depicts the test data set of the system under different operating cases of IM: healthy case (7 samples), fault of shorted turns (1, 3, 5, 7, 9), and fault for 1 and 2 BRB, are obtained under 7 load torques (0.5, 1.5, 2.5, 3.5, 4.5, 5.5 and 6.5 N·m).

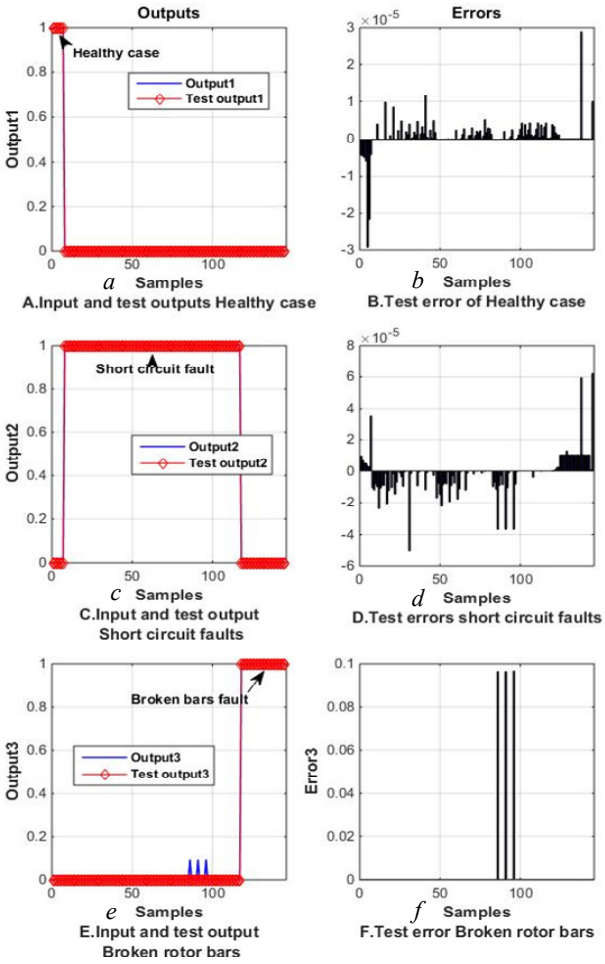

Fig. 9. Test and classification errors of the NN

As a result, the total number of combinations of load variation, shorted turn and BRB was 143 ((7 healthy) + (7×5 load of different severities of ITSC) + (7×5 different load of ITSC) + (7×5 different load and severities of ITSC) + (7×2 different load of BRB) + (7×2 different load + 3 BRB)).

The test output of the NN (T1, T2, T3) is accurately equal to (1, 0, 0), (0, 1, 0), and (0, 0, 1). The NN test outputs and classification errors for faults of ITSC and BRB, respectively is shown in Fig. 9. The test output of NN from (Fig. 9,*a*,*b*) is accurately identical to (1, 0, 0) in healthy state and classification error is very low. The NN output in (Fig. 9,*c*,*d*) give the output (0, 1, 0), with minimal amount of testing error in short circuit faults. As a result, the ITSC can be accurately located by the NN. According to (Fig. 9,*e*,*f*), the NN accurately gives the outputs (0, 0, 1) for the BRB indicating the occurrence of small errors. Therefore, we can observe that the NN can accurately identify the ITSC and BRB faults.

Table 1 shows a comparison of the performance of a simulated model. In this study, the accuracy of ANN is evaluated using the RMSE with the expression given by:

$$RMSE = \sqrt{\frac{\sum_{i=1}^{m}(x_i - x_i^*)^2}{m}}, \qquad (16)$$

where x_i and x_i^* represent respectively the measured and desired outputs; m is the total number of input sets.

The test data are simulated under various wavelet functions, using BiorSplines (bior6.8), ReverseBior (rbior6.8), Symlet (sym8), Coiflet (coif5) and Daubechies (db44) wavelet families. The input of NN are chosen by selecting the pertinent energy, we found 5 energies (E_1, E_2, E_6, E_7, E_8) identified as the most effective. Subsequently, the best classification and the minimum classification error are achieved using Daubechies44 (db44) which found better than any other wavelet transform. The achieved results clearly demonstrate that the db44 of the electromechanical torque signal can used as an effective indicator for stator and rotor condition monitoring.

Table 1

Performance of different wavelets functions with 5 energies (E_1, E_2, E_6, E_7, E_8)

Wavelet mother	bior6.8	rbior 6.8	sym8	coif5	db44
ANN-RMSE (test)	0.0235	0.0164	0.0339	0.0308	0.0011
Classification accuracy, %	97.24	98.16	96.32	97.24	98.62

Conclusions. This paper introduces a precise method for diagnosing inter-turn short circuit (ITSC) and broken rotor bars (BRB) in variable speed drives using discrete wavelet transform (DWT) and artificial neural network (ANN). The proposed approach involves analyzing the electromechanical torque signal of a squirrel cage induction motor (IM) through DWT. This analysis computes the stored energy at each level of decomposition, which then serves as input for an ANN classifier.

The proposed technique has been applied for fault detection under various loads, instances of ITSC, and different occurrences of BRB in the IM. The results obtained are highly significant, demonstrating the ability to automatically detect and locate faults related to BRB and ITSC. The best result is achieved through the application of 5 pertinent energies, particularly using db44. According to the test results, DWT and ANN prove to be a powerful method for diagnosis, offering a means to automatically identify faults under variable load conditions. Future research could further develop this work to determine the specific number of short circuits and BRB, enabling continuous and real-time monitoring.

Conflict of interest. The authors declare no conflict of interest.

REFERENCES

1. Halder S., Bhat S., Zychma D., Sowa P. Broken Rotor Bar Fault Diagnosis Techniques Based on Motor Current Signature Analysis for Induction Motor – A Review. *Energies*, 2022, vol. 15, no. 22, art. no. 8569. doi: https://doi.org/10.3390/en15228569.

2. Babaa F., Bennis O. An accurate inter-turn short circuit faults model dedicated to induction motors. *International Journal of Electrical and Computer Engineering (IJECE)*, 2021, vol. 11, no. 1, pp. 9-16. doi: https://doi.org/10.11591/ijece.v11i1.pp9-16.

3. Adouni A., Marques Cardoso A.J. Thermal Analysis of Low-Power Three-Phase Induction Motors Operating under Voltage Unbalance and Inter-Turn Short Circuit Faults. *Machines*, 2020, vol. 9, no. 1, art. no. 2. https://doi.org/10.3390/machines9010002.

4. Tomczyk M., Mielnik R., Plichta A., Goldasz I., Sułowicz M. Identification of Inter-Turn Short-Circuits in Induction Motor Stator Winding Using Simulated Annealing. *Energies*, 2021, vol. 15, no. 1, art. no. 117. doi: https://doi.org/10.3390/en15010117.

5. M'hamed B., Djamel T., Bessedik S.A., Mohamed-Fouad B. Least square support vectors machines approach to diagnosis of stator winding short circuit fault in induction motor. *Diagnostyka*, 2020, vol. 21, no. 4, pp. 35-41. doi: https://doi.org/10.29354/diag/130283.

6. Bednarz S., Dybkowski M. Induction motor windings faults detection using flux-error based MRAS estimators. *Diagnostyka*, 2019, vol. 20, no. 2, pp. 87-96. doi: https://doi.org/10.29354/diag/109092.
7. Filho P.C.M.L., Santos D.C., Batista F.B., Baccarini L.M.R. Axial Stray Flux Sensor Proposal for Three-Phase Induction Motor Fault Monitoring by Means of Orbital Analysis. *IEEE Sensors Journal*, 2020, vol. 20, no. 20, pp. 12317-12325. doi: https://doi.org/10.1109/JSEN.2020.2999547.
8. Henriques K., Laadjal K., Cardoso A.J.M. Inter-Turn Short-Circuit Fault Detection in Synchronous Reluctance Machines, Based on Current Analysis. *Engineering Proceedings*, 2022, vol. 24, no. 1, art. no. 23. doi: https://doi.org/10.3390/IECMA2022-12884.
9. Alloui A., Laadjal K., Sahraoui M., Marques Cardoso A.J. Online Interturn Short-Circuit Fault Diagnosis in Induction Motors Operating Under Unbalanced Supply Voltage and Load Variations, Using the STLSP Technique. *IEEE Transactions on Industrial Electronics*, 2023, vol. 70, no. 3, pp. 3080-3089. doi: https://doi.org/10.1109/TIE.2022.3172751.
10. Ouamara D., Boukhnifer M., Chaibet A., Maidi A. Diagnosis of ITSC fault in the electrical vehicle powertrain system through signal processing analysis. *Diagnostyka*, 2023, vol. 24, no. 1, pp. 1-10. doi: https://doi.org/10.29354/diag/161309.
11. Sakhara S., Brahimi M., Nacib L., Layadi T.M. Application of a wavelet neural network approach to detect stator winding short circuits in asynchronous machines. *Electrical Engineering & Electromechanics*, 2023, no. 3, pp. 21-27. doi: https://doi.org/10.20998/2074-272X.2023.3.03.
12. Abu Ibaid O.Z.I., Belhamdi S., Abid M., Chakroune S., Mouassa S., Al-Sagar Z.S. Wavelet packet analysis for rotor bar breakage in an inverter induction motor. *Electrical Engineering & Electromechanics*, 2023, no. 3, pp. 3-11. doi: https://doi.org/10.20998/2074-272X.2023.3.01.
13. Defdaf M., Berrabah F., Chebabhi A., Cherif B.D.E. A new transform discrete wavelet technique based on artificial neural network for induction motor broken rotor bar faults diagnosis. *International Transactions on Electrical Energy Systems*, 2021, vol. 31, no. 4, art. no. e12807. doi: https://doi.org/10.1002/2050-7038.12807.
14. Talhaoui H., Ameid T., Kessal A. Energy eigenvalues and neural network analysis for broken bars fault diagnosis in induction machine under variable load: experimental study. *Journal of Ambient Intelligence and Humanized Computing*, 2022, vol. 13, no. 5, pp. 2651-2665. doi: https://doi.org/10.1007/s12652-021-03172-2.
15. Senthil Kumar R., Gerald Christopher Raj I., Alhamrouni I., Saravanan S., Prabaharan N., Ishwarya S., Gokdag M., Salem M. A combined HT and ANN based early broken bar fault diagnosis approach for IFOC fed induction motor drive. *Alexandria Engineering Journal*, 2023, vol. 66, pp. 15-30. doi: https://doi.org/10.1016/j.aej.2022.12.010.
16. Ramu S.K., Vairavasundaram I., Aljafari B., Kareri T. Rotor Bar Fault Diagnosis in Indirect Field–Oriented Control-Fed Induction Motor Drive Using Hilbert Transform, Discrete Wavelet Transform, and Energy Eigenvalue Computation. *Machines*, 2023, vol. 11, no. 7, art. no. 711. doi: https://doi.org/10.3390/machines11070711.
17. Sabir H., Ouassaid M., Ngote N. An experimental method for diagnostic of incipient broken rotor bar fault in induction machines. *Heliyon*, 2022, vol. 8, no. 3, art. no. e09136. doi: https://doi.org/10.1016/j.heliyon.2022.e09136.
18. Bessam B., Menacer A., Boumehraz M., Cherif H. Wavelet transform and neural network techniques for inter-turn short circuit diagnosis and location in induction motor. *International Journal of System Assurance Engineering and Management*, 2017, vol. 8, no. S1, pp. 478-488. doi: https://doi.org/10.1007/s13198-015-0400-4.
19. Almounajjed A., Sahoo A.K., Kumar M.K. Diagnosis of stator fault severity in induction motor based on discrete wavelet analysis. *Measurement*, 2021, vol. 182, art. no. 109780. doi: https://doi.org/10.1016/j.measurement.2021.109780.
20. Kim M.-C., Lee J.-H., Wang D.-H., Lee I.-S. Induction Motor Fault Diagnosis Using Support Vector Machine, Neural Networks, and Boosting Methods. *Sensors*, 2023, vol. 23, no. 5, art. no. 2585. doi: https://doi.org/10.3390/s23052585.
21. Hussein A.M., Obed A.A., Zubo R.H.A., Al-Yasir Y.I.A., Saleh A.L., Fadhel H., Sheikh-Akbari A., Mokryani G., Abd-Alhameed R.A. Detection and Diagnosis of Stator and Rotor Electrical Faults for Three-Phase Induction Motor via Wavelet Energy Approach. *Electronics*, 2022, vol. 11, no. 8, art. no. 1253. doi: https://doi.org/10.3390/electronics11081253.
22. Garcia-Calva T.A., Morinigo-Sotelo D., Fernandez-Cavero V., Garcia-Perez A., Romero-Troncoso R. de J. Early Detection of Broken Rotor Bars in Inverter-Fed Induction Motors Using Speed Analysis of Startup Transients. *Energies*, 2021, vol. 14, no. 5, art. no. 1469. doi: https://doi.org/10.3390/en14051469.
23. Harzelli I., Menacer A., Ameid T. A fault monitoring approach using model-based and neural network techniques applied to input–output feedback linearization control induction motor. *Journal of Ambient Intelligence and Humanized Computing*, 2020, vol. 11, no. 6, pp. 2519-2538. doi: https://doi.org/10.1007/s12652-019-01307-0.
24. Jankowska K., Dybkowski M. Design and Analysis of Current Sensor Fault Detection Mechanisms for PMSM Drives Based on Neural Networks. *Designs*, 2022, vol. 6, no. 1, art. no. 18. doi: https://doi.org/10.3390/designs6010018.
25. Talhaoui H., Ameid T., Aissa O., Kessal A. Wavelet packet and fuzzy logic theory for automatic fault detection in induction motor. *Soft Computing*, 2022, vol. 26, no. 21, pp. 11935-11949. doi: https://doi.org/10.1007/s00500-022-07028-5.
26. Aib A., Khodja D.E., Chakroune S., Rahali H. Fuzzy current analysis-based fault diagnostic of induction motor using hardware co-simulation with field programmable gate array. *Electrical Engineering & Electromechanics*, 2023, no. 6, pp. 3-9. doi: https://doi.org/10.20998/2074-272X.2023.6.01.
27. Mabrouk Y.A., Mokhtari B., Allaoui T. Frequency analysis of stator currents of an induction motor controlled by direct torque control associated with a fuzzy flux estimator. *Electrical Engineering & Electromechanics*, 2023, no. 6, pp. 27-32. doi: https://doi.org/10.20998/2074-272X.2023.6.05.
28. Khelil K., Berrezzek F., Bouadjila T. GA-based design of optimal discrete wavelet filters for efficient wind speed forecasting. *Neural Computing and Applications*, 2021, vol. 33, no. 9, pp. 4373-4386. doi: https://doi.org/10.1007/s00521-020-05251-5.
29. Bengharbi A.A., Laribi S., Allaoui T., Mimouni A. Photovoltaic system faults diagnosis using discrete wavelet transform based artificial neural networks. *Electrical Engineering & Electromechanics*, 2022, no. 6, pp. 42-47. doi: https://doi.org/10.20998/2074-272X.2022.6.07.
30. Akkouchi K., Rahmani L., Lebied R. New application of artificial neural network-based direct power control for permanent magnet synchronous generator. *Electrical Engineering & Electromechanics*, 2021, no. 6, pp. 18-24. doi: https://doi.org/10.20998/2074-272X.2021.6.03.
31. Abid M., Laribi S., Larbi M., Allaoui T. Diagnosis and localization of fault for a neutral point clamped inverter in wind energy conversion system using artificial neural network technique. *Electrical Engineering & Electromechanics*, 2022, no. 5, pp. 55-59. doi: https://doi.org/10.20998/2074-272X.2022.5.09.

Received 30.11.2023
Accepted 15.01.2024
Published 01.05.2024

Reda Rouaibia[1], *Doctor,*
Yacine Djeghader[1], *Associate Professor,*
Lotfi Moussaoui[1], *Associate Professor,*
[1] Department of Electrical Engineering,
Faculty of Science and Technology,
Mohamed-Cherif Messaadia University Souk Ahras, Algeria,
e-mail: r.rouaibia@univ-soukahras.dz (Corresponding Author);
yacine.djeghader@univ-soukahras.dz;
l.moussaoui@univ-soukahras.dz

How to cite this article:
Rouaibia R., Djeghader Y., Moussaoui L. Artificial neural network and discrete wavelet transform for inter-turn short circuit and broken rotor bars faults diagnosis under various operating conditions. *Electrical Engineering & Electromechanics*, 2024, no. 3, pp. 31-37. doi: https://doi.org/10.20998/2074-272X.2024.3.04

UDC 621.314 https://doi.org/10.20998/2074-272X.2024.3.05

M.E. Lahlaci, M. Miloudi, H. Miloudi

Experimental electromagnetic compatibility of conducted electromagnetic interferences from an IGBT and a MOSFET in the power supply

Introduction. *Most electromagnetic compatibility studies carried out in the context of power switch research are generally valid for low frequencies. This frequency restriction appears to be too restrictive for a complete analysis of the electromagnetic interference conducted.* ***The novelty*** *of this work lies in the load-dependent an optimal selection of IGBTs and MOSFETs for least-disturbance power switching in the frequency range from 150 kHz to 30 MHz, based on an optimal experimental selection procedure and show the impact of load value on switch switching and noise generation.* ***Purpose.*** *Analysis of the fundamental possibility of selecting a switching device with a power supply based on an experimental measurement which allows to increase the reliability of the entire mechanism operation and significantly simplify the design.* ***Methods.*** *In this paper, the proposed study is used and compared with experimental results at low and high frequencies. Then, a comparison is made for conducted electromagnetic interference (common-mode and differential-mode) generated by IGBT and MOSFET for different loads, and the proposed methodology is verified on an experiment suitable for predicting terminal overvoltage analysis and conducted electromagnetic interference problems.* ***Practical value.*** *The primary method for establishing a conducted electromagnetic interference source for switching devices is based on IGBT and a MOSFET depending on the resistive load.* References 22, figures 17.

Key words: **electromagnetic interference, electromagnetic compatibility, common-mode, differential-mode, IGBT, MOSFET.**

Вступ. *Більшість досліджень електромагнітної сумісності, які проводяться в контексті досліджень силових вимикачів, зазвичай застосовуються для низьких частот. Це обмеження за частотою видається занадто жорстким щодо повного аналізу електромагнітних перешкод.* ***Новизна*** *даної роботи полягає у залежному від навантаження оптимальному виборі IGBT і MOSFET для комутації потужності з найменшими перешкодами в діапазоні частот від 150 кГц до 30 МГц, на основі оптимальної експериментальної процедури вибору і впливу величини навантаження на перемикання перемикачів і генерацію шуму.* ***Мета***. *Аналіз принципової можливості вибору комутаційного пристрою з джерелом живлення на основі експериментального виміру дозволяє підвищити надійність роботи всього механізму та суттєво спростити конструкцію.* ***Методи***. *У цій статті запропоноване дослідження використовується та порівнюється з експериментальними результатами на низьких та високих частотах. Потім проводиться порівняння кондуктивних електромагнітних перешкод (синфазних та диференціальних), що генеруються IGBT і MOSFET для різних навантажень, і запропонована методологія перевіряється в експерименті, який підходить для прогнозування аналізу перенапруги на клемах і проблем кондуктивних електромагнітних перешкод.* ***Практична цінність***. *Основний метод створення кондуктивного джерела електромагнітних перешкод для комутаційних пристроїв ґрунтується на використанні IGBT та MOSFET залежно від резистивного навантаження.* Бібл. 22, рис. 17.

Ключові слова: **електромагнітні перешкоди, електромагнітна сумісність, синфазний режим, диференціальний режим, IGBT, MOSFET.**

Introduction. The proliferation of devices employed in power electronics has witnessed a significant upsurge in recent times. Rooted in the principles of semiconductor switching, these devices have now permeated diverse domains, including land and air transportation, consumer-focused household applications, and even the realm of renewable energies [1, 2].

The functionality of static converters carries an environmental detriment due to their swift switching intervals marked by substantial amplitudes. These rapid switching processes serve to curtail losses during transitions by virtue of the simultaneous presence of voltage and current within the switches. The orders of magnitude for the gradients of these transitions may span from 100 to 1000 A/μs for dI/dt, while dV/dt values range from 5 to 50 kV/μs [3]. Additionally, the markedly high switching frequency stands as an additional contributor to electromagnetic pollution, varying from 100 Hz to 1 MHz.

Electromagnetic compatibility (EMC) has emerged as a critical design requirement for switching power supplies. The required standards ensure that a system can work satisfactorily in its environment without causing unbearable electromagnetic disruptions to neighboring equipment.

Because the main electromagnetic interference (EMI) sources in power electronics are converter switching and essentially produce conducted emissions [4-8] disturbances can be classified into two types based on their modes of propagation:

1) conducted disturbances, which propagate through electrical conduction;

2) radiated disturbances, which circulate through an electromagnetic field [9-11].

A switch-mode power supply must follow the same piping requirements as most modern electrical equipment.

In the field of power electronics, a conversion chain typically consists of multiple stages (Fig. 1).

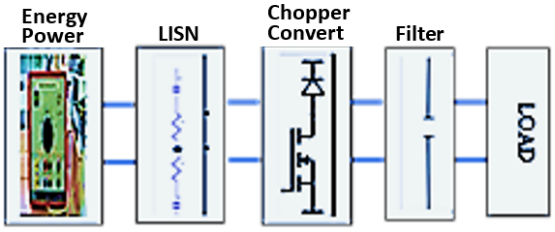

Fig. 1. Multi-stage power converter

These stages often include a rectifier followed by a switching stage, which could be a variable speed drive, a switching power supply, or an inverter for induction heating systems. The assessment of EMC takes place at various levels, including power lines, rectifiers, converters and their control systems, filters, and loads [12-14].

The switching cell and its control energy conversion in power electronics is based on two complementary phases: switching and energy storage. Switching is achieved using power switches with semiconductor

components. There are switches with controlled switching (MOSFET, IGBT, JFET) that require control, and others with natural switching (diode, Schottky). Energy storage occurs in passive components like capacitors and inductors. The integration of these two phases is the principle behind the switching cell. The study of power transistors is not a new issue [15-17], and relevant studies have been carried out throughout the evolution of power systems and power conversion technologies. Power transistors are the primary source of EMI and EMC issues in power equipment.

This paper focuses on the EMI-EMC (common-mode (CM) and differential-mode (DM)) design of high-frequency (150 kHz to 30 MHz) power transistors (MOSFET and IGBT) for high-frequency and high-power applications. A background description and review are provided to assist characterize this work and its originality. The experimental method used for identifying high-frequency behavior is presenting oneself in simple circumstances with only two separate potentials. Considering EMI generated by MOSFET and IGBT during the original design stage can help designers satisfy EMC at a reasonable cost before reality. EMI forecast should be closely paid to in order to save design cycle and expense.

Purpose. Analysis of the fundamental possibility of selecting a switching device with a power supply based on an experimental measurement which allows to increase the reliability of the entire mechanism operation and significantly simplify the design.

The tests EMC in this paper underscore the importance of carefully selecting the type of switching device (IGBT or MOSFET) based on the specific requirements of different loads and switching constraints. MOSFETs are generally preferred for fast switching and low-frequency (LF) applications, while IGBTs are better suited for slower switching and high-frequency (HF) applications. Proper thermal management is also essential to ensure optimal performance. The results of these tests contribute to a better understanding of switching device performance in series chopper applications and guide design choices accordingly.

EMC measurement and standards of conducted EMI. Conducted emissions refer to disruptions in measurable electrical properties that are directly observable at the conductor level (voltage and current). These emissions encompass undesired high-frequency currents that traverse within the device, along with overvoltages that may arise at the load's terminals when powered through an extended cable [18].

To make measurements meaningful and repeatable, it is desirable to decouple the assembly under test from the network, providing a known impedance through which disturbances can be forced to pass. This is the purpose of a device known as a Line Impedance Stabilizing Network (LISN), which is inserted between the network and the assembly under test (Fig. 2).

LISN is equivalent to a filter inserted between the supply network and the input of the equipment under test. Its role is multiple: it isolates the equipment under test from the power supply network, sets the prescribed impedance at the measurement points, and channels conducted disturbances to the measurement receiver.

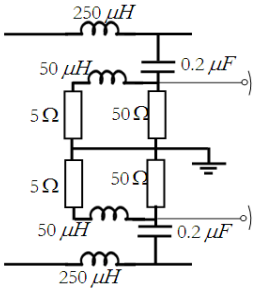

Fig. 2. Line Impedance Stabilization Network (LISN)

Conducted disturbances often pertain to high-frequency currents circulating within the device. The term high-frequency typically encompasses frequencies ranging from 150 kHz to 30 MHz, as this frequency range aligns with the bandwidth regulated by prevailing EMC standards. This current can be dissected into two modes (CM and DM), as depicted in Fig. 3.

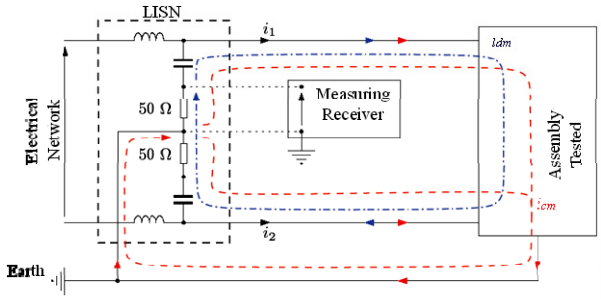

Fig. 3. High-frequency CM (I_{cm}) and DM (I_{dm}) currents

The DM current (I_{dm}) characterizes the portion of the current that forms a loop within the power conductors between the power source and the load. This is the normal current path, but the high-frequency components are undesirable.

The CM current (I_{cm}) refers to the portion of the current that flows through the ground wire. This path typically does not participate in power transfer, but it can carry high-frequency components, especially through capacitive coupling. Regardless of their coupling mode, these high-frequency currents ultimately loop back through the internal impedances of the electrical network, making their measurement dependent on the specific network configuration and layout.

All power transistors are sources of pollution due to parasitic elements coming from the power supplies themselves. Like most electrical equipment today, they must comply with EMC standards. Even if their predominant use in the industrial sector means that they can sometimes escape this constraint, their progressive use in the tertiary sector means that the normative aspect must be met, or at least anticipated. Companies specializing in the design of power supplies and, more generally, of static converters, are today faced with this type of requirement. Power transistor applications, which are now common place in many service sectors, represent some of the most complex power structures in terms of design and modeling.

Each regulatory body has a specific standard for carrying out EMC tests. Measurements are carried out in accordance with EN 55022 [19-22]. The latter imposes a specific measurement protocol. This protocol guarantees the reproducibility and reliability of measurements carried out on the equipment under test. In order to explain the

layout of the various system components and the configuration of the normative measurements, we present the synoptic diagram of the test bench in Fig. 4. The conducted emission test configuration complies with EN 55022. All devices are placed on a copper ground plane.

The equipment under test is placed on a plane electrically isolated from the surrounding area.

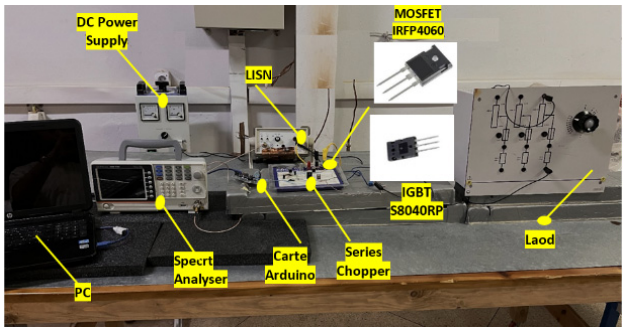

Fig. 4. EMC bench for measuring conducted EMI

In the context of conducting a comparison regarding conducted EMI in CM and DM, involving a series chopper associated with a resistive load, two static converters were utilized for reference purposes: the IGBT reference FGH40N60 and the MOSFET reference IRFP4060, along with a BYT12 diode. An experimental setup was established to assess the conducted EMI, where a chopper (Fig. 5) fed a resistive load at a continuous 24 V voltage level. The primary measurement elements included the LISN connected before the chopper, as well as a spectrum analyzer to measure the conducted disturbances in both CM and DM across various load values.

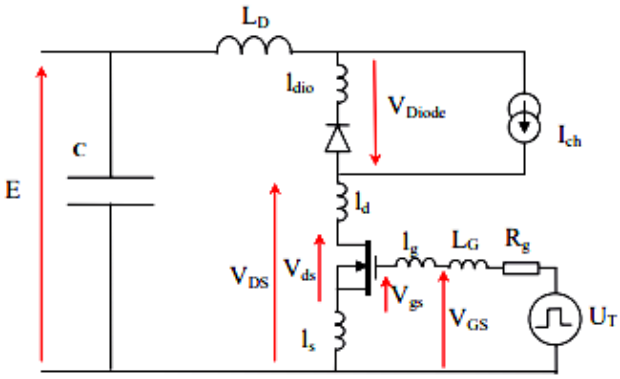

Fig. 5. Chopper (equipment under test)

We have focused on the conducted mode, which is largely responsible for the majority of disturbance phenomena generated by these devices. The distribution of CM and DM currents in the system will be presented. To illustrate their origins, CM currents are essentially transmitted via capacitive CM couplings. Conducted disturbances propagate to other parts of the system by looping through the ground.

For the analysis of EMI produced by the converter, spectral estimates must be referred to EN 55022, the standard for measuring disturbances. To comply with current regulations, a frequency range of 150 kHz to 30 MHz must be taken into consideration. The standard aims to estimate EMI in the measurement receiver at the chopper input.

A method of EMC analysis commonly used in power electronics has been employed. To illustrate this method, we will first use a chopper with the MOSFET (IRFP4060), and then the same chopper with the IGBT (FGH40N60). From there, we'll choose the analysis method and the resulting measurement tool for what would appear to be the most suitable for this study.

Results and discussion. Figures 6, 7 show the frequency spectrum of disturbances after using the MOSFET respectively in CM and DM with different loads (50 Ω, 100 Ω and 200 Ω).

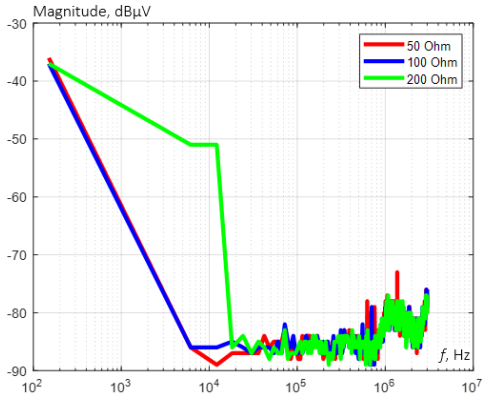

Fig. 6. CM EMI (MOSFET)

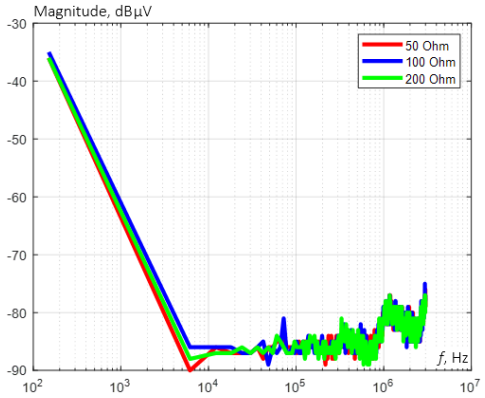

Fig. 7. DM EMI (MOSFET)

When parasitic currents flow through the links in the same direction, closing at equipotential bonding, we speak of CM. In this case, parasitic currents propagate via the parasitic capacitances created between each hot spot subject to voltage variations (MOSFET drain) and the ground plane, and via the parasitic capacitances between the semiconductor and the heat sink. These parasitic currents flow through the two parallel resistors of standardized value equal to 50 Ω.

In DM, when parasitic currents flow in both conductors. These currents are due to the switching of switch currents (MOSFET). Part of the switching current flows through the switching capacitor, and the other part through the two resistors of 50 Ω in series.

In the linear amplification region of the MOSFET transistor, when the input voltage exceeds the threshold voltage, a small current begins to appear at the output. This current creates a voltage across the resistor, causing the output voltage to decrease. Conducted EMI (CM and DM) is very small. Transitioning to the linear region, we observe similar conducted disturbances in both CM and DM. However, once the output current reaches a certain value, the V_{DS} voltage drops below the $V_{GS} - V_{th}$ voltage, as seen in the case of a load equal to 50 Ω in Fig. 8.

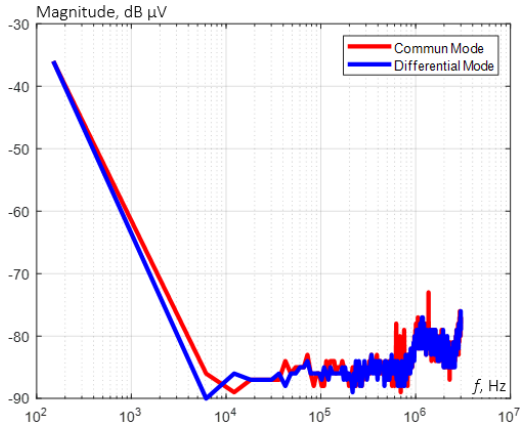

Fig. 8. CM/DM EMI (MOSFET)

As the load increases, the occurrence of interference spikes in the DM increases in the first operating region (switching state or closure) of the switch. This is due to rapid voltage fluctuations exceeding the threshold voltage and significant current appearing at the switch's output (for a load of 200 Ω) (Fig. 9). In contrast, the MOSFET does not exhibit any CM propagation during the switching phase, which is similar to that of the 50 Ω load (Fig. 8).

The conducted interference diagrams in CM observed for the IGBT power switch are nearly identical for different loads (Fig. 10). However, there is a notable interference peak for the 50 Ω and 100 Ω loads compared to the 200 Ω load.

In this study, the behavior of the EMIs (CM and DM) from the two static converters is nearly the same, but with different amplitudes and peaks, and higher with the lower load.

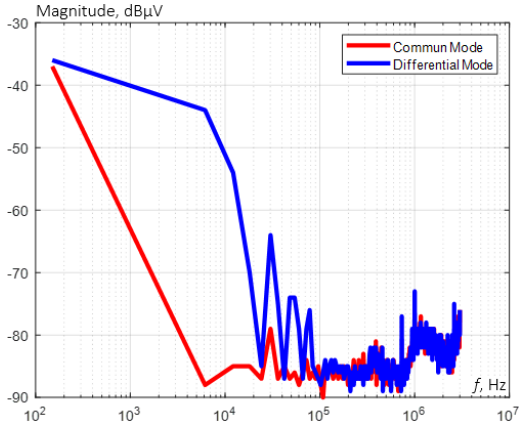

Fig. 9. CM/DM MOSFET

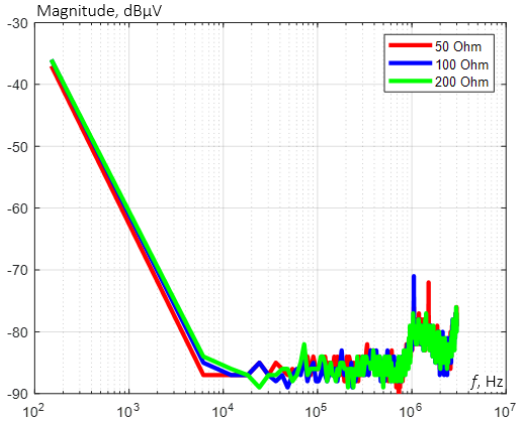

Fig. 10. CM EMI IGBT

In DM, the impedance of the load can play a crucial role. An increase in the resistive load can lead to an increase in differential impedance, which can influence the time required for the current to reach its nominal level in DM. On the other hand, higher loads (200 Ω load in our test) can generate more heat, which can affect the performance of the IGBT device. Elevated temperatures can influence the switching behavior (Fig. 11).

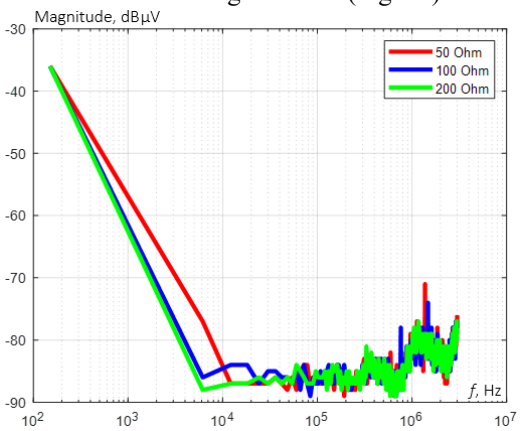

Fig. 11. DM EMI IGBT

The IGBT power switch behaves in a similar manner in both CM and DM for a 50 Ω load (Fig. 12) and a 200 Ω load (Fig. 13). However, for a low load, the IGBT takes longer to transition from the first region to the linear region.

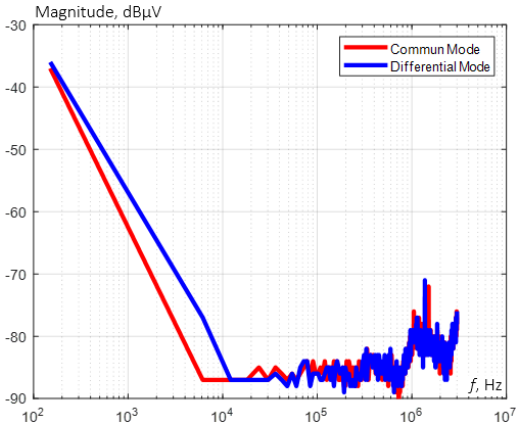

Fig. 12. CM/DM IGBT

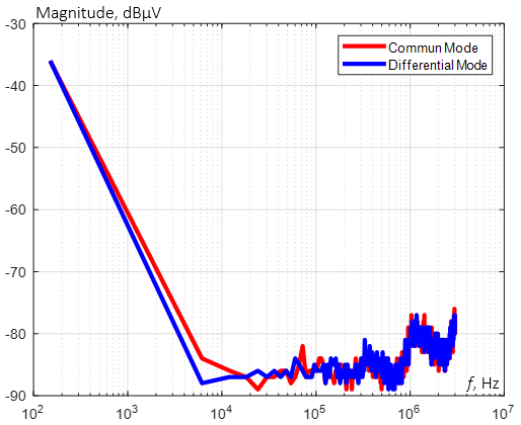

Fig. 13. CM/DM IGBT

In Fig. 14, 15, for a 50 Ω resistive load, both power switches exhibit similar interference patterns. However, in DM, the IGBT may show a more significant switching delay compared to the MOSFET.

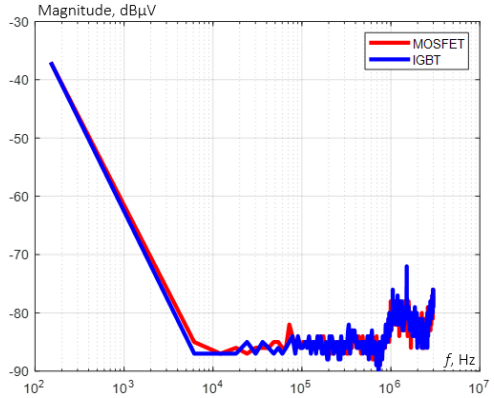

Fig. 14. CM MOSFET/IGBT

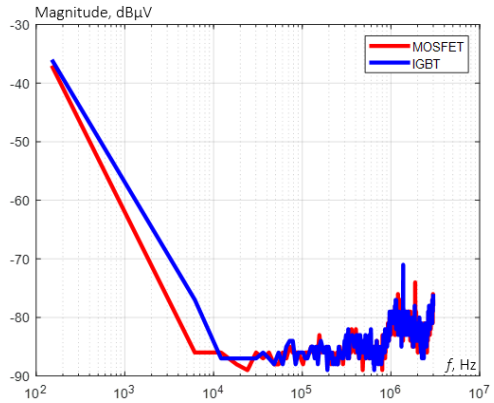

Fig. 15. DM MOSFET/IGBT

This last difference can be attributed to the intrinsic switching times of the two devices. The MOSFET, typically being faster, responds more swiftly in this context, while the IGBT may require more time to reach its switching state in DM with this load.

The conducted (CM and DM) interference tests using a series chopper employing both an IGBT and a MOSFET revealed several key observations.

When the load is increased to 200 Ω, the conducted disturbances in CM (Fig. 16) remain the same as those for a 50 Ω load in both operational regions for both switches. However, in the case of DM (Fig. 17), a significant current appears across the terminals of the load when the input voltage exceeds the threshold voltage for the MOSFET. The IGBT, on the other hand, does not reach saturation in this region.

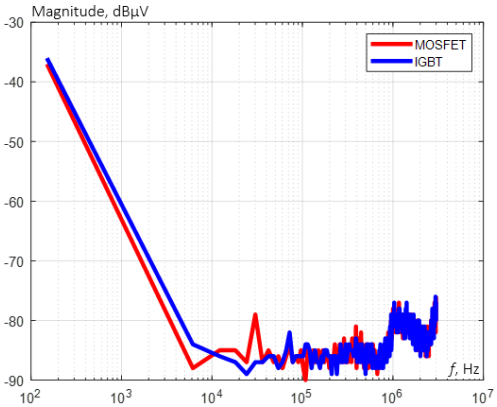

Fig. 16. CM MOSFET/ IGBT

The main difference between IGBTs and MOSFETs is that IGBTs have an additional p-n junction compared to MOSFETs, which gives them the properties of both MOSFETs. The least disruptive power switch is the one that produces the least amount of transients when it is turned on or off. These transients can cause damage to sensitive electronic equipment.

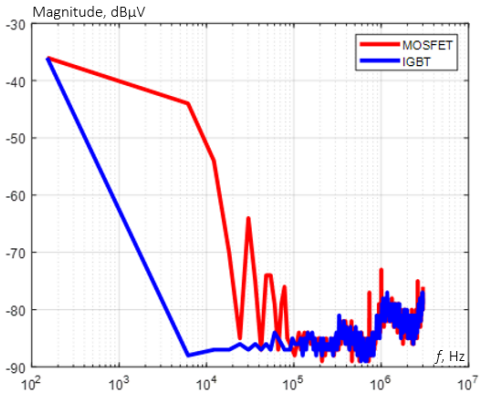

Fig. 17. DM MOSFET/ IGBT

Conclusions.

1. The difference between using an IGBT and a MOSFET is that the IGBT tends to have smoother switching, resulting in fewer high harmonics and less electromagnetic interference (EMI) during switching. This can be advantageous in terms of electromagnetic compatibility as smoother current transitions reduce the potential for EMI emissions. Conversely, MOSFETs, especially when used in high-speed switching applications, can generate higher peaks of EMI due to their rapid switching in the low-frequency (LF) and high-frequency (HF) ranges.

2. MOSFET is better suited for fast switching and low-frequency applications, whereas IGBT is more suitable for LF and HF. The difference in behavior between the IGBT and MOSFET is linked to their intrinsic switching characteristics. MOSFET tend to have shorter switching times, making them faster in responding to variations in load and voltage. Conversely, IGBT may exhibit longer switching delays.

3. The load defines the switch's electrical characteristics, such as rated power, current and voltage. It is important to choose a switch whose characteristics correspond to the load to which it will be connected.

4. Impact of the load value: played a critical role in test results. Resistive loads of varying values influenced interference levels and observed switching delays.

5. Thermal effects: tests also demonstrated that higher loads could generate more heat, potentially affecting the performance of switching devices, particularly IGBT.

Acknowledgments. This research was supported by «La Direction Générale de la Recherche Scientifique et du Développement Technologique (DGRSDT)».

Conflict of interest. The authors declare no conflict of interest.

REFERENCES

1. Miloudi M., Bendaoud A., Miloudi H. Common and differential modes of conducted electromagnetic interference in switching power converters. *Revue Roumaine Des Sciences Techniques Serie Electrotechnique et Energetique*, 2017, vol. 62, no. 3, pp. 246-251.

2. Miloudi H., Bendaoud A., Miloudi M. A method for modeling a common-mode impedance for the AC motor. *Elektrotehniski Vestnik/Electrotechnical Review*, 2017, vol. 84, no. 5, pp. 241-246.

3. Miloudi H., Miloudi M., Gourbi A., Bermaki M.H., Bendaoud A., Zeghoudi A. A high-frequency modeling of AC motor in a frequency range from 40 Hz to 110 MHz. *Electrical Engineering & Electromechanics*, 2022, no. 6, pp. 3-7. doi: https://doi.org/10.20998/2074-272X.2022.6.01.
4. Wunsch B., Skibin S., Forsström V., Stevanovic I. EMC Component Modeling and System-Level Simulations of Power Converters: AC Motor Drives. *Energies*, 2021, vol. 14, no. 6, art. no. 1568. doi: https://doi.org/10.3390/en14061568.
5. Miloudi M., Miloudi H., Bendaoud A., Salhi M.A., Al-Omari A.N. Experimental characterization of the high-frequency isolating power transformer. *Elektrotehniski Vestnik/Electrotechnical Review*, 2019, vol. 86, no. 4, pp. 211-218.
6. Benazza B., Bendaoud A., Slimani H., Benaissa M., Flitti M., Zeghoudi A. Experimental study of electromagnetic disturbances in common and differential modes in a circuit based on two DC/DC boost static converter in parallel. *Electrical Engineering & Electromechanics*, 2023, no. 4, pp. 35-39. doi: https://doi.org/10.20998/2074-272X.2023.4.05.
7. Li Y., Dang Y., Zhang S., Li X., Jin Y., Ben-Abdallah P., Xu J., Ma Y. Radiative Thermal Transistor. *Physical Review Applied*, 2023, vol. 20, no. 2, art. no. 024061. doi: https://doi.org/10.1103/PhysRevApplied.20.024061.
8. Chikhi N., Bendaoud A. Evaluation of Conducted Disturbances Generated by the Chopper-rectifier Association Propagating to the Electrical Network. *European Journal of Electrical Engineering*, 2019, vol. 21, no. 1, pp. 1-6. doi: https://doi.org/10.18280/ejee.210101.
9. Muller D., Schweitzer D.N., Beltle M., Tenbohlen S. An Active Common Mode EMI Filter Approach introducing Predictive Pulsed Compensation. *2019 International Symposium on Electromagnetic Compatibility - EMC EUROPE*, 2019, pp. 1003-1008. doi: https://doi.org/10.1109/EMCEurope.2019.8872104.
10. Kharanaq F.A., Emadi A., Bilgin B. Modeling of Conducted Emissions for EMI Analysis of Power Converters: State-of-the-Art Review. *IEEE Access*, 2020, vol. 8, pp. 189313-189325. doi: https://doi.org/10.1109/ACCESS.2020.3031693.
11. Xu S.-Z., Peng Y.-F., Li S.-Y. Suppression effectiveness research on multi-level EMI filter in thermal electromagnetic interactive filed of explosion-proof three-level NPC converter. *Case Studies in Thermal Engineering*, 2019, vol. 15, art. no. 100510. doi: https://doi.org/10.1016/j.csite.2019.100510.
12. Zeghoudi A., Bendaoud A., Slimani H., Miloudi H., Miloudi M., Chikhi N. Experimental Measurement of Common and Differential Modes for Variable Speed Drive DC Motor. *2022 19th International Multi-Conference on Systems, Signals & Devices (SSD)*, 2022, pp. 532-537. doi: https://doi.org/10.1109/SSD54932.2022.9955933.
13. Mariscotti A., Sandrolini L. Review of models and measurement methods for compliance of electromagnetic emissions of electric machines and drives. *ACTA IMEKO*, 2021, vol. 10, no. 2, pp. 162-173. doi: https://doi.org/10.21014/acta_imeko.v10i2.1066.
14. Touré M.T., Paladian F., Bensetti M., Robert F., Dufour L. Conducted EMI prediction using different levels of MOSFET models in a multi-physics optimization context. *European Journal of Electrical Engineering*, 2016, vol. 18, no. 5-6, pp. 425-439. doi: https://doi.org/10.3166/ejee.18.425-439.
15. Miloudi H., Bendaoud A., Miloudi M., Gourbi A., Slimani H. Common Mode conducted electromagnetic interference in inverter fed-AC motor. *Przeglad Elektrotechniczny*, 2010, vol. 86, no. 12, pp. 272-275.
16. Hamoudi A. *Modélisation et Caractérisation cem D'un Convertisseur DC-AC*. Master's Thesis. Oran University of Science and Technology, 2009. 169 p. (Fra).
17. Douzi Chawki. *Effet du vieillissement par fatigue électrothermique sur la compatibilité électromagnétique des composants de puissance à base de SiC.* Doctor's Thesis. Normandie Université; Université de Sousse (Tunisie), 2019. 193 p. (Fra).
18. Yuwono T., Baharuddin M.H., Misran N., Ismail M., Mansor M.F. A review of measurement of electromagnetic emission in electronic product: Techniques and challenges. *Communications in Science and Technology*, 2022, vol. 7, no. 1, pp. 23-37. doi: https://doi.org/10.21924/cst.7.1.2022.727.
19. Mariscotti A., Sandrolini L., Simonazzi M. Supraharmonic Emissions from DC Grid Connected Wireless Power Transfer Converters. *Energies*, 2022, vol. 15, no. 14, art. no. 5229. doi: https://doi.org/10.3390/en15145229.
20. Wu Y., Yin S., Liu Z., Li H., See K.Y. Experimental Investigation on Electromagnetic Interference (EMI) in Motor Drive Using Silicon Carbide (SiC) MOSFET. *2020 International Symposium on Electromagnetic Compatibility - EMC EUROPE*, 2020, pp. 1-6. doi: https://doi.org/10.1109/EMCEUROPE48519.2020.9245674.
21. Khvitia B., Gheonjian A., Kutchadze Z., Jobava R. A SPICE Model for IGBTs and Power MOSFETs Focusing on EMI/EMC in High-Voltage Systems. *Electronics*, 2021, vol. 10, no. 22, art. no. 2822. doi: https://doi.org/10.3390/electronics10222822.
22. Zeghoudi A., Bendaoud A., Lucache D.-D., Bechekir S., Slimani H., Miloudi M. Frequency Variation Impact on Conducted Disturbances Generated by a SEPIC Converter. *International Journal of Electronics and Electrical Engineering Systems*, 2023, vol. 6, no. 1, pp. 27-32.

Received 07.10.2023
Accepted 16.12.2023
Published 01.05.2024

Mohammed Elamine Lahlaci[1], *PhD*,
Mohamed Miloudi [1], *Lecturer*,
Houcine Miloudi[2], *Lecturer*,
[1] GIDD Laboratory, Department of Electrical Engineering and Automation, Relizane University, Algeria,
e-mail: mohammedelamine.lahlaci@univ-relizane.dz (Corresponding Author);
mohamed.miloudi@univ-relizane.dz
[2] APELEC Laboratory, Djillali Liabes University, Sidi-Bel-Abbes, Algeria,
e-mail: el.houcine@yahoo.fr

How to cite this article:
Lahlaci M.E., Miloudi M., Miloudi H. Experimental electromagnetic compatibility of conducted electromagnetic interferences from an IGBT and a MOSFET in the power supply. *Electrical Engineering & Electromechanics*, 2024, no. 3, pp. 38-43. doi: https://doi.org/10.20998/2074-272X.2024.3.05

UDC 621.314 https://doi.org/10.20998/2074-272X.2024.3.06

V.Y. Romashko, L.M. Batrak, O.O. Abakumova

Obtaining the maximum power from the source using step-up and step-down type pulse regulators that work on battery

Introduction. *Pulse regulators are widely used to match the output resistance of the source with the load resistance in order to ensure the possibility of taking maximum power when the value of the load resistance changes.* ***Problem.*** *In the case of using non-traditional and renewable sources of electrical energy, for a more uniform supply of energy to the load, a battery is often connected to the output of the pulse regulator, which works in buffer mode. In such cases, the load for the pulse regulator will be the battery itself, and the role of the source load will be performed by the input resistance of the regulator. To ensure the mode of operation of the pulse regulator, in which the maximum power will be transmitted from the source to the load, it is necessary to know the regulating characteristics of the regulator. There are works that analyze the regulating characteristics of step-up and step-down pulse regulators, which are used to match the load with the output resistance of the source. At the same time, for the same purpose, pulse regulators of the step-up and step-down type can be used.* ***Goal.*** *The purpose of the work is to analyze the features of the operation of step-up and step-down type pulse regulators in the mode of maximum power transmission from the source to the battery, as well as to determine the conditions under which it is possible and appropriate to use such regulators for the specified purpose.* ***Methodology.*** *The regulating characteristics of step-up and step-down type pulse regulators with sequential and parallel switching on of the controlled key were determined and analyzed, taking into account the presence of a battery at their output.* ***Results****. It is shown that the transfer of energy from the source to the battery is possible only under certain modes of operation of the regulator, which depend on the type of regulator, as well as the amount of voltage on the battery. The conditions under which it is possible to draw the maximum power from the source are determined.* ***Originality.*** *Since the output resistance of the source and the load resistance are of the same order in the maximum power selection mode, the internal resistance of the power source was taken into account when determining the regulating characteristics of the regulators.* ***Practical value.*** *The obtained results made it possible to formulate practical recommendations for a justified choice of the regulator's operating modes, depending on its type and the value of voltage on the battery.* References 15, tables 1, figures 4.

Key words: **source output impedance, matching pulse regulator, battery operation, maximum power transmission, step-up and step-down type regulators.**

Проаналізовано регулювальні характеристики імпульсних регуляторів підвищувально-понижувального типу з урахуванням внутрішнього опору джерела живлення, за умови підключення акумулятора на їх виході. Показано, що за наявності акумулятора, регулятори напруги працюватимуть у режимі регулювання струму заряджання акумулятора. При цьому діапазон регулювання відносного часу замкненого стану ключа буде обмеженим. Дано рекомендації щодо вибору режимів роботи регулятора, за яких забезпечується передавання енергії від джерела до акумулятора, в залежності від схеми регулятора, а також значення напруги на акумуляторі. Визначено умови, за яких забезпечується передавання максимальної потужності від джерела живлення до акумулятора. Бібл. 15, табл. 1, рис. 4.

Ключові слова: **вихідний опір джерела, узгоджувальний імпульсний регулятор, робота на акумулятор, передавання максимальної потужності, регулятори підвищувально-понижувального типу.**

Introduction. When using different types of non-traditional and renewable sources, they strive to obtain the maximum possible amount of electrical energy. For this, the operating point of the source must be at the point of maximum power (MP) on its output characteristic. However, this mode of operation of the source is possible only in the case when the output resistance of the source r coincides with the resistance of its load R [1, 2].

To ensure the possibility of selecting MP from the source in a wide range of changes in the load resistance, a pulse regulator (PR) is switched on between the source and the load, which matches the output resistance of the source with the load resistance [3-6]. In such cases, the role of the source load will be performed by the input resistance of the regulator $R_e = f(R, t^*)$, which is a function of the load resistance of the regulator R, as well as the relative time of the closed state of the regulator key $t^* = t_{closed} / T$ during the period of operation of the key T. By changing the parameter t^* it is possible to ensure the fulfillment of the condition $R_e = r$ in a wide range of changes in the load resistance R.

The amount of energy coming from non-conventional and renewable sources often depends on external conditions. Therefore, to ensure a more uniform supply of energy to the load, a battery is switched on at the PR output, which operates in buffer mode. In such cases, the PR load will be the battery itself, and the source load will be the input resistance of the regulator. Transmission of MP from the source to the battery can be ensured by choosing the appropriate operating mode of the PR [5, 7, 8].

In [9], the conditions under which it is possible and expedient to transfer the MP from the source to the battery using step-up and step-down PRs, as well as the peculiarities of the operation of these regulators in the specified mode, were analyzed. To match the output resistance of the source with the load, well-known PR circuits of the step-up-step type can also be used [10-12].

The goal of the work is to analyze the peculiarities of the step-up and step-down PRs operation in the mode of MP transmission from the source to the battery, as well as to determine the conditions under which it is possible and expedient to use such regulators with the indicated purpose.

Circuits of regulators. Let's consider those variants of IP circuits of the step-up and step-down type, which provide the possibility of sampling MP from the power source [13]. The corresponding circuits of the regulators are presented in Fig. 1, 2.

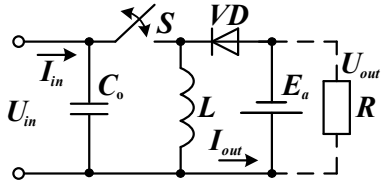

Fig. 1. Regulator of the step-up and step-down type with serial key activation

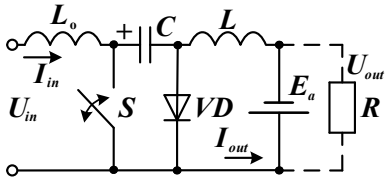

Fig. 2. Regulator of the step-up and step-down type with parallel key activation

We determine and analyze the control characteristics of these regulators, with the help of which the PR operating mode can be determined, in which the MP will be selected from the power source. Since in the MP selection mode, the load resistance and the output resistance of the source are values of the same order, when determining the control characteristics of the regulators, we will take into account the internal resistance of the source, considering it to be *linear*.

The regulator of the step-up and step-down type with serial activation of the key (Fig. 1). If the losses in the elements of the PR circuit are not taken into account, in the continuous current mode of the inductance L, the conditions will always be fulfilled [12]

$$U_{out} = U_{in}\frac{t^*}{1-t^*}; \quad I_{out} = I_{in}\frac{1-t^*}{t^*}. \tag{1}$$

If it is assumed that the internal resistance of the battery is much smaller than the internal resistance of the source, it can be argued that during the regulation process, the output voltage of the regulator will remain practically unchanged and will be equal to the voltage on the battery $U_{out} = E_a$. Therefore, in order for the system to be in a state of equilibrium during the regulation process, the input voltage of the regulator must be equal to

$$U_{in} = U_{out}\frac{1-t^*}{t^*} = E_a\frac{1-t^*}{t^*}, \tag{2}$$

where $t^* = t_{closed} / T$ is the relative time of the closed state of the key S in the period T, t_{closed} is the duration of the closed state of the key.

Due to the presence of the internal resistance of the source, the input voltage of the regulator will change with changes in the consumed current and will be determined by the output characteristic of the source [12]

$$U_{in} = U_{oc} - I_{out}r, \tag{3}$$

where U_{oc} is the no-load voltage of the power source.

Thus, in a state of equilibrium, conditions (2), (3) must be fulfilled simultaneously

$$U_{oc} - I_{in}r = E_a\frac{1-t^*}{t^*}, \tag{4}$$

or moving to relative units [12]

$$1 - I_{in}^* = E_a^*\frac{1-t^*}{t^*}, \tag{5}$$

where $E_a^* = E_a/U_{oc}$; $I_{in}^* = I_{in}/I_{sc}$; $I_{sc} = U_{oc}/r$ is the short-circuit current of the source.

Taking into account that the no-load voltage of the source, as well as the battery voltage, are fixed, by changing the parameter t^*, we will thereby adjust the input and, accordingly, the output current of the regulator

$$I_{in}^* = 1 - E_a^*\frac{1-t^*}{t^*}. \tag{6}$$

Taking into account (1)

$$I_{out}^* = I_{in}^*\frac{1-t^*}{t^*} = \left[1 - E_a^*\frac{1-t^*}{t^*}\right]\frac{1-t^*}{t^*}. \tag{7}$$

Therefore, (6), (7) are the regulating characteristics of PR according to the circuit (Fig. 1).

The regulator of the step-up and step-down type with parallel activation of the key (Fig. 2). For this circuit in the continuous current mode of the inductance L_0, a relationship is valid [12]

$$U_{out} = U_{in} = \frac{1-t^*}{t^*}; \quad I_{out} = I_{in}\frac{t^*}{1-t^*}, \tag{8}$$

where $t^* = t_{open} / T$; t_{open} is the duration of the open state of the key S during the period T.

Therefore, in the steady state of operation, the input voltage of the regulator should be

$$U_{in} = U_{out}\frac{t^*}{1-t^*} = E_a\frac{t^*}{1-t^*}. \tag{9}$$

In order for the system to be in a state of equilibrium, the condition must be fulfilled

$$E_a\frac{t^*}{1-t^*} = 1 - I_{in}r, \tag{10}$$

or in relative units

$$E_a^*\frac{t^*}{1-t^*} = 1 - I_{in}^*. \tag{11}$$

Therefore, the control characteristics of the PR according to the circuit (Fig. 2) will look like this

$$I_{in}^* = \left[1 - E_a^*\frac{t^*}{1-t^*}\right]; \tag{12}$$

$$I_{out}^* = \left[1 - E_a^*\frac{t^*}{1-t^*}\right]\frac{t^*}{1-t^*}. \tag{13}$$

Thus, if there is a battery at the output, the regulators under consideration will operate in the mode of regulating the input and output current (battery charging current). At the same time, the output voltage of the regulators will remain almost constant and equal to the battery voltage.

Analysis of control characteristics of regulators. If there is a battery at the output, the PR will operate in the battery charging current regulation mode. In the case of $t^* = 0$, the power source and the load are disconnected from each other and there will be no energy transfer to the battery. If $t^* > 0$, to ensure the transfer of energy from the source to the battery, the condition $I_{in} > 0$ must be fulfilled. For the circuit (Fig. 1), taking into account (6), this condition takes the form

$$\left[1-E_a^*\frac{1-t^*}{t^*}\right]>0, \qquad (14)$$

and for the circuit (Fig. 2)

$$\left[1-E_a^*\frac{t^*}{1-t^*}\right]>0. \qquad (15)$$

Taking into account that, in general, the parameter t^* can vary in the range [0...1], taking into account (14), (15), we come to the conclusion that in the presence of a battery, the permissible range of changes in the parameter t^* will be limited. For the circuit (Fig. 1), the permissible change of the parameter lies in the range

$$1 \ge t^* > \frac{E_a^*}{E_a^*+1}, \qquad (16)$$

and for the circuit (Fig. 2)

$$0 < t^* < \frac{1}{1+E_a^*}. \qquad (17)$$

Therefore, the higher the voltage on the battery E_a^*, the more limited the permissible range of regulation of the parameter t^* in the PR will be. At the same time, the analysis of (16), (17) shows that the battery voltage can be both higher and lower than the no-load voltage of the power source U_{oc}.

As is known [1], in the case of linear internal resistance of the power source, at the MP point, the relative value of its output current (input current of the PR) should be $I_{in}^* = 0.5$.

Therefore, the condition of MP selection from the source for the regulator circuit (Fig. 1) will look like this

$$1-E_a^*\frac{1-t^*}{t^*}=0.5, \qquad (18)$$

and for the circuit (Fig. 2)

$$1-E_a^*\frac{t^*}{1-t^*}=0.5. \qquad (19)$$

Thus, the MP will be transmitted from the source to the load under the condition that $t^* = t_{MP}^*$, where for the regulator circuit (Fig. 1)

$$t_{MP}^* = \frac{E_a^*}{E_a^*+0,5}, \qquad (20)$$

and for the circuit (Fig. 2)

$$t_{MP}^* = \frac{0,5}{0,5+E_a^*}. \qquad (21)$$

The regulatory characteristics of the considered circuits presented in Fig. 3, 4, confirm the results of the analysis carried out. The main properties of these circuits are similar. However, if for the circuit (Fig. 1) the permissible regulation range is limited to the left [t_{min} ... 1], then for the circuit (Fig. 2) it is limited to the right [0 ... t_{max}]. This is a consequence of the duality of the circuits of the considered regulators [13].

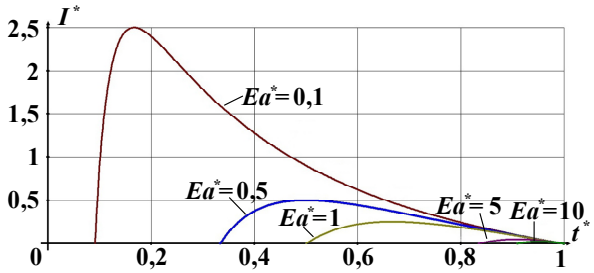

Fig. 3. Regulatory characteristics of PR with serial key activation

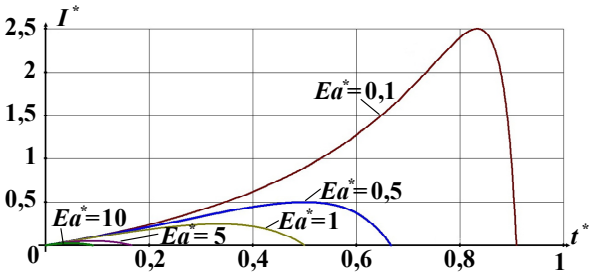

Fig. 4. Regulatory characteristics of PR with parallel key activation

To compare the properties of the four main PR circuits Table 1 shows their main features when operating in the MP transmission mode from the power source to the battery, namely:

- condition of energy transfer from the source to the battery;
- condition of MP selection from the source;
- reasonable battery voltage E_a change range.

Table 1

Conditions of energy transfer from the source to the battery

No.	Regulator type	Energy transfer condition	Condition of MP selection	Reasonable range of change of E_a^*
1	Step-down	$t^* > E_a^*$	$t_{MP}^* = 2E_a^*$	$0,1 \le E_a^* \le 0,5$
2	Step-up	$t^* < 1/E_a^*$	$t_{MP}^* = 1/2E_a^*$	$0,5 \le E_a^* \le 5$
3	Step-up and step-down (Fig. 1)	$t^* > \frac{E_a^*}{1+E_a^*}$	$t_{MP}^* = \frac{E_a^*}{E_a^*+0,5}$	$0,1 \le E_a^* \le 5$
4	Step-up and step-down (Fig. 2)	$t^* < \frac{1}{1+E_a^*}$	$t_{MP}^* = \frac{0,5}{0,5+E_a^*}$	$0,1 \le E_a^* \le 5$

Today, there are modified versions of step-up and step-down PR circuits that differ from the considered ones by the polarity of the output voltage (ZETA and SEPIC converters) [14, 15]. Changing the polarity of the output voltage is achieved by the appropriate construction of the output circuit of the regulator. However, since the main properties of the regulator are determined by the method of construction of its input circuit, and first of all by the method of connecting the controlled key *S*, the obtained results will be valid for the corresponding types of modified circuits of the step-up and step-down type regulators.

Conclusions.

1. If there is a battery at the output, the pulse voltage regulators will operate in the current regulator mode.

2. The nature of the regulation characteristic and the permissible range of regulation depend on the type of regulator and the value of the voltage on the battery.

3. The maximum power from the source will be selected at a certain value of the parameter $t^* = t^*_{MP}$, which is determined by the type of regulator and the value of the voltage on the battery.

4. The pulse regulator of the step-up and step-down type, in comparison with separately the step-up and step-down type regulators, have the widest permissible range of changes in the relative voltage on the battery.

Conflict of interest. The authors of the article declare that there is no conflict of interest.

REFERENCES

1. Panchenko S.V., Ananieva O.M., Babaev M.M. *Theory of electric and magnetic circuits. Textbook*. Kharkiv, UkrDUZT Publ., 2020. 246 p. (Ukr).

2. Louarem S., Kebbab F.Z., Salhi H., Nouri H. A comparative study of maximum power point tracking techniques for a photovoltaic grid-connected system. *Electrical Engineering & Electromechanics*, 2022, no. 4, pp. 27-33. doi: https://doi.org/10.20998/2074-272X.2022.4.04.

3. Twaha S., Zhu J., Yan Y., Li B., Huang K. Performance analysis of thermoelectric generator using DC-DC converter with incremental conductance based maximum power point tracking. *Energy for Sustainable Development*, 2017, vol. 37, pp. 86-98. doi: https://doi.org/10.1016/j.esd.2017.01.003.

4. Olalla C., Clement D., Rodriguez M., Maksimovic D. Architectures and Control of Submodule Integrated DC–DC Converters for Photovoltaic Applications. *IEEE Transactions on Power Electronics*, 2013, vol. 28, no. 6, pp. 2980-2997. doi: https://doi.org/10.1109/TPEL.2012.2219073.

5. Anandhi T.S., PremKumar S. Application of DC-DC boost converter for solar powered traffic light with battery backup. *Indian Journal of Science and Technology*, 2015, vol. 8, no. 32, pp. 1-5. doi: https://doi.org/10.17485/ijst/2015/v8i32/84408.

6. Tseng S.-Y., Wang H.-Y. A Photovoltaic Power System Using a High Step-up Converter for DC Load Applications. *Energies*, 2013, vol. 6, no. 2, pp. 1068-1100. doi: https://doi.org/10.3390/en6021068.

7. Krieger E.M., Arnold C.B. Effects of undercharge and internal loss on the rate dependence of battery charge storage efficiency. *Journal of Power Sources*, 2012, vol. 210, pp. 286-291. doi: https://doi.org/10.1016/j.jpowsour.2012.03.029.

8. Vieira J.A.B., Mota A.M. Implementation of a stand-alone photovoltaic lighting system with MPPT battery charging and LED current control. *2010 IEEE International Conference on Control Applications*, 2010, pp. 185-190. doi: https://doi.org/10.1109/CCA.2010.5611257.

9. Romashko V.Y., Batrak L.M., Abakumova O.O. Features of the work of pulse regulators in the maximum power transmission mode, with the presence of an accumulator at their output. *Electrical Engineering & Electromechanics*, 2023, no. 6, pp. 63-66. doi: https://doi.org/10.20998/2074-272X.2023.6.11.

10. Dinniyah F.S., Wahab W., Alif M. Simulation of Buck-Boost Converter for Solar Panels using PID Controller. *Energy Procedia*, 2017, vol. 115, pp. 102-113. doi: https://doi.org/10.1016/j.egypro.2017.05.011.

11. Shayeghi H., Pourjafar S., Sedaghati F. A Buck-Boost Converter; Design, Analysis and Implementation Suggested for Renewable Energy Systems. *Iranian Journal of Electrical and Electronic Engineering*, 2021, vol. 17, no. 2, p. 1862. doi: https://doi.org/10.22068/IJEEE.17.2.1862.

12. Goncharov Y.P., Budonny O.V., Morozov V.G., Panasenko M.V., Romashko V.Y., Rudenko V.S. *Power conversion equipment. Text book. Part 2.* Kharkiv, Folio Publ., 2000. 360 p. (Ukr).

13. Romashko V.Y., Batrak L.M., Abakumova O.O. Step-up/step-down regulators in maximum power transmission mode. *Electrical Engineering & Electromechanics*, 2022, no. 2, pp. 18-22. doi: https://doi.org/10.20998/2074-272X.2022.2.03.

14. Soedibyo, Amri B., Ashari M. The comparative study of Buck-boost, Cuk, Sepic and Zeta converters for maximum power point tracking photovoltaic using P&O method. *2015 2nd International Conference on Information Technology, Computer, and Electrical Engineering (ICITACEE)*, 2015, pp. 327-332. doi: https://doi.org/10.1109/ICITACEE.2015.7437823.

15. Chavan F.T., Mopari S.S., Swami P.S. Performance analysis of SEPIC and zeta converter for power quality improvement. *International Journal of Scientific and Technology Research*, 2019, vol. 8, no. 12, pp. 1925-1929.

Received 22.11.2023
Accepted 16.01.2024
Published 01.05.2024

V.Y. Romashko[1], *Doctor of Technical Science, Professor,*
L.M. Batrak[1], *PhD, Assistant Professor,*
O.O. Abakumova[1], *PhD, Assistant Professor,*
[1] National Technical University of Ukraine
«Igor Sikorsky Kyiv Polytechnic Institute»,
37, Prospect Beresteiskyi, Kyiv-56, 03056, Ukraine,
e-mail: rvy90593-eds@lll.kpi.ua;
batrakln5@gmail.com (Corresponding Author);
e.o.abakumova@gmail.com

How to cite this article:
Romashko V.Y., Batrak L.M., Abakumova O.O. Obtaining the maximum power from the source using step-up and step-down type pulse regulators that work on battery. *Electrical Engineering & Electromechanics*, 2024, no. 3, pp. 44-47. doi: https://doi.org/10.20998/2074-272X.2024.3.06

UDC 621.3.011 https://doi.org/10.20998/2074-272X.2024.3.07

Yu.M. Vasetsky

Analytical determination of a quasi-stationary electromagnetic field created by magnetic moments and eddy currents in conducting half-space

Aim. *Study of the distribution of a three-dimensional alternating quasi-stationary electromagnetic field at the surface of conducting half-space with strong skin-effect, the source of which is an arbitrarily oriented magnetic moment.* ***Methodology****. The expressions for non-uniform electromagnetic field with strong skin effect are used for the analysis, which is based on the found exact analytical solution of the general three-dimensional problem and the use of expansion into asymptotic series with respect to a small parameter that is proportional to the ratio of the field penetration depth to the distance between the sources of the external field and the surface of body. Specific expressions at the surface are completely determined by the known field of external sources. In this work, the external magnetic moment field is used.* ***Results****. For strong skin effect, expressions for the electric and magnetic field strength are obtained separately for the components of the magnetic moment oriented perpendicularly and parallel to the flat surface between the dielectric and conducting areas. The features of the electromagnetic field distribution are analyzed depending on the value of introduced small parameter. The results are presented for the module and phase shift of the field strength with respect to the phase of the external field source.* ***Originality****. The expressions found for the electromagnetic field appear to be more general than the use of closed contours with alternating current, since they extend types of external field sources and allow the use of the superposition method instead of integration over the entire contour.* ***Practical value****. The found specific analytical expressions of the electromagnetic field at the surface for the external field of magnetic moments significantly simplify the solution of the problems, since they do not require additional solution of the field equations.* References 20, figures 8.

Key words: **three-dimensional quasi-stationary electromagnetic field, strong skin effect, external field of magnetic moments, asymptotic method, analytical solution**.

Мета*. Дослідження в умовах прояву сильного скін-ефекту розподілу на поверхні електропровідного півпростору тривимірного змінного квазістаціонарного електромагнітного поля, джерелом зовнішнього поля якого є довільно орієнтований магнітний момент.* ***Методологія****. Для аналізу використаний аналітичний розв'язок загальної тривимірної задачі для випадку неоднорідного електромагнітного поля при сильному скін-ефекті і використанні розкладання в асимптотичні ряди по малому параметру, який пропорційний відношенню глибини проникнення поля до відстані між джерелами зовнішнього поля і поверхнею тіла. Конкретні вирази на поверхні повністю визначаються відомим полем зовнішніх джерел, в якості яких використовується поле магнітного моменту.* ***Результати****. Для сильного скін-ефекту отримано вирази для напруженостей електричного і магнітного полів окремо для компонентів магнітного моменту, що орієнтовані перпендикулярно і паралельно до плоскої поверхні між діелектричною і електропровідною областями. Проаналізовано особливості розподілу електромагнітного поля в залежності від величини введеного малого параметру, Результати представлено для модулів і зсуву фаз компонентів напруженостей полів відносно фази джерела зовнішнього поля.* ***Оригінальність****. Знайдені вирази для електромагнітного поля уявляються більш загальними, ніж використання замкнених контурів зі зміннім струмом, оскільки розширюють види джерел зовнішнього поля, що враховуються, і дозволяють використати метод суперпозиції замість інтегрування по всьому контуру.* ***Практична цінність****. Знайдені конкретні аналітичні вирази електромагнітного поля на поверхні для зовнішнього поля магнітних моментів значно спрощують вирішення конкретних задач, оскільки не потребують для цього додаткового розв'язку рівнянь поля.* Бібл. 20, рис. 8.

Ключові слова: **тривимірне квазістаціонарне електромагнітне поле, сильний скін-ефект, зовнішнє поле магнітних моментів, асимптотичний метод, аналітичний розв'язок.**

Introduction. The interaction of an alternating electromagnetic field with electrically conducting bodies is accompanied by the manifestation of the skin effect. In high-frequency and short-time pulsed electromagnetic processes, there is a strong skin effect, then the current and electromagnetic field are concentrated in the thin surface layer of the body. In this case, the formulation of mathematical models for calculating the electromagnetic field is significantly simplified. The simplest mathematical model of the ideal skin effect can be imagined, when the characteristic dimensions of the conducting body L significantly exceed the field penetration depth δ. Here, it is enough to consider a stationary problem for a body with ideal electrical conductivity and, accordingly, zero field penetration depth $\delta \to 0$ [1, 2]. In this case, the normal component of the magnetic and the tangential component of the electric fields are equal to zero.

The further development of approximate models of the electromagnetic field penetration into conducting medium at $\delta \neq 0$ is associated, first of all, with studies based on the impedance boundary condition [3, 4].

In the mathematical model proposed by M. Leontovich back in the middle of the 20th century [3], the model with ideal electrical conductivity remained the starting point. From this model, the magnetic field strength tangent to the surface of the conducting body was determined. The bounded depth of field penetration was calculated using the concept of the impedance boundary condition, where the magnetic field strength at the surface of the body is related to the electric field strength by a specific ratio. It is assumed that electromagnetic field locally penetrates into metallic body in the same way as uniform field penetrates into conducting half-space. The model is approximate and one of the issues is determining the limits of the model's application. A detailed analysis of many years of research in the development of the concept of the impedance boundary condition is presented, for example, in [5, 6].

The development of effective methods for solving 3D problems of electromagnetic field theory in a fairly general formulation is a topical problem, despite significant progress in the use of numerical calculation methods. Analytical methods of solving similar problems still have a certain appeal for theoretical research. This is due to their positive aspects. First, there is a wide range of objects where specialized analytical or combined numerical and analytical approaches remain effective.

Such objects include, in particular, systems whose geometric features are characterized by a different nature of the field change in space – a rapid change near concentrated sources of the field or near the interface between media and a much slower one in another region of space with a much larger volume. Secondly, the availability of an analytical solution makes it possible to obtain general features of the formation of a 3D field, and make it possible to carry out an in-depth analysis of the causes and features of physical processes. There is also an opportunity to develop well-grounded approaches to 3D modeling of complex electromagnetic systems. Finally, analytical solutions provide a certain set of exactly solvable problems, which can be a benchmark for comparison when developing other methods for calculating systems of more complex geometry, where obtaining analytical solutions is impossible.

The book [7] presents the exact analytical solution obtained by the author and published in separate articles for alternating and pulsed electromagnetic fields created by a system of spatial contours with a current of arbitrary configuration, located near a magnetized conducting body with a flat surface, where eddy currents are induced. The solution for closed contours was found in the integral form for vector and scalar potentials, magnetic and electric field strengths in dielectric and conducting media without restrictions on the geometry of the contours, medium properties and field frequency. The obtained solution made it possible, in particular, to establish the following general features of field formation [8]. The components of current density and electric field strength, perpendicular to the surface, have a zero value in the entire conducting half-space. The result is also a boundary condition for the normal component of the electric field strength in the dielectric medium, which is completely determined by the known field of external sources. Another consequence of the exact solution is the conclusion that non-uniform electromagnetic field, when penetrating into conducting half-space, always decays with depth faster than uniform field.

Simplification of computational procedures is also necessary for the analytical solution, especially when solving optimization and inverse problems of field theory. The calculation is simplified significantly not only for ideal skin effect at $\delta \to 0$, but also for the strong skin effect in its extended sense, when the distance r between the sources of external field and observation points at the body surface is limited. An effective technique is the expansion of potentials and field vectors into an asymptotic series [9, 10] with respect to the small parameter $\varepsilon = \mu\delta / \left(\sqrt{2r}\right) < 1$, where μ is the relative magnetic permeability of the conducting medium. This representation also allows to draw further conclusions regarding the general features of the 3D electromagnetic field formation. In particular, it was established that at the flat boundary the field strength is determined not only by the value of the components of known external field, as in the model of ideal skin effect, but also by its derivatives along the coordinate perpendicular to the media interface. Thus, the effect of field non-uniformity at the surface is determined, and the distribution of the field at the surface does not require the solution of additional boundary value problems.

The peculiarity of the applied power asymptotic series of the Poincaré type [11, 12] is the limited number of their members N. This is due to the error of determining each term of the series, which increases with the increase in the value of the parameter ε and the number of the series term n. Therefore, there is such a number of terms at which the error is minimal and further increasing their number only increases the error. In [9, 10], issues of the limits of application of the asymptotic method for the general case of an arbitrary external field, error analysis, determine of the number of terms of limited series, as well as their optimal number are presented. In addition, when calculating the value of the field due to the error in determining the terms of the series, their values are taken into account with a weight function, the value of which depends on the error estimate.

In [9], in particular, it is shown that calculations with sufficient accuracy can be performed for the value of the small parameter $\varepsilon \le 0.3$. This condition is fulfilled in many technological processes, where it is necessary to ensure a strong interaction between the electromagnetic field of inductor and the conducting body. For example, in devices for high-frequency induction heating of flat metal products [13, 14], the distance between the inductor and the body usually does not exceed h = 3 cm. In this case, at ε = 0.3, for example, for brass products (μ = 1, $\gamma = 1.25 \cdot 10^7$ Ω^{-1} m^{-1}) at h = 0.03 m calculations can be performed for frequencies $f = \omega/2\pi \ge 125$ Hz. In equipment for exposure to a strong field to improve the mechanical properties of metal products [15, 16], the distance is h = 0.01-0.02 m. In this case, at h = 0.01 m for aluminum (μ = 1, $\gamma = 3.71 \cdot 10^7$ Ω^{-1} m^{-1}) permissible frequencies are $f \ge 380$ Hz. It should be noted that the devices for the technological processes indicated here are examples of objects in the development of which the calculation methods under investigation can be used.

Sources of the external field can be not only contours with alternating current. In the general case, sources of the external field can also be represented by a system of magnetic moments [17]. This representation is even more convenient, since in the quasi-stationary approximation the contour must be closed and cannot be divided into parts [18]. At the same time, the principle of superposition is valid for the magnetic field of the system of magnetic moments. Each magnetic moment $\boldsymbol{m}$ is a individual field source whose vector $\boldsymbol{A}$ ($\nabla \cdot \boldsymbol{A} = 0$) and scalar φ_m magnetic potentials in a non-magnetic medium

$$\boldsymbol{A} = \frac{\mu_0}{4\pi}\frac{\boldsymbol{m}\times\boldsymbol{r}}{r^3} = -\frac{\mu_0}{4\pi}\boldsymbol{m}\times\nabla\frac{1}{r}; \qquad \varphi_m = \frac{\boldsymbol{m}\cdot\boldsymbol{r}}{4\pi r^3} = -\frac{1}{4\pi}\boldsymbol{m}\cdot\nabla\frac{1}{r} \tag{1}$$

determine the same magnetic field strength $\boldsymbol{H}$

$$\boldsymbol{H} = \frac{1}{\mu_0}\nabla\times\boldsymbol{A} = -\nabla\varphi_m = \frac{1}{4\pi}\left[\frac{3\boldsymbol{m}\cdot\boldsymbol{r}}{r^4}\frac{\boldsymbol{r}}{r} - \frac{\boldsymbol{m}}{r^3}\right], \tag{2}$$

here the vector $\boldsymbol{r}$ is directed from the point of source (moment) to the observation point.

Each contour with current I_0, for the electromagnetic field of which calculation expressions are given in [7], can be replaced by a surface S resting on a closed contour with field sources in the form of a double layer of magnetic charges (magnetic moments) $d\boldsymbol{m} = \mu_0 I_0 dS\boldsymbol{n}$, where $\mu_0 I_0 \boldsymbol{n}$ is the surface density vector of the distributed magnetic moment directed along the normal $\boldsymbol{n}$ to the surface (Fig. 1).

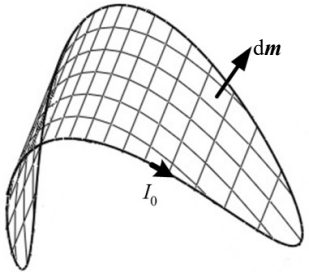

Fig. 1. Replacement of a contour with a current by the surface of a double layer of magnetic charges (magnetic moments)

Now, in contrast to the found expressions for the contour, the calculations allow the application of the principle of superposition with the summation of the fields created by the system of magnetic moments covering the surface *S*. As the distance from the source of the field to the observation point increases, the number of magnetic moments that provide the required accuracy decreases. At a considerable distance, the field source can be represented by one total magnetic moment that creates the field (1), (2).

Currently, despite the fairly general nature of the use of the field of magnetic moments, there are not enough specific studies of their application to represent the field of external sources in the asymptotic method of calculating the electromagnetic field. Therefore, the study of the possibility of their application in the practice of analytical calculations of 3D quasi-stationary fields is a topic problem.

The goal of the work is to obtain specific calculation relationships and to study the features of the distribution for non-uniform quasi-stationary electromagnetic field at the surface of conducting half-space created by external source in the form of one magnetic moment and eddy currents in conducting medium which change in time according to a sinusoidal law under the conditions of strong skin effect.

Mathematical model. It is assumed that near the conducting half-space with electrical conductivity γ and relative magnetic permeability μ at a distance h in dielectric non-magnetic medium there is a magnetic moment $\dot{\boldsymbol{m}} = \dot{\boldsymbol{m}}_{\parallel} + \dot{\boldsymbol{m}}_{\perp}$ that varies in time according to a sinusoidal law with cyclic frequency ω (Fig. 2). Here and in the below, complex amplitudes are denoted by a dot above the corresponding symbol.

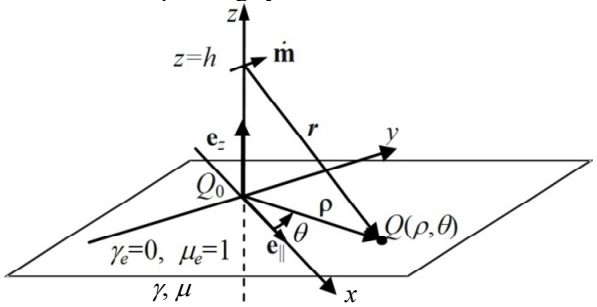

Fig. 2. The location of the magnetic moment nearby conducting half-space

In the general case, the magnetic moment is arbitrarily oriented relative to the media interface: the component $\dot{\boldsymbol{m}}_{\parallel} = \dot{m}_{\parallel}\boldsymbol{e}_{\parallel}$ is oriented parallel to the surface along the unit vector $\boldsymbol{e}_{\parallel}$; the component $\dot{\boldsymbol{m}}_{\perp} = \dot{m}_z \boldsymbol{e}_z$ is oriented along the unit vector normal to the surface $\boldsymbol{e}_z$.

The solution of the problem for the electromagnetic field at the surface between dielectric and conducting areas based on the exact solution for the system: «an arbitrary spatial contour with sinusoidal current as a source of the external field – a conducting half-space» [7]. It was shown in [8] that in the case of strong skin effect in the extended sense when $\varepsilon < 1$, taking into account the external field non-uniformity at the surface of conducting body with flat surface, the electric and magnetic field strengths are completely determined by the magnetic field strength of external sources $\dot{\boldsymbol{H}}_0$. The resulting expressions in the form of expansion into limited asymptotic series for the tangential and normal components of the electric $\dot{\boldsymbol{E}} = \dot{\boldsymbol{E}}_{\parallel} + \dot{\boldsymbol{E}}_{\perp}$ and magnetic $\dot{\boldsymbol{H}} = \dot{\boldsymbol{H}}_{\parallel} + \dot{\boldsymbol{H}}_{\perp}$ field strengths are as follows:

- Tangential components of fields that are the same at the surface in dielectric and conducting media:

$$\dot{\boldsymbol{E}}_{\parallel}(z=0) = \zeta \sum_{n=0}^{N} 2a_n(\mu)\left(\frac{\varepsilon r}{\sqrt{j}}\right)^n \left\{\frac{\partial^{(n)}}{\partial z^n}\boldsymbol{e}_z \times \dot{\boldsymbol{H}}_{0\parallel}\right\}\Bigg|_{z=0}; \quad (3)$$

$$\dot{\boldsymbol{H}}_{\parallel}(z=0) = -\sum_{n=0}^{N+1} 2a_{n-1}(\mu)\left(\frac{\varepsilon r}{\sqrt{j}}\right)^n \left\{\frac{\partial^{(n)}\dot{\boldsymbol{H}}_{0\parallel}}{\partial z^n}\right\}\Bigg|_{z=0}, \quad (4)$$

where $\zeta = p/\gamma$ is the surface impedance, $p = \sqrt{j\omega\mu\mu_0\gamma}$ is the propagation constant, j is the imaginary unit. In (3), (4) it is taken into account that $\varepsilon r/\sqrt{j} = \mu/p$. The $a_n(\mu)$ are the coefficients of the Taylor series expansion of the function

$$1/w = \sum_{n=0}^{\infty} a_n(\mu)\left(\chi/\sqrt{j}\right)^n, \text{ where } w(\chi) = \frac{\chi}{\sqrt{j}} + \sqrt{1+\left(\frac{\chi}{\mu\sqrt{j}}\right)^2},$$

it is assumed $a_{-1} = -1$. The number N of terms of the limited asymptotic series is determined, first of all, by the value of small parameter ε [9, 10].

- Normal components of the electric $\dot{\boldsymbol{E}}_{\perp}^{+}$, $\dot{\boldsymbol{E}}_{\perp}^{-}$ and magnetic $\dot{\boldsymbol{H}}_{\perp}^{+}$, $\dot{\boldsymbol{H}}_{\perp}^{-}$ fields at different sides of the surface in the dielectric (z = 0+0) and conducting (z = 0–0) media are different.

At any point of the electrically conducting medium, the component of the electric field intensity directed perpendicular to the surface is equal to zero for arbitrary values of the parameter ε and then at the surface of the body in dielectric medium the electric field strength is completely determined by the induced electric field of external sources which is considered as known

$$\dot{\boldsymbol{E}}_z(z<0) = 0; \quad \dot{E}_{\perp}^{+} = -2j\omega\dot{A}_{0z}(z=0), \quad (5)$$

where $\dot{A}_{0z}(z=0)$ is the normal component of the vector potential of the magnetic field of external sources.

Taking into account the continuity of the normal component of the magnetic flux density, the expressions for the normal components of the strength on different sides of the surface are

$$\dot{\boldsymbol{H}}_{\perp}^{+} = \mu \dot{\boldsymbol{H}}_{\perp}^{-} = -\sum_{n=0}^{N} 2a_n(\mu)\left(\frac{\varepsilon\, r}{\sqrt{j}}\right)^{n+1}\left\{\frac{\partial^{(n+1)}\dot{\boldsymbol{H}}_{0\perp}}{\partial z^{n+1}}\right\}\Bigg|_{z=0}. \quad (6)$$

The zero term of the asymptotic series in (3), (4) corresponds to approximate model in which it is assumed that the field at the surface is uniform and the normal component of the magnetic field strength is zero. At the same time, the value of the tangential magnetic field at the surface corresponds to the magnetic field at the surface of a body with ideal conductivity and, accordingly, zero field penetration depth $\delta \to 0$.

Expressions (3) – (6) take into account the non-uniformity of the field of external sources. This is evidenced by the presence in the expressions of derivatives with respect to coordinates directed perpendicular to the surface of interface media. The influence of the non-uniformity of the electromagnetic field for tangential components is revealed in terms of the series with numbers $n \geq 1$. The normal component of the external field is already taken into account in the first term of the asymptotic series.

The given expressions of electromagnetic field distribution are approximate. In the calculation examples presented below, the value of the small parameter does not exceed the assumed value $\varepsilon = 0.3$. The number of terms of the asymptotic series was equal to four ($N = 3$). At the same time, according to the estimates made in [9, 10], the relative error in determining the field strengths did not exceed the value $\Delta_N = 5\cdot 10^{-3}$.

The electric and magnetic components of the field at the flat surface of the conducting body are calculated below separately according to expressions (3), (4), (6) for the components of the magnetic moment oriented along the normal and parallel to the surface.

Electromagnetic field of magnetic moment $\boldsymbol{m}_{\perp}$ oriented along the normal to the surface. The external magnetic field of the magnetic moment $\dot{\boldsymbol{m}}_{\perp} = \dot{m}_z \boldsymbol{e}_z$ has axial symmetry, and it is convenient to write its expression in the cylindrical coordinate system (ρ, θ, z) with standard basis vectors ($\boldsymbol{e}_{\rho}$, $\boldsymbol{e}_{\theta}$, $\boldsymbol{e}_z$) directed along the corresponding coordinates. Then, in accordance with (2), the magnetic moment creates the following field at arbitrary point of the space

$$\dot{\boldsymbol{H}}_0 = \frac{1}{4\pi}\left[3\frac{(\dot{\boldsymbol{m}}\cdot\boldsymbol{r})\boldsymbol{r}}{r^5} - \frac{\dot{\boldsymbol{m}}}{r^3}\right] = \\ = \frac{\dot{m}_z}{4\pi}\left[3\frac{(z-h)^2}{r^5} - \frac{1}{r^3}\right]\boldsymbol{e}_z + \frac{\dot{m}_z}{4\pi}3\frac{(z-h)\rho}{r^5}\boldsymbol{e}_{\rho}. \quad (7)$$

The parameter ε depends on the distance r between the source and observation points. At the point Q_0 at the surface directly below the magnetic moment the distance $r = h$ is minimal and parameter ε takes its maximum value. Accordingly, at this point the error of the approximate calculation method is the largest.

For further analysis, we will use the single maximum value of the small parameter $\varepsilon_m = \mu\delta/\left(h\sqrt{2}\right) = \varepsilon\left(r/h\right)$. Using the h and ε_m values, the surface impedance is found to be $\varsigma = \sqrt{j\omega\mu_0 h\varepsilon_m}$.

By substituting the value of the external magnetic field (7) into the expressions for the field strengths (3), (4), (6), we obtain their distribution along the radial coordinate ρ at the surface of the conducting body, depending on the value of the small parameter ε_m, as well as the height of the location h and cyclic field frequency ω.

The normalized values of the electric and magnetic field strengths are entered as follows:

$$\dot{\boldsymbol{E}}_{\parallel}^{*} = \dot{\boldsymbol{E}}_{\parallel}\Big/\left(\frac{\mu_0\dot{m}_z\omega}{4\pi h^2}\right) \quad \text{and} \quad \dot{\boldsymbol{H}}^{*} = \dot{\boldsymbol{H}}\Big/\left(\frac{\dot{m}_z}{4\pi h^3}\right).$$

The expression for the normalized value of the tangential component of the electric field strength takes the following form:

$$\dot{\boldsymbol{E}}_{\parallel}^{*} = \boldsymbol{e}_{\theta}\sqrt{j}\,6\frac{\rho}{h}\varepsilon_m\sum_{n=0}^{N}a_n\left(\frac{\varepsilon_m}{\sqrt{j}}\right)^{n}h^{n+4}\frac{\partial^{(n)}}{\partial z^n}\left(\frac{z-1}{r^5}\right)\Bigg|_{z=0}. \quad (8)$$

In turn, the normalized values of the tangential and normal to the surface components of the magnetic field strength are revealed

$$\dot{\boldsymbol{H}}_{\parallel}^{*} = -\boldsymbol{e}_{\rho}\,6\frac{\rho}{h}\sum_{n=0}^{N+1}a_{n-1}\left(\frac{\varepsilon_m}{\sqrt{j}}\right)^{n}h^{n+4}\frac{\partial^{(n)}}{\partial z^n}\left(\frac{z-1}{r^5}\right)\Bigg|_{z=0}; \quad (9)$$

$$\dot{\boldsymbol{H}}_{\perp}^{*} = \boldsymbol{e}_z\,2\sum_{n=0}^{N}a_n\left(\frac{\varepsilon_m}{\sqrt{j}}\right)^{n+1}h^{n+4}\frac{\partial^{(n+1)}}{\partial z^{n+1}}\left(\frac{2(z-1)^2-\rho^2}{r^5}\right)\Bigg|_{z=0}. \quad (10)$$

From the presented dependencies, it can be seen that in this case of axisymmetric electromagnetic field, the electric field strength has only one azimuthal component, and the magnetic field strength is represented by radial and normal components.

In Fig. 3–5, the dependencies of the distribution of the normalized components of the complex-value amplitudes of the electric and magnetic field strengths are given as

$$\dot{E}_{\theta}^{*} = \pm\left|\dot{E}_{\theta}^{*}\right|\exp\left(j\varphi_{E\theta}\right) \quad \text{and} \quad \dot{H}_{k}^{*} = \pm\left|\dot{H}_{k}^{*}\right|\exp\left(j\varphi_{Hk}\right)$$

where $k = \rho, z$. The sign «–» before the module of the complex-value amplitude is used to indicate the opposite to the selected direction of the field vector component. In this case, at the same time, the phase shift angle relative to the phase of the magnetic moment changes by π.

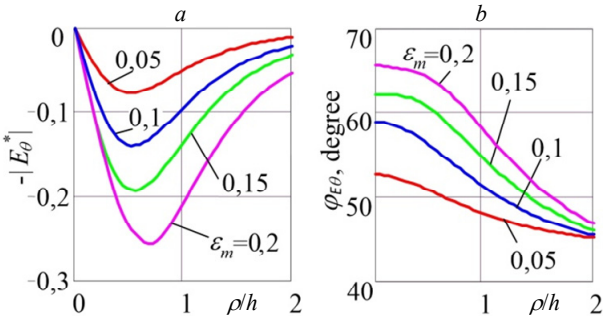

Fig. 3. Distribution along the surface of the module $-\left|\dot{E}_{\theta}^{*}\right|$ (*a*) and the phase shift angle $\varphi_{E\theta}$ (*b*) of the tangential component of the electric field strength for the source $\dot{\boldsymbol{m}}_{\perp}$

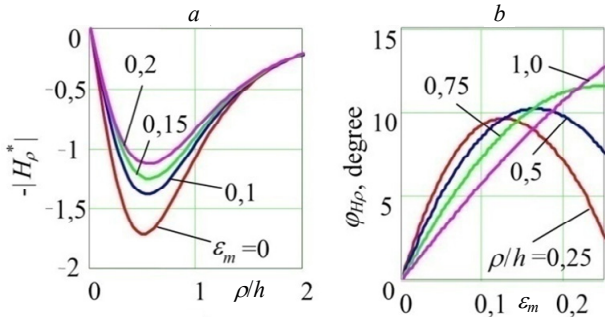

Fig. 4. Radial component of the magnetic field strength: dependence of the module $-\left|\dot{H}^*_\rho\right|$ on the radial coordinate (*a*); dependence of the phase shift angle $\varphi_{H\rho}$ on the parameter ε_m (*b*)

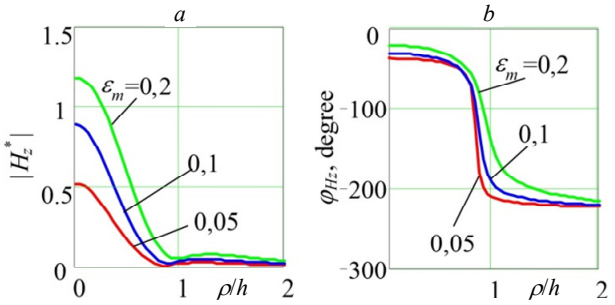

Fig. 5. Distribution along the surface of the module $\left|\dot{H}^*_z\right|$ (*a*) and phase shift angle φ_{Hz} (*b*) of the normal component of magnetic field strength

For an ideal skin effect at $\varepsilon_m \to 0$, the tangential strength of the electric field, as well as the normal component of the magnetic field, are equal to zero. In this case, the tangential strength of the magnetic field is equal to double value of the tangential component of external magnetic field [9]. Such field is used in a simplified model of the diffusion of a locally uniform field into a conducting body. In this case of the field of the magnetic moment, the phase shift is equal to zero, the tangential component is directed towards the radial coordinate (9), reaches its maximum value at the points of the circle of radius $\rho = h/2$ and is equal to

$$\dot{H}^*_{\|\max} = -6 \cdot 0{,}5 \Big/ \sqrt{0{,}5^2 + 1} = -1{,}717 \cdot$$

From the data presented in Fig. 3–5 it can be seen that with an increase in the parameter ε, that is, with increase in the influence of the external electromagnetic field non-uniformity during its diffusion into the conducting half-space, the character of the field distribution over the surface changes.

The tangential component of the electric field (Fig. 3) is no longer zero and increases with the growth of the parameter ε. On the contrary, the tangent component of the magnetic field strength decreases with increasing ε. At the same time, as can be seen from Fig. 4,*b*, the dependence on the parameter ε of the phase shift has a non-monotonic character.

For non-uniform field at the bounded thickness of the skin layer, that is, in the case of $\varepsilon > 0$, the normal component of the magnetic field strength is no longer zero. Note that even for the parameter $\varepsilon \cong 0.2$, the normal component $\left|\dot{H}^*_z\right|$ becomes commensurate with the tangential component $\left|\dot{H}^*_\rho\right|$ and neglecting this field component in simplified models can lead to significant calculation errors. We also note that the normal component of the magnetic field becomes insignificant at the distance of $\rho/h \geq 0.8$. In the area $\rho/h \geq \approx 0.8 \div 1.0$, the phase shift of the normal component of field changes sharply by approximately 180°. This means that in this area there is change in the direction of normal component of field compared to the direction in the area $\rho/h \leq 0.8$.

Note also that the magnetic field is elliptically polarized. This is evidenced by the fact that, as can be seen from Fig. 4,*b* and Fig. 5,*b* that the phases of the mutually perpendicular magnetic field components $\dot{H}^*_\rho$ and $\dot{H}^*_z$ are differ from each other.

Electromagnetic field of magnetic moment $\boldsymbol{m}_\|$, oriented parallel to the surface. In contrast to the previous case of normally oriented magnetic moment, the magnetic field of magnetic moment $\dot{\boldsymbol{m}}_\| = \dot{m}_\| \boldsymbol{e}_\|$ oriented parallel to the surface of media interface is convenient to write in the Cartesian coordinate system (x, y, z), the x and y axes of which lie at the surface, and the x axis is directed along the projection of the vector $\dot{\boldsymbol{m}}_\|$ to flat surface (Fig. 2). The standard basis vectors of the coordinate system are ($\boldsymbol{e}_x$, $\boldsymbol{e}_y$, $\boldsymbol{e}_z$).

The external magnetic field of the considered magnetic moment in the Cartesian coordinate system has all three components

$$\dot{\boldsymbol{H}}_0 = \frac{\dot{m}_\|}{4\pi}\left[\frac{2x^2 - y^2 - (z-h)^2}{r^5}\boldsymbol{e}_x + \frac{3xy}{r^5}\boldsymbol{e}_y + \frac{x(z-h)}{r^5}\boldsymbol{e}_z\right]. \quad (11)$$

After substituting (11) into expressions (3), (4), (6) for the electric and magnetic field strengths at the surface of media interface, we obtain

$$\dot{\boldsymbol{E}}_\| = \frac{\mu_0 \dot{m}_\| \omega}{4\pi h^2}\sqrt{j}\,2\varepsilon_m \times$$

$$\times\left\{\begin{aligned}&\boldsymbol{e}_y \sum_{n=0}^{N} a_n \left(\frac{\varepsilon_m}{\sqrt{j}}\right)^n h^{n+3} \frac{\partial^{(n)}}{\partial z^n}\left(\frac{2x^2 - y^2}{r^5} - \frac{(z-1)^2}{r^5}\right)\Bigg|_{z=0} - \\ &-\boldsymbol{e}_x \sum_{n=0}^{N} a_n \left(\frac{\varepsilon_m}{\sqrt{j}}\right)^n h^{n+3} \frac{\partial^{(n)}}{\partial z^n}\left(\frac{3xy}{r^5}\right)\Bigg|_{z=0}\end{aligned}\right\}; \quad (12)$$

$$\dot{\boldsymbol{H}}_\| = \frac{\dot{m}_\|}{4\pi h^3}\,2\times$$

$$\times\left\{\begin{aligned}&-\boldsymbol{e}_x \sum_{n=0}^{N} a_{n-1} \left(\frac{\varepsilon_m}{\sqrt{j}}\right)^n h^{n+3} \frac{\partial^{(n)}}{\partial z^n}\left(\frac{2x^2 - y^2}{r^5} - \frac{(z-1)^2}{r^5}\right)\Bigg|_{z=0} + \\ &+\boldsymbol{e}_y \sum_{n=0}^{N} a_{n-1} \left(\frac{\varepsilon_m}{\sqrt{j}}\right)^n h^{n+3} \frac{\partial^{(n)}}{\partial z^n}\left(\frac{3xy}{r^5}\right)\Bigg|_{z=0}\end{aligned}\right\}; \quad (13)$$

$$\dot{\boldsymbol{H}}_\perp = \frac{\dot{m}_\|}{4\pi h^3}\boldsymbol{e}_z\, 2\sum_{n=0}^{N} a_n \left(\frac{\varepsilon_m}{\sqrt{j}}\right)^{n+1} h^{n+4} \frac{\partial^{(n+1)}}{\partial z^{n+1}}\left(\frac{x(z-1)}{r^5}\right)\Bigg|_{z=0}. \quad (14)$$

In this case, the electromagnetic field at the surface of the half-space is symmetrical about the x axis. The components of the electric $\dot{E}_{\|x}$ and magnetic $\dot{H}_{\|y}$ field

strengths have even symmetry, the components $\dot{E}_{\|y}$, $\dot{H}_{\|x}$, $\dot{H}_{\perp z}$ of the electromagnetic field have odd symmetry relative to the x axis.

An understanding of the electromagnetic field formation can be obtained if we first consider the ideal skin effect. In this case, it is sufficient to consider the formation of a magnetic field only in dielectric medium. The method of mirror images can be used to calculate the magnetic field of the moment located above the media interface. In the case of ideal skin effect, the general solution of the problem for finding the magnetic field is reduced to taking into account the current of the source and mirrored from the surface of the contour with the oppositely directed current [7]. This representation for magnetic moments, in contrast to currents, is reduced to the same direction of the tangential components and the opposite direction of the normal components of the initial $\boldsymbol{m}$ and mirrored $\boldsymbol{m}_1$ moments [17] (Fig. 6,*a*).

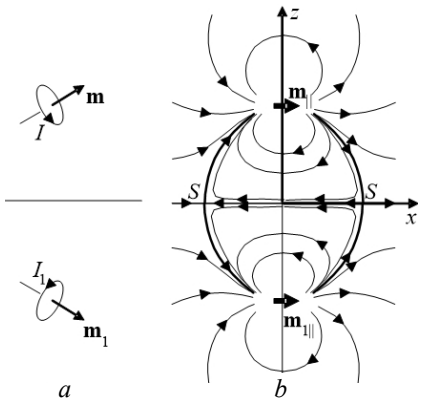

Fig. 6. The structure of the magnetic field of the magnetic moment located over half-space with ideal conductivity

The structure of the magnetic field of two equally directed magnetic moments $\boldsymbol{m}_{\|}$ and $\boldsymbol{m}_{1\|}$ (Fig. 6,*b*) is convenient to analyze by defining critical points [19, 20] at which the vector field is zero. Let's find such points in the vertical plane $y = 0$. The field component perpendicular to this plane is zero $H_y = 0$. Due to the symmetry of the two magnetic moments, the field component perpendicular to the x axis and directed along the z axis is also zero $H_z = 0$. It remains to find the zero value of the H_x component on the x axis. Both magnetic moments have the same H_x field components. As a result, we get for this component

$$H_x = \boldsymbol{H}\cdot\boldsymbol{e}_x = 2\frac{1}{4\pi}\left[\frac{3(\boldsymbol{m}_{\|}\cdot\boldsymbol{r})}{r^4}\frac{(\boldsymbol{r}\cdot\boldsymbol{e}_x)}{r} - \frac{\boldsymbol{m}_{\|}\cdot\boldsymbol{e}_x}{r^3}\right] = \\ = \frac{m_{\|}}{2\pi}\left(\frac{3x^2}{r^5} - \frac{1}{r^2}\right) = \frac{m_{\|}}{2\pi}\frac{2x^2 - h^2}{r^5}. \quad (15)$$

It follows from this that the critical points of the field in the plane $y = 0$ are located at the points $x = \pm h/\sqrt{2}$ of the axis parallel to the direction of the magnetic moments. These are critical points of the hyperbolic type (saddle) S, through which the separatrixs pass – the field lines (shown by bold lines), which separate areas with different character of field formation. In Fig. 6,*b* for clarity, magnetic field lines are shown not only above the surface of the body, but also in the area $z < 0$, where the field is absent in the case of an ideal skin effect.

Figure 7 illustrates the dependence of the various components of the magnetic field strength on the coordinates at the plane and on the value of the small parameter ε_m, the difference from zero of which indicates the influence of the bounded value of the penetration depth of the non-uniform electromagnetic field. In all figures, the dependencies for the ideal skin effect $\varepsilon = 0$ are shown by bold curves.

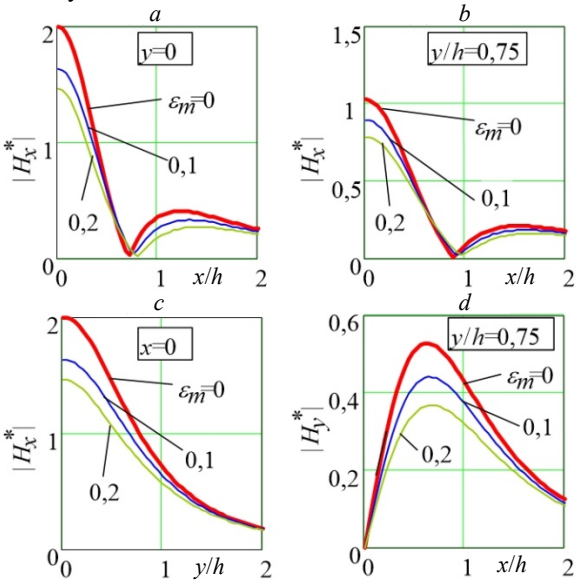

Fig. 7. Distribution of the tangential component of the magnetic field at the media interface for the source $\dot{\boldsymbol{m}}_{\|}$

As can be seen from Fig. 6,*b*, at $\varepsilon_m = 0$, the tangential component of the magnetic field strength at the surface of the body changes direction when passing through critical points S. This feature of the field distribution is also shown in Fig. 7,*a*. When $\varepsilon_m > 0$, when the eddy currents no longer flow along the surface, but occupy a certain layer of finite thickness, a general tendency to decrease the magnetic field is observed. Here, the position of the critical hyperbolic point practically does not change.

When moving away from the plane $y = 0$, the longitudinal (parallel to the direction of the magnetic moment) component of the magnetic field strength decreases (Fig. 7,*c*). The zero value of this component still exists. However, not all components of the field strength are equal to zero at the corresponding points of the surface when $y \neq 0$. The tangential strength component perpendicular to the x axis will be different from zero (Fig. 7,*d*). This feature is illustrated in Fig. 8.

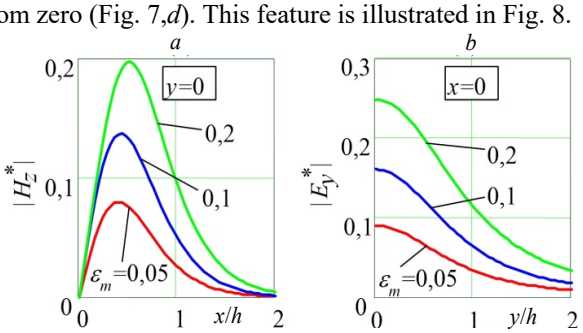

Fig. 8. Distribution over the surface of the modules of the normal component of the magnetic field (*a*) and the tangential component of the electric field (*b*) for the source $\boldsymbol{m}_{\|}$

The normal component of the magnetic field strength (Fig. 8,*a*) remains insignificant compared to the maximum value of the tangential component of the magnetic field (Fig. 7,*a*). But in the area near critical points of the field, the normal component becomes dominant.

The electric field strength under the external field of the horizontal magnetic moment (Fig. 8,*b*) is comparable in value to the electric field created by the action of the magnetic moment oriented normal to the surface (Fig. 5).

Conclusions. From the presented results for both the normally oriented magnetic moment and the moment directed parallel to the media interface, it follows that mathematical models with ideal skin effect at $\delta \to 0$ have a limited scope of application. In the case of non-uniform field of external sources, when the field penetration depth is commensurate with the distance between the source and conducting body, it is necessary to use more correct mathematical models for electromagnetic field. Analytical approaches using the expansion of the field into asymptotic series based on the introduced small parameter ε are convenient way of describing the electromagnetic field.

The specific expressions found for the electromagnetic field at the surface between the dielectric and conducting half-space under the action of arbitrarily oriented magnetic moment appear to be more general than the use of closed contours with alternating current, since they expand the types of considered external field sources and allow the use of the superposition method instead of integration over the whole contour.

In cases that allow the use of the conducting half-space model with strong skin effect, specific expressions for the field at the surface are found, which are completely determined by the known field of external sources (in this case, the field of magnetic moments). This significantly simplifies the solution of the corresponding problems, since there is no need to separately solve the field equations.

Further development of research can be aimed at determining the field under the action of other types of sources of a non-uniform external field, finding the impedance boundary condition for such fields, and finally, as a general program, spreading the applied approach to systems with curvilinear surfaces of media interface.

Acknowledgment. The work was carried out under the project «Development of theory and modeling of transient electrophysical processes in conducting and dielectric media of pulsed electromagnetic systems» (code: Barrier-3), funded by the National Academy of Sciences of Ukraine.

Conflict of interest. The author declares no conflict of interest.

REFERENCES

1. Landau L.D., Lifshitz E.M. *Electrodynamics of Continuous Media*. Elsevier Ltd, 1984. 475 p. doi: https://doi.org/10.1016/B978-0-08-030275-1.50024-2.

2. Simonyi K. *Foundation of Electrical Engineering*. Elsevier Ltd, 1963. 865 p. doi: https://doi.org/10.1016/c2013-0-02694-1.

3. Leontovich M.A. On the Approximate Boundary Conditions for Electromagnetic Field on the Surface of Highly Conducting Bodies. *Radio Wave Propagation Studies*, 1948, pp. 5-12. (Rus).

4. Yuferev S., Ida N. *Surface Impedance Boundary Conditions: A Comprehensive Approach*. CRC Press, 2018. 412 p. doi: https://doi.org/10.1201/9781315219929.

5. Berdnik S.L., Penkin D.Y., Katrich V.A., Penkin Y. M., Nesterenko M.V. Using the concept of surface impedance in problems of electrodynamics (75 years later). *Radio Physics and Radio Astronomy*, 2014, vol. 19, no. 1, pp. 57-80. doi: https://doi.org/10.15407/rpra19.01.057.

6. Berdnyk S., Gomozov A., Gretskih D., Kartich V., Nesterenko M. Approximate boundary conditions for electromagnetic fields in electrodmagnetics. *Radioelectronic and Computer Systems*, 2022, no. 3, pp. 141-160. doi: https://doi.org/10.32620/reks.2022.3.11.

7. Vasetsky Y., Zaporozhets A. Electromagnetic Field Near Conducting Half-Space: Theory and Application Potentials. *Lecture Notes in Electrical Engineering*, 2023, vol. 1070, 124 p. doi: https://doi.org/10.1007/978-3-031-38423-3.

8. Vasetsky Y.M. Penetration of non-uniform electromagnetic field into conducting body. *Electrical Engineering & Electromechanics*, 2021, no. 2, pp. 43-53. doi: https://doi.org/10.20998/2074-272X.2021.2.07.

9. Vasetsky Y., Zaporozhets A. Approximate Mathematical Models for Analysis of Alternating Electromagnetic Field of Sources Near Conducting Body. Electromagnetic Field Near Conducting Half-Space. *Lecture Notes in Electrical Engineering*, 2023, vol. 1070, pp. 33-67. doi: https://doi.org/10.1007/978-3-031-38423-3_2.

10. Vasetskyi Y., Mazurenko I. Parameters for calculation of three-dimensional electromagnetic field by asymptotic expansion method. *Computational Problems of Electrical Engineering*, 2020, vol. 10, no. 1, pp. 37-44. doi: https://doi.org/10.23939/jcpee2020.01.037.

11. Nayfeh A.H. *Introduction to Perturbation Techniques*. Wiley-VCH, 1993. 536 p.

12. Smirnov V.I. *A Higher Mathematics Course, Complex variables, special functions. vol. 3, part 2*. Oxford, Pergamon Press, 1964. 700 p.

13. Rudnev V., Loveless D., Cook R., Black M. *Handbook of Induction Heating*. London, Taylor & Francis Ltd, 2017. 772 p. doi: https://doi.org/10.1201/9781315117485.

14. Lucia O., Maussion P., Dede E.J., Burdio J.M. Induction Heating Technology and Its Applications: Past Developments, Current Technology, and Future Challenges. *IEEE Transactions on Industrial Electronics*, 2014, vol. 61, no. 5, pp. 2509-2520. doi: https://doi.org/10.1109/TIE.2013.2281162.

15. Raschepkin A.P., Kondratenko I.P., Karlov O.M., Kryshchuk R.S. A method for calculating electromagnetic field of a spiral type induction system for magnetopulse processing of non-magnetic metal strips with a ferromagnetic shield. *Technical Electrodynamics*, 2022, no 2, pp. 43-51. (Ukr). doi: https://doi.org/10.15407/techned2022.02.043.

16. Lobanov L.M., Pashchyn M.O., Mykhodui O.L., Sydorenko Y.M. Effect of the Indenting Electrode Impact on the Stress-Strain State of an AMg6 Alloy on Electrodynamic Treatment. *Strength of Materials*, 2017, vol. 49, no. 3, pp. 369-380. doi: https://doi.org/10.1007/s11223-017-9877-1.

17. Polivanov K.M. *Theoretical Bases of Electrical Engineers. Vol. 3. Theory of Electromagnetic Field*. Moscow, Leningrad, Energiia Publ., 1965. 352 p. (Rus).

18. Tamm I.E. *Fundamentals of the Theory of Electricity*. Moscow, Mir Publ., 1979. 684 p. (Rus).

19. Novikov S.R., Fomenko A.T. *Basic elements of differential geometry and torology*. Springer, 1990. 500 p.

20. Theisel H., Rössl C., Weinkauf T. Topological Representations of Vector Fields. *Mathematics and Visualization*, 2008, pp 215-240. doi: https://doi.org/10.1007/978-3-540-33265-7_7.

Received 13.11.2023
Accepted 15.01.2024
Published 01.05.2024

Yu.M. Vasetsky[1], *Doctor of Technical Science, Professor,*
[1] Institute of Electrodynamics National Academy of Sciences of Ukraine,
56, Prospect Beresteiskyi, Kyiv-57, 03057, Ukraine,
e-mail: yuriy.vasetsky@gmail.com (Corresponding Author)

How to cite this article:
Vasetsky Yu.M. Analytical determination of a quasi-stationary electromagnetic field created by magnetic moments and eddy currents in conducting half-space. *Electrical Engineering & Electromechanics*, 2024, no. 3, pp. 48-54. doi: https://doi.org/10.20998/2074-272X.2024.3.07

UDC 621.3.022: 621.3.015.52: 621.319.53: 629.7 https://doi.org/10.20998/2074-272X.2024.3.08

M.I. Baranov, S.G. Buriakovskyi

Electrical engineering equipment for generating and measuring of complete pulse current of artificial lightning in the conditions of high-voltage electrophysics laboratory

Goal. *Decision of problem scientific and technical task on the reliable generating and measuring in the conditions of high-voltage electrophysics laboratory basic component of complete pulse current of artificial lightning with the rationed amplitude-temporal parameters (ATPs) with the use of the modernized generator of current of lightning of type of UITOM-1.* ***Methodology.*** *Bases of the applied electrical engineering, electrodynamics and electrophysics, electrophysics bases of technique of high-voltage and high pulse currents, bases of high-voltage pulse technique and measuring technique.* ***Results.*** *Information, which specify on a decision at Research and Design Institute «Molniya» of National Technical University «Kharkiv Polytechnic Institute» problem scientific and technical task, related to the reliable generating and measuring in the conditions of high-voltage electrophysics laboratory of complete pulse current of artificial lightning, which contains pulse A- (repeated pulse D-), intermediate B- and long-term C- (shortened long C*-) components of this current, is resulted, ATPs which answer the hard technical requirements of normative documents of the USA of SAE ARP 5412: 2013, SAE ARP 5414: 2013 and SAE ARP 5416: 2013. Short information is indicated about the applied electrical circuits of separate high-voltage generators of pulse currents of condenser type of GIC-A (GIC-D), GIC-B and GIC-C (GIC-C*), which it is worked as synchronous appearance on the general electrical loading in composition the modernized powerful high voltage generator of complete pulse e current of artificial lightning of type of UITOM-1, and in-use high-voltage measuring facilities which contain the heavy-current low-resistance shunts of type of SHK-300 for simultaneous registration with their help on examinee on stability to lightning devices objects of aviation and space-rocket technique of ATPs proper component of complete i pulse current of artificial lightning. Technical examples are resulted and the row of results of practical application of the indicated domestic powerful high-voltage proof-of-concept electrophysics equipment is described at the tests of elements of some aircrafts (ACs) on resistibility to the direct action on them of complete pulse current of artificial lightning with rationed ATPs.* ***Originality.*** *A problem is formulated and having the important applied value in area of aviation and space-rocket technique for the leading countries of the world scientific and technical task on the reliable generating and measuring in the conditions of high-voltage electrophysics laboratory indicated component of complete pulse current of artificial lightning with rationed ATPs and concrete electro-technological ways and hardware are indicated for its successful decision.* ***Practical value.*** *The use of the modernized powerful high-voltage generator of complete pulse current of artificial lightning of type of UITOM-1 developed in practice and created in Ukraine will allow to conduct the real verification on resistibility to the action of lightning of different side systems, devices and construction elements, containing metallic and composition materials, both again developed and modernized ACs, that will be instrumental in the increase of vitality of such ACs in the extreme terms of their flight and stay in an electrical active earthly atmosphere with flowing in it storm electrical discharges.* References 30, tables 3, figures 20.

Key words: **pulse current of artificial lightning, modernized high-voltage generator of current of lightning, shunt, generating, measuring, components of current of lightning.**

Приведені дані, які вказують на вирішення в НДПКІ «Молнія» НТУ «ХПІ» проблемної науково-технічної задачі, пов'язаної з надійним генеруванням і вимірюванням в умовах високовольтної електрофізичної лабораторії повного імпульсного струму штучної блискавки, що містить імпульсну А- (повторну імпульсну D-), проміжну В- і тривалу С- (укорочену тривалу С-) компоненти даного струму, які відповідають технічним вимогам нормативних документів США SAE ARP 5412: 2013, SAE ARP 5414: 2013 і SAE ARP 5416: 2013. Вказані відомості про застосовані електричні схеми окремих високовольтних генераторів імпульсних струмів конденсаторного типу ГІС-А (ГІС-D), ГІС-В і ГІС-С (ГІС-С*), що синхронно працюють на загальне електричне навантаження у складі модернізованого потужного високовольтного генератора струму штучної блискавки типу УИТОМ-1, і використовувані високовольтні вимірювальні засоби, які містять удосконалені низькоомні шунти типу ШК-300 для одночасній реєстрації за їх допомогою на випробовуваних на блискавкостійкість пристроях об'єктів авіаційної і ракетно-космічної техніки амплітудно-часових параметрів (АЧП) відповідних компонент повного імпульсного струму штучної блискавки. Приведені технічні приклади і описані деякі результати практичного застосування вказаного модернізованого вітчизняного високовольтного електрофізичного обладнання при випробуваннях елементів вітчизняних літальних апаратів на стійкість до прямої дії на них основних компонент імпульсного струму штучної блискавки з нормованими АЧП.* Бібл. 30, табл. 3, рис. 20.

Ключові слова: **імпульсний струм штучної блискавки, модернізований високовольтний генератор струму блискавки, шунт, генерування, вимірювання, компоненти струму блискавки.**

Relevance of the topics. The direct (indirect) effect of powerful natural thunderstorm long spark discharges (lightning) on objects of aviation and rocket and space technology during their stay in the Earth's electrically active atmosphere can lead to accidental damage to their metal (composite) structural parts (elements) and irreversible failure of their electrical equipment and on-board systems (for example, computer equipment, control, navigation and communication systems), which can have catastrophic consequences [1-7]. No less dangerous are direct lightning strikes to ground technical objects (for example, TV and radio antennas, energy objects and their overhead power lines) [1, 3, 8]. Here, the main factors of damage to the specified objects are powerful electromagnetic disturbances arising from the propagation of a high-current plasma channel of lightning in the air and causing the appearance in the on-board (internal) electrical circuits of these objects of large electrical currents (overvoltages and shock currents caused by them), as well as large pulse currents flowing in the zone of local attachment of the lightning plasma channel on their surfaces and which are characterized by strong electrothermal and electrodynamic action [1, 3, 9]. In this regard, various electrotechnical approaches and surge protection devices are used for lightning protection of the specified technical objects [1-3, 10, 11].

According to [4-9], a reliable method of checking the used electrotechnical approaches and fail-safe devices when providing lightning protection equipment and systems for both aircrafts (ACs) and ground objects is their full-scale test for the direct (indirect) effect of powerful artificial thunderstorm spark discharges reproduced in the conditions of a high-voltage electrophysical laboratory. For the practical implementation of such electromagnetic tests of ACs and other technical objects, appropriate powerful high-voltage electrical test equipment is required.

In [7, 9], the circuit of a high-voltage electrical installation is indicated, which allows, in accordance with the technical requirements of the NATO Standard AESTR-500: 2016, to form an aperiodic current pulse of a time shape of 50 μs/500 μs with amplitude of up to ±10 kA on various devices and systems of ACs tested for lightning resistance at constant voltage of the electric charge of its capacitor bank up to ±2 kV. At the same time, in accordance with the technical requirements of US regulatory documents [12-14], other amplitude-time parameters (ATPs) of individual components of the full pulse current of artificial lightning are required during lightning resistance tests of on-board systems, component parts and elements of the aircraft (Table 1).

Table 1*

Normalized ATPs of the main components of the full pulse current of artificial lightning [12-14]

Lightning current component	I_{mL}, kA	I_c, kA	q_L, C	J_a, 10^6 J/Ω	τ_f, μs	τ_{p1}, ms
A	200±20	–	–	2±0,4	≤50	≤0,5
B	–	2±0,4	10±1	–	–	5±0,5
C	0,2-0,8	–	200±40	–	–	$(0,25\text{-}1)\cdot10^3$
*C**	–	≥0,4	6-18	–	–	15-45
D	100±10	–	–	0,25±0,05	≤25	≤0,5

*Note. I_{mL} – the amplitude of the lightning current pulse; $I_c \approx q_L/\tau_p$ – the average value of the pulse current; q_L – the amount of charge flowing in the current pulse; J_a – the integral of the action of the lightning current pulse; τ_f, τ_{p1} – respectively, the duration of the front of the current pulse between the levels (0.1-0.9) I_{mL} and the duration of the lightning current pulse at the level ≤0.1 I_{mL}

At the same time, it should be noted that, according to [12-14], depending on the AC's area affected by lightning in the Earth's atmosphere, its full pulse current may contain the following main components, the ATPs of which differ significantly from each other: pulse *A*- (repeated pulse *D*-), intermediate *B*- and long-term *C*- (shortened long *C**-) components. Moreover, in the practice of electromagnetic tests on the lightning resistance of technical devices and on-board systems of civil and military ACs, the following combinations of the specified components of the full pulse current of artificial lightning are most often used [9, 12-14]: *A*-, B- and *C*-components (area 3 of damage); *A*-, *B*- and *C**-components (area 1*A* of damage); *D*-, *B*- and *C**-components (area 2*A* of damage). The sequence of flow of these components of the lightning current for the corresponding zones of damage to the AC in the atmospheric air by the lightning discharge must correspond to the order indicated above, and each of the given components of the lightning current must monotonically transition into another one.

To meet the technical requirements [12-14], [15] shows a diagram of a powerful high-voltage electrical installation, which was intended for testing on-board systems and AC elements for lightning resistance. The practice of operating a powerful lightning current generator (LCG) according to [15] revealed a number of technical deficiencies in its construction circuits and operation: insufficient protection of the used high-voltage capacitors in a total number of several hundred pieces of pulse current generators (PCGs) of LCG from emergency shock currents with amplitude of up to ±500 kA in the microsecond time range; lack of recommendations for the simultaneous selection of the lengths h_1–h_3 of the insulating air gaps in the used high-voltage high-current commutators of PCG when changing the levels of their charging electric voltage U_c, as well as the length h_e of the air gap between the edge of the electrically explosive wire (EEW) and the tested sample (TS) of the AC; the presence of cases of non-synchronous parallel operation in the LCG circuits of its individual generators GIC-*A*, GIC-*D*, GIC-*B*, GIC-*C** and GIC-*C* on the total R_LL_L – the load of the TS of the corresponding AC, which excludes obtaining the necessary according to the requirements [12-14] test pulses of artificial lightning current.

From the data in Table 1 for the indicated ATPs, the component of the full pulse current of artificial lightning and the application of the necessary for their practical production of the PCG, built on the basis of individual high-voltage LCG of the capacitor type, it follows that the development and creation of such PCG in the field of high-voltage pulse technology (HPT) is a complex scientific and technical task. At the same time, the one related to the simultaneous registration from one high-voltage measuring device at once of at least three components of the pulse current of artificial lightning with ATP, which are sharply different from each other, turns out to be an equally difficult task. One of the indirect confirmations of this is the fact that at present we do not know the electrotechnological construction circuits and technical designs of similar high-voltage PCGs and means for measuring lightning currents, which were given in the open literature of the leading countries of the world.

The goal of the article is to solve the problematic scientific and technical task of reliable generation and measurement in the conditions of a high-voltage electrophysical laboratory of the main components of the full pulse current of artificial lightning with normalized ATPs using a modernized PCG of the UITOM-1 type.

1. Electrotechnological circuits of the construction of a powerful UITOM-1 type PCG. Figure 1 shows the modernized electrical circuit of the construction of a powerful high-voltage PCG of the UITOM-1 type [16], which includes five separate high-voltage LCG (GIC-*A*, GIC-*D*, GIC-*B*, GIC-*C* and GIC-*C**) with the possibility of their parallel and reliable synchronous operation on a common low-impedance active-inductive R_LL_L – load in the mode selected by the researcher for the formation of the corresponding components of the full pulse current of artificial lightning. The necessary combination of the components of the full pulse current of artificial lightning and the corresponding powerful high-voltage PCG,

specified in accordance with the technical requirements of the specified regulatory documents [12-14], is carried out with the help of electrical switches X1-X4 (Fig. 1) and which allow them to be manually switched on or off from the electromagnetic circuit of TS tests.

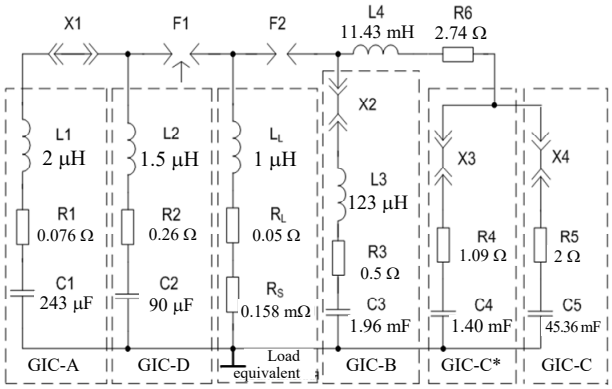

Fig. 1. Improved electrical circuit for the construction of a powerful high-voltage PCG of the UITOM-1 type with one common electric R_LL_L – load and discharge circuits of its separate high-voltage generators working in parallel GIC-*A*, GIC-*D*, GIC-*B*, GIC-*C* and GIC-*C** (F_1, F_2 – three- and two-electrode high-current air commutators for nominal constant voltage of ±50 kV and ±5 kV; X1-X4 – electrical switches; R_S ≈(0.158±0.005) mΩ – active resistance of the SHK-300M1 type measuring shunt; R1- R5, *R*1-*R*5, *L*1-*L*3 – intrinsic electrical parameters of discharge circuits of high-voltage generators GIC-*A*, GIC-*D*, GIC-*B*, GIC-*C** and GIC-*C*; *R*6, *L*4 – electrical parameters of forming *RL* elements for discharge circuits of high-voltage generators GIC-*C* and GIC-*C**) [16]

It should be noted that the GIC-*D* generator in the improved LCG circuit of the UITOM-1 type is assembled from 30 parallel-connected pulse capacitors of the IK-50-3 type, which are part of the GIC-*A* generator. In this regard, during the operation of GIC-*D* in the electrical circuit of the LCG, the switch X1 is removed and the GIC-*A* generator is switched off from the working circuit of the LCG (Fig. 1). This decision allows to significantly save time and material resources when creating this LCG.

With the selected electrical circuit for the formation of the necessary components, according to the requirements [12-14], the full pulse current of artificial lightning, reliable synchronization of the operation of the corresponding PCG in the LCG is ensured by the supply from a separate high-voltage pulse generator of the GVZI-100 type [16] to the middle control steel electrode of the three-electrode air switch F_1 (Fig. 2) for nominal constant voltage of ±50 kV of high-voltage rapidly decaying sinusoidal voltage pulse with amplitude of ±100 kV of microsecond duration, which causes activation of both air switch F_1 (see Fig. 1, 2) and two-electrode air switch F_2 (Fig. 3) for nominal DC voltage of ±5 kV. To ensure reliable operation of the three-electrode commutator F_1 of the improved LCG, the polarity of this voltage pulse from the GVZI-100 generator is selected opposite to the charge polarity of the capacitor batteries of the used PCG. Our modernized electrotechnological circuit for artificial lightning pulse current introduction into the TS contains, in accordance with the requirements of regulatory documents [12-14], a thin copper EEW with diameter of ~0.1 mm and length of l_e≈50 mm, separated from the surface of the TS by air gap of length h_e≈2 mm. During the electric explosion (EE) of a thin EEW above the surface of the TS in the local zone of introduction into it of the given components of the simulated lightning current from a powerful LCG, a low-temperature plasma is formed, through which the charges of the pre-charged high-voltage capacitor batteries of the LCG flow into the investigated TS. In Fig. 4 with the help of a Canon A-530 type digital camera, the moment of synchronous activation of the indicated air switches F_1 and F_2 and the explosion of the EEW in the formation circuit using an improved powerful UITOM-1 type LCG (see Fig. 1) of standardized *A*-, *B*- and *C**- components of the full current of artificial lightning (area 1*A*) was recorded in the TS of one of the devices of the domestic AC [17].

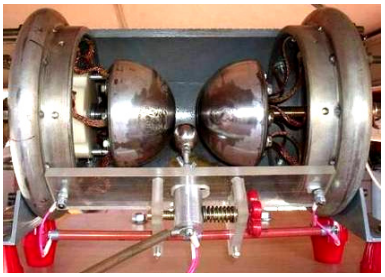

Fig. 2. General view of the high-voltage three-electrode high-current air commutator F_1 of cascade type with massive main hemispherical electrodes made of steel St. 3 grade at nominal constant voltage of ±50 kV and pulse current with amplitude I_{mL} up to ±300 kA [16]

Fig. 3. General view of the high-voltage two-electrode high-current air commutator F_2 with graphite electrodes of a rectangular shape for nominal constant voltage of ±5 kV and charge q_L up to ±300 C, which is placed in the discharge circuit of a powerful LCG of the UITOM-1 type [16]

Fig. 4. General view of the desktop of a powerful modernized LCG of the UITOM-1 type at the moment of synchronous electrical activation of three charged powerful high-voltage test generators of pulsed currents GIC-*A*, GIC-*B* and GIC-*C** during lightning resistance tests (area 1A) of the TS of the device of the domestic LA [17]

Let us point out that when the charging constant voltage U_{c1} in powerful high-voltage generators GIC-*A*

and GIC-*D* changes in the range $U_{c1} \approx \pm(28-33)$ kV in the three-electrode commutator F_1 (Fig. 2), the length of the air gaps between its steel (two main and one controlling) the electrodes should numerically be $h_1 \approx 4$ mm and $h_2 \approx 9$ mm, and when changing the charging DC voltage U_{c2} in high-voltage generators GIC-*B*, GIC-*C* and GIC-*C** in the range $U_{c2} \approx \pm(3.6-4.5)$ kV in the two-electrode commutator F_2 (Fig. 3), the length of the air gap between its graphite electrodes is chosen equal to $h_3 \approx 3$ mm [16]. At the same time, the physical conditions for atmospheric air must correspond to [18]: pressure $P_a \approx (1.013\pm0.015)\cdot10^5$ Pa; absolute temperature $T_a \approx (293.15\pm10)$ K; relative humidity $\beta_a \approx (45\pm25)$ %.

Note that in Fig. 4, on the left is the TS of the AC device with the corresponding copper EEW, which glows brightly when its EE is in the discharge circuit of a powerful LCG and which is connected to the non-potential (grounded) steel electrode of the commutator F_1 (Fig. 1); above, we can see the F_1 commutator of a powerful LCG with a high-current pulse spark that glows brightly, rigidly fixed on the desktop; at the bottom of the LCG desktop, the F_2 commutator is shown with its pulse spark channel, which also glows brightly.

Figure 4 visually illustrates the correctness of the electrotechnological solutions proposed and indicated by us above to ensure reliable synchronous parallel operation of individual high-voltage generators GIC-*A* (GIC-*D*), GIC-*B* and GIC-*C* (GIC-*C**) when creating a modernized powerful UITOM-1 type LCG.

Table 2 shows the main electrical characteristics of individual high-voltage generators GIC-*A*, GIC-*B*, GIC-*C*, GIC-*C** and GIC-*D*, which are part of the improved powerful UITOM-1 type LCG.

Table 2

Technical characteristics of the generators GIC-*A*, GIC-*B*, GIC-C, GIC-*C** and GIC-*D*, which are included in the UITOM-1 type LCG

PCG name	Number of capacitors	Type of capacitors	Total capacity C_g, mF	Energy intensity W_g, kJ
GIC-*A*	111	IK-50-3	0,333	416,2
GIC-*B*	14	IM-6-140	1,96	24,5
GIC-*C*	324	IM-5-140	45,36	567,0
GIC-*C**	10	IM-6-140	1,4	17,5
GIC-*D*	30	IK-50-3	0,09	112,5

From the data in the Table 2 it follows that the total number of high-voltage pulse capacitors with a metal case of three types (IK-50-3, IM-6-140 and IM-5-140 [19]) in a powerful UITOM-1 type LCG is 489. At the same time, the total nominal electrical energy $W_{g\Sigma}$ stored by the high-voltage pulse capacitors of this LCB is equal to $W_{g\Sigma} \approx 1.25$ MJ. At the price of 1 kJ of electric energy stored by powerful high-voltage electrophysical equipment of the capacitor type, equal to the application case of its formation on an electrical load of pulse currents of micro- and millisecond duration of approximately $1000 [20-22], the cost of construction of such a powerful high-voltage LCB will be at least $1.25 million. As we can see, the development and creation of a powerful high-voltage, high-current LCB of the UITOM-1 type (Fig. 5) is associated not only with significant scientific and technical difficulties, but also with large financial costs.

Fig. 5. General view of the improved powerful high-voltage LCB of the UITOM-1 type (in the foreground is a work table with a three-electrode switch F_1 for nominal constant voltage of ±50 kV and an air extraction system, and in the background is an individual high-voltage powerful generators GIC-*A* (GIC-*D*), GIC-*B*, GIC-*C* and GIC-*C**)

It is important to point out that in the improved LCB of the UITOM-1 type, all high-voltage pulse capacitors of generators GI*S*-*A*, GIC-*D*, GIC-*B*, GIC-*C* and GIC-*C** are equipped with resistive systems to protect them from the action of emergency shock currents in the LCB [23].

The data of the system of reliable protection of impulse capacitors in the modernized LCB are based on the use of high-voltage constant graphite-ceramic resistors of the TVO-60 type with nominal value of 24 Ω and 100 Ω [24], which sharply limit the operation of the LCB in emergency modes (for example, in the event of an electrical breakdown of the internal or external insulation of its pulse capacitors) shock pulse currents and dissipate the thermal energy released at the same time on them.

Thanks to:

- performed modernization in accordance with the technical solution [23] of resistive circuits for protection against emergency shock pulse currents with calculated amplitude of up to ±500 kA of high-voltage pulse capacitors of separate powerful generators GIC-*A* (GIC-*D*), GIC-*B*, GIC-*C* and GIC-*C** (Table 2),
- improvement of the circuit of controlled electric start from a separate high-voltage generator type GVZI-100 [16] of the three-electrode air commutator F_1 (Fig. 2) and the two-electrode air commutator F_2 (Fig. 3),
- recommended simultaneous selection of the lengths h_1-h_3 of the air gaps in the used high-voltage commutators F_1 and F_2 of the high-current discharge circuits of the specified LCBs and the length h_e of the air gap between the edge of the EEW and the TS of the object, the modernized PCG of the UITOM-1 type, despite the similarity of the electrotechnological circuits used earlier in the PCG [15] for the construction of discharge circuits of the corresponding LCGs (Fig. 1), has a significant difference from the PCG, which was proposed in [15]. This difference of powerful high-voltage PCG ensures more reliable operation of the modernized PCG of the UITOM-1 type in comparison with PCG [15] when generating pulses of full current of artificial lightning (Table 1) according to technical requirements [12-14].

2. Results of measurement of the main components of artificial lightning current in the discharge circuit of a powerful UITOM-1 type PCG. In [25, 26], the main methods of measuring ultra- and high-pulse voltage in electrical installations during tests of various electrical engineering and electric power equipment are given. As for the methods of measuring high pulse currents (HPC) in the

field of HPT, certain technical techniques and means for this were given in [20-22, 27, 28]. Unfortunately, for the practical implementation of complex metrological tasks related to the simultaneous measurement of a number of components of the full pulse current of lightning in a powerful PCG of the UITOM-1 type, given in [20-22, 27, 28], materials and data on high-voltage measuring devices designed for simultaneous registration with the help of one meter, both HPC (with amplitude I_{mL} of tens and hundreds of kiloamperes) and relatively weak pulse currents (with amplitude I_{mL} of hundreds and tens of amperes) in a wide time interval of their flow in the discharge circuits of its series of parallel operating LPC (from units microseconds to hundreds of milliseconds), was not enough. In connection with this, the authors had to independently develop, create and modernize non-standardized high-voltage high-current meters of similar electric pulse currents, which are able to reliably register the necessary components of the pulse current of artificial lightning on the total electric R_LL_L – load when individual high-voltage LCG of this PCG is activated [16, 17, 29, 30].

Figures 6-10 show the main typical oscillograms of pulse *A*-, intermediate *B*-, long-term *C*-, shortened long *C**- and repeated pulse *D*- components of the full pulse current of artificial lightning with normalized ATPs according to [12-14], which were obtained in a high-current discharge circuit of a powerful high-voltage PCG of the UITOM-1 type, which contains the lightning resistance-tested TS made of aluminum alloy D16 of the fuel tank skins of one of the modernized domestic aircraft «An» [17].

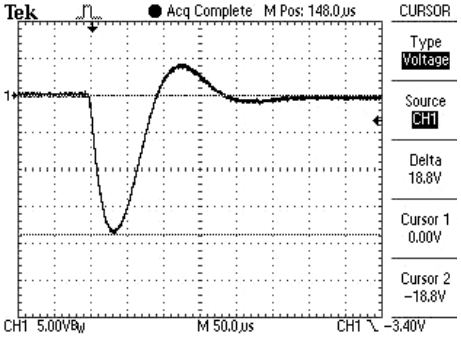

Fig. 6. Oscillogram of the pulse *A*- component of the artificial lightning current with normalized ATP in the discharge circuit of the GIC-*A* generator of the powerful UITOM-1 type PCB (U_{c1}≈−29.7 kV; I_{mA1}≈−211.7 kA; J_{aA}≈2.09·10^6 J/Ω; t_{mA1}≈32 − time corresponding to the first amplitude I_{mA1}; τ_{fA}≈t_{mA1}/1.6≈20 µs; τ_{p1A}≈500 µs; vertical scale − 56.3 kA/div; horizontal scale − 50 µs/div)

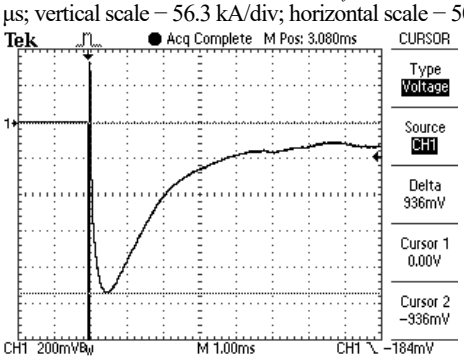

Fig. 7. Oscillogram of the intermediate *B*- component of the artificial lightning current with normalized ATP in the high-current discharge circuit of the high-voltage generator GIC-*B* of the powerful PCG type UITOM-1 (U_{c2}≈−4 kV; I_{mB}≈−5.27 kA; I_{cB}≈−2.08 kA; q_{LB}≈−10.4 C; τ_{p1B}≈5 ms; vertical scale − 1126 A/div; horizontal scale − 1 ms/div)

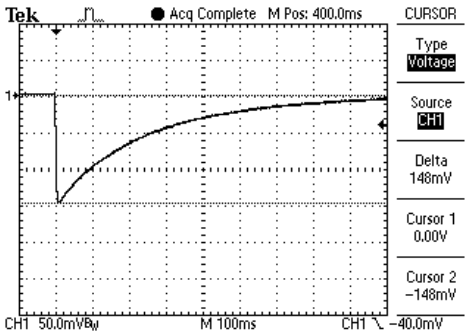

Fig. 8. Oscillogram of the long-term *C*- component of the full current of artificial lightning with normalized ATP in the discharge circuit of the high-voltage GIC-*C* generator of the powerful PCG of the UITOM-1 type (U_{c2}≈−4 kV; I_{mC}≈−833 A; q_{LC}≈−186.2 C; τ_{fC}≈7 ms; τ_{p1C}≈1000 ms; vertical scale − 281.5 A/div; horizontal scale − 100 ms/div)

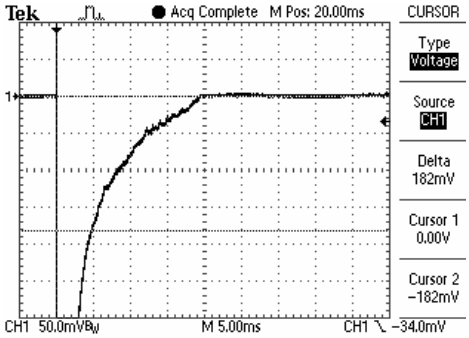

Fig. 9. Oscillogram of the shortened long-term *C**- component of the full pulse current of artificial lightning with normalized ATP in the discharge circuit of the high-voltage generator GIC-*C** of the powerful PCG type UITOM-1 (U_{c2}≈−4 kV; I_{mC*}≈−1148 A; τ_{pC*}≈14.8·ms; q_{LC*}≈−6.16 C; I_{cC*}≈q_{LC*}/τ_{pC*}≈−416 A)

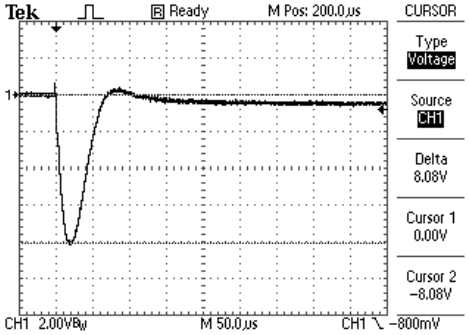

Fig. 10. Oscillogram of the repeated pulse *D*- component of the full pulse current of artificial lightning with normalized ATP in the discharge circuit of the GIC-*D* generator of the powerful high-voltage PCG of the UITOM-1 type (U_{c1}≈−33 kV; I_{mD1}≈−102 kA; t_{mD1}≈20 µs − time, which corresponds to the amplitude I_{mD1}; τ_{fD}≈t_{mD1}/1.6≈12.5 µs; τ_{p1D}≈500 µs; J_{aD}≈0.26·10^6 J/Ω)

The powerful high-voltage PCG of the UITOM-1 type is equipped with several high-current meters (improved disk coaxial low-resistance shunts of the ShK-300 type) of artificial lightning pulse current components, the main technical characteristics of which are given in Table 3.

The novelty of shown in Fig. 6-10 oscillograms consists in the fact that they are obtained on the specified TS with the help of modernized electrotechnological circuits for the formation of these components of the full pulse current of artificial lightning in the discharge circuit of the UITOM-1 type PCG, as well as high-voltage measuring devices, which are based on high-current low-resistance shunts of the type ShK-300 (Table 3). Note that for the simultaneous

measurement of several components of the full pulse current of artificial lightning, generated in the discharge circuit of the improved high-voltage PCG of the UITOM-1 type, it was necessary to develop and create a measuring matching special voltage divider (SVD), which is connected at the output of the used in similar high-voltage measurements of the cable communication line (Fig. 11).

The modernization of the measuring instruments carried out by us was to exclude, when measuring in the discharge circuit of a high-voltage PCG of the UITOM-1 type of the corresponding components of the artificial lightning current, a high electric potential enters the channels of digital storage oscilloscopes (DSOs). As it is known, applying such a potential to the input of the DSO leads to its failure. The following new technical solution was proposed: the radio-frequency coaxial cable of the length l_c of the communication line, which connects the measuring shunt of the ShK-300 type with the SVD and the DSO, must be placed in an additional copper braid screen, which must be securely grounded before the SVD.

Fig. 11. General view of a high-voltage measuring shunt of the ShK-300M type, connected to the input of an additionally shielded radio-frequency coaxial cable of the RK 75-7-11 brand l_c≈70 m long, the output of which is connected to the input of the SPN-300 shielded matching voltage divider with two output coaxial 1:1 and 1:2 connectors for the coordinated connection of the measuring channels of three DSOs to them (for example, Tektronix TDS 1012 series) with simultaneous registration in the discharge circuit of a powerful UITOM-1 type PCG at once of three components of the full pulse current of artificial lightning with different ATPs [16]

Table 3*

Main technical characteristics of high-voltage high-current shunts of the ShK-300M, ShK-300M1 and ShK-300M2 type

Shunt name	Value of the characteristic			
	R_S, mΩ	K_S, A/V	L_S, nH	Mass, kg
ShK-300M	0,178±0,005	$\frac{K_{SA}\approx 11260}{K_{SC}\approx 5630}$	10±0,3	3,0
ShK-300M1	0,158±0,005	$\frac{K_{SA}\approx 12625}{K_{SC}\approx 6312}$	10±0,3	3,1
ShK-300M2	0,080±0,003	$\frac{K_{SA}\approx 25000}{K_{SC}\approx 12500}$	10±0,3	3,2

*Note. R_S, L_S – the active resistance (mΩ) and inductance (nH) of the shunt; $K_S\approx 2/R_S$ – the shunt conversion factor, A/V; K_{SA} – the shunt conversion factor when measured in the discharge circuit of the UITOM-1 type PCG the ATPs of *A*- and *D*- components of the artificial lightning current, A/V (from the 1:1 connector of the SPN-300 type divider [16]); K_{SC} – the shunt conversion factor when measured in the discharge circuit of the UITOM-1 type PCG of the ATPs of *B*-, *C*- and *C**- component of the artificial lightning current, A/V (from the 1:2 connector of the SPN-300 type divider [16]).

Figure 12 shows the electrical diagram of the coordinated connection of the high-voltage shunt of the ShK-300M1 type with its measuring coaxial resistor (MCR) to the measuring coaxial cable (MCC), SVD and the corresponding DSO.

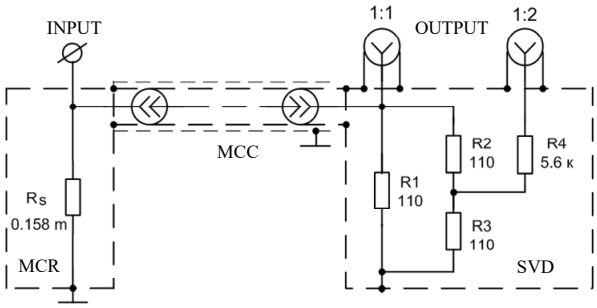

Fig. 12. Schematic electrical diagram of connecting a high-voltage shunt of the SHK-300M1 type to a low-voltage measuring circuit of a communication cable line and DSO (the shunt MCR with an active resistance R_S≈0.158 mΩ, which is connected to the input of the communication line cable; MCC brand RK 75-7-11 of the triaxial communication line; SVD, which coordinates the operation of the shunt, MCC and DSO inputs and is connected to the output of the MCC, which transmits an electrical signal from the zone of the steel disk of the shunt to the SVD and DSO)

According to Fig. 12, we can see that at the output of the MCC cable, the additional copper cylindrical shield of which is reliably grounded before the SVD, the SVD is connected, which coordinates the operation of the shunt, the MCC and the inputs of the DSO and which is made of concentrated resistors R1−R3 with nominal value of 110 Ω with total active resistance equal to the wave resistance of the MCC cable Z_c ≈ 75 Ω. The task of the SVD applied in the circuit of the high-voltage shunt of the ShK-300M1 type is to ensure not only the agreed mode of operation of the measuring circuit of this shunt, but also the simultaneous registration of several oscillograms of the corresponding components of the full current of artificial lightning of micro- and millisecond duration with amplitude values that differ sharply. For this purpose, this SVD was equipped with two output coaxial connectors 1:1 and 1:2 (Fig. 12).

To strengthen the mutual decoupling of coaxial connectors 1:1 and 1:2 in the SVD by increasing the input resistance of the output connector 1:2, an additional concentrated resistor R4 with nominal value of 5.6 kΩ is electrically connected to its potential electrode (see Fig. 12). At the same time, the SVD is performed in the form of a separate low-voltage device that is connected to the output of the MCC coaxial cable of an additionally shielded triaxial communication line and is placed in a shielded metal case (see Fig. 11), which must be reliably isolated from the grounded edge of the additional copper cylindrical screen of the MCC.

The SPN-300 type voltage divider (Fig. 11) has two coaxial connectors 1:1 and 1:2, which are designed for the coordinated connection of the corresponding outputs to the inputs of the measuring channels of the DSO. At the same time, according to Table 3, the specified connectors 1:1 and 1:2 of SPN-300 are characterized by different conversion factors K_S of the used measuring shunts when registering with their help ATPs as *A*- and *D*- components of artificial lightning current (in this case they are denoted as K_{SA}), as well as *B*-, C- and *C**- components of artificial lightning current (in this case they are designated as K_{SC}).

Figure 13 shows a general view of the improved measuring high-current disk shunt of the ShK-300M1

type, used in the discharge circuit of the powerful UITOM-1 type PCG.

Fig. 13. General view of a high-voltage measuring shunt of the ShK-300M1 type, connected to the collector of a high-current discharge circuit of a powerful UITOM-1 type PSG

Coaxial designs of measuring shunts of the ShK-300 type (Table 3), which are used as part of a powerful high-voltage PSG of the UITOM-1 type, are characterized by small values of their own electrical parameters – inductance L_S (no more than 11 nH) and active resistance R_S (no more than 0.2 mΩ), which ensures a small influence of the $R_S L_S$ – parameters of the measuring shunts on the electromagnetic processes occurring in the $R_L L_L$ – load (see Fig. 1).

Figure 14 schematically shows the design of the measuring high-voltage high-current shunt of the ShK-300M2 type in its longitudinal section.

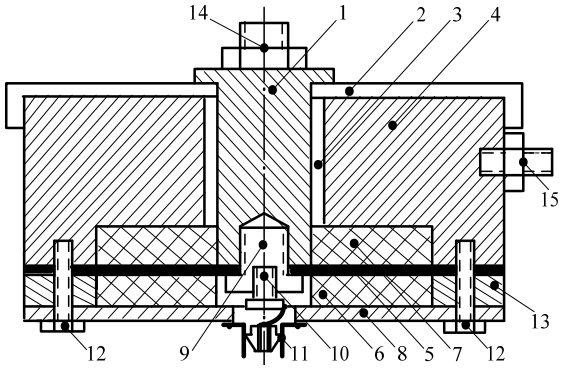

Fig. 14. Schematic representation of the improved design of the high-voltage coaxial disk shunt of the ShK-300M2 type in its longitudinal axial section (1 – massive internal cylindrical brass electrode; 2, 3 – insulating bushings made of fluoroplastic; 4 – massive external cylindrical brass electrode; 5 – measuring high-resistance steel disc of thickness h_S =2 mm; 6, 7 – massive pressing insulating discs; 8 – banded brass disc; 9, 10, 12 – steel fastening screws; 11 – output coaxial connector type SR-75; 13 – massive brass clamping ring; 14, 15 – input (potential) and output (grounded) elements of the brass bolt connection of the shunt to the high-current discharge circuit of the powerful UITOM-1 type PSG

A significant difference between the improved designs of high-voltage high-current shunts of the ShK-300M1 and ShK-300M2 type [16, 29, 30] from the ShK-300M shunt specified in [15] is the use of a high-resistance manganin disc instead of a thin-walled (thickness h_S≈0.3 mm) disc. which is subjected to huge electrothermal and electrodynamic shocks measured in the discharge circuit of the LCG of powerful pulses of the full current of artificial lightning and from which the drop of the pulse voltage U_S from the passage of the corresponding components of the pulse current of artificial lightning through it is removed, a disk with thickness of h_S = (1-2) mm of stainless steel grade 12X18H10T. The practice of operating a measuring shunt of the ShK-300M type with a manganin disc as part of the LCG according to [15] showed that after ~100 measurements, its disc cannot withstand the further action of powerful electrothermal loads and it fails.

Using the data of Table 3 and the numerical indicators (in fractions or units of volts) registered on the DSO screen using a high-voltage measuring shunt of the corresponding type of pulse voltage drop U_S, the desired value of the pulse current I_L of artificial lightning, which is generated and measured in laboratory conditions in the LCG circuit, is determined in the form: $I_L \approx K_S \cdot U_S$.

When deciphering the oscillograms (Fig. 6-10) obtained in the discharge circuit of a powerful PCG type UITOM-1 of the main components of the pulse current of artificial lightning and determining the numerical values of their ATPs, the following calculation analytical relationships can be used:

- for sinusoidal decaying current in the discharge circuit of a modernized PCG of the UITOM-1 type:

- when calculating the action integrals J_{aA} and J_{aD}, respectively, for A- and D- components of the artificial lightning current:

$$J_{aA} \approx k_A^2 I_{mA1}^2 [T_A (4\Delta_A)^{-1} - \Delta_A T_A /(4\Delta_A^2 + 16\pi^2)]; \quad (1)$$

$$J_{aD} \approx k_D^2 I_{mD1}^2 [T_D (4\Delta_D)^{-1} - \Delta_D T_D /(4\Delta_D^2 + 16\pi^2)], \quad (2)$$

where $I_{mA1}(I_{mD1})$, $I_{mA3}(I_{mD3})$, $T_A(T_D)$, $\Delta_A(\Delta_D)$ are, respectively, the first and third current amplitudes $I_A(I_D)$, the period and the logarithmic decrement of oscillations for the pulse A- and repeated pulse D- components of the artificial lightning current; $\Delta_A=\ln(I_{mA1}/I_{mA3})$, $\Delta_D=\ln(I_{mD1}/I_{mD3})$ are, respectively, the logarithmic decrement of oscillations for the pulse A- and repeated pulse D- components of the artificial lightning current; $k_A = [\exp(-0{,}5\pi^{-1}\Delta_A \operatorname{arcctg} 0{,}5\pi^{-1}\Delta_A)\sin(\operatorname{arcctg} 0{,}5\pi^{-1}\Delta_A)]^{-1}$, $k_D = [\exp(-0{,}5\pi^{-1}\Delta_D \operatorname{arcctg} 0{,}5\pi^{-1}\Delta_D)\sin(\operatorname{arcctg} 0{,}5\pi^{-1}\Delta_D]^{-1}$ are, respectively, the normalizing coefficients for the pulse A- and repeated pulse D- components of the full pulse current of artificial lightning;

- when calculating electric charges q_{LA} and q_{LD}, respectively, for the sinusoidal A- and D- components of the full pulse current of artificial lightning:

$$q_{LA} \approx 2\pi k_A I_{mA1} T_A /(\Delta_A^2 + 4\pi^2); \quad (3)$$

$$q_{LD} \approx 2\pi k_D I_{mD1} T_D /(\Delta_D^2 + 4\pi^2). \quad (4)$$

- for aperiodic pulse current in the discharge circuit of a powerful PCG at $R_{1(2)} \geq 2[L_{1(2)}/C_{1(2)}]^{1/2}$:

- when calculating the action integrals J_{aA} and J_{aD} for the aperiodic A- and D- components of the lightning current:

$$J_{aA} \approx k_A^2 I_{mA}^2 [0{,}658\tau_{pA} - 0{,}633\tau_{fA}]; \quad (5)$$

$$J_{aD} \approx k_D^2 I_{mD}^2 [0{,}658\tau_{pD} - 0{,}633\tau_{fD}], \quad (6)$$

where $I_{mA}(I_{mD})$ are, respectively, the amplitudes of the aperiodic pulse A- and repeated pulse D- components of the full current of artificial lightning; $\tau_{fA}(\tau_{fD})$ is, respectively, the duration of the pulse front of A- and D- components of the full lightning current at their level (0.1-0.9)·I_{mA} or (0.1-0.9)·I_{mD}; $\tau_{pA}(\tau_{pD})$ is the duration of pulses

of *A*- and *D*- components of the full artificial lightning current at their level of $0{,}5I_{mA}$ or $0{,}5I_{mD}$, respectively; $k_A=[(\alpha_{1A}/\alpha_{2A})^n - (\alpha_{1A}/\alpha_{2A})^m]^{-1}$, $k_D=[(\alpha_{1D}/\alpha_{2D})^l - (\alpha_{1D}/\alpha_{2D})^k]^{-1}$ are, respectively, normalizing coefficients for aperiodic pulse *A*- and repeated pulse *D*- component of the full pulse current of artificial lightning; $\alpha_{1A}\approx 0{,}76/\tau_{pA}$; $\alpha_{2A}\approx 2{,}37/\tau_{fA}$; $\alpha_{1D}\approx 0{,}76/\tau_{pD}$; $\alpha_{2D}\approx 2{,}37/\tau_{fD}$; $n=\alpha_{1A}/(\alpha_{2A}-\alpha_{1A})$; $m=\alpha_{2A}/(\alpha_{2A}-\alpha_{1A})$; $l=\alpha_{1D}/(\alpha_{2D}-\alpha_{1D})$; $k=\alpha_{2D}/(\alpha_{2D}-\alpha_{1D})$;

- when calculating electric charges q_{LA} and q_{LD}, respectively, for aperiodic *A*- and *D*- components of the full pulse current of artificial lightning:

$$q_{LA}\approx k_A I_{mA}[1{,}315\tau_{pA}-0{,}422\tau_{fA}]; \quad (7)$$

$$q_{LD}\approx k_D I_{mD}[1{,}315\tau_{pD}-0{,}422\tau_{fD}]. \quad (8)$$

Let us point out that formulas (7), (8) can be used in the calculations of the corresponding ATPs for intermediate *B*-, long-term *C*- and shortened long-term *C**- components of the full pulse current of artificial lightning.

3. Technical examples and results of tests on lightning resistance of some AC devices on a powerful UITOM-1 type PCG. Figure 15 shows the results of the direct shock simultaneous action in the high-current discharge circuit of the modernized PCG of the UITOM-1 type on the TS of the sheet cladding of the AC made of aluminum alloy of the AMr2M brand with thickness of h = 1 mm of the pulse *A*- and long-term *C*- components of the pulse current of artificial lightning with normalized ATPs.

Fig. 15. General view of the outer rounded zone of through burning with radius $r_e\approx$13 mm of a sheet TS when testing on the lightning resistance of the AC cladding of the aluminum alloy of the AMr2M brand with thickness of h=1 mm from the simultaneous action on it in the discharge circuit of a powerful PCG type UITOM-1 of pulse *A*- ($I_{mA1}\approx$–216 kA; $t_{mA1}\approx$32 μs – time corresponding to the first amplitude I_{mA1} of the current pulse; $\tau_{p1A}\approx$500 μs; $J_{aA}\approx 2{,}19\cdot 10^6$ J/Ω) and the long-term *C*- ($I_{mC}\approx$–869 A; $t_{mC}\approx$11 ms – time that corresponds to the current pulse amplitude I_{mC}; $\tau_{fC}\approx$7 ms; $\tau_{p1C}\approx$1000 ms; $q_{LC}\approx$–194.3 C) component of the full current of artificial lightning with normalized ATP

Figure 16 shows the results of the indicated according to Fig. 15 the destructive electrothermal effect on the TS of the sheet covering of the AC made of aluminum alloy of the AMr2M brand with thickness of h = 1 mm of the pulse *A*- and long-term *C*- components of the current of artificial lightning with the corresponding normalized ATP from its inner surface.

Figure 17 shows the results of tests on lightning resistance (damage area 1*A*) in the discharge circuit of a powerful high-voltage PCG of the UITOM-1 type with thickness h = 1.2 mm of a flat duralumin panel of the fuel tank lining of the domestic aircraft «An».

Fig. 16. General view of the inner rounded zone of the through burning of the sheet TS during the lightning resistance test of the AC cladding of the aluminum alloy of the AMr2M brand with thickness of h = 1 mm from the combined action on it in the discharge circuit of a powerful high-voltage PCG of the UITOM-1 type of pulse *A*- and long-term *C*- components of the full current of artificial lightning with normalized ATP

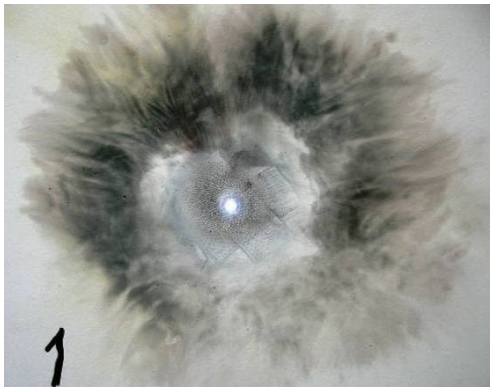

Fig. 17. General view from the side of the anchoring zone of the results of through burning on the outer surface of the TS of the flat duralumin panel with thickness of h=1.2 mm of the fuel tank lining of the domestic aircraft «An» of the plasma channel simulated in the discharge circuit of a powerful high-voltage PCG of the UITOM-1 type of artificial thunderstorm discharge with radius $r_e\approx$3.7 mm of its wall from the direct action of normalized *A*- $I_{mA1}\approx$–199.5 kA; $t_{mA1}\approx$42 μs; $\tau_{p1A}\approx$500 μs; $J_{aA}\approx 1.99\cdot 10^6$ J/Ω), *B*- ($I_{mB}\approx$–6.16 kA; $I_{cB}\approx$–2220 A; $q_{LB}\approx$–11.1 K; $\tau_{p1B}\approx$5 ms) and *C**- ($I_{mC*}\approx$–1112 A; $\tau_{p1C*}\approx$13.6·ms; $q_{LC*}\approx$–5.79 K; $I_{cC*}\approx q_{LC*}/\tau_{p1C*}\approx$–426 A) components of the full pulse current of artificial lightning (damage area 1*A*) [17]

Figure 18 presents the results of direct action in the discharge circuit of a powerful high-voltage PCG of the UITOM-1 type, only of the pulse *A*- component of artificial lightning with the ATP normalized according to the requirements [12-14] on the TS of the composite skin of the aircraft.

Figures 15-18 clearly indicate that the indicated experimental sheet metal and composite samples of ACs cannot withstand high-energy electrothermal action from the high-current channel of artificial lightning with normalized ATPs of its main current components.

In order to reflect the complex nature of the performed full-scale electromagnetic research on the modernized UITOM-1 type PCG, Fig. 19,*a*,*b* show the results of the direct action in the discharge circuit of this

high-voltage, high-current PCG on a factory-made pilot model of a domestically produced aircraft receiving-transmitting antenna of a powerful pulse *A*- component of the artificial lightning current with normalized ATPs.

Fig. 18. General view of the damage zone with diameter up to 100 mm with through burning in sheet TS with thickness h=2.9 mm of the experimental composite cladding of the aircraft, tested for lightning resistance in the discharge circuit of a powerful high-voltage PCG of the UITOM-1 type, when it is directly affected by only the pulse *A*- component of the artificial lightning current with normalized ATP (I_{mA1}≈−212 kA; t_{mA1}≈32 μs; τ_{p1A}≈500 μs; J_{aA}≈2.11·10^6 J/Ω) [16]

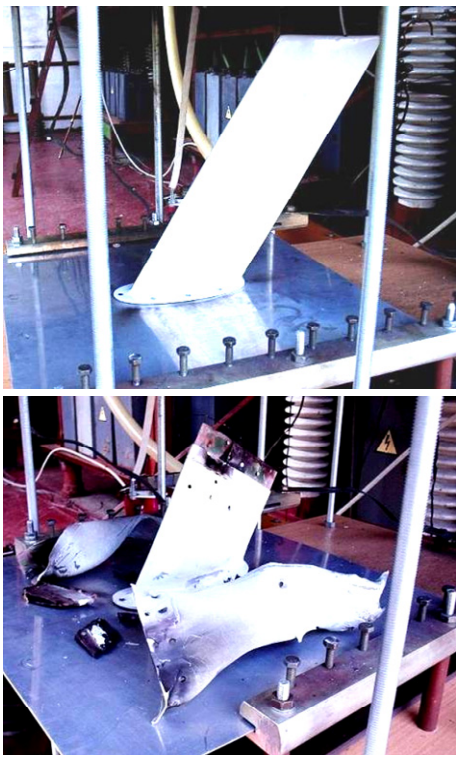

Fig. 19. General view of the experimental model of the aviation receiving-transmitting antenna of the AC before (*a*) and after (*b*) direct action on it in the high-current discharge circuit of the modernized powerful PCG of the UITOM-1 type of the pulse *A*-component of the artificial lightning current with normalized ATP (I_{mA1}≈−211.9 kA; t_{mA1}≈32 μs; τ_{p1A}≈500 μs; J_{aA}≈2,1·10^6 J/Ω) [16]

From the experimental data of Fig. 19, it follows that the experimental model of the receiving-transmitting antenna of the domestic aviation equipment, developed and created without taking into account the current requirements for lightning protection, cannot withstand lightning resistance tests according to the requirements of US regulatory documents [12-14]. Here, it was destroyed and disabled due to the specified impact of the powerful pulse *A*- component of the artificial lightning current (see Fig. 19,*b*).

Figures 20,*a*,*b* show the results of the test of the TS panel of the fuel tank of the «An» design aircraft with a hatch cover made of D16 aluminum alloy for lightning resistance (to sparks in its middle from a lightning strike in the aircraft) for area 1*A* under direct action on this TS with the help of a copper EEW from pulse current generators (GIC-*A*, GIC-*B* and GIC-*C**) of a powerful modernized high-voltage PSG of the UITOM-1 type, of the necessary *A*-, *B*- and *C**- components of the artificial lightning pulse current with standardized ATPs (U_{c1}≈−30 kV; U_{c2}≈−4 kV) to the corresponding points directly on its duralumin cover of the hatch.

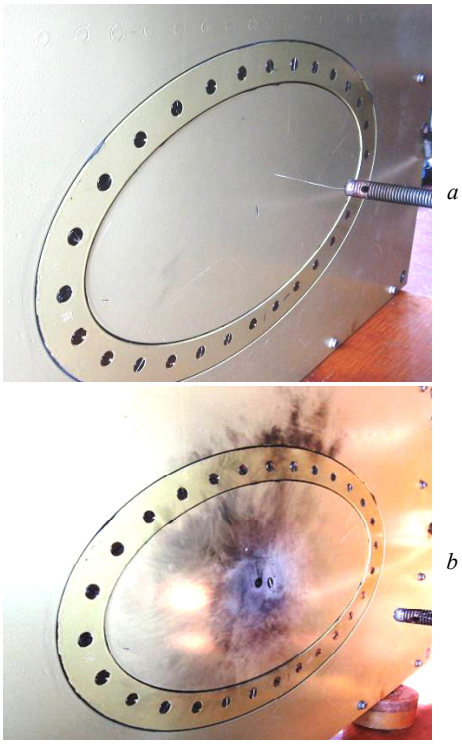

Fig. 20. External view of the TS of the panel of the domestic aircraft with hatch cover and D16 aluminum alloy fuel tank ring with stiffeners and various variants of their metallization before (*a*) and after (*b*) direct simultaneous action on it in the discharge circuit of the modernized powerful high-voltage PCG of the UITOM-1 type of normalized *A*- (I_{mA1}≈−196 kA; t_{mA1}≈42 μs; τ_{p1A}≈500 μs; J_{aA}≈2.13·10^6 J/Ω), *B*- (I_{mB}≈−7.32 kA; I_{cB}≈−2431 A; q_{LB}≈−12.4 C; τ_{p1B}≈5.1 mc) and *C**- (I_{mC*}≈−1032 A; τ_{p1C*}≈15·ms; q_{LC*}≈−7.2 C; I_{cC*}≈q_{LC*}/τ_{p1C*}≈−480 A) components of the full pulse current of artificial lightning (the zone of damage to the AC in atmospheric air by lightning discharge 1*A*)

Obtained according to Fig. 20 experimental data indicate that for damage area 1*A*, the action of *A*-, *B*-, and *C**- components of the lightning current with standardized ATPs on the TS of the panel of the cladding of the AC fuel tank made of aluminum alloy D16 with hatch cover leads to the penetration of the corresponding electric discharge products (black soot around the sealing perimeter of the lid of this hatch and sparks recorded by our camera) from the direct action of lightning discharges simulated in laboratory conditions to the area of its inner surface, which can lead to an explosion of steam in the fuel tank of the AC and its catastrophe.

From the experimental data obtained in the open air in the conditions of a high-voltage electrophysical laboratory (see Fig. 15-20), despite their fragmentary nature, the conclusion follows that the metal (composite) elements of the aircraft structure and the receiving and transmitting radio technical devices of the AC before their manufacture and implementation in practice, should be checked in the conditions of a high-voltage electrophysical laboratory for electromagnetic compatibility and resistance to direct action on them of the corresponding components of the full pulse current of artificial lightning (see Table 1).

Conclusions. Currently, Research and Design Institute «Molniya» of National Technical University «Kharkiv Polytechnic Institute» has at its disposal a powerful, modernized high-voltage PCG of the UITOM-1 type with improved high-voltage high-current measuring devices included in its composition, which are capable of reliably generating and measuring the main components in the conditions of a high-voltage electrophysical laboratory full pulse current of artificial lightning operating in the open air and to test the lightning resistance of various on-board devices (systems) of objects of aviation and rocket and space technology. It is shown that in the high-current discharge circuit of the indicated powerful high-voltage PCG, the pulse *A*- (repeated pulse *D*-), intermediate *B*- and long-term *C*- (shortened long-term *C**-) components of the full pulse current of artificial lightning are simulated, the ATPs of which satisfy the strict technical requirements of regulatory documents of the USA SAE ARP 5412: 2013, SAE ARP 5414: 2013 and SAE ARP 5416: 2013. Field electromagnetic tests of aviation and rocket-space equipment being developed and modernized for resistance to direct action on its main on-board devices (systems) and structural elements with metal and composite materials of the specified main components of the full pulse current of artificial lightning will contribute to increasing the survivability of the aircrafts in the conditions of their flight and stay in the electrically active Earth's atmosphere with powerful lightning pulse spark discharges.

Acknowledgment. The work was carried out with the support of the Ministry of Education and Science of Ukraine (project DB No. 0123U101704).

Conflict of interest. The authors declare no conflict of interest.

REFERENCES

1. Uman M.A. Natural and artificially-initiated lightning and lightning test standards. *Proceedings of the IEEE*, 1988, vol. 76, no. 12, pp. 1548-1565. doi: https://doi.org/10.1109/5.16349.

2. Uman M.A., Rakov V.A. A critical review of nonconventional approaches to lightning protection. Bulletin *of the American Meteorological Society*, 2002, vol. 83, no. 12, pp. 1809-1820. doi: https://doi.org/10.1175/BAMS-83-12-1809.

3. Kravchenko V.I. *Lightning. Electromagnetic factors and their damaging effects on technical equipment*. Kharkiv, NTMT Publ., 2010. 292 p. (Rus).

4. *MIL-STD-464A. Department of Defense Interface Standard: Electromagnetic Environmental Effects, Requirements for Systems*. 19 December 2002, 162 p.

5. Uman M.A. *Lightning*. Moscow, Mir Publ., 1972. 327 p. (Rus).

6. *DO-160G. Environmental Conditions and Test Procedures for Airborne Equipment*. USA, 2011. 438 p.

7. *AECTP-500. NATO Standard Electromagnetic Environmental Effects Tests and Verification. Edition E Version 1.* Brussels, NSO Publ., 2016. 1125 p.

8. *IEC 62305-1: 2010. Protection against Lightning. Part 1: General Principles*. Geneva, IEC Publ., 2010. 72 p.

9. Baranov M.I., Buriakovskyi S.G., Kniaziev V.V., Rudenko S.S. Analysis of characteristics and possibilities of high-voltage electrical engineering complex Scientific-&-Research Planning-&-Design Institute «Molniya» of NTU «KhPI» for the tests of objects of energy, armament, aviation and space-rocket technique on electric safety and electromagnetic compatibility. *Electrical Engineering & Electromechanics*, 2020, no. 4, pp. 37-53. doi: https://doi.org/10.20998/2074-272X.2020.4.06.

10. Piantini A., Janiszewski J.M. The influence of the upward leader on lightning induced voltages. *Proceedings of the 23rd International Conference on Lightning Protection (ICLP)*, 1996, vol. 1, pp. 352-357.

11. Guerrieri S., Nucci C.A., Rachidi F., Rubinstein M. On the influence of elevated strike objects on directly measured and indirectly estimated lightning currents. *IEEE Transactions on Power Delivery*, 1998, vol. 13, no. 4, pp. 1543-1555. doi: https://doi.org/10.1109/61.714865.

12. *SAE ARP 5412: 2013. Aircraft Lightning Environment and Ralated Test Waveforms*. SAE Aerospace. USA, 2013. 56 p.

13. *SAE ARP 5414: 2013. Aircraft Lightning Zoning*. SAE Aerospace. USA, 2013, 33 p.

14. *SAE ARP 5416: 2013. Aircraft Lightning Test Methods*. SAE Aerospace. USA, 2013, 145 p.

15. Baranov M.I., Koliushko G.M., Kravchenko V.I., Nedzel'skii O.S., Dnyshchenko V.N. A current generator of the artificial lightning for full-scale tests of engineering objects. *Instruments and Experimental Techniques*, 2008, vol. 51, no. 3, pp. 401-405. doi: https://doi.org/10.1134/S0020441208030123.

16. Baranov M.I. *Selected topics of Electrophysics. Monograph in 4 vols. Vol. 4. Effects of interaction of physical bodies with fields and currents*. Kharkiv, FOP Panov A.N. Publ., 2023. 552 p. (Ukr).

17. Baranov M.I., Buriakovskyi S.G., Hrytsenko A.S., Kostiuk V.A. Results of investigations of thermal resistibility of prototypes of aluminum alloy panels of fuel tank of airplane to direct action of normalized components of artificial lightning current. *Electrical Engineering & Electromechanics*, 2019, no. 6, pp. 29-38. doi: https://doi.org/10.20998/2074-272X.2019.6.04.

18. Kuhling H. *Handbook of Physics*. Moscow, Mir Publ., 1982. 520 p. (Rus).

19. Berzan V.P., Gelikman B.Yu., Guraevskyi M.N., Ermuratskyi V.V., Kuchinskyi G.S., Mezenin O.L., Nazarov N.I., Peregudova E.N., Rud' V.I., Sadovnikov A.I., Smirnov B.K., Stepina K.I. *The Electrical capacitors and capacitor units. Reference Book*. Moscow, Energoatomizdat Publ., 1987. 656 p. (Rus).

20. Knopfel' G. *Ultra strong pulsed magnetic fields*. Moscow, Mir Publ., 1972. 391 p. (Rus).

21. Dashuk P.N., Zayents S.L., Komel'kov V.S., Kuchinskiy G.S., Nikolayevskaya N.N., Shkuropat P.I., Shneerson G.A. *The technique of large pulsed currents and magnetic fields*. Moscow, Atomizdat Publ., 1970. 472 p. (Rus).

22. Vovchenko A.I., Bohuslavsky L.Z., Myroshnychenko L.N. Trends in development of high-powered high-voltage pulse current generators in the Institute of Pulse Processes and Technology of Ukraine (review). *Technical electrodynamics*, 2010, no. 5, pp. 69-74. (Rus).

23. Baranov M.I., Rudakov S.V. Development of new charts of capacitance-resistance defense of high-voltage capacitors of powerful capacity stores of energy from emergency currents.

Electrical Engineering & Electromechanics, 2015, no. 6, pp. 47-52. (Rus). doi: https://doi.org/10.20998/2074-272X.2015.6.08.
24. Baranov M.I, Bocharov V.A., Nosenko M.A. Limit characteristics of the scattered pulse power and high-power ceramic resistors bulk type TVO-60. *Bulletin of NTU «KhPI». Series: Technique and electrophysics of high voltage*, 2007, no. 20, pp. 45-56. (Rus).
25. Shwab A. *High voltage measurements*. Moscow, Energy Publ., 1973. 233 p. (Rus).
26. Kuzhekin I.P. *Test facilities and measurements on high voltage*. Moscow, Energy Publ., 1980. 136 p. (Rus).
27. Wada A., Horii K. Measurement of Lightning Current by Magnetizing Effect of Magnetic Tape. *IEEJ Transactions on Power and Energy*, 1991, vol. 111, no. 1, pp. 45-50. doi: https://doi.org/10.1541/ieejpes1990.111.1_45.
28. Hussein A.M., Janischewskyj W., Chang J.-S., Shostak V., Chisholm W.A., Dzurevych P., Kawasaki Z.-I. Simultaneous measurement of lightning parameters for strokes to the Toronto Canadian National Tower. *Journal of Geophysical Research: Atmospheres*, 1995, vol. 100, no. D5, pp. 8853-8861. doi: https://doi.org/10.1029/95JD00543.
29. Baranov M.I., Kniaziev V.V., Rudakov S.V. The Coaxial Shunt for Measurement of Current Pulses of Artificial Lightning with the Amplitude up to ±220 kA. *Instruments and Experimental Techniques*, 2018, vol. 61, no. 4, pp. 501-505. doi: https://doi.org/10.1134/S0020441218030156.
30. Baranov M.I., Buriakovskyi S.G., Rudakov S.V. The metrology support in Ukraine of tests of objects of energy, aviation and space-rocket engineering on resistibility to action of pulses of current (voltage) of artificial lightning and commutation pulses of voltage. *Electrical Engineering & Electromechanics*, 2018, no. 5, pp. 44-53. doi: https://doi.org/10.20998/2074-272X.2018.5.08.

Received 16.11.2023
Accepted 08.01.2024
Published 01.05.2024

M.I. Baranov[1]*, Doctor of Technical Science, Professor,*
S.G. Buriakovskyi[1]*, Doctor of Technical Science, Professor,*
[1] Research and Design Institute «Molniya»
of National Technical University «Kharkiv Polytechnic Institute»,
47, Shevchenko Str., Kharkiv, 61013, Ukraine,
e-mail: baranovmi49@gmail.com (Corresponding Author);
sergbyr@i.ua

How to cite this article:
Baranov M.I., Buriakovskyi S.G. Electrical engineering equipment for generating and measuring of complete pulse current of artificial lightning in the conditions of high-voltage electrophysics laboratory. *Electrical Engineering & Electromechanics*, 2024, no. 3, pp. 55-65. doi: https://doi.org/10.20998/2074-272X.2024.3.08

UDC 621.319 https://doi.org/10.20998/2074-272X.2024.3.09

E. El Sherkawy, L.S. Nasrat, M. Rihan

The effect of thermal ageing on electrical and mechanical properties of thermoplastic nanocomposite insulation of power high-voltage cables

This research explores the thermal ageing influence on the Low Density Polyethylene (LDPE) dielectric properties, which is utilised as electrical insulation in high-voltage cables. An accelerated thermal ageing test was done at four temperature ranges ranging from 25 °C to 120 °C to define the degree of material deterioration under thermal ageing and to prevent its failure. LDPE composite samples were made by adding aluminium oxide (Al_2O_3) inorganic filler in two different grain sizes (nano and micro) with various concentrations. The effect of adding inorganic filler on the acceleration of the thermal ageing of the polymer was studied by heating the samples for different periods of time and measuring the dielectric strength of the samples. The obtained results show that thermal ageing considerably affects the electrical properties of the material. The LDPE/Al_2O_3 nanofiller sample has the highest dielectric strength value at different temperatures. Thermogravimetric analysis was used to investigate the thermal characteristics of materials. The mechanical characteristics of LDPE polymer are studied using tensile strength and elongation at break tests. References 27, table 4, figures 6.

Key words: **low density polyethylene, nano filler, micro filler, dielectric strength, thermal ageing, thermogravimetric analysis.**

У цьому дослідженні вивчається вплив термічного старіння на діелектричні властивості поліетилену низької щільності (LDPE), який використовується як електрична ізоляція у високовольтних кабелях. Випробування на прискорене термічне старіння було проведено в чотирьох температурних діапазонах від 25 до 120 °C, щоб визначити ступінь руйнування матеріалу при термічному старінні і запобігти його виходу з ладу. Композитні зразки LDPE були виготовлені шляхом додавання неорганічного наповнювача з оксиду алюмінію (Al_2O_3) з двома різними розмірами зерен (нано та мікро) у різних концентраціях. Вплив додавання неорганічного наповнювача на прискорення термічного старіння полімеру вивчали шляхом нагрівання зразків протягом різних періодів часу та вимірювання діелектричної міцності зразків. Отримані результати показують, що термічне старіння істотно впливає на електричні властивості матеріалу. Зразок нанонаповнювача LDPE/Al_2O_3 має найбільше значення діелектричної міцності за різних температур. Термогравіметричний аналіз використовувався для дослідження термічних характеристик матеріалів. Механічні характеристики полімеру LDPE вивчаються з використанням випробувань на міцність на розрив та подовження при розриві. Бібл. 27, табл. 4, рис. 6.

Ключові слова: **поліетилен низької щільності, нанонаповнювач, мікронаповнювач, діелектрична міцність, термічне старіння, термогравіметричний аналіз.**

Introduction. Super insulating polymers are commonly employed in high voltage insulators, particularly in high voltage cables. Thermal oxidation processes may occur for the insulation layers in contact with the cable core due to the high working temperature of the cable (around 90 °C) because of loading or overloading for short durations, resulting to insulation degradation and even failure. As a result, many researchers have been interested in the ageing and insulating properties of polymers in this environment [1, 2]. To create materials with better electrical and thermal properties, nanofillers were chosen to be added to polyethylene due to the high surface area presented to the matrix [3, 4]. Interestingly, with several weight percents of nanoparticles, PE-based nanocomposite can promote insulation properties effectively, which could be attributed to the nanoparticle-matrix interface [5, 6].

According to existing research on polyethylene insulating materials, filling nanoparticles can reduce the creation of space charge and enhance the dielectric, mechanical, and thermal properties of polyethylene [7-9]. Numerous studies make use of inorganic filler oxides like MgO, SiO_2, TiO_2, BN, etc., as well as how the improvement of polymer properties is impacted by the grain size of the filler (nano or micro) [10-12]. When evaluating the future application of polyethylene nanocomposites, the extended service life of insulating materials cannot be overlooked. Thermal ageing has been shown to have a major impact on the qualities of polyethylene materials, with numerous modifications possible, including variations in physicochemical parameters and microstructure [13]. During thermal ageing, several oxygenated compounds of low molecular weight may form in polyethylene, which may have a major influence on the space charge behavior of polyethylene insulating material [14, 15].

The purpose of this paper was to determine whether Al_2O_3 nano- and micro-particles, which have been shown to improve the dielectric strength of LDPE composites, can maintain these electrical properties after thermal ageing. To conduct thermal ageing tests, we chose four different percentages of nano composites and four different percentages of micro composites. The thermal properties of composites after thermal ageing were investigated using the thermogravimetric analysis (TGA) test. The dielectric strength test was used to evaluate the electrical characteristics of LDPE/Al_2O_3 composites after thermal ageing and the anti-thermal ageing mechanism offered by nanoparticles.

Literature review. Thermal deterioration of LDPE has been investigated. Chemical and electrical testings were performed on LDPE plaques that had been thermally stressed at high temperature (110 °C). Changes in the imaginary component of the dielectric constant have been connected to contributions from oxidation and morphological changes inside polymers. This comparison may serve as the starting point for the creation of non-destructive methods for electrical measurements-based polymer diagnostics [16, 17].

Nanoparticles improve the anti-thermal ageing capability of PE-based nanocomposites. The three metal oxides – magnesium oxide (MgO), zinc oxide (ZnO), and silicon dioxide were combined to form nanocomposites with a 1 wt.% concentration in each. Fourier-transform infrared spectra revealed that LDPE/MgO nano filler composites had the best anti-thermal ageing performance when compared to LDPE/SiO_2 nanocomposites, which had the worst using dielectric characteristics and space charge dispersion. The capacity of nanocomposites to maintain electrical properties was then investigated [18].

The zeolite/LDPE nano filler samples were produced and thermally aged to produce samples with varying ageing times. It was demonstrated that nano-zeolite doping may be an efficient way to stop the internal structure of the nanocomposite from being damaged by thermal ageing; during thermal ageing, carbonyl and hydroxyl levels considerably decreased and crystallinity greatly increased. The nanocomposite's shape and ageing resistance were greatly enhanced by nano-zeolite doping. It was discovered during the dielectric strength test that nano doping may significantly increase DC and AC breakdown field strength and stability during thermal ageing. Nanocomposite's dielectric constant can be decreased, and the rate of dielectric loss did not alter noticeably as the material aged [19].

During thermal ageing, the crystallinity and space charge accumulation characteristics of pure LDPE and LDPE/TiO_2 samples were assessed using a pulse electro-acoustic method system and a differential scanning calorimeter. It was determined that TiO_2 nano filler may increase LDPE crystallinity, and the capacity of LDPE/TiO_2 to reduce space charge was substantial at a TiO_2 mass concentration of 1 %. Furthermore, thermal ageing can degrade the microstructure and impair material crystallinity, increasing the sources of space charge [20].

Methods. Sample preparation. The basic polymer utilised was additive-free LDPE with a particle diameter of less than 0.2 mm on average, a melt flow index of 2 g/10 min at 190 °C, and a density of 0.91-0.925 mg/cm^3. It was purchased from SABIC, KSA, in the form of granules. The nano particles used were Al_2O_3 inorganic fillers with two different grain sizes (micro filler with a 60 µm particle size and nano filler with a 50 nm particle size). In a twin-screw extruder at 448 K, LDPE and filler particles were melt-blended. Nanocomposites were made in concentrations of 1 wt.%, 3 wt.%, 5 wt.%, and 7 wt.%, and micro composites were made in concentrations of 10 wt.%, 20 wt.%, 30 wt.%, and 40 wt.%. Composite samples were press-moulded at 433 K and at a pressure of 10 MPa to produce sheets with dimensions of 150 mm by 150 mm and a thickness of about 1 mm.

Samples were thermally aged in a fixed-temperature vacuum oven at 25 °C, 60 °C, 100 °C, and 120 °C at regular intervals (0, 10, 20, and 30 min). The aged samples were subjected to dielectric strength testing.

Table 1 shows the weight of the LDPE composite mixture (g) used in the manufacture of samples. It also shows the added weight of the LDPE polymer and the added weight of the Al_2O_3 filler at each mixing ratio.

Table 1

Different samples compositions

Sample		Symbol	LDPE, g	Al_2O_3, g
LDPE		B	150	0
LDPE + micro Al_2O_3	10 %	M10	135	15
	20 %	M20	120	30
	30 %	M30	105	45
	40 %	M40	90	60
LDPE + nano Al_2O_3	1 %	N1	148.5	1.5
	3 %	N3	145.5	4.5
	5 %	N5	142.5	7.5
	7 %	N7	139.5	10.5

Thermal ageing test. Heat causes some physical and chemical changes in polymers. These variations are determined by the severity of the temperature and the length of exposure. High temperatures do not always cause the polymer material to decompose. Prolonged exposure to high temperatures, on the other hand, will cause gradual changes in physical properties, eventually leading to collapse. The cable is subjected to overloads and short-circuit currents. When the current exceeds the rated value, it raises the temperature of the core. The electrical performance of the cable is affected by repeatedly exposing the insulation layers adjacent to the core to high temperatures. Thermal ageing of the samples is performed to determine the effect of temperature increases on the dielectric strength value. Thermal ageing was tested according to [21].

The required procedures and precautions to obtain highly accurate readings for each sample during the thermal ageing test are as follows:

- Before beginning thermal ageing tests, clean and dry the samples.
- The samples were heated to different temperatures (25 °C, 60 °C, 100 °C, and 120 °C) during specified periods of time (0, 10, 20, and 30 min) using a fixed-temperature oven, as shown in Fig. 1.
- As shown in Fig. 2, the dielectric strength of the aged samples was measured. The measurement was repeated ten times with three samples exposed to the same conditions, and an average value was taken for the experimental readings.
- The time intervals between successive tests of each sample should be suitable and sufficient.
- To apply electrical safety requirements, all testing circuit linkages must be correct.
- The voltage was gradually raised until the voltage breakdown occurred at a nearly constant rate of 2 kV/s. The dielectric strength was recorded.

Fig. 1. Fixed temperature oven

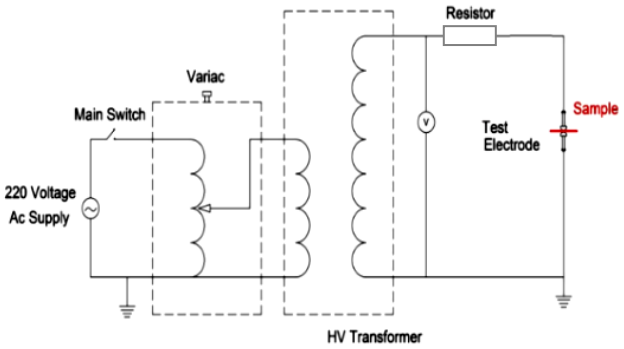

Fig. 2. Dielectric strength schematic diagram

Thermogravimetric analysis (TGA) test. TGA is a key test for understanding and identifying material thermal

characteristics. TGA is a thermal test that calculates the weight loss of volatile components with temperature rise uniformly. According to [22], based on weight loss at high temperatures as well as thermal stability in a brief period, it is a great approach for figuring out the filler and polymer content. The TGA test was carried out in the NSI nitrogen environment using Perkin-Elmer equipment [23-26]. Approximately 10 mg of Al_2O_3/LDPE samples were sliced and heated from 35 °C to 700 °C while the samples were weighed and shown on the computer screen.

Mechanical analysis. Tensile strength (MPa) and elongation at break (%) are critical metrics for characterizing polymer mechanical performance and determining the influence of inorganic filler. A Zwick Roell LTM electrodynamic testing device was used to assess the tensile strength (MPa) and elongation at break (%) of the composite specimens. A schematic representation is shown in Fig. 3. The test results were evaluated using [27].

Results and analysis. Thermal ageing measurements. Table 2 shows average results for the dielectric strength of LDPE loaded with varied percentages of Al_2O_3 inorganic filler thermally strained over different time intervals at different temperatures.

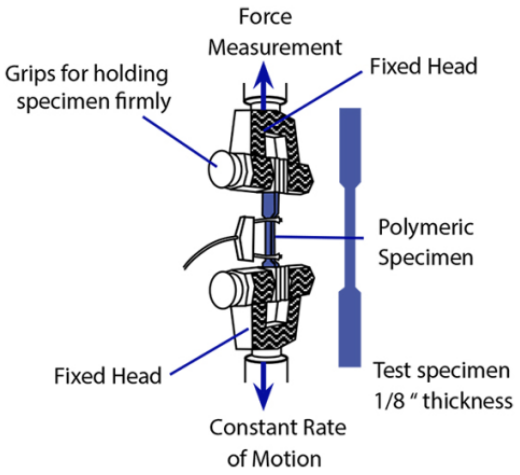

Fig. 3. Schematic diagram for measuring the tensile strength of LDPE composite samples

Table 2 shows that, when compared to neat and micro filled with LDPE, all LDPE micro composites have increased dielectric strength. When compared to other concentrations of the same particle size of filler, the micro Al_2O_3 composite of 30 % has the highest dielectric strength value.

Table 2

Average dielectric strength for micro- and nano-Al_2O_3 composite samples thermal stressed at 25 °C, 60 °C, 100 °C, 120 °C for different times 10 min, 20 min, 30 min

Sample	Average dielectric strength, kV/mm											
	at 25 °C			at 60 °C			at 100 °C			at 120 °C		
	10 min	20min	30min	10 min	20min	30min	10 min	20min	30min	10 min	20min	30min
B	20.45	18.28	17.08	18.33	16.02	15.11	14.61	12.08	11.21	12.77	11	9.89
M10	25.81	25.27	24.71	22.83	22.29	21.74	20.38	19.85	19.29	16.55	16.02	15.46
M20	28.59	28.17	27.64	25.66	25.21	24.69	22.46	22.01	21.49	18.04	17.59	17.07
M30	32.67	32.25	31.74	30.54	20.09	29.58	27.34	26.91	26.39	23.94	23.49	22.95
M40	29.77	29.25	28.7	26.59	26.06	25.5	24.00	23.47	22.97	21.09	20.55	20.01
N1	26.89	26.69	26.12	25.81	24.38	24.00	23.11	21.83	21.11	20.39	19.08	18.27
N3	29.09	27.84	27.06	26.55	25.28	25.00	24.25	23.54	22.86	22.35	20.89	20.03
N5	35.61	35.18	34.68	34.31	33.72	33.04	32.04	31.32	30.85	29.67	28.86	28.3
N7	39.85	39.34	38.79	36.96	35.12	34.56	34.37	32.89	32.31	31.85	30.34	29.74

Table 2 also shows that the electrical properties of LDPE composites filled with Al_2O_3 are reliable at 7 % nano particle size and have a dielectric strength greater than that of micro Al_2O_3.

As shown in Table 2, the dielectric strength of nano Al_2O_3 composites is greater than that of micro Al_2O_3 composites at all concentrations. By increasing the filler concentration, the LDPE composite achieves maximum dielectric strength. The dielectric strength decreases when the filler concentration exceeds critical values.

The physical properties of the samples, such as shrinkage and deformation, are affected by continuously raising the temperature (Fig. 4). High temperatures reduce dielectric strength. Lower filler contents, such as in nano composite, can result in greater flexibility, ease of processing during product manufacturing, and improved electrical performance of polymers.

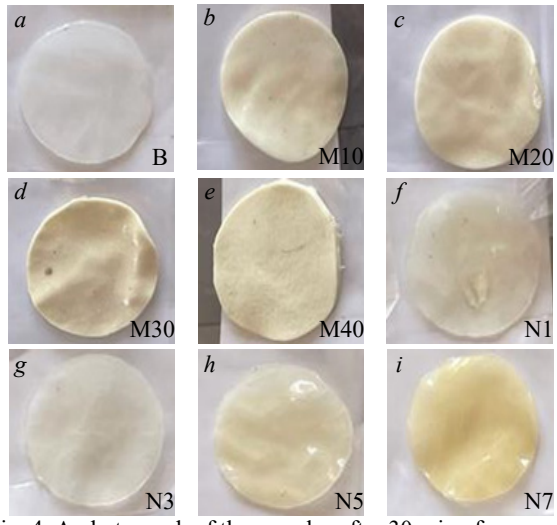

Fig. 4. A photograph of the samples after 30 min of exposure to a temperature of 120 °C

Thermogravimetric analysis. TGA provides the variation in the weight of sample loss with respect to temperature in a controlled environment. The release of moisture or gases from the material's breakdown causes weight loss as the temperature rises. TGA provides ageing stability information within short test times.

TGA analyses of the samples were done to comprehend the thermal performance. TGA of samples with various micro Al_2O_3 loadings is displayed in Fig. 5.

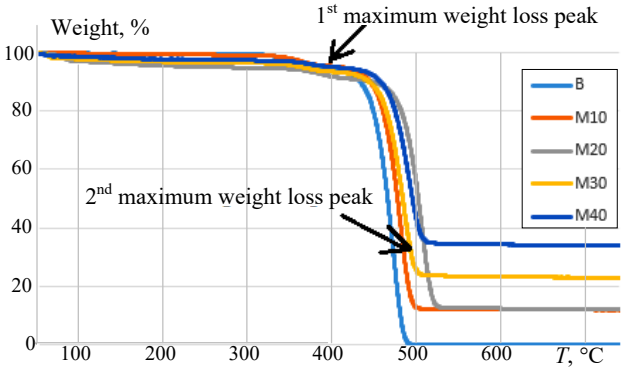

Fig. 5. TGA for LDPE with different micro Al_2O_3 filler concentration

Temperature has no discernible impact on weight for all samples in the temperature range of 35 °C to 450 °C, as demonstrated in Fig. 4. The 1st maximum weight loss peak on the TGA curve above 450 °C is caused by Al_2O_3 filler water loss. The burning of the LDPE side chains may be the cause of the 2nd maximum weight loss peak. When the temperature was raised from 35 °C to 700 °C, the weight loss of pure LDPE was the least. When compared to all composite samples and a blank one, the weight loss of composites filled with 40 wt.% micro Al_2O_3 provides the highest thermal stability.

Figure 6 studies the effect of thermal stability on LDPE samples filled with various concentrations of nano Al_2O_3 filler to determine changes in the weight of a sample in relation to changes in temperature. Thermal stability is the ability of a polymeric material to withstand the effects of heat while preserving its properties, such as toughness, strength, or elasticity, at a certain temperature.

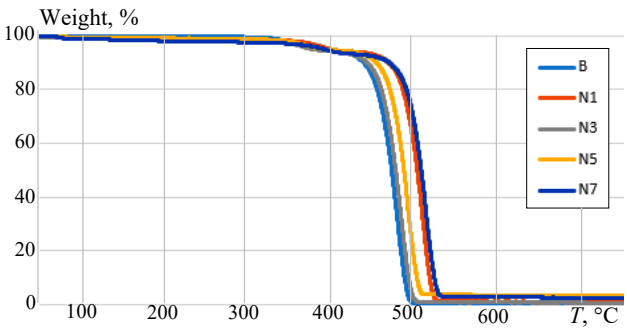

Fig. 6. TGA for LDPE with different nano Al_2O_3 filler concentration

Mechanical test results. Studying the tensile strength of LDPE composite samples. The maximum stress that a material can sustain when being stretched or pulled before necking is known as tensile strength. The load at break is divided by the initial minimum cross-sectional area to determine tensile strength.

The results from 3 samples of each test have been averaged to reduce error because the sheet's structure is not homogeneous and because the sheet (20 cm × 20 cm) obtained through mixing is not. Table 3 displays the tensile strength of micro and nano Al_2O_3 filled LDPE composites as a function of filler loading.

Table 3

Tensile strength (MPa) for nano and micro Al_2O_3/LDPE composites

Sample	Tensile strength, MPa			Average values of tensile strength
	1st	2nd	3rd	
B	10.27	6.73	7.4	8.13
N1	9.83	8.61	12.24	10.23
N3	10.83	12.75	9.23	10.93
N5	11.88	11.27	10.96	11.37
N7	11.36	14.32	11.91	12.53
M10	11.25	10.13	10.19	10.53
M20	10.32	12.31	12.75	11.8
M30	10.19	12.10	12.3	11.75
M40	12.21	10.92	10.41	11.18

As shown in Table 3, LDPE composites with Al_2O_3 loading improve tensile strength at a 7 wt.% loading level. As the amount of micro Al_2O_3 increases, the tensile strength of LDPE composites decreases in all values.

Table 3 indicates that increasing micro Al_2O_3 concentrations result in a substantial improvement in tensile strength. In comparison to the other concentrations for the same filler, LDPE loaded with 7 wt.% nano Al_2O_3 records the highest tensile strength.

Studying the elongation at break of LDPE composite samples. Table 4 displays the elongation at break characteristics off LDPE composites with micro- and nano sized Al_2O_3 loadings.

Table 4

Elongation at break for nano and micro LPDE/Al_2O_3 composites

Sample	Elongation at break (Ɛ-F max %)			Average values of elongation at break
	1st	2nd	3rd	
B	110.32	101.8	103.52	105.21
N1	116.54	114.36	109.65	113.2
N3	129.23	117.65	121.39	122.7
N5	142.5	135.62	136.85	138.32
N7	144.92	136.42	140.85	140.73
M10	105.52	106.58	113.52	108.54
M20	120.65	125.02	119.54	121.7
M30	112.65	118.2	111.95	114.3
M40	102.35	100.65	98.9	100.63

For LDPE composite samples, the values of elongation at break decrease as the amount of micro Al_2O_3 increases.

Table 4 demonstrates how the addition of nano Al_2O_3 can enhance elongation at break. When nano Al_2O_3 is added at a 7 wt.% concentration, the composite exhibits greater break elongation than pure LDPE.

Discussion. By interfering with the polymer crystal and filling spaces and gaps, an inorganic filler – whether micro or nanosized – works to improve the fundamental polymer's electrical, mechanical, and thermal properties.

Heat exposure of the insulator throughout various operating situations reduces the cable's lifespan. It is critical to conduct a thermal ageing test to determine the effect of temperature and exposure duration on the value of the polymer's dielectric strength. According to the results of the thermal ageing test, the value of the insulating strength declined as the time of temperature exposure increased.

Compared to the percentage of micro filler, a small amount of nano filler gave better results in dielectric strength and tensile strength. Dielectric properties of LDPE composite loaded with Al_2O_3 are reliable at 7 wt.% nano scale and have maximum dielectric strength.

Conclusions. This paper demonstrated the effect of adding micro- and nano- Al_2O_3 to Low Density Polyethylene (LDPE) composites. The experimental results lead to the following conclusions:

- The physical properties of the samples are affected when they are exposed to high temperatures for extended periods of time. This effect causes deformations in the samples, which cause them to become more solid.
- The high temperature and the length of time that the samples are exposed to high temperatures have a negative impact on their dielectric strength.
- The thermal ageing has been decreased by adding Al_2O_3 filler to LDPE.
- With the addition of nano filler, the electrical performance has been greatly enhanced. Lower filler contents, as in nano composite, can contribute to greater flexibility, ease of processing during product manufacturing, and improved thermal ageing performance of samples.
- The optimal Al_2O_3 filler concentration for reducing thermal ageing in LDPE composites is 7 % nano Al_2O_3.
- Thermogravimetric analysis (TGA) of nano composite outperforms that of micro composite. A7 wt.% nano Al_2O_3 filler composite provided the best dielectric strength and TGA.
- The addition of micro-Al_2O_3 filler reduced the mechanical properties of LDPE. By increasing the amount of nano-Al_2O_3 filler in the sample to 7 wt.%, the tensile strength (MPa) and elongation at break (%) characteristics are enhanced.

In the future, it is proposed to blend two or three fillers with LDPE and investigate their electrical, mechanical, physical, and thermal characteristics. It is also suggested that composite samples be immersed in water to investigate the effect of water leakage on the electrical characteristics of the insulator.

Acknowledgements. The authors would like to thank the South Valley University Department of Electrical Engineering, the staff of the High Voltage Laboratory at the Faculty of Engineering, Aswan University, the National Research Centre (Polymers and Dyes Department), and the National Institute of Standards (NIS) for their assistance in preparing the samples and conducting the experiments on them.

Conflict of interest. The authors declare no conflict of interest.

REFERENCES

1. Shimada A., Sugimoto M., Kudoh H., Tamura K., Seguchi T. Degradation distribution in insulation materials of cables by accelerated thermal and radiation ageing. *IEEE Transactions on Dielectrics and Electrical Insulation*, 2013, vol. 20, no. 6, pp. 2107-2116. doi: https://doi.org/10.1109/TDEI.2013.6678859.

2. Wang Y., Wang C., Zhang Z., Xiao K. Anti-thermal aging properties of low-density polyethylene-based nanocomposites. *IEEE Transactions on Dielectrics and Electrical Insulation*, 2018, vol. 25, no. 3, pp. 1003-1013. doi: https://doi.org/10.1109/TDEI.2018.006783.

3. Huang X., Xie L., Yang K., Wu C., Jiang P., Li S., Wu S., Tatsumi K., Tanaka T. Role of interface in highly filled epoxy/BaTiO 3 nanocomposites. Part II- effect of nanoparticle surface chemistry on processing, thermal expansion, energy storage and breakdown strength of the nanocomposites. *IEEE Transactions on Dielectrics and Electrical Insulation*, 2014, vol. 21, no. 2, pp. 480-487. doi: https://doi.org/10.1109/TDEI.2013.004166.

4. Wang C., Wang J., Wu C., Li W., Yang Z., Wu K. Study on Thermal Conductivity of BNNs/Mg(OH) 2 /LDPE Composites Based on Melt Blending Method. *2021 IEEE International Conference on the Properties and Applications of Dielectric Materials (ICPADM)*, 2021, pp. 214-217. doi: https://doi.org/10.1109/ICPADM49635.2021.9493996.

5. Kong X., Du B., Li J., Zhang Z., Xiao M., Zhu W., Su J., Jiang T., Liang H., Yang D., Pan X. Effects of high thermal conductivity LDPE/BN composites on temperature field distribution and ampacity of power cable. *2018 12th International Conference on the Properties and Applications of Dielectric Materials (ICPADM)*, 2018, pp. 45-48. doi: https://doi.org/10.1109/ICPADM.2018.8401025 .

6. Wang X., Lv Z., Wu K., Chen X., Tu D., Dissado L.A. Study of the factors that suppress space charge accumulation in LDPE nanocomposites. *IEEE Transactions on Dielectrics and Electrical Insulation*, 2014, vol. 21, no. 4, pp. 1670-1679. doi: https://doi.org/10.1109/TDEI.2014.004292.

7. Zhang C., Ren Z., Ren Q., Zhao H. Influence of nanoparticle morphology on the direct current dielectric properties of polypyrrole/LDPE nanocomposites. *Fuhe Cailiao Xuebao/Acta Materiae Compositae Sinica*, 2023, vol. 40, no. 5, pp. 2598-2608. doi: https://doi.org/10.13801/j.cnki.fhclxb.20220809.009.

8. Maur S., Chakraborty B., Dalai S., Chatterjee B. Investigation on Effects of Thermal Ageing on LDPE Based on Polari zation and Depolarization Currents. *2020 IEEE 1st International Conference for Convergence in Engineering (ICCE)*, 2020, pp. 200-204. doi: https://doi.org/10.1109/ICCE50343.2020.9290689.

9. Guo C., Li J., Gao Y., Liu B., Du B. Effect of Nanoparticle Type on Charge Transport Characteristics of LDPE/Micro-BN composite with High Thermal Conductivity. *2023 IEEE 4th International Conference on Electrical Materials and Power Equipment (ICEMPE)*, 2023, pp. 1-4. doi: https://doi.org/10.1109/ICEMPE57831.2023.10139611.

10. Kong X., Du B., Li J., Xiao M., Mu J. Effects of high thermal conductivity on power cable ampacity with LDPE/BN composites. *2017 IEEE Conference on Electrical Insulation and Dielectric Phenomenon (CEIDP)*, 2017, pp. 505-508. doi: https://doi.org/10.1109/CEIDP.2017.8257649.

11. Wang Y., Wang C., Zhang Z., Xiao K. Anti-thermal aging ability of low density polyethylene enhanced by MgO nanoparticles. *2017 IEEE Conference on Electrical Insulation and Dielectric Phenomenon (CEIDP)*, 2017, pp. 497-500. doi: https://doi.org/10.1109/CEIDP.2017.8257595.

12. Li Y., Wu J., Yin Y. Study on Conductivity Characteristics of LDPE/SiO2 Nanocomposite at High Temperature. *2023 IEEE 4th International Conference on Electrical Materials and Power Equipment (ICEMPE)*, 2023, pp. 1-4. doi: https://doi.org/10.1109/ICEMPE57831.2023.10139744.

13. Wang Y., Wang C., Zhang Z., Xiao K. Effect of Nanoparticles on the Morphology, Thermal, and Electrical Properties of Low-Density Polyethylene after Thermal Aging. *Nanomaterials*, 2017, vol. 7, no. 10, art. no. 320. doi: https://doi.org/10.3390/nano7100320.

14. Li Z., Liu N., Gabriel S., Chen G. Thermal ageing and its impact on charge trapping parameters in LDPE. *2017 IEEE Conference on Electrical Insulation and Dielectric Phenomenon (CEIDP)*, 2017, pp. 820-823. doi: https://doi.org/10.1109/CEIDP.2017.8257609.

15. Luyt A.S., Gasmi S.A., Malik S.S., Aljindi R.M., Ouederni M., Vouyiouka S.N., Porfyris A.D., Pfaendner R., Papaspyrides C.D. Artificial weathering and accelerated heat ageing studies

on low-density polyethylene (LDPE) produced via autoclave and tubular process technologies. *Express Polymer Letters*, 2021, vol. 15, no. 2, pp. 121-136. doi: https://doi.org/10.3144/expresspolymlett.2021.12.
16. Wang Y., Wang C., Zhang Z., Xiao K. Anti-thermal aging properties of low-density polyethylene-based nanocomposites. *IEEE Transactions on Dielectrics and Electrical Insulation*, 2018, vol. 25, no. 3, pp. 1003-1013. doi: https://doi.org/10.1109/TDEI.2018.006783.
17. Hedir A., Slimani F., Moudoud M., Bellabas F., Loucif A. Impact of Thermal Constraint on the Low Density Polyethylene (LDPE) Properties. *Lecture Notes in Electrical Engineering*, 2020, vol. 599, pp. 952-960. doi: https://doi.org/10.1007/978-3-030-31680-8_92.
18. Suraci S.V., Fabiani D., Mazzocchetti L., Maceratesi V., Merighi S. Investigation on Thermal Degradation Phenomena on Low Density Polyethylene (LDPE) through Dielectric Spectroscopy. *2018 IEEE Conference on Electrical Insulation and Dielectric Phenomena (CEIDP)*, 2018, pp. 434-437. doi: https://doi.org/10.1109/CEIDP.2018.8544734.
19. Han B., Yin C., Chang J., Pang Y., Lv P., Song W., Wang X. Study on the Structure and Dielectric Properties of Zeolite/LDPE Nanocomposite under Thermal Aging. *Polymers*, 2020, vol. 12, no. 9, art. no. 2108. doi: https://doi.org/10.3390/polym12092108.
20. Wang Y., Li Y., Zhang Z. Space Charge Accumulation Characteristics of LDPE/TiO_2 Nanocomposites under Thermal Aging. *2018 IEEE Conference on Electrical Insulation and Dielectric Phenomena (CEIDP)*, 2018, pp. 129-132. doi: https://doi.org/10.1109/CEIDP.2018.8544767.
21. *ASTM D 3045: Standard Practice for Heat Ageing of Plastics Without Load*. ASTM International, West Conshohocken, PA, 2020, 6 p.
22. *ASTM E1131: Standard test method for compositional analysis by thermogravimetry*. ASTM International, West Conshohocken, PA, 2020, 6 p.
23. Zheng Y., Tao L., Yang X., Huang Y., Liu C., Zheng Z. Study of the thermal behavior, kinetics, and product characterization of biomass and low-density polyethylene co-pyrolysis by thermogravimetric analysis and pyrolysis-GC/MS. *Journal of Analytical and Applied Pyrolysis*, 2018, vol. 133, pp. 185-197. doi: https://doi.org/10.1016/j.jaap.2018.04.001.
24. Jana R.N., Mukunda P.G., Nando G.B. Thermogravimetric analysis of compatibilized blends of low density polyethylene and poly(dimethyl siloxane) rubber. *Polymer Degradation and Stability*, 2003, vol. 80, no. 1, pp. 75-82. doi: https://doi.org/10.1016/S0141-3910(02)00385-3.
25. Pyra K., Tarach K.A., Janiszewska E., Majda D., Gora-Marek K. Evaluation of the Textural Parameters of Zeolite Beta in LDPE Catalytic Degradation: Thermogravimetric Analysis Coupled with FTIR Operando Studies. *Molecules*, 2020, vol. 25, no. 4, art. no. 926. doi: https://doi.org/10.3390/molecules25040926.
26. Marcilla A., Gomez-Siurana A., Odjo A.O., Navarro R., Berenguer D. Characterization of vacuum gas oil–low density polyethylene blends by thermogravimetric analysis. *Polymer Degradation and Stability*, 2008, vol. 93, no. 3, pp. 723-730. doi: https://doi.org/10.1016/j.polymdegradstab.2007.12.010.
27. ASTM D412: Standard test methods for vulcanized rubber and thermoplastic elastomers – tension. West Conshohocken, PA, 2016. 14 p.

Received 07.11.2023
Accepted 09.01.2024
Published 01.05.2024

Eman El Sherkawy[1]*, PhD, Assistant Instructor,*
Loai S. Nasrat[2]*, Professor,*
Mahmoud Rihan[3]*, Associate Professor,*
[1] Electrical Power and Machines Engineering Department,
The High Institute of Engineering and Technology El Tod,
Luxor, Egypt,
e-mail: eelsherkawy@gmail.com (Corresponding Author)
[2] Electrical Power and Machines Engineering Department,
Faculty of Engineering, Aswan University, Aswan, Egypt,
e-mail: loaisaad@yahoo.com
[3] Electrical Power and Machines Engineering Department,
Faculty of Engineering, South Valley University, Qena, Egypt,
e-mail: mahmoudrihan@eng.svu.edu.eg

How to cite this article:
El Sherkawy E., Nasrat L.S., Rihan M. The effect of thermal ageing on electrical and mechanical properties of thermoplastic nanocomposite insulation of power high-voltage cables. *Electrical Engineering & Electromechanics*, 2024, no. 3, pp. 66-71. doi: https://doi.org/10.20998/2074-272X.2024.3.09

UDC 621.313 https://doi.org/10.20998/2074-272X.2024.3.10

G. Boudechiche, O. Aissa, M. Sarra, I. Griche

Solar shunt active power filter based on optimized direct power control strategy with disturbance rejection principle

Introduction. *This paper focuses on a renewable energy system coupled to a dual purpose power grid via a parallel active power filter for injecting photovoltaic energy into the grid and improving the power quality in the presence of the non-linear load.* ***The novelty*** *of the work consists in the combination of two advanced techniques – Fuzzy Logic Controller (FLC) and the optimized Anti-Windup Fractional Order Proportional-Integral Differentiator (AW-FOPID) regulator based on Particle Swarm Optimization with the Spreading Factor (PSO-SF) algorithm, applied to the improved Direct Power Control (DPC) strategy under different conditions related to climate changes and healthy or infected electrical network.* ***Purpose.*** *Its main role is to improve the power quality and reject the perturbations deforming the electrical network under distorted, unbalanced and balanced grid voltage conditions. Besides, the FLC is employed the Maximum Power Point Tracking (MPPT) under any weather conditions. In addition, the optimized AW-FOPID controller leads to keep the DC bus voltage at its reference value with small undershoots and overshoots in the voltage with a short response time in steady or dynamic states.* ***Methods****. The rejection of disturbances affecting the grid is offered by the improved DPC. On the other hand, an intelligent method based on fuzzy logic was used MPPT under any weather conditions. Furthermore, an AW-FOPID regulator based on PSO-SF algorithm is used to keep the DC bus voltage at its reference value with small undershoots and overshoots in the voltage, while keeping a fast response time.* ***Results.*** *The proposed system control is evaluated in various states of power source: distorted, unbalanced, and balanced by simulation using MATLAB/Simulink. The simulation results illustrate the effectiveness and performance of the studied control strategies.* References 26, tables 8, figures 16.

Key words: **improved direct power control, particle swarm optimization, disturbance rejection principle, fuzzy maximum power point tracking.**

Вступ. *У цій статті основна увага приділяється системі відновлюваної енергії, що з'єднана з енергосистемою подвійного призначення через паралельний фільтр активної потужності для подачі фотоелектричної енергії в мережу та покращення якості електроенергії за наявності нелінійного навантаження.* ***Новизна*** *роботи полягає у поєднанні двох передових методик – Fuzzy Logic Controller (FLC) та оптимізованого регулятора Anti-Windup Fractional Order Proportional-Integral Differentiator (AW-FOPID) на основі оптимізації рою частинок з коефіцієнтом розширення (PSO-SF), що застосовується до покращеної стратегії прямого управління потужністю (DPC) у різних умовах, пов'язаних зі змінами клімату та справною або зараженою електричною мережею.* ***Мета***. *Його основна роль полягає в покращенні якості електроенергії та усуненні збурень, що деформують електричну мережу в умовах спотвореної, незбалансованої та збалансованої напруги мережі. Крім того, у FLC використовується система відстеження точки максимальної потужності (MPPT) за будь-яких погодних умов. Крім того, оптимізований контролер AW-FOPID дозволяє підтримувати напругу шини постійного струму на опорному значенні з невеликими відхиленнями і викидами напруги з коротким часом відгуку в стані динамічного стану.* ***Методи***. *Відмова від перешкод, що впливають на мережу, забезпечує покращений DPC. З іншого боку, інтелектуальний метод, заснований на нечіткій логіці, використовувався MPPT за будь-яких погодних умов. Крім того, регулятор AW-FOPID, заснований на алгоритмі PSO-SF, використовується для підтримки опорного значення напруги постійного струму шини з невеликими відхиленнями і викидами напруги, зберігаючи при цьому малий час відгуку.* ***Результати***. *Пропоноване управління системою оцінюється у різних станах джерела живлення: спотвореному, незбалансованому та збалансованому шляхом моделювання з використанням MATLAB/Simulink. Результати моделювання ілюструють ефективність та продуктивність вивчених стратегій управління.* Бібл. 26, табл. 8, рис. 16.

Ключові слова: **покращене пряме керування потужністю, оптимізація рою частинок, принцип придушення перешкод, нечітке відстеження точки максимальної потужності.**

1. Introduction. Energy production is a major concern in the future because it is considered one of the engines of sustainability of development projects [1]. Currently, fossil fuels provide the majority of the world's energy (gas, oil, and coal). Excessive use of non-renewable energy depletes reserves of this type of energy and contributes to greenhouse gas emissions, which pollute the environment and deadly threat to organisms [2]. Solar energy's availability is as an environmentally friendly, limitless, and free power source on the entire glob's surface [3]. Meanwhile, the growing usage of non-linear loads in the residential sector, and industrial sectors, causes problems related to the quality of energy [4]. These devices act as generators of harmonic currents inducing a consumption of reactive power [5]. To remedy these disadvantages, a curative solution consists in connecting a filtering device composing of an inverter in parallel with the system: nonlinear load – three-phase power source [6]. This Shunt Active Power Filter (SAPF) injects a current that opposes the reactive power and current harmonics emitted by the nonlinear load, to eventually makes the source current sinusoidal and in phase with its voltage, is frequently used [7, 8]. In the literature, many commands schemes have been adopted to control the SAPF. Hysteresis current approach is one of the most known methods [9]. However, it operates with a variable switching frequency [6]. To overcome such problem, authors have been suggested other commands such as Direct Power Control (DPC) [10, 11]. This command does not need Pulse-Width Modulation (PWM) or current control loops [12]. DPC is represented by a reference to the active power and another reference of the zero reactive power [13]. Nevertheless, these methods present also some issues related to high sampling rate and variable switching frequency [5]. To remedy these disadvantages, it is important to introduce other DPC structures. These later are represented in the DPC with space vector modulation which is used a linear Proportional Integral (PI) controllers and modulator of voltage instead of a hysteresis comparators and switching table [14]. However, this method requires the use of setting of the PI regulators and

coordinate transforms. For this reason, researchers, suggest other technique that known as predictive DPC, characterized by high accuracy [15]. Although this method needs complex calculations [9]. Nevertheless, when the aforementioned commands are used in distorted or unbalanced conditions of the power source, the performance of the system is deteriorated with degradation of the Total Harmonic Distortion (THD) contents which appears in input currents.

Goal of the article. This paper presents a new DPC method in order to improve the power quality under distorted, unbalanced or balanced grid voltage conditions. Moreover, this command needs to have zero disturbance references in reactive and active power.

Various regulators are used to keep the DC-link voltage at its desired value. Among them, the traditional PI regulator, which offers an excellent responsiveness in steady state [16], but performs poorly in transient states [11]. To remedy this problem, the suggested regulator in this paper is performed by an Anti-Windup Fractional Order Proportional-Integral Differentiator AW-FO($PI^{\varepsilon}D^{\eta}$) regulator, replacing the traditional PI regulator that maintains the DC-link voltage at its reference value. This AW-FO($PI^{\varepsilon}D^{\eta}$) regulator with two extra freedom degrees ε and η presents shorter response time and better dynamic response compared to the traditional PI regulator [17, 18]. In contrast to the traditional PI regulator used in DPC, which has poor responses in dynamic conditions, the output of the AW-FOPID regulator contributes to the delivery of the active power. Concerning the setting of the AW-FOPID parameters, Particle Swarm Optimization (PSO) technique is used to minimize the objective function. In fact, this is the first time that the optimized AW-FOPID regulator has been integrated into the new DPC configuration.

As the irradiation varies, several techniques of Maximum Power Point Tracking (MPPT) have been proposed [19, 20]. In our research, Fuzzy Logic Controller (FLC) has been used to track the MPPT and to solve the problem of the rapidly changing irradiance [9]. This work proposes a combination of two advanced techniques, the optimized AW-FOPID and FLC, applied to the Improved DPC (IDPC) strategy under different conditions related to climate changes and healthy or infected electrical network.

2. Description of solar SAPF controlled by the IDPC with optimized AW-FOPID regulator based on PSO-SF algorithm.

2.1. Description of IDPC strategy for the SAPF. The rejection of disturbances affecting the grid is provided by the IDPC command. Its principle role consists to eliminate the unwanted harmonics of the source currents due to contamination and unbalance of the power in the presence of the photovoltaic (PV) system. The IDPC approach needs no reactive and active power perturbation reference to reject the influence of the deformed electrical network as shown in Fig. 1 [21]. The currents participating to the calculation of reactive and active powers are assessed as follows:

$$\begin{bmatrix} \xi I_{sa} \\ \xi I_{sb} \\ \xi I_{sc} \end{bmatrix} = \begin{bmatrix} I_{sa} \\ I_{sb} \\ I_{sc} \end{bmatrix} - \begin{bmatrix} I_{sa}^{*} \\ I_{sb}^{*} \\ I_{sc}^{*} \end{bmatrix}. \quad (1)$$

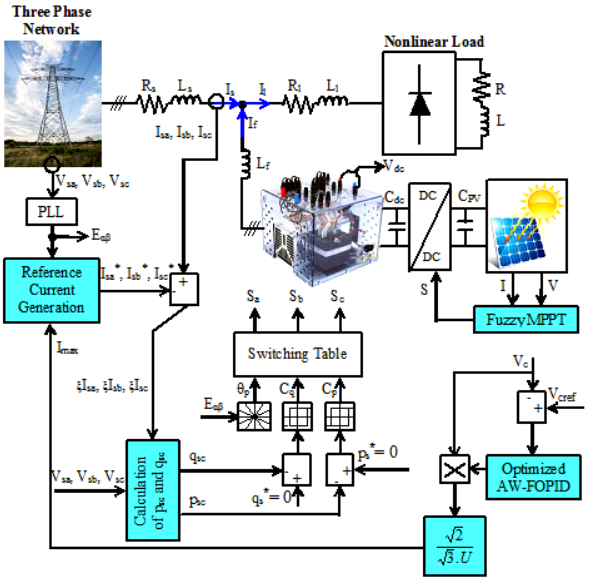

Fig. 1. SAPF articulated on the IDPC method with PV system

In the IDPC, the amplitude of the input currents I_{max} is given by the multiplication of the output voltage regulator AW-FOPID by the measured V_c voltage. This first result obtained is multiplied by a value gain $\sqrt{2}/\sqrt{3}U$. So, fundamental terms of these currents are delivered from the phase-locked loop block. The three reference source currents can be formulated as:

$$\begin{bmatrix} I_{sa}^{*} \\ I_{sb}^{*} \\ I_{sc}^{*} \end{bmatrix} = \begin{bmatrix} I_{\max}\sin(\omega t) \\ I_{\max}\sin(\omega t - 2\pi/3) \\ I_{\max}\sin(\omega t + 2\pi/3) \end{bmatrix}. \quad (2)$$

Substitution (2) in (1) gives the following equation:

$$\begin{bmatrix} \xi I_{sa} \\ \xi I_{sb} \\ \xi I_{sc} \end{bmatrix} = \begin{bmatrix} I_{sa} \\ I_{sb} \\ I_{sc} \end{bmatrix} - \begin{bmatrix} I_{\max}\sin(\omega t) \\ I_{\max}\sin(\omega t - 2\pi/3) \\ I_{\max}\sin(\omega t + 2\pi/3) \end{bmatrix}. \quad (3)$$

Consequently, instantaneous reactive and active powers (Q_{sc} and P_{sc}) provided by the harmonic component:

$$Q_{sc} = \frac{1}{\sqrt{3}}\left[(V_{sb} - V_{sc})\xi I_{sa} + (V_{sc} - V_{sa})\xi I_{sb} + (V_{sa} - V_{sb})\xi I_{sc}\right]; \quad (4)$$

$$P_{sc} = V_{sa}\xi I_{sa} + V_{sb}\xi I_{sb} + V_{sc}\xi I_{sc}, \quad (5)$$

where I_{sa}, I_{sb}, I_{sc}, V_{sa}, V_{sb}, V_{sc} are the distorted or unbalanced source currents and voltages of the phase A, B, C.

In this IDPC controller, the references of the active and reactive powers are set to zero value to ensure rejection of grid disturbances which are emitted by the load and to achieve a sinusoidal input current. For this reason, both reference active (psc^{*}) and reference reactive (qsc^{*}) powers and are set to zero.

2.2. AW-FOPID regulator based on PSO with the spreading factor (PSO-SF) algorithm.

Optimized AW-FOPID regulator. The traditional PI regulator suffers from some problem in the transient states [16]. To remedy this issue, the proposed regulator is performed by AW-FO($PI^{\varepsilon}D^{\eta}$), replacing the traditional PI regulator to keep the DC bus voltage at its reference value with small undershoots and overshoots in the voltage. The AW-FO$PI^{\varepsilon}D^{\eta}$ has a general form that includes the derivative η and the integral ε actions order, which are not integers

(Fig. 2). From Fig. 2, the transfer function of the optimized AW-FOPID regulator is given:

$$G(s)=\frac{U(s)}{E(s)}=K_p+K_i s^{-\varepsilon}+K_d s^{\eta}, \quad (6)$$

where K_d, K_p, K_i are the derivative, proportional and integral gain factors, respectively; η, ε are the derivative and integral orders respectively; $Y(s)$ is the output signal; $R(s)$ is the input signal, $E(s)$ is the error; $C(s)$ is the plant's transfer function. It is obvious that the choice of η and ε gives the traditional regulators, i.e. PI regulator (η = 0) and PID regulator (ε, η = 1).

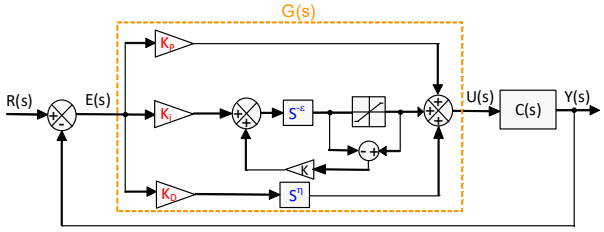

Fig. 2. General form regulator

a) Fractional Order Method. The technique suggested by Oustaloup in 1995 [17] adequate to approximate the Fractional Order (FO) to Laplace transfer functions. The Oustaloup's approximation model's term s^{β} is valid in the range [–1; 1]. s^{β} as an FO integrator if $\beta\in[-1; 0]$ and as an FO differentiator if $\beta\in[0; 1]$. In addition, this approximation employs a recursive distribution of zeroes and poles. So, the Oustaloup's approximation is evaluated as:

$$s^{\beta}=K\prod_{k=-M}^{M}\frac{s+\omega_k'}{s+\omega_k}, \quad (7)$$

where:

$$K=\omega_h^{\beta}, \quad (8)$$

$$\omega_k=\omega_b\left(\frac{\omega_h}{\omega_b}\right)^{\left(\frac{k+M+0.5(1+\beta)}{2M+1}\right)}, \quad (9)$$

$$\omega_k'=\omega_b\left(\frac{\omega_h}{\omega_b}\right)^{\left(\frac{k+M+0.5(1-\beta)}{2M+1}\right)}, \quad (10)$$

where ω_h, ω_b are the high and low frequencies, respectively; K is the adjustment gain; M is the number of zeros and poles; ω_k and ω_k' are respectively the poles and zeros of interval k; $(2M+1)$ is the approximation function order.

b) PSO with the Spreading Factor (PSO-SF). Depending on (6), the optimized AW-FOPID regulator has 5 parameters to be tuned (K_d, K_i, K_p, η, ε). Therefore, the PSO technique is used to tune the AW-FOPID parameters by minimizing the objective function f. PSO is a stochastic optimization algorithm based on the behaviour of swarms such as birds and fish [22-24]. In PSO technique, particle is regarded a potential solution for determining the best solution to the problem. Moreover, the position of a particle is influenced by its own best found position. The best position of the particle i is given as:

$$y_i(t+1)=\begin{cases}y_i(t) & \text{if} \quad f(x_i(t+1))\ge f(y_i(t)),\\ x_i(t+1) & \text{if} \quad f(x_i(t+1))< f(y_i(t)),\end{cases} \quad (11)$$

where f is the objective function; x_i is the particle's current position which is updated at time step t.

The basic PSO equations can be represented as:

$$x_i(t+1)=x_i(t)+V_i(t+1), \quad (12)$$

$$v_{i,j}=\omega\cdot v_{i,j}(t)+c_1\cdot\Delta_1+c_2\cdot\Delta_2, \quad (13)$$

where:

$$\Delta_1=r_{1,j}\cdot\left(y_{i,j}(t)-x_{i,j}(t)\right); \quad (14)$$

$$\Delta_2=r_{2,j}\cdot\left(y_j^n(t)-x_{i,j}(t)\right), \quad (15)$$

where c_1, c_2 are the acceleration constants, $v_{i,j}$ is the j^{th} element of the velocity vector of the i^{th} particle; $r_{1,j}$, $r_{2,j}$ are the random coefficients; ω is the inertia weight. This operation is stopped when the velocity updates tend to zero.

In PSO algorithm, each particle must update its own best individual objective function in each iteration. The individual objective function of each particle is calculated by using the integral time absolute error (MSE – Mean Squared Error):

$$MSE=\sum_{t_s=0}^{N}e^2\Big/N, \quad (16)$$

where t_s is the time rang of simulation; N is the total number of points for which the optimization is carried out; e is the error signal.

In this work, PSO with the spreading factor (PSO-SF) [25] is used instead of standard PSO to set the AW-FOPID regulator parameters. By applying the PSO-SF technique, the acceleration coefficient (c_1 and c_2) and inertia weight (ω) are given:

$$c_1=c_2=2\cdot(1-(\text{current epoch}/\text{total epoch})); \quad (17)$$

$$\omega=e^{(-\text{current epoch}/(SF\times\text{total epoch}))}; \quad (18)$$

where SF = 0.5(spread + deviation).

The algorithm's instructions to be followed of the tuning this regulator by PSO-SF:

1. Initialize the parameters of the 5 controller parameters: position range varies from 0.01 to 15; inertia weight ω from 0 to 1; velocity range varies from –0.001 to 0.5; acceleration c_1 and c_2 from 0.01 to 2;
2. Distribute particles at random within predefined ranges;
3. Evaluate the objective function by using (16) with MSE tending to 0;
4. Update new individual fitness if the present individual fitness is better to the prior individual fitness;
5. Identify the best particle objective function among the swarm;
6. Update the new population fitness if the present population fitness is better than the prior population fitness;
7. Use (12), (13) to determine the velocity and update the position;
8. Use (17), (18) to determine the new acceleration coefficients c_1 and c_2 and the inertia weight ω;
9. End.

2.3. Fuzzy MPPT. FLC is employed for tracking the MPP of PV array under any weather conditions [3]. This algorithm is very efficient for both nonlinear and linear systems [26]. The FLC has 3 steps: fuzzification, defuzzification and rules inference. The inputs of fuzzy MPPT are usually represented by a change in error ΔE and an error E [9]:

$$\begin{cases} E(k) = \Delta P / \Delta V; \\ \Delta E(k) = E(k) - E(k-1), \end{cases} \quad (19)$$

where:

$$\Delta V = V(k) - V(k-1); \quad (20)$$

$$\Delta P = P(k) - P(k-1); \quad (21)$$

where $V(k-1)$, $V(k)$, $P(k-1)$, $P(k)$ are respectively the voltage and the power of the PV at the sampling times $(k-1)$ and k [9].

The input variables $\Delta E(k)$ and $E(k)$ of fuzzy MPPT are divided into 5 fuzzy sets: Negative Small (*NS*), Positive Big (*PB*), Positive Small (*PS*), Zero (ZO) and Negative Big (*NB*). The rule base connects the fuzzy inputs to the fuzzy output by the syntax: «if *L* and *M*, then *N*» [9] (Table 1).

Table 1

Fuzzy MPPT

$\downarrow E/\Delta E \rightarrow$	*NB*	*NS*	*ZO*	*PS*	*PB*
NB	*PS*	*PB*	*PB*	*NB*	*NS*
NS	*ZO*	*PS*	*PS*	*NS*	*ZO*
ZO	*ZO*	*ZO*	*ZO*	*ZO*	*ZO*
PS	*ZO*	*NS*	*NS*	*PS*	*ZO*
PB	*NS*	*NB*	*NB*	*PB*	*PS*

The incremental duty cycle ΔD is calculated as [9]:

$$\Delta D = \sum_{j=0}^{n} w_j \Delta D_j \Big/ \sum_{j=0}^{n} w_j , \quad (22)$$

where ΔD_i is the value corresponding to ΔD; w is the weighting factor; n is the maximum number of effective rules.

Finally, the duty cycle is calculated by adding this modification to the control's prior value:

$$D(k+1) = D(k) + \Delta D(k). \quad (23)$$

3. Presentation and discussion of results. To validate the performance and feasibility of the approaches suggested in this paper, several simulation tests were run in the MATLAB/Simulink. Table 2 lists the parameters that were used for these tests.

Table 2

Parameters for the simulation

Parameter	Value	Parameter	Value
L_s, mH	0.1	L_l, mH	0.566
R_s, Ω	0.1	R_l, Ω	0.01
Switching frequency (DC/AC converter), kHz	20	Switching frequency (DC/DC boost converter), kHz	5
V_s, V	70	V_{cref}, V	227.68
f_s, Hz	50	C_{pv}, µF	20
L, mH	10	L_{pv}, mH	3
R, Ω	40	K_i	60
L_f, mH	2.5	K_d	0.011
R_f, Ω	0.01	K_p	0.95
C_{dc}, µF	2200	N	2
η	0.5	ε	0.4

Figure 3 illustrates the relationship between the current I and power P generated by the PV generator in response to different solar irradiation profiles G. Initially, prior to time t = 0.5 s, no power or current is produced when the solar irradiation is at zero. Subsequently, from 0.5 s to 2 s, the PV's power and current follow specific trajectories determined by the irradiation profile. During this period, the irradiation gradually rises from 0 to 800 W/m^2 until t = 0.9 s, resulting in the generation of 30 A with 4 kW output by using the FLC. At t = 0.9 s, the solar irradiation decreases from 800 to 300 W/m^2, leading to a decline in current from 30 A to 10 A and power from 4 kW to 1.43 kW. Then, at t = 1.3 s, the solar irradiation increases again, reaching 1000 W/m^2 and maintaining this level, thereby providing 5 kW with 40 A output.

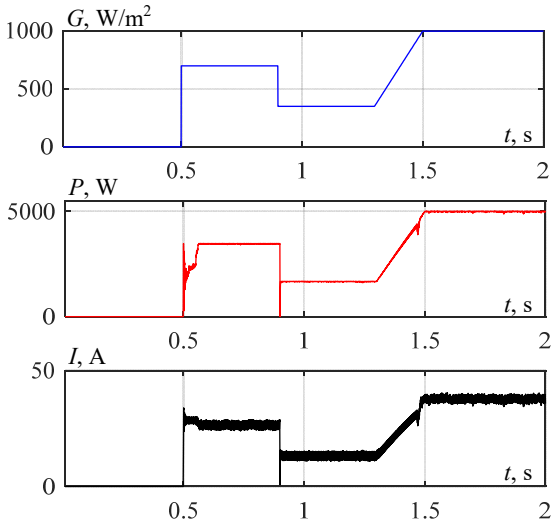

Fig. 3. Irradiation profile, power and current of the PV module

Figure 4 illustrates powers evolutions, obtained by the IDPC with optimized AW-FOPID and FLC MPPT. When the solar irradiation G = 0, the grid supplies the power P_s to the non-linear load P_l. Subsequently, upon the integration of the PV system, during the time interval [0.5, 2] s, the PV generator caters to the load's power demand P_f, with any excess power being fed back into the electrical network. From 0.1 to 2 s, the grid's reactive power Q_s is reduced to zero following the installation of the SAPF.

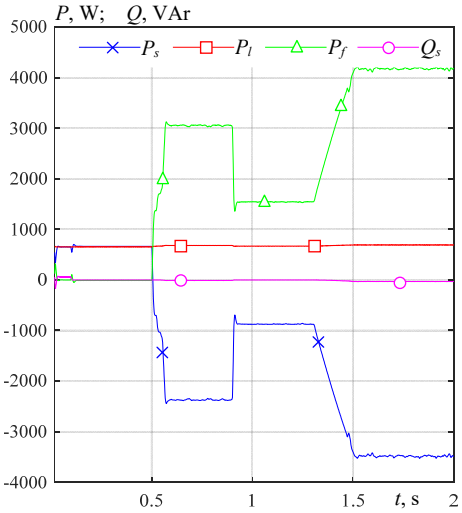

Fig. 4. Powers evolution for the proposed DPC

Figures 5, 7 display the current I_s and voltage V_s waveforms of the source, load current I_l and filter current I_f before and after filtering with and without the PV module.

In the absence of filtering and without PV integration, the source current exhibits distortion and deformation, with a THD of 30.35 %. However, upon the insertion of the SAPF at t = 0.1 s, the source current transforms into a sinusoidal waveform and synchronizes with the network voltage. Consequently, the THD is significantly reduced to 3.33 % for the IDPC with optimized AW-FOPID and 1.68 % for the IDPC with PI control (Table 3). Subsequently, during the period from

0.5 s to 2 s, SAPF comes into operation, ensuring that the source currents remain sinusoidal and in opposite phase to their corresponding voltages. As a result, the THD further decreases to 2.47 % for the IDPC with optimized AW-FOPID and 1.57 % for the IDPC with PI control (Table 3).

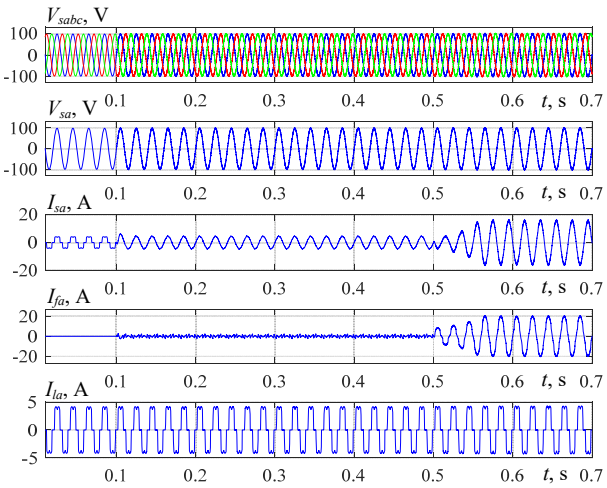

Fig. 5. Zoomed-in view on the SAPF articulated on IDPC with FLC and optimized AW-FOPID regulator: source currents and voltages, load and filter currents

Table 3
Comparison of source current THD for balanced network voltage

Control	Source current THD, %		
	Without SAPF	SAPF without PV	SAPF with PV
IDPC approach with optimized AW-FOPID regulator	30.35	3.33	2.47
IDPC approach with standard PI regulator	30.35	01.68	1.57

The DC-link voltage V_c stabilizes at its reference value V_{cref} during the introduction of the SAPF, and at each change in irradiation it returns to V_{cref}, justified by the exchange of energy between the nonlinear load, the grid, and the SAPF as shown in Fig. 6, 8 and Table 4.

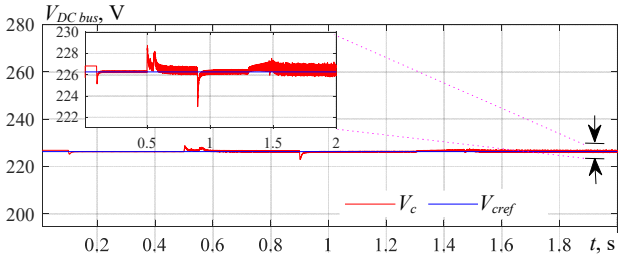

Fig. 6. Zoom on DC-link voltage of the SAPF articulated on IDPC with FLC and optimized AW-FOPID regulator

During the period [0.1, 0.5] s, where G = 0, it can be seen that V_c decreases from 226.27 V to 225.12 V for optimized AW-FOPID and 159.99 V for PI with response time 0.0182 s and 0.13 s, respectively. When G = 800 W/m^2 during [0.5-0.9] s, it can be noticed that V_c increases from 226.27 V to 229.26 V for optimized AW-FOPID and 265.7 V for PI with response time 0.077 s and 0.19 s, respectively. When G = 300 W/m^2 during the period [0.9-1.3] s, it can be observed that V_c decreases from 226.27 V to 221.99 V for optimized AW-FOPID and 193.68 V for PI with response time 0.047 s and 0.12 s, respectively. Finally, in the period [1.3-2] s, where G = 1000 W/m^2, it can be seen that V_c increases from 226.27 V to 227.3 V for optimized AW-FOPID and 237.5 V for PI with response time 0.174 s and 0.29 s, respectively.

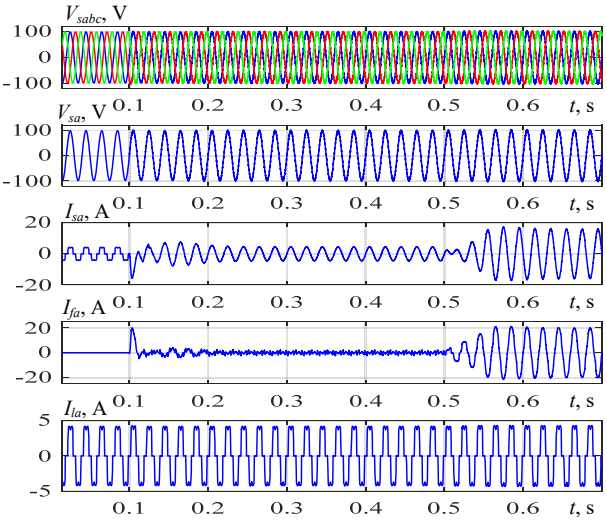

Fig. 7. Zoom of SAPF articulated on IDPC with FLC and PI regulator: source currents and voltages, load and filter currents

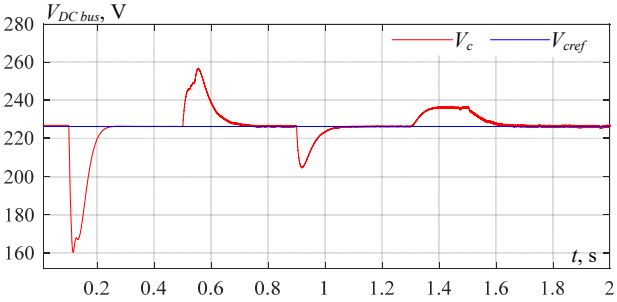

Fig. 8. Zoom on DC-link voltage of the SAPF articulated on IDPC equipped with FLC and PI regulator

Table 4
Comparison of the optimized AW-FOPID with traditional PI regulator under **balanced** network voltage and variations in solar irradiation

Control	IDPC approach with optimized AW-FOPID regulator	IDPC approach with PI regulator
SAPF without PV ΔV, V	Voltage drop of 1.15	Voltage drop of 66.28
SAPF without PV Δt, s	0.0182	0.13
SAPF with PV ΔV, V	Overshoot of 2.99	Overshoot of 39.43
	Voltage drop of 4.28	Voltage drop of 32.59
	Overshoot of 1.03	Overshoot of 11.23
SAPF with PV Δt, s	0.077	0.19
	0.047	0.12
	0.174	0.29

The optimized AW-FOPID regulator demonstrates notable advantages over the traditional PI regulator under balanced network voltage and varying solar irradiation conditions. Figures 6, 8 and Table 4 present the performance comparison, highlighting the following key aspects:

- *Voltage drops*. The optimized AW-FOPID regulator exhibits reduced voltage drops compared to the traditional PI regulator. This means that the AW-FOPID controller maintains a more stable voltage profile, minimizing fluctuations and ensuring a smoother operation.

• *Voltage overshoots*. The optimized AW-FOPID regulator also shows smaller voltage overshoots than the traditional PI regulator. This implies that the AW-FOPID controller achieves better control over the system's response, preventing excessive deviations and maintaining tighter regulation.

• *Short response time*. The optimized AW-FOPID regulator achieves a shorter response time compared to the traditional PI regulator. This indicates that the AW-FOPID controller can rapidly adapt to changes in the system, providing quicker and more accurate adjustments.

In summary, the optimized AW-FOPID regulator outperforms the traditional PI regulator in terms of voltage stability, response speed, and overall system control, making it a more efficient and effective choice for systems operating under balanced network voltage and varying solar irradiation conditions.

Unbalanced and distorted network voltages tests. A first test based on unbalanced network voltages is performed to test the robustness of the IDPC: V_{sa} = 70 V, V_{sb} = 120 V, V_{sc} = 60 V. The simulation results of the SAPF articulated on IDPC equipped with the optimized AW-FOPID, PI regulator and FLC, operating under unbalanced network voltage, are shown in Fig. 9, 11.

Figures 9, 11 display the source currents and voltages, the load currents and filter currents, after and before filtering, with and without PV array under unbalanced network voltages. Before filtering and without PV, the source current is deformed with THD is 30.32 %. After the SAPF is inserted at the instant 0.1 s, the source current becomes sinusoidal and synchronizes with network voltage. The THD in this situation is 3.76 % for the IDPC with optimized AW-FOPID and 3.21 % for the IDPC with PI (Table 5). Then from 0.5 to 2 s, the SAPF starts operating, where the source currents stay sinusoidal and in opposition phase with the corresponding voltages. So, THD is 4.57 % for the IDPC with optimized AW-FOPID and 3.8 % for the IDPC with PI (Table 5).

Table 5

Comparison of source current THD for unbalanced network voltage

Control	THD of source current, %	
	IDPC approach with optimized AW-FOPID regulator	IDPC approach with standard PI regulator
Without SAPF	30.32	30.32
SAPF without PV	3.76	3.21
SAPF with PV	4.57	3.8

During the period [0.1, 0.5] s, where G = 0, it can be seen that V_c increases from 226.27 V to 242.16 V for optimized AW-FOPID with response time 7.65 ms. The simulation results of the solar SAPF articulated on the IDPC equipped with the optimized AW-FOPID, PI regulator and FLC controller, operating under unbalanced network voltage, are shown in Fig. 9, 11. Whereas, it can be observed that V_c decreases from 226.27 V to 225.06 V for optimized AW-FOPID and 169.89 V for PI with response time 8 ms and 0.109 s, respectively. However, when G = 800W/m^2 during [0.5-0.9] s, it can be noticed that V_c increases from 226.27 V to 229.79 V for optimized AW-FOPID and 275.1 V for PI with response time 22.5 ms and 0.155 s, respectively.

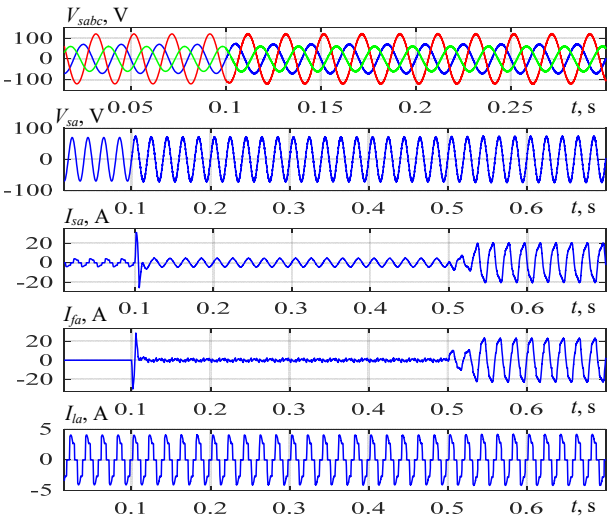

Fig. 9. Zoom of SAPF articulated on the IDPC with FLC and optimized AW-FOPID regulator under unbalanced network voltages: source currents and voltages, load and filter currents

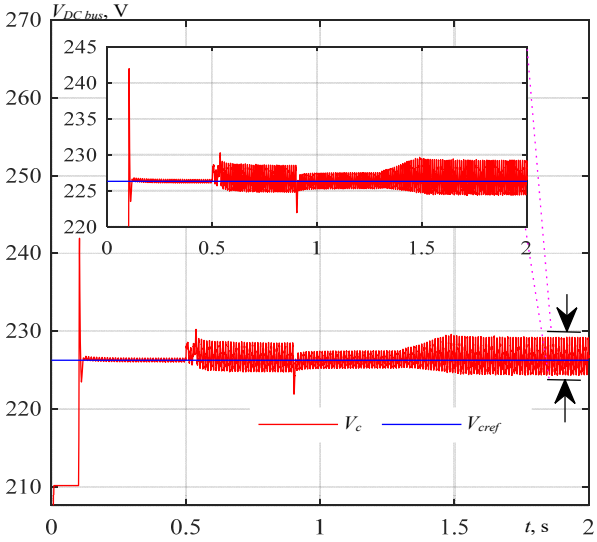

Fig. 10. Zoom on DC-link voltage of the SAPF articulated on the IDPC with FLC and optimized AW-PID regulator under unbalanced network voltages

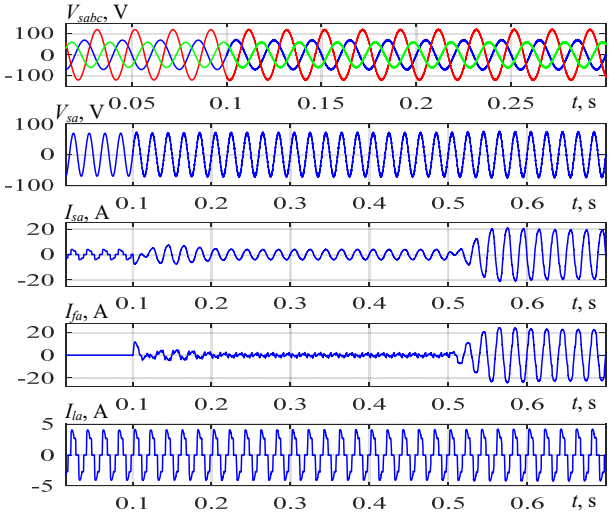

Fig. 11. Zoomed of SAPF articulated on the IDPC with FLC and PI regulator under unbalanced network voltages: source currents and voltages, load and filter currents

During the insertion of the SAPF, the DC-link voltage V_c stabilizes at its reference value V_{cref}. Additionally, at each

change in solar irradiation, the DC-link voltage returns to the reference value V_{cref} (Fig. 10, 12, Table 6). Then, when $G = 300$ W/m^2 during the period [0.9-1.3] s, it can be observed that V_c decreases from 226.27 V to 220.54 V for optimized AW-FOPID and 188 V for PI with response time 16.93 ms and 0.12 s, respectively. Finally, in the period [1.3-2] s, where $G = 1000$ W/m², it can be seen that V_c increases from 226.27 V to 246.81 V for PI with response time 0.7 s.

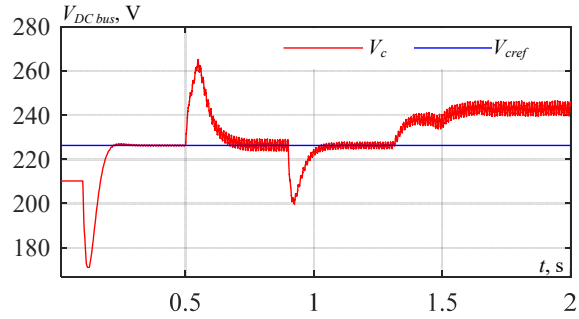

Fig. 12. Zoom on DC-link voltage of the SAPF articulated on the IDPC equipped with FLC and PI regulator under unbalanced network voltages

Table 6

Comparison of the optimized AW-FOPID with traditional PI regulator under **unbalanced** network voltage and variations in solar irradiation

Control	IDPC approach with optimized AW-FOPID regulator	IDPC approach with PI regulator
SAPF without PV ΔV, V	Overshoot of 15.89 Voltage drop of 1.21	Voltage drop of 56.38
SAPF without PV Δt, s	0.00765 0.008	0.109
SAPF with PV ΔV, V	Overshoot of 3.52 Voltage drop of 5.73	Overshoot of 48.83 Voltage drop of 38.27 Overshoot of 20.54
SAPF with PV Δt, s	0.0225 0.01693	0.155 0.12 0.7

In summary, the optimized AW-FOPID controller demonstrates better performance in maintaining the DC-link voltage V_c closer to its reference value V_{cref} during varying solar irradiation. It achieves faster response times and smaller voltage deviations compared to the traditional PI controller in most situations.

As a result, the optimized AW-FOPID regulator has a smaller voltage drops and overshoots with a short response time under unbalanced network voltage with variations in solar irradiation compared to those obtained from the traditional PI controller (Fig. 10, 12, Table 6).

The second test of the IDPC approach's robustness is articulated on network voltage distortion. In this test, the fundamental input voltages are superimposed with the fifth harmonic voltage. The simulation results of the solar SAPF articulated on the IDPC equipped with the optimized AW-FOPID, PI regulator and FLC controller, operating under distorted network voltage (Fig. 13, 15).

Figures 13, 15 present the waveforms of source currents and voltages, load currents, and filter currents before and after filtering, with and without the PV array under distorted network conditions. Initially, the source current is distorted and deformed with a THD of 36.9 %.

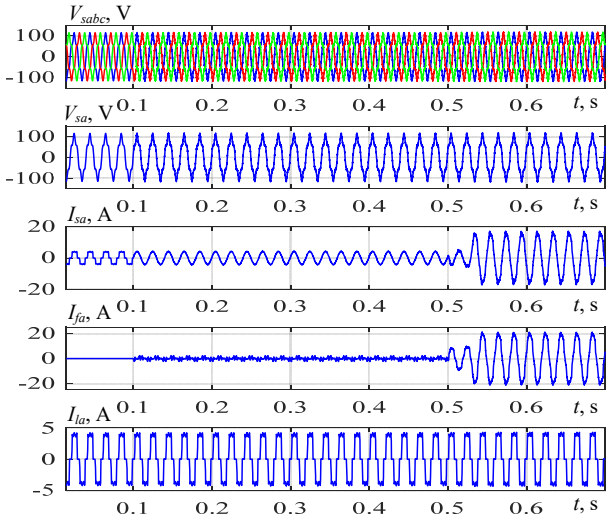

Fig. 13. Zoom of SAPF articulated on IDPC with FLC and optimized AW-PID regulator under distorted network voltages: source currents and voltages, load and filter currents

Upon the insertion of the SAPF at $t = 0.1$ s, the source current undergoes significant improvement, transforming into a sinusoidal waveform and synchronizing with the network voltage. The THD reduces to 2.97 % for the IDPC with optimized AW-FOPID and 3.02 % for the IDPC with PI control (Table 7).

Subsequently, from 0.5 s to 2 s, the SAPF becomes operational, resulting in the source currents remaining sinusoidal and in opposition phase to their corresponding voltages. During this period, the THD is 4.62 % for the IDPC with optimized AW-FOPID and 3.15 % for the IDPC with PI control (Table 7).

During the introduction of the SAPF, the DC-link voltage V_c stabilizes at its designated value V_{cref}, and whenever there is a change in solar irradiation, it returns to this reference value (Fig. 14, 16, Table 8).

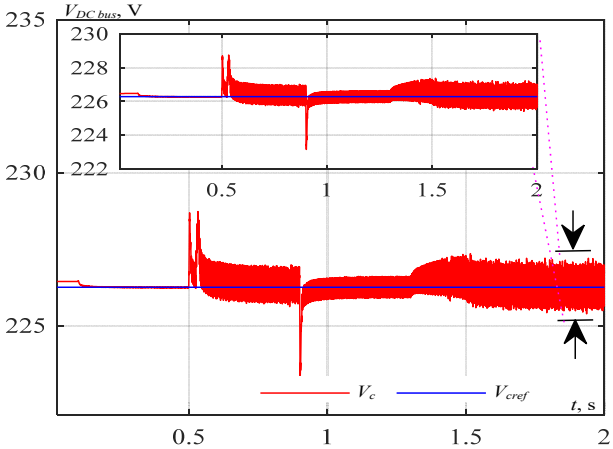

Fig. 14. Zoom on DC-link voltage of the SAPF articulated on the IDPC equipped with FLC and optimized AW-PID regulator under distorted network voltages

Table 7

Comparison of source current THD under distorted network voltage with variations in solar irradiation

Control	THD of source current, %	
	IDPC approach with optimized AW-FOPID regulator	IDPC approach with standard PI regulator
Without SAPF	36.9	36.9
SAPF without PV	2.97	3.02
SAPF with PV	4.62	3.15

Table 8

Comparison of the optimized AW-FOPID with classical PI under distorted grid voltage with variations in solar irradiation

Control	IDPC approach with optimized AW-FOPID regulator	IDPC approach with PI regulator
SAPF without PV ΔV, V	Overshoot of 1.64	Voltage drop of 69.27
SAPF without PV Δt, s	0.1	0.13
SAPF with PV ΔV, V	Overshoot of 3.29 Voltage drop of 4.28	Overshoot of 40.73 Voltage drop of 32.28 Overshoot of 12.23
SAPF with PV Δt, s	0.052 0.0296	0.18 0.15 0.313

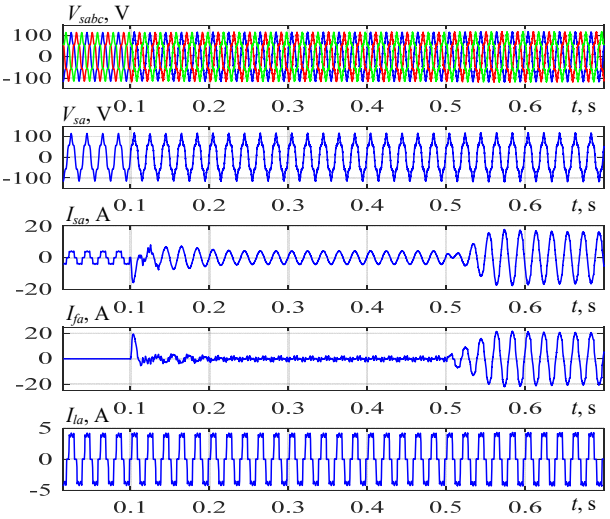

Fig. 15. Zoom of SAPF articulated on IDPC with FLC and PI regulator under distorted network voltages: source currents and voltages, load and filter currents

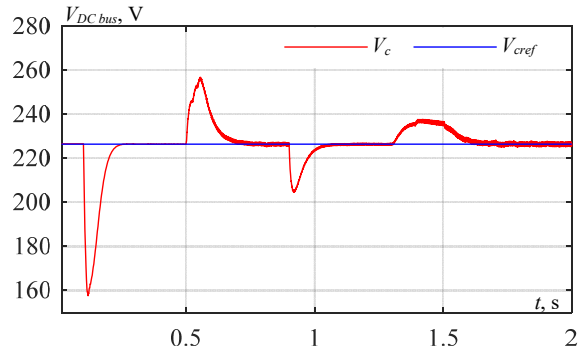

Fig. 16. Zoom on DC-link voltage of the SAPF articulated on the IDPC equipped with FLC and PI regulator under distorted network voltages

Let's summarize the observations during different periods:

• **Period [0.1, 0.5] s (G = 0).**

Optimized AW-FOPID: V_c increases from 226.27 V to 227.91 V with a response time 0.1 s.

PI: V_c decreases from 226.27 V to 157 V with a response time 0.13 s.

• **Period [0.5, 0.9] s (G = 800 W/m²):**

Optimized AW-FOPID: V_c increases from 226.27 V to 229.56 V with a response time 0.052 s.

PI: V_c increases from 226.27 V to 267 V with a response time 0.18 s.

• **Period [0.9, 1.3] s (G = 300 W/m²):**

Optimized AW-FOPID: V_c decreases from 226.27 V to 221.99 V with a response time 0.0296 s.

PI: V_c decreases from 226.27 V to 193.99 V with a response time 0.15 s.

• **Period [1.3, 2] s (G = 1000 W/m²):**

PI: V_c increases from 226.2 V to 238.5 V with a response time 0.313 s.

In summary, the DC-link voltage V_c in the system remains stable at the reference value V_{cref} during SAPF insertion and readjusts to this value at every change in solar irradiation. The optimized AW-FOPID regulator successfully maintains V_c close to its reference value with faster response times with fewer and smaller voltage deviations in most situations compared to the traditional PI regulator. However, during G = 1000 W/m², the PI regulator exhibits a higher response time and a slightly higher V_c value compared to the optimized AW-FOPID regulator. As a result, the optimized AW-FOPID regulator has a smaller voltage drops and overshoots with a short response time under distorted network voltage with variations in solar irradiation compared to those obtained from the traditional PI controller, as represented in Fig. 14, 16 and Table 8.

4. Conclusions. This paper investigates an improved Direct Power Control (DPC) articulated on optimized Anti-Windup Fractional Order Proportional-Integral Differentiator (AW-FOPID) regulator for a double-stage grid-interconnected photovoltaic system, associated with a Shunt Active Power Filter (SAPF). The primary objective is to reject the perturbations deforming the electrical network and ensures agreeable total harmonic distortion under distorted, unbalanced and balanced grid voltage conditions. The particle swarm optimization algorithm is employed to tune the parameters of the AW-FOPID regulator by minimizing an objective function. Therefore, the improved DPC strategy ensures efficient delivery of SAPF by replacing the traditional PI controller with the optimized AW-FOPID regulator. Moreover, a fuzzy logic controller is integrated into the system to effectively track the maximum power point under diverse weather conditions. The study's results demonstrate the superior performance of studied control strategies in terms of response time, undershoots and overshoot in the DC link voltage under distorted, unbalanced and balanced network voltage with variations in solar irradiation compared to those obtained from the traditional PI regulator.

Conflict of interest. The authors declare no conflict of interest.

REFERENCES

1. Mansouri N., Lashab A., Guerrero J.M., Cherif A. Photovoltaic power plants in electrical distribution networks: a review on their impact and solutions. *IET Renewable Power Generation*, 2020, vol. 14, no. 12, pp. 2114-2125. https://doi.org/10.1049/iet-rpg.2019.1172.

2. Lashab A., Sera D., Hahn F., Juarez Camurca L., Liserre M., Guerrero J.M. A Reduced Power Switches Count Multilevel Converter-Based Photovoltaic System With Integrated Energy Storage. *IEEE Transactions on Industrial Electronics*, 2021, vol. 68, no. 9, pp. 8231-8240. doi: https://doi.org/10.1109/TIE.2020.3009594.

3. Abouadane H., Fakkar A., Sera D., Lashab A., Spataru S., Kerekes T. Multiple-Power-Sample Based P&O MPPT for Fast-Changing Irradiance Conditions for a Simple Implementation. *IEEE Journal of Photovoltaics*, 2020, vol. 10, no. 5, pp. 1481-1488. doi: https://doi.org/10.1109/JPHOTOV.2020.3009781.

4. Youcefa B., Massoum A., Barkat S., Wira P. Backstepping Direct Power Control for Power Quality Enhancement of Grid-connected Photovoltaic System Implemented with PIL Co-simulation Technique. *Advances in Modelling and Analysis C*, 2019, vol. 74, no. 1, pp. 1-14. doi: https://doi.org/10.18280/ama_c.740101.
5. El Ouanjli N., Motahhir S., Derouich A., El Ghzizal A., Chebabhi A., Taoussi M. Improved DTC strategy of doubly fed induction motor using fuzzy logic controller. *Energy Reports*, 2019, vol. 5, pp. 271-279. doi: https://doi.org/10.1016/j.egyr.2019.02.001.
6. Aissa O., Moulahoum S., Colak I., Babes B., Kabache N. Analysis and experimental evaluation of shunt active power filter for power quality improvement based on predictive direct power control. *Environmental Science and Pollution Research*, 2018, vol. 25, no. 25), pp. 24548-24560. doi: https://doi.org/10.1007/s11356-017-0396-1.
7. Bourouis B., Djeghloud H., Benalla H. Energy efficiency of a 3-level shunt active power filter powered by a fuel-cell / battery DC bus with regulated duty cycles. *Electrical Engineering & Electromechanics*, 2021, no. 5, pp. 30-38. doi: https://doi.org/10.20998/2074-272X.2021.5.05.
8. Chemidi A., Benhabib M.C., Bourouis M.A. Performance improvement of shunt active power filter based on indirect control with a new robust phase-locked loop. *Electrical Engineering & Electromechanics*, 2022, no. 4, pp. 51-56. doi: https://doi.org/10.20998/2074-272X.2022.4.07.
9. Boudechiche G., Sarra M., Aissa O., Lashab A. Intelligent Solar Shunt Active Power Filter Based on Direct Power Control Strategy. *Lecture Notes in Networks and Systems*, 2021, vol. 174, pp. 467-477. doi: https://doi.org/10.1007/978-3-030-63846-7_44.
10. Noguchi T., Tomiki H., Kondo S., Takahashi I. Direct power control of PWM converter without power-source voltage sensors. *IEEE Transactions on Industry Applications*, 1998, vol. 34, no. 3, pp. 473-479. doi: https://doi.org/10.1109/28.673716.
11. Sarra M., Belkaid A., Colak I., Boudechiche G., Kayisli K. Fuzzy-MPPT Controller Based Solar Shunt Active Power Filter. *2022 11th International Conference on Renewable Energy Research and Application (ICRERA)*, 2022, pp. 436-440. doi: https://doi.org/10.1109/ICRERA55966.2022.9922873.
12. Essoussi B., Moutabir A., Bensassi B., Ouchatti A., Zahraoui Y., Benazza B. Power Quality Improvement using a New DPC Switching Table for a Three-Phase SAPF. *International Journal of Robotics and Control Systems*, 2023, vol. 3, no. 3, pp. 510-529. doi: https://doi.org/10.31763/ijrcs.v3i3.1042.
13. Naamane D., Laid Z., Fateh M. Power Quality Improvement Based on Third-Order Sliding Mode Direct Power Control of Microgrid-Connected Photovoltaic System with Battery Storage and Nonlinear Load. *Iranian Journal of Science and Technology, Transactions of Electrical Engineering*, 2023, vol. 47, no. 4, pp. 1473-1490. doi: https://doi.org/10.1007/s40998-023-00627-4.
14. Liu X., Qiu L., Wu W., Ma J., Fang Y., Peng Z., Wang D. Efficient model-free predictive power control for active front-end modular multilevel converter. *International Journal of Electrical Power & Energy Systems*, 2021, vol. 132, art. no. 107058. doi: https://doi.org/10.1016/j.ijepes.2021.107058.
15. Lhachemi H., Prieur C., Trelat E. PI Regulation of a Reaction–Diffusion Equation With Delayed Boundary Control. *IEEE Transactions on Automatic Control*, 2021, vol. 66, no. 4, pp. 1573-1587. doi: *https://doi.org/10.1109/TAC.2020.2996598*.
16. Boudechiche G., Sarra M., Aissa O., Gaubert J.-P., Benlahbib B., Lashab A. Anti-Windup FOPID-Based DPC for SAPF Interconnected to a PV System Tuned Using PSO Algorithm. *European Journal of Electrical Engineering*, 2020, vol. 22, no. 4-5, pp. 313-324. doi: https://doi.org/10.18280/ejee.224-503.
17. Oustaloup A. *La dérivation non entière: théorie, synthèse et applications*. Paris, 1995. 508 p. (Fra).
18. Oustaloup A., Levron F., Mathieu B., Nanot F.M. Frequency-band complex noninteger differentiator: characterization and synthesis. *IEEE Transactions on Circuits and Systems I: Fundamental Theory and Applications*, 2000, vol. 47, no. 1, pp. 25-39. doi: https://doi.org/10.1109/81.817385.
19. Zerzouri N., Ben Si Ali N., Benalia N. A maximum power point tracking of a photovoltaic system connected to a three-phase grid using a variable step size perturb and observe algorithm. *Electrical Engineering & Electromechanics*, 2023, no. 5, pp. 37-46. doi: https://doi.org/10.20998/2074-272X.2023.5.06.
20. Louarem S., Kebbab F.Z., Salhi H., Nouri H. A comparative study of maximum power point tracking techniques for a photovoltaic grid-connected system. *Electrical Engineering & Electromechanics*, 2022, no. 4, pp. 27-33. doi: https://doi.org/10.20998/2074-272X.2022.4.04.
21. Bouafia A., Gaubert J.P., Chaoui A. Direct power control scheme based on disturbance rejection principle for three-phase PWM AC/DC converter under different input voltage conditions. *Journal of Electrical Systems*, 2012, vol. 8, no. 4, pp. 367-383.
22. Abdelkader B., Merabti A., Yamina B. Using PSO algorithm for power flow management enhancement in PV-battery grid systems. *International Journal of Power Electronics and Drive Systems (IJPEDS)*, 2023, vol. 14, no. 1, pp. 413-425. doi: https://doi.org/10.11591/ijpeds.v14.i1.pp413-425.
23. Kennedy J., Eberhart R. *Particle swarm optimization*. *Proceedings of ICNN'95 - International Conference on Neural Networks*, 1995, vol. 4, pp. 1942-1948. doi: https://doi.org/10.1109/ICNN.1995.488968.
24. Benslimane A., Benslimane Y. Increase Stability and Efficiency in PV-Battery-Grid Systems Using PSO Algorithm. *European Journal of Electrical Engineering*, 2022, vol. 24, no. 2, pp. 113-121. doi: https://doi.org/10.18280/ejee.240206.
25. Abd Latiff I., Tokhi M.O. Fast convergence strategy for Particle Swarm Optimization using spread factor. *2009 IEEE Congress on Evolutionary Computation*, 2009, pp. 2693-2700. doi: https://doi.org/10.1109/CEC.2009.4983280.
26. Leopoldino A.L.M., Freitas C.M., Monteiro L.F.C.Analysis of the Hybrid PSO-InC MPPT for Different Partial Shading Conditions. *Advances in Electrical and Computer Engineering*, 2022, vol. 22, no. 2, pp. 29-36. doi: https://doi.org/10.4316/AECE.2022.02004.

Received 19.10.2023
Accepted 15.12.2023
Published 01.05.2024

Ghania Boudechiche[1], *Doctor of Engineering,*
Oualid Aissa[2], *Associate Professor,*
Mustapha Sarra[1], *Full Professor*,
Issam Griche[3], *Associate Professor,*
[1] ETA Laboratory, Electronics Department,
University Mohamed El-Bachir El-Ibrahimi of Bordj Bou Arreridj, Algeria,
e-mail: ghania.boudechiche@univ-bba.dz (Corresponding Author); mustapha.sarra@univ-bba.dz
[2] LPMRN Laboratory, Faculty of Sciences and Technology,
University Mohamed El-Bachir El-Ibrahimi of Bordj Bou Arreridj, Algeria,
e-mail: oualid.aissa@univ-bba.dz
[3] Department of Electrical Engineering,
University of Bouira, Algeria,
e-mail: griche_issam@yahoo.fr

How to cite this article:
Boudechiche G., Aissa O., Sarra M., Griche I. Solar shunt active power filter based on optimized direct power control strategy with disturbance rejection principle. *Electrical Engineering & Electromechanics*, 2024, no. 3, pp. 72-80. doi: https://doi.org/10.20998/2074-272X.2024.3.10

Матеріали приймаються за адресою:
Кафедра "Електричні апарати", НТУ "ХПІ", вул. Кирпичева, 2, м. Харків, 61002, Україна
Електронні варіанти матеріалів по e-mail: a.m.grechko@gmail.com

Довідки за телефонами: +38 067 359 46 96 Гречко Олександр Михайлович

Передплатний індекс: 01216